Vol. 286, No. 2, February 18, 1994 ISSN 0003-2670

ANALYTICA CHIMICA ACTA

An international journal devoted to all branches of analytical chemistry

ELSEVIER

ANALYTICA CHIMICA ACTA

Scope. *Analytica Chimica Acta* publishes original papers, rapid publication letters and reviews dealing with every aspect of modern analytical chemistry. Reviews are normally written by invitation of the editors, who welcome suggestions for subjects. Letters can be published within **four months** of submission. For information on the Letters section, see inside back cover.

Submission of Papers

Americas

Prof. Harry L. Pardue
Department of Chemistry
1393 BRWN Bldg, Purdue University
West Lafayette, IN 47907–1393
USA

Tel:(+1-317) 494 5320
Fax:(+1-317) 496 1200

Computer Techniques

Prof. J.T. Clerc
Universität Bern
Pharmazeutisches Institut
Baltzerstrasse 5, CH-3012 Bern
Switzerland

Tel:(+41-31) 6314191
Fax:(+41-31) 6314198

Prof. Sarah C. Rutan
Department of Chemistry
Virginia Commonwealth University
P.O. Box 2006
Richmond, VA 23284-2006
USA
Tel:(+1-804) 367 1298
Fax:(+1-804) 367 7517

Other Papers

Prof. Alan Townshend
Department of Chemistry
The University
Hull HU6 7RX
Great Britain

Tel:(+44-482) 465027
Fax:(+44-482) 466410

Prof. Willem E. van der Linden
Laboratory for Chemical Analysis
Department of Chemical Technology
Twente University of Technology
P.O. Box 217, 7500 AE Enschede
The Netherlands
Tel:(+31-53) 892629
Fax:(+31-53) 356024

Prof. Paul Worsfold
Dept. of Environmental Sciences
University of Plymouth
Plymouth PL4 8AA
Great Britain

Tel:(+44-752) 233006
Fax:(+44-752) 233009

Submission of an article is understood to imply that the article is original and unpublished and is not being considered for publication elsewhere. *Anal. Chim. Acta* accepts papers in English only. There are no page charges. Manuscripts should conform in layout and style to the papers published in this issue. See inside back cover for "Information for Authors".

Publication. *Analytica Chimica Acta* appears in 16 volumes in 1994 (Vols. 281–296). *Vibrational Spectroscopy* appears in 2 volumes in 1994 (Vols. 6 and 7). Subscriptions are accepted on a prepaid basis only, unless different terms have been previously agreed upon. It is possible to order a combined subscription (*Anal. Chim. Acta* **and** *Vib. Spectrosc.*).
Our p.p.h. (postage, packing and handling) charge includes surface delivery of all issues, except to subscribers in the U.S.A., Canada, Australia, New Zealand, China, India, Israel, South Africa, Malaysia, Thailand, Singapore, South Korea, Taiwan, Pakistan, Hong Kong, Brazil, Argentina and Mexico, who receive all issues by air delivery (S.A.L.–Surface Air Lifted) at no extra cost. For Japan, air delivery requires 25% additional charge of the normal postage and handling charge; for all other countries airmail and S.A.L. charges are available upon request.

Subscription orders. Subscription prices are available upon request from the publisher. Subscription orders can be entered only by calendar year and should be sent to: Elsevier Science B.V., Journals Department, P.O. Box 211, 1000 AE Amsterdam, The Netherlands. Tel: (+31-20) 5803 642, Telex: 18582, Telefax: (+31-20) 5803598, to which requests for sample copies can also be sent. Claims for issues not received should be made within six months of publication of the issues. If not they cannot be honoured free of charge. Readers in the U.S.A. and Canada can contact the following address: Elsevier Science Inc., Journal Information Center, 655 Avenue of the Americas, New York, NY 10010, U.S.A. Tel: (+1-212) 6333750, Telefax: (+1-212) 6333990, for further information, or a free sample copy of this or any other Elsevier Science journal.
Advertisements. Advertisement rates are available from the publisher on request.

US mailing notice – Analytica Chimica Acta (ISSN 0003-2670) is published 3 times a month (total 42 issues) by Elsevier Science B.V. (Molenwerf 1, Postbus 211, 1000 AE Amsterdam). Annual subscription price in the USA US$ 3035.75 (valid in North, Central and South America), including air speed delivery. Second class postage paid at Jamaica, NY 11431. *USA Postmasters*: Send address changes to Anal. Chim. Acta, Publications Expediting, Inc., 200 Meacham Av., Elmont, NY 11003. Airfreight and mailing in the USA by Publications Expediting.

ANALYTICA CHIMICA ACTA

An international journal devoted to all branches of analytical chemistry

(Full texts are incorporated in CJELSEVIER, a file in the Chemical Journals Online database available on STN International; Abstracted, indexed in: Aluminum Abstracts; Anal. Abstr.; Biol. Abstr.; BIOSIS; Chem. Abstr.; Curr. Contents Phys. Chem. Earth Sci.; Engineered Materials Abstracts; Excerpta Medica; Index Med.; Life Sci.; Mass Spectrom. Bull.; Material Business Alerts; Metals Abstracts; Sci. Citation Index)

VOL. 286 NO. 2 CONTENTS FEBRUARY 18, 1994

(Continued overleaf)

Analytica Chimica Acta, 286 (1994) 135–153
Elsevier Science B.V., Amsterdam

Genetic algorithms in wavelength selection: a comparative study

C.B. Lucasius [1], M.L.M. Beckers and G. Kateman

Laboratory for Analytical Chemistry, Faculty of Science, Katholieke Universiteit, Nijmegen, Toernooiveld 1, 6525 ED Nijmegen (Netherlands)

(Received 16th September 1993)

Abstract

This paper presents a comparative study involving a genetic algorithm, simulated annealing, and stepwise elimination, as methods for wavelength selection in multi-component analysis. The wavelength selection criteria used are the selectivity and accuracy after Lorber, and the minimal mean squared error after Sasaki. The genetic algorithm generally performed best. Stepwise elimination performed surprisingly good despite its local search heuristic. Simulated annealing performed worst, which is remarkable in view of the fact that this method is widely praised in the literature for properties similar to those of genetic algorithms, e.g., a probabilistic, non-local search heuristic.

Keywords: Genetic algorithms; Wavelength selection; Data reduction; Multi-component analysis

Multi-component analysis (MCA) is the simultaneous determination of analyte concentrations in a mixture of components (analytes) from their spectra or absorption curves by means of a least squares fit, assuming that Beer-Lambert's law holds. It may greatly speed up the overall analysis time and therefore enjoys much attention. However, poorly defined effects – e.g. overlap of spectral bands, component interactions, deviations from Beer- Lambert's law at high absorbances, etc. – may lead to a bad *accuracy* and *precision*.

A frequently applied strategy to improve the accuracy, is wavelength selection based on criteria such as selectivity and/or sensitivity [1], discussed below; the quality of the data is improved, hence more accurate concentration estimates are obtained.

Correspondence to: C.B. Lucasius, Laboratory for Analytical Chemistry, Faculty of Science, Katholieke Universiteit, Nijmegen, Toernooiveld 1, 6525 ED Nijmegen (Netherlands).

[1] Present address: Department of Chemistry, Dalhousie University, Halifax, NS B3H 4J3 (Canada).

In order to improve the precision, other criteria should be used, e.g. the minimum mean squared error [2], discussed below; the quality of the model is improved, hence more precise concentration estimates are obtained.

The precision generally becomes better as more wavelengths are selected; the best precision is attained when all wavelengths in the spectrum are selected. However, this is accompanied by a loss in accuracy. Thus, since accuracy and precision are two competing objectives, the best compromise between both is often sought through simultaneous optimization.

In the remainder, the following notations are regularly used:

n: number of components contained in the mixture subjected to MCA;

m: number of wavelengths selected from the spectrum, to conduct MCA;

M: number of wavelengths contained in the spectrum.

In this way, the wavelength selection problem can be defined as the problem to select, according to

SSDI 0003-2670(93)E0532-C

some predefined criterion, the optimal subset of m wavelengths among the M wavelengths contained in the spectrum, where $n \leqslant m \leqslant M$.

The next subsections provide an overview of the methods and criteria used in this comparative study, and explain the complexity of the wavelength selection problem, in general.

Methods for wavelength selection

Various methods for wavelength selection have been proposed in the literature [2–8]. Recently, we demonstrated the viability of genetic algorithms (GAs) in tackling wavelength selection problems [9]. The present paper may be regarded as a continuation of that work. In particular, it addresses the question that should logically be asked next: where do GAs stand relative to other search techniques applied in wavelength selection? To obtain a first indication of the answer to this question, a comparison is made with two other search techniques that have been applied before in wavelength selection:

(i) • Stepwise elimination (SE) [5];
(i) • Simulated annealing (SA) KAL89 (see also [3,10]).

Both SE and SA enjoy considerable interest, and are relatively simple to implement.

SE, which probably enjoys the longest tradition of application, is based on a deterministic, local (greedy) search heuristic. Local search is generally deemed as sensitive to getting trapped in local optima, but may nevertheless turn out to be adequate, depending on the nature of the problem.

SA, which has more recently gained popularity, is based on a probabilistic, non-local search heuristic and is therefore generally regarded as robust, i.e. insensitive to getting trapped in local optima. Since GAs, too, are based on a probabilistic, non-local search heuristic, the comparison between the GA and SA may be considered particularly important.

Complexity of wavelength selection

This section briefly inspects the complexity of wavelength selection problems, and how different search strategies deal with that.

Qualitatively, the complexity of wavelength selection problems may be phrased as follows: they can not be solved in an analytical (i.e. deductive) way, hence a search-based (i.e. inductive) strategy, or optimization, is needed. Abovementioned SE, SA, and GA are, of course, just a few examples of search strategies that can be used.

A more quantitative definition of the complexity of wavelength selection problems considers the formal size of the search space, i.e. the collection of all possible subsets of m wavelengths that can be drawn from the source set of M wavelengths. Thereby, it is important to realize that wavelength selection problems belong to the more general class of subset selection problems, and therefore may have certain properties that some subset selection problems are known to have. One such property is *NP*-completeness [11,12]. An *NP*-complete problem is a problem that features the highest level of complexity in that no other problem exists for which it is more difficult to find an algorithm that solves the problem in $O(M^{\alpha})$, or polynomial, time. (M is the problem dimensionality, or, in our case, the number of wavelengths contained in the spectrum; α is a non-negative constant.) That is, any proposed algorithm is likely to solve the problem in $O(\alpha^{M})$, or exponential, time. Strickly, "solving the problem" means that the globally optimal solution, or global solution for short, is found. In many cases, however, it is practically difficult or even impossible to verify whether a particular solution represents the global solution, but it may still be considered acceptable. As a rule, adequate local solutions are found in a considerably shorter time. Also, a particular algorithm that finds the global solution in exponential time, may find adequate local solutions in polynomial time.

A simple example of an exponential time algorithm in wavelength selection, is enumerative search (i.e. systematic, or exhaustive, search). All possible subsets are scanned – i.e. approximately 2^{M} subsets when $n \leqslant m \ll M$, as usually is the case. In this way, enumerative search guarantees that the globally optimal subset will be found. However, its major drawback is that even for moderately sized data sets (typically $100 \leqslant M \leqslant 200$), the time required to obtain the result lies far beyond what is practically feasible.

In order to achieve a running time within reasonable time, other methods scan a much smaller portion of the search space, but thereby always risk missing the global solution. For instance, SE (which, like other incremental stepping heuristics, e.g. [13], can easily be shown to have time complexity $O(M^2)$) samples an extremely tiny portion of the search space due to its local nature; this makes SE generally sensitive to local optima, as pointed out above. SA and GAs, on the other hand, are both generally praised for the fact that they search in a non-local way, yet may find adequate solutions in polynomial time [14–16].

Overview of criteria for subset evaluation

Search may be viewed as a sequence of intendedly improving guesses made at the global solution. In the wavelength selection problem these guesses are candidate subsets of wavelengths proposed by the search heuristic concerned. The candidate subsets are evaluated, i.e. assigned a score, by a predefined objective function, or optimality criterion, or *evaluation criterion*. The scores delivered by the evaluation criterion are used in order to give direction to the search.

(We should comment that the term "evaluation criterion" is not customary in the literature on wavelength selection; instead, one speaks of a "selection criterion". However, the term selection criterion also exists in GA jargon; there it has an entirely different meaning, as becomes clear in below. Thus, the term "evaluation criterion" is used hereafter to avoid confusing ambiguous use of the term "selection criterion".)

The following evaluation criteria are applied in this study:

SEL (Section *Selectivity and sensitivity*);
ACC (Section *Accuracy*);
MMSE (Section *Minimum mean squared error after Sasaki*).

Overview of criteria for method validation

Search methods are mutually compared on the basis of a *method validation criterion*. Various method validation criteria are conceivable, e.g.:

(1) the quality of the solution found by the method;
(2) the amount of computation time required by the method;
(3) the amount of computer memory required by the method;
(4) the ease of developing and implementing the method;
(5) the ease of using the method.

For the purposes of this pilot study, mainly the first among these general method validation criteria is considered. It can be defined more specifically in different ways; the quality criteria used in this study are:

HIT (Section *Hitting the global optimum*);
PE (Section *Percentage error and relative standard deviation*);
RSD(same section).

As becomes apparent below, these criteria have in common that they verify the extent to which the solution found by the search method concerned, satisfies available foreknowledge about the problem domain.

THEORY

This section discusses the following evaluation criteria for wavelength selection in MCA: SEL (selectivity) and ACC (accuracy) after Lorber [17] and MMSE (minimum mean squared error) after Sasaki et al. [2].

SEL is a measure of the degree of non-overlap between the different component spectra. The subset of wavelengths that features the lowest overall overlap (hence the highest overall selectivity) should yield the most accurate component concentration estimation.

MMSE is a measure of the variance in the concentration vector (originating from the expectation of the noise). In general, larger subsets of wavelengths yield a smaller MMSE, i.e. a better precision in the concentration estimates; simultaneously, though, the accuracy in those estimates becomes worse, as pointed out above.

ACC is actually not a measure of accuracy (notwithstanding this name). It is in fact composed of two precisions, one for the calibration and the other for the total measurement. Like MMSE, it promotes the selection of large subsets

of wavelengths to achieve a better precision in the concentration estimates.

Summarizing, SEL is a measure of accuracy, while MMSE and ACC are measures of precision.

From here on, the following notations are used. Matrices are denoted by uppercase characters. Vectors are denoted by lowercase characters. The superscripts T and t denote transposed matrices and vectors, respectively. $\|\mathbf{x}\|$ is the Euclidian norm of arbitrary vector $\mathbf{x}$; it is calculated as the square root of the sum of the squared elements. $\mathbf{I}$ is the identity matrix. The subscript i denotes a selected wavelength ($i = 1,\ldots,m$). The subscript j denotes a component ($j = 1,\ldots,n$).

Multi-component analysis

For the determination of component concentrations in a mixture, the linear additive model after Beer-Lambert is frequently applied:

$$d_1 = a_{11} \cdot c_1 + a_{12} \cdot c_2 + \ldots + a_{1n} \cdot c_n$$
$$d_2 = a_{21} \cdot c_1 + a_{22} \cdot c_2 + \ldots + a_{2n} \cdot c_n$$
$$\vdots$$
$$d_m = a_{m1} \cdot c_1 + a_{m2} \cdot c_2 + \ldots + a_{mn} \cdot c_n$$

where d_i is the measured absorbance at wavelength i, and a_{ij} is the known absorption coefficient at wavelength i for component j. Using matrix notation, the linear system of equations can be abbreviated as:

$$\mathbf{d} = \mathbf{S} \cdot \mathbf{c}$$

or

$$\mathbf{d} = \mathbf{A} \cdot \mathbf{C}_0^{-1} \cdot \mathbf{c} \qquad (1)$$

where

- $\mathbf{d}$: m-dimensional response vector (absorbances);
- $\mathbf{c}$: n-dimensional concentration vector;
- $\mathbf{S}$: $m \times n$ sensitivity matrix;
- $\mathbf{A}$: $m \times n$ scaled sensitivity matrix (molar absorption coefficients) or calibration matrix;
- $\mathbf{C}_0^{-1}$: $n \times n$ diagonal matrix of inverse concentrations ($c_{0,i}$) that correspond to the absorption coefficients in $\mathbf{A}$.

For the moment, assume $m = M$ (all wavelengths selected). Finding the solution of Eqn. 1 is particularly easy when every component has a strong absorbance peak at a particular wavelength, without interference of the other components at that wavelength. This is for instance the case in a two-component system ($n = 2$) where component j_a absorbs strongly at wavelength i_a but hardly at wavelength i_b, whereas component j_b absorbs strongly at wavelength i_b but hardly at wavelength i_a. At these two wavelengths there is (almost) no overlap of the absorption curves, hence the individual selectivities, and thus the overall selectivity, are high. Equation 1 can then be solved for the appropriate two wavelengths (i_a and i_b, $m = 2$) selected among the M wavelengths.

Similarly, in a highly selective n-component system, Eqn. 1 can be solved by selecting the appropriate $m = n$ wavelengths among the M wavelengths. However, many multi-component systems are poorly selective in practice (e.g. in UV spectrometry), as different components often absorb strongly at the same wavelengths. Equation 1 can then only be solved by using $m > n$ wavelengths among the M wavelengths, provided that the individual absorption curves are not linearly dependent.

Several factors can influence the mutual linear dependency of the individual absorption curves, e.g. pH, ionic strength, the concentration of salts or other interferents. It is generally not evident how these factors should be manipulated to reduce the linear dependency. On the other hand, wavelength selection based on criteria such as selectivity or sensitivity, can be used to select a subset of wavelengths in which the linear dependency between individual components is reduced as much as possible. By using this subset, the overlap between the individual absortion curves is reduced, hence the selectivity is maximal; or, phrased mathematically, the molar absorption coefficient vectors of the individual components approach orthogonality as much as possible.

The formal solution of Eqn. 1 is given by the least-squares fit (estimate):

$$\hat{\mathbf{c}} = (\mathbf{S}^T \cdot \mathbf{S})^{-1} \cdot \mathbf{S}^T \cdot \mathbf{d}$$

when $m = n$ or when $m > n$ and the rank of $\mathbf{S}$ (or $\mathbf{A}$) is n. However, this approach fails when the rank of $\mathbf{S}$ (or $\mathbf{A}$) is k, and $k < n$; the problem

must then be solved using the $n \times m$ generalized inverse $\mathbf{S}^+$ (or $\mathbf{A}^+$) [18]:

$$\hat{\mathbf{c}} = \mathbf{S}^+ \cdot \mathbf{d}$$

or

$$\hat{\mathbf{c}} = \mathbf{A}^+ \cdot \mathbf{C}_0 \cdot \mathbf{d} \qquad (2)$$

The generalized inverse is calculated by means of a singular value decomposition (SVD) [19,20].

Figures of merit after Lorber

The figures of merit introduced by Lorber [17] are a series of quality features for an analytical method that include the error propagation, the signal-to-noise ratio, the limit of detection, the precision, the accuracy, the sensitivity, and the selectivity. These figures are all calculated using the *net analyte signal*, which is defined as that part of the spectrum of a component in a mixture that is orthogonal to the spectra of the other components in that mixture. (Only the orthogonal part is relevant, because the part of the spectrum of a particular component that is not orthogonal to the other spectra, is a linear combination of the spectra of the other components.)

The net analyte signal, $\mathbf{a}_j^*$, is defined as a multiplication of $\mathbf{a}_j$ with its projection matrix:

$$\mathbf{a}_j^* = \left(\mathbf{I} - \mathbf{A}_j \cdot \mathbf{A}_j^+\right) \cdot \mathbf{a}_j$$

where: $\mathbf{a}_j$ is the jth column vector in $\mathbf{A}$; $\mathbf{A}_j$ is the $\mathbf{A}$-without-$\mathbf{a}_j$ matrix, hence $m \times (n-1)$; $\mathbf{A}_j^+$ is the generalized inverse of $\mathbf{A}_j$.

Likewise

$$\mathbf{d}_j^* = \left(\mathbf{I} - \mathbf{A}_j \cdot \mathbf{A}_j^+\right) \cdot \mathbf{d}_j$$

Selectivity and sensitivity. When the jth row of $\mathbf{A}^+$ is denoted by $\mathbf{y}_j$, then for each component separately Eqn. 2 becomes $c_j = c_{0,j} \cdot \mathbf{y}_j^t \cdot \mathbf{d}$. The net analyte signal is now calculated as [17]:

$$\mathbf{a}_j^* = \frac{\mathbf{y}_j}{\|\mathbf{y}_j\|^2}$$

All figures of merit defined by Lorber are expressed in terms of this formulation of the net analyte signal or its vector norm. For instance, Lorber defines selectivity for the jth component as:

$$\mathrm{SEL}_j = \frac{\|\mathbf{a}_j^*\|}{\|\mathbf{a}_j\|} \qquad (3)$$

The sensitivity for each individual components is now given by:

$$\mathrm{SEN}_j = \frac{\|\mathbf{a}_j^*\|}{\mathbf{c}_{0,j}} \qquad (4)$$

The overall selectivity, i.e. the selectivity for the mixture, is defined as:

$$\mathrm{SEL} = \frac{n}{\Sigma_{j=1}^{n} \mathrm{SEL}_j^{-1}}$$

(The perhaps more straightforward definition $\mathrm{SEL} = \Sigma_{j=1}^{n} \mathrm{SEL}_j / n$ is not adequate, because the overall selectivity is dominated by the component with the worst selectivity.)

Precision For $m > n$, the error in $\mathbf{d}$ (the response data) may be calculated as:

$$\epsilon_d = \left[\frac{\mathbf{d}^t \cdot \left(\mathbf{I} - \mathbf{A} \cdot \mathbf{A}^+\right) \cdot \mathbf{d}}{m-n}\right]^{\frac{1}{2}}$$

or estimated by [7]:

$$\epsilon_d = \left[\frac{\left(\mathbf{d} - \hat{\mathbf{d}}\right)^2}{m-n}\right]^{\frac{1}{2}}$$

where $\hat{\mathbf{d}}$ is the estimated $\mathbf{d}$. For $m = n$, ϵ_d has to be determined in a different way, e.g. Malinowski's error function [8]. However, as the noise in the data may be expected to exhibit normal behavior (zero mean, constant variance), ϵ_d may be assumed constant. Zscheile [21] found $\epsilon_d = 2.0\%$ for a data set that we also use in this study (see below). Lorber found $\epsilon_d = 1.3\%$ for the same data set, but he continued to use 2.0% nevertheless [17].

The relative precision in $\mathbf{d}$ for the sample, is the ratio of ϵ_d to the total measurement $\|\mathbf{d}\|$.

Accuracy. The accuracy in an analytical quantity is influenced by several factors that cause deviation from its true value, namely:

(1) the precision in the measured response of the unknown sample;
(2) the precision in measuring the calibration data;
(3) inadequacy of the assumed linear model to describe the true model.

To find an expression for the accuracy, Lorber [17] assumed that only the first two factors con-

tribute to the accuracy. The accuracy can then be defined as the sum of the two contributing precisions. Hence, it is expected that upon using this evaluation criterion, the precision in the concentration estimation will improve; indeed, the term accuracy is not used in its proper sence, as pointed out above. Moreover, since factor 3 is not incorporated in the definition, it may be expected that systematic errors cannot be detected.

Assuming $\epsilon_d = \epsilon_a$ (error of calibration), it can be deduced [22] that Lorber's accuracy is given by:

$$\mathrm{ACC}_j = \left(\frac{1}{\mathrm{SEL}_j \cdot \|\mathbf{a}_j\|} + \frac{1}{\mathrm{SEN}_j \cdot c_j} \right) \cdot \epsilon_d$$

where SEL_j and SEN_j are as defined in Eqns. 3 and 4, respectively.

The overall accuracy, i.e. the accuracy for the mixture, is defined as [6]:

$$\mathsf{ACC} = \frac{\Sigma_{j=1}^{n} \mathrm{ACC}_j}{n} \qquad (6)$$

Minimum mean squared error after Sasaki

The minimum mean squared error criterion was used by Sasaki et al. [2]. It calculates the difference between the theoretical component concentrations and their estimates, hence the variance in the concentration vector, that originates from the expectation value of the noise.

Starting from Beer-Lambert's linear additive model $\mathbf{d} = \mathbf{A} \cdot \mathbf{c} + \mathbf{e}$, for which the solution $\hat{\mathbf{c}} = \mathbf{A}^{-1} \cdot \mathbf{d}$ applies, provided $\mathbf{A}$ is square and not singular, the minimum mean squared error is defined as:

$$\mathsf{MMSE} = E\left\{ \sum_{j=1}^{n} | c_j - \hat{c}_j |^2 \right\} \rightarrow \min$$

where E is the expectation operator, and $\hat{c}_j$ is the estimated c_j. This equation can be rewritten as:

$$\mathsf{MMSE} = Tr\left\{ \mathbf{A}^{-1} \cdot \mathbf{W}^{-1} \cdot (\mathbf{A}^{-1})^T \right\}$$

where Tr is the trace operator, and $\mathbf{W} = E\{\mathbf{e} \cdot \mathbf{e}^t\}$, the $n \times n$ autocorrelation matrix of the noise, $\mathbf{e}$.

Assuming that $\mathbf{e}$ obeys an uncorrelated process with zero mean and constant variance σ^2, this equation can be rewritten as:

$$\mathsf{MMSE} = \sigma^2 \cdot Tr\left\{ (\mathbf{A}^T \cdot \mathbf{A})^{-1} \right\}$$

It applies to the determinate case. In the overdeterminate case one should use:

$$\mathsf{MMSE} = \sigma^2 \cdot Tr\left\{ \mathbf{A}^{+} \cdot (\mathbf{A}^T)^{+} \right\} \qquad (7)$$

Use of the evaluation criteria

Summarizing, the evaluation criteria of importance in this study are: the maximization criterion SEL (Eqn. 5) for improvement of accuracy, and the minimization criteria ACC (Eqn. 6) and MMSE (Eqn. 7) for improvement of precision.

For conformity, we decided to cast ACC and MMSE into maximization criteria. Equivalent maximization criteria can be accomplished in several ways, e.g. $-\mathsf{ACC}$ and $-\mathsf{MMSE}$, respectively, or ACC^{-1} and MMSE^{-1}, respectively.

Numerical values delivered by maximization criteria are referred to by different names in the literature – e.g. utility, quality, profit, merit, record, rate, score, fitness, etc. – depending mainly on the problem domain or search method concerned. The term fitness is part of GA jargon, but will nevertheless be used hereafter in descriptions concerning SA and SE as well, for further conformity.

Casting ACC and MMSE into equivalent maximization criteria does, however, not change the aforementioned fact that the subset of wavelengths considered as globally optimal, is the total set of wavelengths ($m = M$). Hence, since the solution is known in advance, search based on ACC or MMSE alone, as opposed to search based on SEL alone, is not particularly challenging.

More importantly, though, in view of the aforementioned trade-off between accuracy and precision, combined criteria such as e.g. SEL/ACC and SEL/MMSE seem better choices from an analytical-chemical point of view. However, combined criteria complicate the search and thus would unduly interfere with our main purpose to

better understand the search methods on a comparative basis.

Based on the above considerations, the following evaluation criteria were chosen in this study:
(i) SEL;
(ii) $(m\text{ACC})^{-1}$;
(iii) $(m\text{MMSE})^{-1}$.
(In the latter two cases, the multiplication by m is to ensure that optimal subsets of wavelengths may well comprise $m < M$ wavelengths.)

EXPERIMENTAL

This section briefly describes the search methods used for wavelength selection in this study, and the method validation criteria used for their mutual comparison.

For the comparison to be meaningful, several conditions are kept invariant with respect to the methods. These are discussed first.

Invariant conditions

Invariant conditions in this comparative study are: the data set, the representation of candidate subsets of wavelengths, the computer language in which the methods were programmed, the computer hardware platform on which the programs for the methods were run, and how the solution obtained after a run is defined.

Data set. The data set used in this study is a set of absorption coefficients (a_{ij}) for the four RNA nucleotides A, C, G, and U ($n = 4$), measured at 36 equidistant UV wavelengths ($M = 36$), and a spectrum (**d**) of a mixture of these compounds, measured at these wavelenths. This data set – hereafter called `RNA.dat` – was obtained from the literature [21] and has been analyzed in numerous other studies as well.

The choice of `RNA.dat` is primarily motivated by the fact that it is accompanied by foreknowledge which can be used for verification of results obtained by the search methods. (Verification is considered important at the present stage wherein still much can be learned as to how the search methods, especially the GA, perform in wavelength selection.) The following two avenues for verification are available.

Firstly, since `RNA.dat` is comparatively small ($M = 36$), it is possible to find globally optimal subsets of wavelengths through enumerative search (see above) within merely a night of computation on a fast computer. In this way, the GA, SA, and SE can be judged as to whether they manage to find the global optimum.

Secondly, since the mixture was created from known amounts of components, the true concentrations, c_j, of these components are known. In this way, the concentrations estimated from any subset of wavelengths (using Eqn. 2) can be compared with the true concentrations. The true concentrations are [21]:
c_1: 0.0000144 moles A/liter;
c_2: 0.0000155 moles C/liter;
c_3: 0.0000151 moles G/liter;
c_4: 0.0000154 moles U/liter.

Representation. Candidate subsets in any of the methods used are represented, or encoded, as binary strings, or *bitstrings*. Each bitstring comprises M bits that mask the M wavelengths in the spectrum: bit value 1 stands for "select the corresponding wavelength", whereas bit value 0 stands for "do not select the corresponding wavelength". An example of this so-called *binary subset encoding* [23–25] is the following 36-bit bitstring:

101010101010101010101010101010101010

which proposes the selection of all odd-indexed wavelengths among 36 wavelengths.

It is important to realize that binary subset encoding, as described above for the purpose of wavelength selection, is constrained in that the number of 1-bits in a bitstring – or, effectively, the number of selected wavelengths – may not be smaller than n (since otherwise Eqn. 1 can not be solved). How this encoding constraint is observed by the methods used, follows from their description given below.

Software. All software needed for this study was programmed in the computer language C (ANSI standard). The SA and SE methods were programmed from scratch. The GA was programmed using the software library GATES [24,25], comprising domain-independent routines (written in C, ANSI standard).

The aforementioned SVD routine for computation of the generalized inverse was adopted from [26] (with minor adaptations to achieve a better interfacing with other routines).

Hardware. The programs for the methods were run on a SUN computer (Sparc Station 2), under the UNIX operating system.

Definition of the solution. The solution found in a run by any of the methods, is defined as: the best candidate subset of wavelengths encountered during the run.

Methods

This section briefly describes the GA, SA, and SE as they were implemented for the purposes of this study.

GA. GAs comprise a large family of non-local search techniques [15,16,27–31] which employ a probabilistic search heuristic based loosely upon the principles of natural evolution according to Darwin [32]; a detailed general treatise aimed at chemists can be found in [23,33,34]. Recently, GAs have been applied to a variety of subset selection problems [9,13,35–37], including wavelength selection problems in UV and NIR spectrometry.

In general, GAs maintain a population of N strings which represent candidate solutions that are in a constant competition for survival. Using generalized evolutionary operators such as selection, recombination, and mutation, the population evolves dynamically towards improvement in a number of time steps, or generations. Thereby, N (a control parameter) remains constant; a suitable value for N normally lies between 50 and 500.

Our GA operates as follows. First, all bits in the N bitstrings comprising the population are set to a random binary value (0 or 1). In this form, the population enters the evolution cycle, which is briefly discussed next.

The first step in the evolution cycle involves decoding the bitstrings, and to evaluate the thus obtained candidate subsets of wavelengths using the evaluation criterion of interest (see above). In doing so, the fitnesses of the bitstrings are obtained.

The second step in the evolution cycle involves scaling the fitnesses in a way considered appropriate for the selection criterion used in the next step: reproduction. The fitness scaling proceeds in two consecutive steps: (1) linear scaling, and (2) normalization; further details can be found in, inter alia, [23,25].

The third step in the evolution cycle is reproduction: N copies are made of N strings indicated, or "selected", in the population. The strings are selected probabilistically with an expected rate proportional to their scaled fitness; this selection criterion has become known as roulette selection. Accordingly, the new set of N bitstrings, called the temporary population, may be expected to feature a higher fitness, on average. (*Note:* the selection criterion mentioned here performs selection of bitstrings, i.e. not of wavelengths.)

The fourth step in the evolution cycle is a random pairing of the bitstrings in the temporary population. Pairing serves the next step: recombination.

The fifth step in the evolution cycle is the application of a recombination procedure: a recombination operator is applied to all pairs of bitstrings assigned in the preceding step. The bitstrings in each pair of bitstrings exchange fractions in a way such that the loss of implicit information relevant for the search task is minimal; this principle is generally referred to as the *building block principle*. The recombination operator in the GA used here is **B_MX**, discussed in, inter alia, [23,25].

The sixth step in the evolution cycle is the application of a mutation procedure: a mutation operator is applied to all bitstrings in the temporary population in order to invert the value of a small fraction of randomly selected bits. This serves to ensure that all parts of the search space remain reachable for the recombination operator, especially in the later stages of the search when population diversity is lost. The mutation operator in the GA used here is **B_M**, discussed in, inter alia, [23,25].

The seventh step closes the evolution cycle: the population is replaced by the temporary population.

The following remarks on the above GA scheme scheme are in place:

(1) Related to the probabilistic nature of the GA, a termination criterion needs to be predefined, which, if it succeeds, stops execution; the best-so-far solution is then presented to the user. In our case, the termination criterion is simple: it succeeds after a predetermined target number of generations, chosen amply beyond the approximate point where one expects convergence to set in; this point can be found empirically by inspecting some preliminary runs.

(2) Strickly speaking, the bitstring modification operators – **B_MX** and **B_M** – are not compatible with aforementioned encoding constraint, because they do not include provisions against bitstring modifications that result in a number of 1-bits smaller than n. However, the rate by which illegal bitstrings are incidentally produced may be considered extremely low. This may be appreciated intuitively by addressing the following question (assuming data set `RNA.dat`, i.e. $M = 36$ and $n = 4$): what is the probability by which the number of 1-bits that occur among 36 random bit values is less than 4? The answer is: $1 + 36 + 630 + 7140$ (the number of subsets comprising 0, 1, 2 or 3 items that can be drawn from 36 items) divided by 2^{36} (the total number of subsets that can be drawn from 36 items) – i.e. approximately $1.1 \cdot 10^{-7}$. Of course, this is merely a rough estimate, as the GA samples the search space probabilistically rather than randomly. Nonetheless, it was empirically established that the rate at which the GA violates the encoding constraint as it searches, is indeed extremely low; on the rare occasions that an illegal bitstring is incidentally produced, it is simply lethalized (i.e. assigned zero fitness).

(3) Whether the recombination operator **B_MX** complies with the building block principle, depends on whether the sequence of M bits comprising a bitstring is chosen such that bits which correlate strongly/weakly (in the sense of contributions to the bitstring's fitness) are placed at close/remote distance in the bitstring. A sequence for which this is the case, is called a *connected sequence* of bits; for details, the reader is referred to [25].

To make an educated guess at a connected sequence of bits is, however, difficult in complex wavelength selection problems. In fact, one is forced to choose an ad hoc sequence of bits, since empirically testing **B_MX** for all $(M!)$ possible sequences of bits is practically not feasible.

In our case (`RNA.dat`), too, no effort was made to find an optimal sequence of bits; the order of the 36 bits comprising a bitstring was simply chosen according to the numerical order of the corresponding wavelengths as they occur in the spectrum. We briefly examined the implications of this choice by checking whether the recombination operator **B_UX** – discussed in, inter alia, [23,25] – would perform better. (The performance of **B_UX** is independent of the sequence in which the bits appear in a bitstring; this operator may be considered a better choice when a high proportion of the bits are correlated.) It turned out that **B_UX** and **B_MX** perform comparably, hence there was no apparent need to switch to **B_UX**.

Configuration. After a fair amount of hand optimization based on general guidelines in the literature [16,38] (and on our past experience with GAs), roughly the best configuration was found to be:

N	: ?
Maximum generation	: 500
Selective reproduction	: fitness-proportional
Fitness scaling mode	: linear
Sensitivity	: 6.0
Recombination mode	: **B_MX** (2 breakpoints)
p_r	: ?
Mutation mode	: **B_M**
p_m	: ?

(For a more detailed explanation of the configurational terminology, the reader is referred to [23,25].) As indicated by ?-marks, the entries for the parameters N, p_r, and p_m are variable. In this way, an experimental design involving these parameters can be conducted, thus taking into account the empirical fact that optimal GA configuration generally depends to some extent on the problem domain implied by the evaluation criterion used; it is expected that these parameters substantially affect performance. A central composite experimental design was chosen [39].

Results obtained in using this design are shown below.

(It should be emphasized that the experimental design was only used in order to obtain a configuration that is likely to result in finding the global optimum; it was not used to fit the responses according to an assumed model.)

SA. SA comprises a family of non-local optimization methods, which employ probabilistic search heuristics based on principles of physical cooling of a solid [14,40,41]. More precisely, SA is based on the analogy between the simulation of the annealing of a solid and the problem of solving a large optimization problem. In its original meaning, annealing is the process of heating a solid and then cooling it slowly so as to remove strain and crystal imperfections. In this process, the free energy of the solid is minimized. The initial heating is necessary to avoid that the system gets trapped into a local minimum. Virtually every well-behaved function can be viewed as the free energy of some system, hence studying and imitating how nature reaches a minimum through an annealing process, indeed potentially yields optimizing algorithms.

An annealing process, either real or simulated (SA), can be modeled as a so-called Markov process: a sequence of states that are interconnected by state transitions at consecutive time steps; in simulated annealing applied to the wavelength selection problem, the states are candidate subsets of wavelengths.

In real annealing, the transition probability P_{vw} between consecutive states v and w is given by:

$$P_{vw} = \begin{cases} \exp\left(\dfrac{-(\mathscr{E}_w - \mathscr{E}_v)}{kT}\right) & \text{if } \mathscr{E}_w > \mathscr{E}_v \\ 1 & \text{otherwise} \end{cases}$$

where $\exp(-(\mathscr{E}_v - \mathscr{E}_w)/(kT))$ is the so-called Metropolis factor; $\mathscr{E}$ is free energy (which must be minimized), k is a constant (the Boltzmann constant), and T is temperature. Note that trials for transitions to lower or equal energy ($\mathscr{E}_w \leqslant \mathscr{E}_v$) are always accepted. In contrast, trials for transitions to higher energy ($\mathscr{E}_w > \mathscr{E}_v$) are accepted only probabilistically: upon failure, the trial is rejected and a new transition is tried; upon success, the unfavorable state is accepted, thus enabling escape of local minima.

In SA, the transition probability P_{vw} between consecutive states v and w is given by:

$$P_{vw} = \begin{cases} \exp\left(\dfrac{\mathscr{F}_w - \mathscr{F}_v}{\tau}\right) & \text{if } \mathscr{F}_w < \mathscr{F}_v \\ 1 & \text{otherwise} \end{cases}$$

where $\exp((\mathscr{F}_w - \mathscr{F}_v)/\tau)$ is an equivalent of the Metropolis factor; $\mathscr{F}$ is fitness (which must be maximized), τ is a control parameter (an equivalent of temperature). Note that trials for transitions to higher or equal fitness ($\mathscr{F}_w \geqslant \mathscr{F}_v$) are always accepted. In contrast, trials for transitions to lower fitness ($\mathscr{F}_w < \mathscr{F}_v$) are accepted only probabilistically: upon failure, the trial is rejected and a new transition is tried; upon success, the unfavorable state is accepted, thus enabling escape of local maxima; this is, however, less likely to happen when τ is decreased.

An important diagnostic parameter in SA is the so-called accepts/trials ratio, hereafter abbreviated as A/T; it is of importance in optimizing SA configuration.

In practice, SA is usually conducted as follows [41]. The search is subdivided into a number of consecutive chains. These so-called Markov chains are equally sized, i.e. they comprise the same number of states. The length of the Markov chains and their number, are control parameters. According to an empirical rule of thumb, the initial value of τ should be such that A/T lies approximately between 0.7 and 1.0. In going from one Markov chain to the next, τ is decreased by a small amount; this results in a lower expected A/T, thus forcing the search to converge. Many functions are conceivable that describe the decrement in τ in dependence of the serial index of the next Markov chain; in many cases, including ours, an exponentially decaying function is chosen. The SA is terminated when A/T approaches 0.0. Note that in SA (as described here), like in the GA (as described above), the termination criterion is based on empirical observations.

The extent to which one state is perturbed for a transition to the next state, is called the step

size – another control parameter in SA. In our case, the first state is a random M-bit bitstring, and each transition from one bitstring to the next, is performed by flipping a predetermined number of randomly selected bits in the bitstring; thus, the step size is measured as a Hamming distance. Note that the bitstrings are modified in a way similar to how the mutation operator **B M** in the GA modifies bitstrings. However, like in the GA, the rate by which illegal bitstrings are incidentally produced is empirically found to be extremely low.

Recently Kalivas introduced an alternative form of the simulated annealing algorithm in analytical chemistry, which he called generalized simulated annealing (GSA) [10]. In GSA, the Metropolis factor has been modified to:

$$P_{vw} = \exp\left(\frac{\tau(\mathscr{F}_v - \mathscr{F}_w)}{\mathscr{F}_v - \mathscr{F}_o}\right)$$

where $\mathscr{F}_o$ is the optimal fitness value. Evidently, here a difficulty lies in the fact that the optimal fitness value has to be known beforehand. (In part, a way around this problem is to adjust this parameter during a run, i.e. to replace it by the best-so-far fitness value.) In our study, all experiments involving SA were repeated using GSA, but as the results were generally not any better, they are omitted from this paper.

Configuration. After a fair amount of hand optimization based on general guidelines in the literature [41], roughly the best configuration was found to be:

Length of Markov chains : 100,000
Number of Markov chains : 40
Step size : 5 bits

Because of the analogy with cooling a solid, in SA a *specific heat* parameter can be defined. It is defined as the average fitness observed in a Markov chain, divided by the decrement in τ after that Markov chain is completed. When a solid is slowly cooled, the specific heat suddenly increases when a phase transition takes place. Hence, finding a value of τ at which the specific heat suddenly increases, should indicate that an important change has taken place. (This can also be deduced from other factors that are monitored during a run. For instance, at a phase transition, also the average fitness observed in a Markov chain will increase, while the standard deviation thereof will decrease.) It follows from the theory of SA [41] that one is likely to find the global optimum at $\tau = \tau_o$ – the value of τ where the specific heat is maximal, i.e. where a phase transition takes place. Once τ_o has been found, a new SA run – involving a *single, longer* Markov chain at $\tau = \tau_o$ – is performed to search for the optimal solution; this Markov chain is longer by a factor $(A/T)^{-1}$.

SE. SE is conducted as follows. Starting from a bitstring comprised of 1-bits only (i.e. $m = M$, all wavelengths selected), in each among $M - n$ iterations that follow, a 1-bit is replaced by a 0- bit; the 1-bit is selected according the largest gain in fitness observed upon the replacement. Thus, when SE terminates, the number of 1-bits in the bitstring has been reduced to n.

Evidently, SE is deterministic (non-probabilistic). Also, SE automatically complies with aforementioned encoding constraint, as, evidently, the number of 1-bits in the string never becomes less than n during the search.

Configuration. SE can not be configured, since it is free of control parameters.

Method validation criteria

This section describes the method validation criteria used in this study: HIT (hitting the global optimum in a run), PE (percentage error in the concentration estimate of a component), and RSD (relative standard deviation in the concentration estimate of a component). These criteria have in common that they judge search methods according to the quality of the solution found, as pointed out in above.

It is important to realize that no definite conclusions can be drawn from validations of the GA and SA. This may be ascribed to two sources of error. The first source of error lies in the fact that the GA and SA are probabilistic; hence, since only a finite number of runs can be carried out, statistical uncertainty in the outcome always exists. The second source of error resides in the fact that the optimal configuration of the GA and SA is generally unknown, which should be ascribed

to the huge and complex configuration space; at best, the comparison between the GA and SA can be made fair by spending an equal amount of effective effort in empirically optimizing their configuration.

Hitting the global optimum. HIT is a boolean method validation criterion, defined as the answer to the question: has the globally optimal subset of wavelengths – known in advance by way of enumerative search – been hit (i.e. found) in a run performed by the search method concerned? HIT is considered the most important method validation criterion in this study.

Percentage error and relative standard deviation. Both PE and RSD compare a component concentration, estimated from a particular subset of wavelengths (using Eqn. 2), with the true component concentration; PE is a measure of the accuracy in this estimate, whereas RSD is a measure of the precision in this estimate.

PE is defined in a straightforward way as:

$$\mathrm{PE} = \frac{|c_j - \hat{c}_j|}{c_j} \cdot 100\%$$

where: c_j is the true concentration of component j (see Section *Data set*); $\hat{c}_j$ is the estimated concentration of component j, for a particular subset of wavelengths.

RSD is defined as [21]:

$$\mathrm{RSD} = \frac{s_{c_j}}{\| \bar{c}_j \|} \cdot 100\%$$

where $\bar{c}_j$ (mean) and s_{c_j} (standard deviation) are obtained as follows:

(1) Solve Eqn. 1, and store the value thereby obtained for **c** (Eqn. 2);
(2) Form **A′** (a new value for **A**) and **d′** (a new value for **d**) by setting:
$a'_{ij} = a_{ij} + \epsilon/100 \cdot u \cdot a_{ij}$
$d'_j = d_j + \epsilon/100 \cdot u \cdot d_j$
where: $\epsilon = \epsilon_a = \epsilon_d = 2\%$ (the RSD in a_{ij} and d_j, see Section *Precision* above); u is a standard normally distributed random variable (mean 0 and standard deviation 1);
(3) Solve Eqn. 1 using $\mathbf{A} = \mathbf{A}'$ and $\mathbf{d} = \mathbf{d}'$, and store the new value, **c′**, thereby obtained for **c**;
(4) Repeat steps 2 and 3 many times (here 100) and then go to step 5;
(5) Using the sequence of values **c′** for **c** thus obtained, calculate the mean and standard deviation of each c_j – that is, $\bar{c}_j$ and s_{c_j}, respectively.

From the above described procedure, it becomes clear that RSD is a measure of the instability of Eqn. 1, i.e. a measure of the susceptibility to changes in the solution of the system caused by small changes in the absorption coefficients, a_{ij}. It is assumed that the RSD is larger than ϵ, hence Eqn. 1 will amplify the original error in the data (a_{ij}).

RESULTS AND DISCUSSION

This section discusses the results obtained in the experimental strategy implied by the foregoing.

Using selectivity after Lorber

Based on the evaluation criterion SEL, first the global solution is determined; then, the solutions found by SE, the GA, and SA, respectively, are presented and commented on; finally, concentration estimates derived from the global solution are examined.

The global solution. Enumerative search was conducted in order to find the globally optimal subset of wavelengths according to SEL; results are listed in Table 1. In this way, it became possible to validate the GA, SA, and SE, as to whether they succeed in HITting the SEL-optimal subset.

SE. The results of SE using SEL are listed in Table 2.

TABLE 1

Enumerative search using SEL. The bold-faced line indicates the global optimum

m	SEL	Subset
4	0.2362	1/11/29/36
5	**0.2402**	**1/11/29/35/36**
6	0.2387	1/3/12/29/35/36
7	0.2372	1/2/12/28/29/35/36

TABLE 2

SE using SEL

m	SEL	Subset
4	0.2355	1/12/28/36
5	0.2367	1/12/28/35/36
6	0.2373	1/2/12/28/35/36
7	0.2372	1/2/12/28/29/35/36

Although the global solution was not HIT, the solution found (for $m = 6$) is near-optimal and therefore probably adequate, in practice. This may be considered an important result, since SE conducts only nearly 660 evaluations in the search space [9], which compares very favorably with the formal size of the search space (ca. 2^{36}, or ca. $6.87 \cdot 10^{10}$). However, it should be borne in mind that since SE employs a local search heuristic, the fitness of the solution found, may drop drastically below optimum when more complex, larger data sets are concerned; SE seems an unstable strategy.

GA. The results of the GA using SEL, obtained in 15 experiments according to a three-factor central composite design, are listed in Table 3.

It can be seen that the global solution was HIT for two configurations (experiments 10 and 13). Upon repeating the experiments a number of times (for different random initial populations), it was observed that these configurations sometimes fail to HIT the global solution, whereas other configurations succeed in HITting the global solution. This underscores two important aspects of robustness that are typical of GAs in general [23]: (1) GAs are not easily misled by sub-optima in the search space; (2) GA performance is not dramatically affected by small changes in configuration.

TABLE 3

GA using SEL, in 15 experiments according to a three-factor central composite design. Bold-faced lines indicate the global optimum

No.	N	p_r	p_m	SEL	Subset
1	75	0.7	0.005	0.2383	1/3/12/28/35/36
2	75	0.9	0.005	0.2349	1/3/12/28/35
3	125	0.7	0.005	0.2313	1/2/11/28/36
4	125	0.9	0.005	0.2373	1/2/12/28/35/36
5	75	0.7	0.015	0.2296	1-3/13/38/29/32/35/36
6	75	0.9	0.015	0.2373	1/2/12/28/35/36
7	125	0.7	0.015	0.2372	1/2/12/28/29/35/36
8	125	0.9	0.015	0.2281	1-3/11/12/28/29/32/35/36
9	150	0.8	0.01	0.2221	1/2/12/28/29/32/35
10	**100**	**0.8**	**0.01**	**0.2402**	**1/11/29/35/36**
11	50	0.8	0.01	0.2022	1-9/12/13/27-29/31-34
12	100	0.8	0.0001	0.2383	1/3/12/28/35/36
13	**100**	**0.8**	**0.02**	**0.2402**	**1/11/29/35/36**
14	100	0.6	0.01	0.2402	1/11/29/35/36
15	100	1.0	0.01	0.2349	1/3/12/28/35

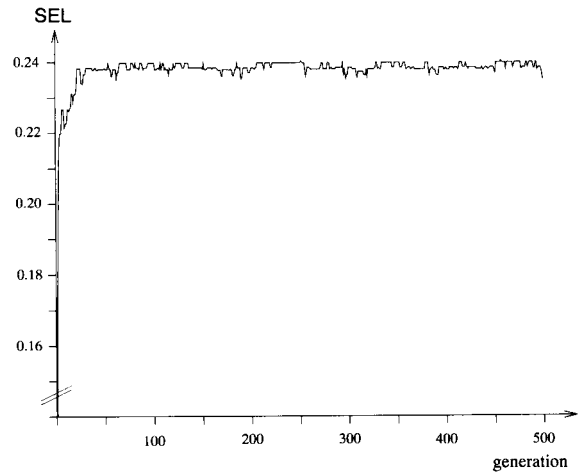

Fig. 1. Evolution of SEL for the best bitstring in the population, in a run with $N = 150$, $p_r = 0.8$, and $p_m = 0.01$.

In order to obtain a quantitative indication of the first type of robustness, experiment 10 was repeated ten times: the average fitness of the respective solutions was 0.2381, with a standard deviation of 0.001.

For an arbitrary run according to experiment 9, Fig. 1 shows the evolution of SEL for the best bitstring in the population. From this figure it can be seen that (near-)optimal solutions are found after approximately 80 generations, i.e. the GA conducts approximately 12,000 evaluations in the search space (since $N = 150$). Although this number is almost 2 orders of magnitude larger than the number of evaluations in SE, it still compares favorably with the formal size of the search space. More importantly, though, the running time is still acceptable (approximately 20 min real-time, using aforementioned hardware).

SA. The results of SA using SEL are listed in Table 4.

TABLE 4

SA using SEL. The bold-faced line indicates maximal specific heat [a]

τ	A/T	Specific heat	SEL	
			Average	St. dev.
0.2	0.940	0.0112	0.1164	0.0213
0.1	0.889	0.0434	0.1187	0.0206
0.08	0.860	0.062	0.1197	0.0202
0.06	0.822	0.1067	0.1212	0.0197
0.05	0.772	0.1570	0.1168	0.0195
0.04	0.738	0.2200	0.1246	0.0189
0.03	0.654	0.3807	0.1274	0.0186
0.02	0.502	0.9057	0.1337	0.0193
0.019	0.422	1.2689	0.1256	0.0205
0.018	0.427	1.2820	0.1269	0.0197
0.017	0.366	1.4989	0.1279	0.0210
0.016	0.350	1.7206	0.1308	0.0214
0.015	0.297	1.8721	0.1319	0.0233
0.014	0.272	3.925	0.1370	0.0259
0.013	0.198	3.4082	0.1398	0.0261
0.012	0.202	4.0156	0.1408	0.0249
0.0115	0.165	3.9722	0.1404	0.0233
0.011	0.136	5.2446	0.1440	0.0228
0.0105	0.125	4.1083	0.1442	0.0292
0.01	0.149	6.1109	0.1564	0.0231
0.0099	0.095	4.3903	0.1480	0.0225
0.0098	0.081	5.5977	0.15508	0.0277
0.0097	0.094	4.9859	0.1481	0.0231
0.0096	**0.072**	**12.9099**	**0.1607**	**0.0322**
0.0095	0.107	5.6549	0.1592	0.0220
0.0094	0.085	6.9519	0.1507	0.0239
0.0093	0.073	7.638	0.1556	0.0263
0.0092	0.040	0	0.1839	0.0314
0.0091	0.040	10.6744	0.1784	0.0327
0.009	0.050	11.2034	0.1673	0.0277
0.0089	0.050	5.4951	0.1634	0.0271
0.0088	0.051	5.4488	0.1544	0.0214
0.0087	0.053	7.3825	0.1565	0.0226
0.0086	0.029	8.9277	0.1749	0.0289
0.0085	0.034	6.8040	0.1762	0.0238
0.0084	0.027	6.4091	0.1517	0.0327
0.0083	0.034	7.6949	0.1713	0.0211
0.0082	0.027	9.2461	0.1724	0.0255
0.008	0.053	6.858	0.1657	0.0225
0.007	0.034	7.9346	0.1823	0.0261

[a] New run for $\frac{100,000}{0.072}$ iterations at $\tau = 0.0096$: Subset: 1/3/7/14/28/34-36; SEL: 0.2215.

It can be seen that the global solution was not HIT, regardless of the fact that SA conducts by far the largest number of evaluations in the search space. Moreover, the solution found by SA is inferior to the near-optimal solution found by SE.

TABLE 5

PE for all wavelengths, and PE for SEL-optimal subset (1/11/29/35/36, Table 1)

j	PE for all wavelengths	PE for SEL-optimal subset
1 (A)	31.1	0.7
2 (C)	6.1	6.6
3 (G)	6.0	6.6
4 (U)	35.1	1.3

Similar results were obtained in runs at other τ values for which a high specific heat was observed.

Concentration estimation. The accuracy (PE) and precision (RSD) in the estimates of the component concentrations, for both the entire set of wavelengths (as a reference) and the SEL-optimal subset of wavelengths, are listed in Tables 5 and 6, respectively.

From these tables, the following general tendencies can be inferred. The selection of wavelengths (rather than using the entire set of wavelengths) leads to a much better accuracy in the concentration estimates for components 1 (A) and 4 (U), but also to a much worse precision in the concentration estimates for component 4 (U).

Similar general tendencies (relative to using the entire set of wavelengths) were observed for the subsets of wavelengths found by the GA, SA, and SE, respectively; which of these methods performs better, based upon validation by PE or RSD, could not be decided.

Using accuracy after Lorber

Based on the evaluation criterion $(m\text{ACC})^{-1}$, first the global solution is determined; then, the

TABLE 6

RSD for all wavelengths, and RSD for SEL-optimal subset (1/11/29/35/36, Table 1)

j	RSD for all wavelengths	RSD for SEL- optimal subset
1 (A)	27.4	23.6
2 (C)	3.1	5.2
3 (G)	6.6	11.1
4 (U)	17.4	35.2

TABLE 7

Enumerative search using $(m\text{ACC})^{-1}$. The bold-faced line indicates the global optimum

m	$(m\text{ACC})^{-1}$	Subset
4	**0.0164**	**1/15/28/35**
5	0.0147	1/15/27/28/35
6	0.0135	1/2/15/27/28/35

solutions found by SE, the GA, and SA, respectively, are presented and commented on; finally, concentration estimates derived from the global solution are examined.

Comments are limited to trends not mentioned in the *Using selectivity after Lorber* section above.

The global solution. Enumerative search was conducted in order to find the globally optimal subset of wavelengths according to $(m\text{ACC})^{-1}$; results are listed in Table 7.

SE. The results of SE using $(m\text{ACC})^{-1}$ are listed in Table 8.

It can be seen that the global solution was HIT.

GA. The results of the GA using $(m\text{ACC})^{-1}$, obtained in 15 experiments according to a three-factor central composite design, are listed in Table 9.

It can be seen that the global solution was HIT for three configurations (experiments 6, 10 and 11).

For an arbitrary run according to experiment 9, Fig. 2 shows the evolution of $(m\text{ACC})^{-1}$ for the best bitstring in the population.

SA. The results of SA using $(m\text{ACC})^{-1}$ are listed in Table 10.

It can be seen that the global solution was not HIT.

Concentration estimation. The accuracy (PE) and precision (RSD) in the estimates of the component concentrations, for both the entire set of wavelengths (as a reference) and the $(m\text{ACC})^{-1}$-optimal subset of wavelengths, are listed in Tables 11 and 12, respectively.

TABLE 8

SE using $(m\text{ACC})^{-1}$. The bold-faced line indicates the global optimum

m	$(m\text{ACC})^{-1}$	Subset
4	**0.0164**	**1/15/28/35**
5	0.0147	1/15/27/28/35
6	0.0135	1/2/15/27/28/35

TABLE 9

GA using $(m\text{ACC})^{-1}$, in 15 experiments according to a three-factor central composite design. Bold-faced lines indicate the global optimum

No.	N	p_r	p_m	$(m\text{ACC})^{-1}$	Subset
1	75	0.7	0.005	0.0162	1/16/27/35
2	75	0.9	0.005	0.0163	1/15/27/35
3	125	0.7	0.005	0.0163	1/15/27/35
4	125	0.9	0.005	0.0161	1/15/27/34
5	75	0.7	0.015	0.0161	1/15/27/34
6	**75**	**0.9**	**0.015**	**0.0164**	**1/15/28/35**
7	125	0.7	0.015	0.0161	1/15/27/34
8	125	0.9	0.015	0.0161	1/15/27/34
9	150	0.8	0.01	0.0161	1/15/27/34
10	**100**	**0.8**	**0.01**	**0.0164**	**1/15/28/35**
11	**50**	**0.8**	**0.01**	**0.0164**	**1/15/28/35**
12	100	0.8	0.0001	0.0162	1/14/27/35
13	100	0.8	0.02	0.0163	1/15/27/35
14	100	0.6	0.01	0.0163	1/16/28/35
15	100	1.0	0.01	0.0161	1/15/27/34

Using minimum mean squared error after Sasaki

Based on the evaluation criterion $(m\text{MMSE})^{-1}$, first the global solution is determined; then, the

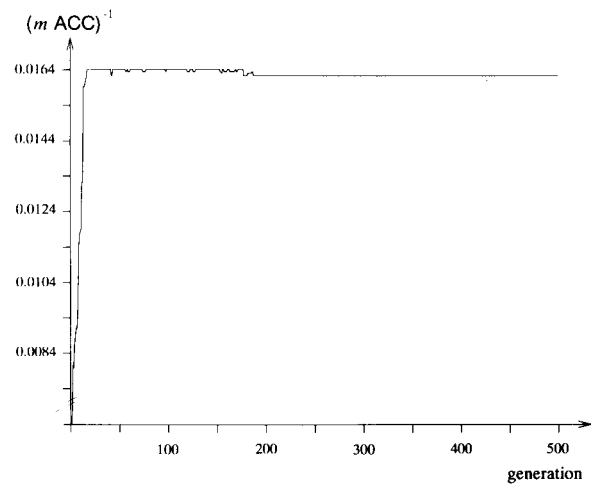

Fig. 2. Evolution of $(m\text{ACC})^{-1}$ for the best bitstring in the population, in a GA-run with $N = 150$, $p_r = 0.8$, and $p_m = 0.01$.

TABLE 10

SA using $(m\text{ACC})^{-1}$. The bold-faced line indicates maximal specific heat[a]

τ	A/T	Specific heat	$(m\text{ACC})^{-1}$	
			Average	St. dev.
0.005	0.803	0.1432	0.00361	0.00189
0.0045	0.784	0.1579	0.00376	0.00183
0.004	0.763	0.1928	0.00380	0.00177
0.0038	0.755	0.2204	0.00379	0.00177
0.0035	0.737	0.2340	0.00389	0.00173
0.0032	0.713	0.2819	0.00393	0.00168
0.003	0.710	0.3061	0.00390	0.00165
0.0029	0.691	0.2995	0.00394	0.00162
0.0028	0.687	0.3377	0.00396	0.00163
0.0027	0.681	0.3697	0.00400	0.00157
0.0026	0.674	0.3364	0.00402	0.00155
0.0025	0.657	0.3628	0.00404	0.00151
0.0024	0.653	0.4211	0.00402	0.00154
0.0023	0.637	0.4297	0.00410	0.00145
0.0022	0.623	0.4444	0.00413	0.00146
0.0021	0.614	0.4951	0.00414	0.00144
0.002	0.601	0.5594	0.00413	0.00143
0.0019	0.579	0.5231	0.00425	0.00137
0.0018	0.571	0.6229	0.00420	0.00137
0.0017	0.548	0.5745	0.00426	0.00132
0.0016	0.537	0.6155	0.00427	0.00125
0.0015	0.506	0.6756	0.00436	0.00123
0.0014	0.489	0.7283	0.00438	0.00121
0.0013	0.441	0.7950	0.00458	0.00141
0.0012	0.412	1.1109	0.00454	0.00121
0.0011	0.391	1.1435	0.00459	0.00117
0.001	0.355	1.1647	0.00465	0.00108
0.0009	0.304	1.5856	0.00478	0.00109
0.0008	0.256	2.0708	0.00497	0.00116
0.0007	0.178	3.4543	0.00530	0.00126
0.0006	0.129	3.5515	0.00553	0.00126
0.0005	**0.063**	**8.9944**	**0.00636**	**0.00148**
0.0004	0.038	4.2052	0.00611	0.00119
0.0003	0.012	4.2184	0.00663	0.00067
0.0002	0.004	0	0.00787	0.00029
0.0001	0	0	0.00835	0.00101
9e-05	0	0	0.00770	0.00042
8e-05	0	0	0.00891	0.00056
7e-05	0	0	0.00956	0.00012
6e-05	0	0	0.00956	0.00011

[a] New run for $\frac{100,000}{0.063}$ iterations at $\tau = 0.0005$: Subset: 1/14/15/23/28/29/36; $(m\text{ACC})^{-1}$: 0.01082.

solutions found by SE, the GA, and SA, respectively, are presented and commented on; finally, concentration estimates derived from the global solution are examined.

TABLE 11

PE for all wavelengths, and PE for $(m\text{ACC})^{-1}$-optimal subset (1/15/28/35, Table 7)

j	PE for all wavelengths	PE for $(m\text{ACC})^{-1}$-optimal subset
1 (A)	31.1	0.9
2 (C)	6.1	6.6
3 (G)	6.0	5.3
4 (U)	35.1	3.8

TABLE 12

RSD for all wavelengths, and for $(m\text{ACC})^{-1}$-optimal subset (1/15/28/35, Table 7)

j	RSD for all wavelengths	RSD for $(m\text{ACC})^{-1}$-optimal subset
1 (A)	27.4	30.7
2 (C)	3.1	5.6
3 (G)	6.6	12.9
4 (U)	17.4	44.7

Comments are limited to trends not mentioned in the *using selectivity after Lorber* section above.

The global solution. Enumerative search was conducted in order to find the globally optimal subset of wavelengths according to $(m\text{MMSE})^{-1}$; results are listed in Table 13.

SE. The results of SE using $(m\text{MMSE})^{-1}$ are listed in Table 14.

TABLE 13

Enumerative search using $(m\text{MMSE})^{-1}$. The bold-faced line indicates the global optimum

m	$(m\text{MMSE})^{-1}$	Subset
4	0.3325	1/15/28/35
5	**0.3442**	**1/15/27/28/35**
6	0.3408	1/2/15/27/28/35

TABLE 14

SE using $(m\text{MMSE})^{-1}$

m	$(m\text{MMSE})^{-1}$	Subset
4	0.3275	1/18/28/35
5	0.3424	1/18/27/28/35
6	0.3377	1/2/18/27/28/35
7	0.3253	1/2/18/27/28/35/36

TABLE 15

GA using $(m\text{MMSE})^{-1}$, in 15 experiments according to a three-factor central composite design. Bold-faced lines indicate the global optimum

No.	N	p_r	p_m	$(m\text{MMSE})^{-1}$	Subset
1	**75**	**0.7**	**0.005**	**0.3442**	**1/15/27/28/35**
2	**75**	**0.9**	**0.005**	**0.3442**	**1/15/27/28/35**
3	**125**	**0.7**	**0.005**	**0.3442**	**1/15/27/28/35**
4	**125**	**0.9**	**0.005**	**0.3442**	**1/15/27/28/35**
5	75	0.7	0.015	0.3289	1/2/18/26/27/28/35
6	**75**	**0.9**	**0.015**	**0.3442**	**1/15/27/28/35**
7	**125**	**0.7**	**0.015**	**0.3442**	**1/15/27/28/35**
8	**125**	**0.9**	**0.015**	**0.3442**	**1/15/27/28/35**
9	**150**	**0.8**	**0.01**	**0.3442**	**1/15/27/28/35**
10	**100**	**0.8**	**0.01**	**0.3442**	**1/15/27/28/35**
11	**50**	**0.8**	**0.01**	**0.3442**	**1/15/27/28/35**
12	**100**	**0.8**	**0.0001**	**0.3442**	**1/15/27/28/35**
13	**100**	**0.8**	**0.02**	**0.3442**	**1/15/27/28/35**
14	100	0.6	0.01	0.3368	1/15/27/28/34
15	**100**	**1.0**	**0.01**	**0.3442**	**1/15/27/28/35**

Although the global solution was not HIT, the solution found (for $m = 5$) is near-optimal.

GA. The results of the GA using $(m\text{MMSE})^{-1}$, obtained in 15 experiments according to a three-factor central composite design, are listed in Table 15.

It can be seen that the global solution was HIT for all configurations, except two (experiments 5 and 14).

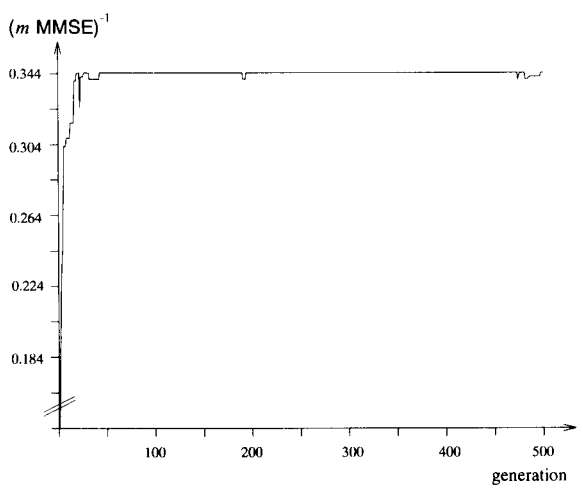

Fig. 3. Evolution of $(m\text{MMSE})^{-1}$ for the best bitstring in the population, in a GA-run with $N = 150$, $p_r = 0.8$, and $p_m = 0.01$.

For an arbitrary run according to experiment 9, Fig. 3 shows the evolution of for the best bitstring in the population.

SA. The results of SA using $(m\text{ACC})^{-1}$ are listed in Table 16.

TABLE 16

SA using $(m\text{MMSE})^{-1}$. The bold-faced line indicates maximal specific heat [a]

τ	A/T	Specific heat	$(m\text{MMSE})^{-1}$	
			Average	St. dev.
0.06	0.734	0.2140	0.1372	0.0276
0.05	0.695	0.2785	0.1393	0.0261
0.04	0.631	0.3964	0.1428	0.0251
0.035	0.589	0.4716	0.1449	0.0241
0.03	0.537	0.6268	0.1475	0.0236
0.025	0.467	0.8361	0.1511	0.0234
0.02	0.375	1.2670	0.1561	0.0226
0.018	0.329	1.5717	0.1591	0.0231
0.016	0.283	1.9882	0.1615	0.0230
0.014	0.224	3.0682	0.165	0.0234
0.012	0.147	4.1554	0.1759	0.0272
0.011	0.092	4.9576	0.1925	0.0353
0.01	0.089	5.3885	0.1832	0.0248
0.0098	0.070	6.9065	0.1902	0.0287
0.0096	0.073	9.1335	0.1855	0.0258
0.0094	0.069	9.7859	0.1882	0.0269
0.0092	0.071	5.4202	0.1827	0.0212
0.0091	0.040	5.9473	0.2068	0.0331
0.0090	0.051	8.8869	0.1931	0.0264
0.0089	0.059	8.2737	0.1874	0.0238
0.0088	0.043	8.3779	0.1986	0.0282
0.0087	0.042	6.7122	0.1940	0.0236
0.0086	0.029	8.8079	0.2068	0.0274
0.0085	0.030	9.3625	0.2057	0.0280
0.0084	0.033	9.6110	0.2027	0.0276
0.0083	0.026	7.3339	0.2061	0.0256
0.0082	0.043	6.8667	0.1892	0.0213
0.0081	0.033	10.0626	0.1961	0.0249
0.0080	0.038	7.8922	0.1916	0.0212
0.0079	0.032	6.0395	0.1948	0.0239
0.0078	0.029	9.3227	0.1982	0.0248
0.0077	0.005	0	0.2326	0.0174
0.0076	0	0	0.2417	7.435e-08
0.0075	0.002	7.3025	0.2381	0.0141
0.0074	0.011	7.4185	0.2103	0.0202
0.0073	**0.015**	**13.1857**	**0.2092**	**0.0232**
0.0072	0.016	5.8281	0.2029	0.0202
0.0071	0.003	0	0.2344	0.0187
0.007	0	0	0.2445	4.881e-07
0.0068	0	0	0.2444	4.881e-07

[a] New run for $\frac{100,000}{0.015}$ iterations at $\tau = 0.0073$: Subset: 1/2/10/15/27/28/35/36; $(m\text{MMSE})^{-1}$: 0.2867.

TABLE 17

PE for all wavelengths, and PE for $(m\text{MMSE})^{-1}$-optimal subset (1/15/27/28/35, Table 13)

j	PE for all wavelengths	PE for $(m\text{MMSE})^{-1}$-optimal subset
1 (A)	31.1	6.2
2 (C)	6.1	2.5
3 (G)	6.0	2.0
4 (U)	35.1	1.6

TABLE 18

RSD for all wavelengths, and RSD for $(m\text{MMSE})^{-1}$-optimal subset (1/15/27/28/35, Table 13)

j	RSD for all wavelengths	RSD for $(m\text{MMSE})^{-1}$-optimal subset
1 (A)	27.4	28.5
2 (C)	3.1	6.1
3 (G)	6.6	11.3
4 (U)	17.4	31.5

It can be seen that the global solution was not HIT.

Concentration estimation. The accuracy (PE) and precision (RSD) in the estimates of the component concentrations, for both the entire set of wavelengths (as a reference) and the $(m\text{MMSE})^{-1}$-optimal subset of wavelengths, are listed in Tables 17 and 18, respectively.

Conclusions

A comparative study involving a genetic algorithm, simulated annealing, and stepwise elimination, as methods for wavelength selection in multi-component analysis, was presented. For each of the three evaluation criteria used in this study, the genetic algorithm succeeded in finding the globally optimal solution. In contrast, simulated annealing failed in finding the globally optimal solution for each of the evaluation criteria. Stepwise elimination succeeded in finding the global optimum only for one of the evaluation criteria; for the other two, near-optimal solutions were found.

Although these results seem to indicate a general trend, no definite conclusions can be drawn, since optimal configurations for genetic algorithms and simulated annealing are generally unknown. Standard methodology to that end is not available; at best, the comparison can be made fair by devoting equal amounts of effective effort towards optimal configurations of the respective methods.

Furthermore, since results will generally depend on the data set used, other trends may be observed when more complex, larger data sets are subjected to wavelength selection by the methods used in this study. In particular, it is reasonable to expect that stepwise elimination will feature a dramatic drop in performance due to its greedy nature.

This research was carried out under the auspices of the Dutch Foundation for Chemical Research (SON) on behalf of the Dutch Foundation for Informatics (Computing Science) Research (SION) with financial aid from the Dutch Organization for Scientific Research (NWO), Grant 700-344-007. Contributions to this work by W.A.C. van der Heijden, W.G.F. van Duijnhoven, N.M. Faber, and M.J.P. Gerritsen, are gratefully acknowledged.

REFERENCES

1 P.A. Salamin, H. Bartels and P. Forster, Chemom. Intell. Lab. Syst., 11 (1991) 57.
2 K. Sasaki, S. Kawata and S. Minami, Appl. Spectrosc., 40 (1986) 185.
3 J.H. Kalivas, Chemom. Intell. Lab. Syst., 15 (1992) 1.
4 J.H. Kalivas, N. Roberts and J.M. Sutter, Anal. Chem., 61 (1989) 2024.
5 A. Junker and G. Bergmann, Fresenius' Z. Anal. Chem., 278 (1976) 191.
6 J.H. Kalivas, Appl. Spectrosc., 41 (1987) 1338.
7 W.P. Carry, K.R. Beebe, B.R. Kowalski, D.L. Illman and T. Hirschfeld, Anal. Chem., 58 (1986) 149.
8 E.R. Malinowski, Anal. Chim. Acta, 134 (1982) 129.
9 C.B. Lucasius and G. Kateman, Trends Anal. Chem., 10 (1991) 254.
10 J.H. Kalivas, J. Chemom., 5 (1991) 37.
11 M.R. Garey and D.S. Johnson, Computers and Intractability: A Guide to the Theory of NP-Completeness, Freeman, San Francisco, CA, 1979.
12 F. Maffioli, in N. Christofides, A. Mingozzi, P. Toth and C. Sandi (Eds.), Combinatorial Optimization, Wiley, New York, 1993, Chap. 5.

13 C.B. Lucasius, A.D. Dane and G. Kateman, Anal. Chim. Acta, 282 (1993) 647.
14 S. Kirkpatrick, C.D. Gelatt, Jr., and M.P. Vecchi, Science, 220 (1983) 671.
15 J.H. Holland, Adaptation in Natural and Artificial Systems. University of Michigan Press, Ann Arbor, MI, 1975. Revised print: MIT Press, Cambridge, MA, 1992.
16 D.E. Goldberg, Genetic Algorithms in Search, Optimization, and Machine Learning, Addison-Wesley, Reading, MA, 1989.
17 A. Lorber, Anal. Chem., 58 (1986) 1167.
18 N. Noble, Applied Linear Algebra, Prentice Hall, New York, 1969.
19 G.E. Forsythe, M.A. Malcolm and C.B. Moler, Computer Methods for Mathematical Computations, Prentice Hall, NJ, 1977.
20 P.E. Gill, W. Murray and M.H. Wright, Practical Optimization, Academic Press, London, 1981.
21 F.P. Zscheile, H.C. Murray, G.A. Baker and R.G. Peddicord, Anal. Chem., 34 (1962) 1776.
22 L.L. Juhl and J.H. Kalivas, Anal. Chim. Acta, 207 (1988) 125.
23 C.B. Lucasius and G. Kateman, Chemom. Intell. Lab. Syst., (1994) in press.
24 C.B. Lucasius and G. Kateman, Comput. Chem., (1994) in press.
25 C.B. Lucasius and G. Kateman, Comput. Chem., (1994) in press.
26 W.H. Press, B.P. Flannery, S.A. Teukolsky and W.T. Vetterling, Numerical Recipes in C: The Art of Scientific Computing, Cambridge University Press, New York, 1988.
27 L. Davis(Ed.), Handbook of Genetic Algorithms, Van Nostrand Reinhold, New York, 1991.
28 Y. Davidor, Genetic Algorithms and Robotics: A Heuristic Strategy for Optimization, World Scientific, Singapore, 1991.
29 Z. Michalewicz, Genetic Algorithms + Data Structures = Evolution Programs, Artificial Intelligence Series, Springer-Verlag, Berlin, 1992.
30 J.H. Holland, Scientific American, 267 (1992) 44.
31 J.R. Koza, Genetic Programming: On the Programming of Computers by Means of Natural Selection, MIT Press, Cambridge, MA, 1992.
32 C. Darwin, The Origin of Species by Means of Natural Selection: the Preservation of Favoured Races in the Struggle for Life, John Murray, London, 1859. First edition text, edited with an introduction by J.W. Burrow, published in Pinguin Books 1968.
33 C.B. Lucasius and G. Kateman, Chemom. Intell. Lab. Syst., 19 (1993) 1.
34 C.B. Lucasius, Towards Genetic Algorithm Methodology in Chemometrics, PhD thesis, Katholieke Universiteit Nijmegen, Nijmegen, Netherlands, 1993.
35 W. Siedlecki and J. Sklansky, Pattern Recognition Letters, 10 (1989) 335.
36 T.-H. Li, C.B. Lucasius and G. Kateman, Anal. Chim. Acta, 268 (1992) 123.
37 R. Leardi, R. Boggia and M. Terrile, J. Chemom., 6 (1992) 267.
38 J.J. Grefenstette, IEEE Transactions on Systems, Man, and Cybernetics, IEEE, SMC-16(1), January/February 1986. Vol.16(1), p. 122.
39 D.L. Massart, B.G.M. Vandeginste, S.N. Deming, Y. Michotte and L. Kaufman, Chemometrics: A Textbook, Elsevier, Amsterdam, 1988.
40 E.H.L. Aarts and J.H.M. Korst, Simulated Annealing and Boltzmann Machines. A Stochastic Approach to Combinatorial Optimization and Neural Computing, Wiley, Chichester, 1989.
41 P.J.M. van Laarhoven and E.H.L. Aarts, Simulated Annealing: Theory and Applications. Mathematics and its Applications (East European Series), Reidel, Dordrecht, 1987.

Analytica Chimica Acta, 286 (1994) 155–167
Elsevier Science B.V., Amsterdam

New spray chamber for use in flow-injection plasma emission spectrometry

Min Wu, Yolanda Madrid [1], Jake A. Auxier and Gary M. Hieftje

Department of Chemistry, Indiana University, Bloomington, IN 47405 (USA)

(Received 15th April 1993; revised manuscript received 23rd July 1993)

Abstract

The use of flow-injection analysis (FIA) in atomic emission spectrometry (AES) is often compromised by the relatively large dead volume and washout time of conventional nebulizer-spray chamber combinations. This problem is particularly acute when a microwave-induced plasma (MIP) is used as the AES source, because of the low flow rates ordinarily employed with an MIP and because of the limited tolerance of an MIP to solvent loading. In the present study, these problems have all been largely overcome through use of a novel spray chamber design and an MIP based on the microwave plasma torch (MPT). The MPT offers the advantages of a high tolerance to the introduction of aqueous aerosols, a central channel that exhibits enhanced energy coupling between the plasma and sample species, and low detection limits. A new low-volume spray chamber developed in our laboratory, coupled with the MPT, provides far shorter washout times than conventional units. Preliminary work on analyzing aqueous samples directly without desolvation has demonstrated that the use of air as a carrier has made it possible for a 200-μl injection volume to achieve the same sensitivity of detection as offered by continuous nebulization. Detection limits are in the range of 5–50 ng ml^{-1} for most elements studied. Also, the relative standard deviation (R.S.D.) for analyte signals is readily maintained at 2.5%. Organic solvents were also explored as the carrier for flow-injection analysis; under optimized conditions sensitivity dropped less than half for ethanol and by 40% for methanol, compared to performance with water as the carrier. This suggests the attractiveness of the new spray chamber-MIP combination as an element-selective detector for liquid chromatography (LC).

Keywords: Atomic emission spectrometry; Flow injection; Interface, HPLC; Microwave plasma torch; Spray chamber

A variety of emission sources, including chemical flames, the inductively coupled plasma (ICP), the glow discharge, and the microwave-induced plasma (MIP), have been investigated for use in atomic emission spectrometry. Among these, the microwave-induced plasma offers the advantages of high sensitivity, applicability to nonmetal detection, low cost, and convenience of operation [1]. However, existing MIP devices, such as the Beenakker cavity [2], surfatron [3] and capacitively coupled microwave plasma (CMP) [4] suffer from a number of limitations. These shortcomings include a limited amount of energy available for sample atomization, a susceptibility to solvent loading, and an undesirable incidence of matrix interferences. As a result, the most successful use of the MIP to date has been as an element-selective detector for gas chromatography and supercritical fluid chromatography, where there is no need to vaporize particulate aerosols [5].

Recently, several alternative MIP support structures have been proposed and described to improve power transfer from the microwave generator to the plasma, in hopes of overcoming the

Correspondence to: G.M. Hieftje, Indiana University, Department of Chemistry, Chemistry Building, Bloomington, IN 47405 (USA).

[1] On leave from Department of Analytical Chemistry, Faculty of Chemistry, Complutense University, Madrid (Spain).

SSDI 0003-2670(93)E0576-S

limitations mentioned above [6–10]. One of them, the microwave plasma torch (MPT) works substantially differently from other MIP support devices and offers a number of advantages over them [5,11]. The MPT supports a toroidal, flame-like plasma at atmospheric pressure, making it especially easy to use and to interface to either an emission or a mass spectrometer. Also, unlike other MIP arrangements, the MPT exhibits excellent resistance to detuning caused by changes in plasma density, making it possible to introduce aqueous or organic solutions directly into the plasma over a relatively wide range of solution flow rates.

Not surprisingly, an attractive application of such a plasma source is as an element-selective detector for liquid chromatography (LC) or supercritical fluid chromatography (SFC) [5]. In such applications, as in flow-injection analysis (FIA) and in the interfacing of an inductively coupled plasma with LC [12], the characteristics of the sample-introduction system are critical. A useful interface between an MPT and either LC or FIA should produce minimal broadening of sample peaks but should offer uniform aerosol delivery to the plasma, a relatively high sample-uptake rate to match typical LC or FIA mobile-phase flow rates of 1–2 ml min^{-1}, a narrow aerosol droplet-size distribution, and small droplet sizes. These demands are most likely to be met by a nebulizer that is interfaced to a spray chamber of small size. Although a number of smaller spray chambers have been described [13–16], they have all suffered from a number of limitations, including low efficiency, poor droplet-size discrimination, reduced sensitivity, or a greater incidence of interelement interferences. Also, none has been developed with the express intention of being used with FIA or LC [17–18]. In contrast, the new miniature vertical rotary spray chamber developed in this laboratory [19] has demonstrated lower memory effects, more rapid sample washout, better detection limits and higher solvent transport efficiency than even conventional spray chambers. In the present study, this new spray chamber has been evaluated for use in FIA-MPT emission spectrometry. Continuous solution nebulization was used for initial and plasma-optimization studies. Flow injection was then used to produce transient signals to test those criteria that are critical in applications such as FIA and LC. The new spray chamber is shown to offer substantial gains over competitive devices in virtually all performance criteria.

EXPERIMENTAL

Experimental systems

Microwave plasma torch (MPT) emission system. The microwave plasma torch has been described in detail elsewhere [11]. It is an all-metal structure and consists of three concentric metal tubes, with integral provision for impedance matching and frequency tuning. The Ar plasma-support gas is introduced into the intermediate tube and sample aerosol is carried into the central tube by a second Ar flow (carrier-gas flow). The plasma was maintained at 200 W in most experiments by a modified [20] microwave generator (MicroNow) at 2.45 GHz.

For calibration plots and studies of matrix effects, a 0.35-m focal-length spectrometer (GCA/McPherson) was used. The entrance and exit slits of the monochromator were set at 40 μm for MPT emission studies to provide the highest signal-to-background performance without producing a nonlinear detector response. A 175-mm focal-length quartz lens projected the plasma image at unity magnification onto the entrance slit of the monochromator. The observation zone was centered 6 mm above the tip of the central tube of the torch. Radiation transmitted by the monochromator was detected by an RCA 1P28 photomultiplier tube operated at −900 V. A Keithley (model 414S) picoammeter was used as a current-to-voltage converter, and was coupled to a National Instruments NB-MIO-16XL-18 A/D data-acquisition interface board installed in a Macintosh IIfx computer. A computer-simulated chart recorder was used with the Macintosh computer to collect and analyze the data.

Inductively coupled plasma emission system. The spray chamber was tested also with the 27.12 MHz inductively coupled plasma emission system used earlier [19]. This latter system was used at

1.0 kW of rf power, 14.0 l min^{-1} coolant Ar flow rate, 0.75 l min^{-1} intermediate Ar flow rate, 0.75 l min^{-1} carrier Ar gas flow rate, an observation height of 15 mm above the load coil and with a 10 μg ml^{-1} solution of Mg as the sample. The emission signal from Mg(II) at 280.3 nm was monitored for the comparison.

Reagents

Metal ion solutions were prepared from analytical reagent-grade (Mallinckrodt) or ACS reagent-grade (MCB or Fisher Scientific) salts or directly by dilution of AAS standard solutions (Fisher Scientific). All solutions were stored in polypropylene containers (Nalgene). Copper was used as a test element for optimization of the microwave plasma torch. The organic solvents used for this study were analytical-grade ethanol and methanol (Fisher Scientific).

Sample introduction

A locally fabricated glass-concentric nebulizer and a vertical rotary spray chamber [19] were utilized. Details of the spray-chamber design are provided in the next section. Two optimized spray chambers [19], with diameters of 4 and 6 cm, were evaluated for sample introduction. The effect of different carrier media (air, water and organic solvent) on the FI signals was also evaluated.

The carrier-solution flow from a Gilson Minipuls 2 peristaltic pump was either introduced directly into the nebulizer-spray chamber combination or discrete aliquots of solution were introduced by FIA with a Rheodyne Model 5042 electrically actuated injection valve and PTFE sampling loop. The PTFE tubing used for connections has an inner diameter of 0.5 mm and an outer diameter of 1.5 mm. Four different sample loops were used, with volumes of 75, 200, 250, and 500 μl for discrete sample introduction. The FIA injection valve was placed as close as possible to the nebulizer/spray chamber assembly by means of a connecting tube less than 60 cm in length.

TABLE 1

Dimensions and transport efficiencies for alternative designs of the vertical rotary spray chamber

Chamber diameter (cm)	Dimple diameter (cm)	Dimple depth (cm)	Transport efficiency (%)
4.0	1.0	0.95	0.88
4.0	2.4	1.27	2.65 [a]
4.0	3.5	1.27	0.72
6.0	none	–	1.60
6.0	1.0	1.27	2.90 [a]
6.0	2.0	1.27	3.10
6.0	4.0	1.27	1.60
Scott type	110 ml volume		1.90

[a] Selected for further study.

RESULTS AND DISCUSSION

Optimization of spray-chamber design

A spray chamber intended for use in FIA–atomic spectrometry has demands placed upon it that do not exist in conventional atomic spectrometric measurements. To make the new vertical rotary spray chamber suitable for this application, its dimensions were optimized; criteria used in this optimization were solvent transport efficiency, memory effect (sample washout time) and noise frequency characteristics. Because each spray chamber had to be fabricated individually, and because a number of spray-chamber dimensions might be altered, it was not feasible to employ a fully systematic optimization strategy. Instead, two dimensions were targeted for study here: the diameter of the prolate spheroid that constitutes the bulk of the spray-chamber body [19] and the diameter of the dimple impressed into that body to serve as an impact surface and a feature to reduce spray-chamber volume and alter flow patterns within it. The set of designs that were tested initially is compiled in Table 1.

Transport efficiency. Aerosol transport efficiency was measured by means of the silica-gel collection method described elsewhere [21]. The generated aerosol and solvent vapor issuing from the chosen spray chamber were directed into a U-tube packed with dry silica gel. The transport efficiency was calculated as the ratio of the mass of solvent collected by the silica gel and the amount of liquid introduced into the nebulizer.

Obviously, this method does not discriminate between solvent vapor and wet aerosol.

The results of this study are compiled in Table 1. The largest transport efficiency is 3.1% for a 6-cm diameter chamber having a 2-cm rounded dimple in its bottom. However, almost the same efficiency (2.9%) was produced by a 6-cm spray chamber with a 1-cm diameter dimple. Because this latter spray chamber had been used in an earlier study [19], a body of experience had already been acquired with it; it was therefore selected for use in the investigations described below. The highest efficiency determined with a 4-cm chamber was 2.65%, for a unit with a 2.4-cm diameter dimple. This design was also selected for further characterization and comparison with the 6-cm chamber. All other designs exhibited lower efficiencies and were not included in subsequent studies.

The size of the dimple seems to be significant in determining the transport efficiency of the vertical rotary spray chamber, especially the 4-cm diameter device. Presumably, a dimple that is too small does not serve well as an impact surface, whereas an excessively large dimple disrupts gas-flow patterns undesirably. Further study will be required to determine the particular function of the dimple in chambers of different diameter. Also, from preliminary results it appears that the shape of the dimple might affect performance. These matters will be the subject of future reports. Importantly, both the 4-cm and 6-cm spray chambers that were selected for further study offer higher efficiency than a commercially available Scott-type spray chamber, which yields only 1.9% with the same carrier-gas flow rate and solution uptake rate.

Memory effect and washout time. Figure 1 compares washout times for the selected 4-cm and 6-cm chambers to that of a conventional Scott-type spray chamber. Washout time is defined here as the period required for a signal to fall to 1% of its initial value [22]; the value was determined here by tracing the decay of a Mg(II) 280.3 nm emission signal from the ICP after the Mg sample solution was replaced by a water blank. The 6-cm and 4-cm chambers have washout times of 18.2 ± 2.8 s and 5.2 ± 2.7 s, respectively, at least an order of magnitude less than that of the double-barrel Scott-type chamber. Also, it should be evident from a glance at Fig. 1 that the definition for washout time adopted here is extremely conservative. If the parameter were defined as the time required for a signal to fall to 5% (instead of 1%) of its original value, the figures drop to approximately 2 s and 3 s for the 4-cm and 6-cm chambers, respectively. In contrast, the time for the Scott-type spray chamber remains beyond 60 s, even with this more liberal definition. Thus, for many routine ICP-OES measurements, the new spray chambers would offer a sample throughput rate that is 30 to 50 times greater than that possible with the conventional Scott chamber.

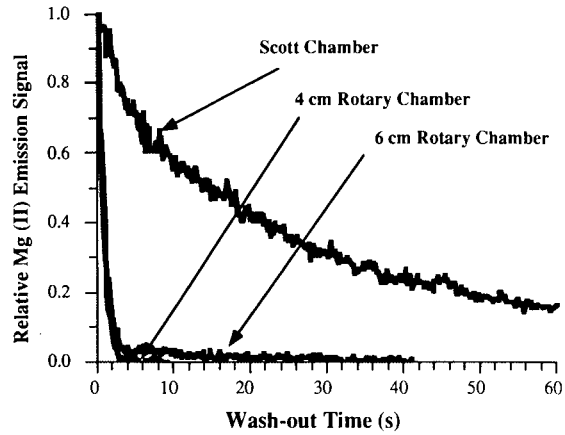

Fig. 1. Comparison of washout times for 4-cm, 6-cm and Scott-type spray chambers coupled to a 27.12 MHz ICP system operating at 1.0 kW, 0.75 l min^{-1} carrier-gas flow rate, 15 mm above load coil and 2.0 ml min^{-1} solution delivery rate.

The sample washout time (1% definition) was determined also for the 4-cm spray chamber coupled to the MPT system, where Cu I emission at 324.8 nm was monitored. The washout time for a 10 ppm Cu solution was determined as a function of carrier-solution flow rate; as shown in Fig. 2, the washout time ranges from 3.3 to 1 s over the range of solution pumping rates that were studied.

Noise characteristics. Figure 3 compares noise amplitude spectra from the three spray chambers for the Mg II 280.3 nm emission feature from the ICP. For all three types of chambers (4-cm, 6-cm,

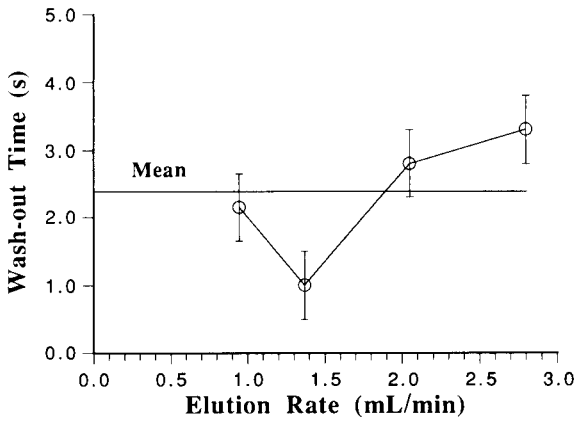

Fig. 2. Washout time as a function of sample-solution delivery rate for the 4-cm vertical rotary spray chamber interfaced to a microwave plasma torch system operating under the conditions listed in Table 2. The washout time (1% definition) was calculated from the average of three replicate runs.

and Scott-type) drift ($1/f$ noise) was dominant below 10 Hz; also, audio-frequency noise features were apparent in the vicinity of 200–300 Hz, in agreement with what others have reported [23]. Over the entire spectral region from dc to 500 Hz, the 6-cm chamber produced the lowest noise amplitude among the three units. Further, above 40 Hz the 4-cm chamber generated a lower noise level than the Scott-type design, which was overall the noisiest device of the three.

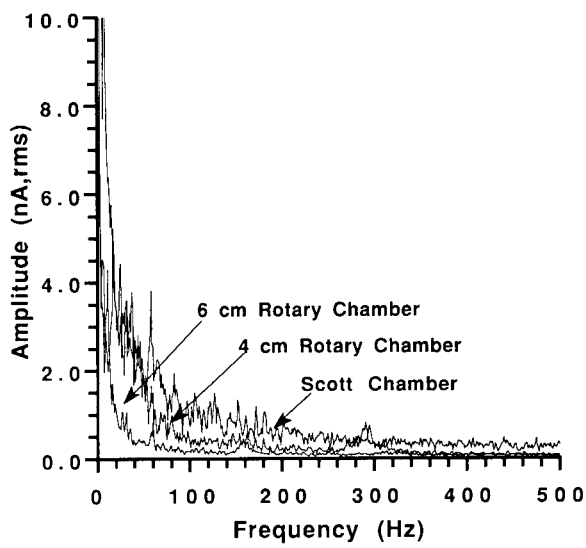

Fig. 3. Comparison of noise amplitude spectra of Mg II emission at 280.3 nm for the 4-cm, 6-cm and Scott-type spray chambers interfaced to a 27.12 MHz ICP. Operating conditions as in Fig. 1.

Noise amplitude spectra were obtained for the three spray chambers also when they were interfaced to the MPT. The general behavior is similar to that shown in Fig. 3 for the ICP. However, it is useful to examine in more detail the influence of a sample aerosol on the MPT noise spectra. The resulting comparison, shown in Fig. 4 for the 4-cm vertical rotary spray chamber, has been normalized in amplitude by dividing the ac noise value at each frequency by the dc emission value, the resulting ratio being expressed as %R.S.D. For clarity, the noise spectra have been intentionally offset vertically from each other; the true difference in the baseline (white) noise levels is insignificant. From these normalized spectra, it is clear that the introduction of a pure aqueous aerosol into the MPT does little but to introduce a new low-frequency noise peak near 6 Hz and to modify the positions of the higher-frequency audio noise peaks. These same noise-spectral features have been observed also in previous studies in which different sample-introduction systems (an ultrasonic nebulizer (USN) [24] and a hydride-generation system [25]) were used. Presumably, they arise from gas-flow vortex structures in the MPT tail flame and could be reduced through optimization of gas flow rates, integration time and the observation location. Overall, it appears that the main noise sources come from the MPT system instead of from the 4-cm spray chamber.

Of course, the influence of the noise spectra in Figs. 3 and 4 on practical measurements will depend on the integration time that is employed; high-frequency background fluctuations will have little effect on a dc measurement performed with a long time constant. Therefore, a detailed study was performed to assess the effect of integration time on the relative standard deviation of the background (%R.S.D.B). Although this study pertains especially to continuous-flow measurement, it helps to characterize the spray chamber more fully. The results, shown in Fig. 5 for the MPT system coupled with the 4-cm spray chamber, indicate that the best background precision

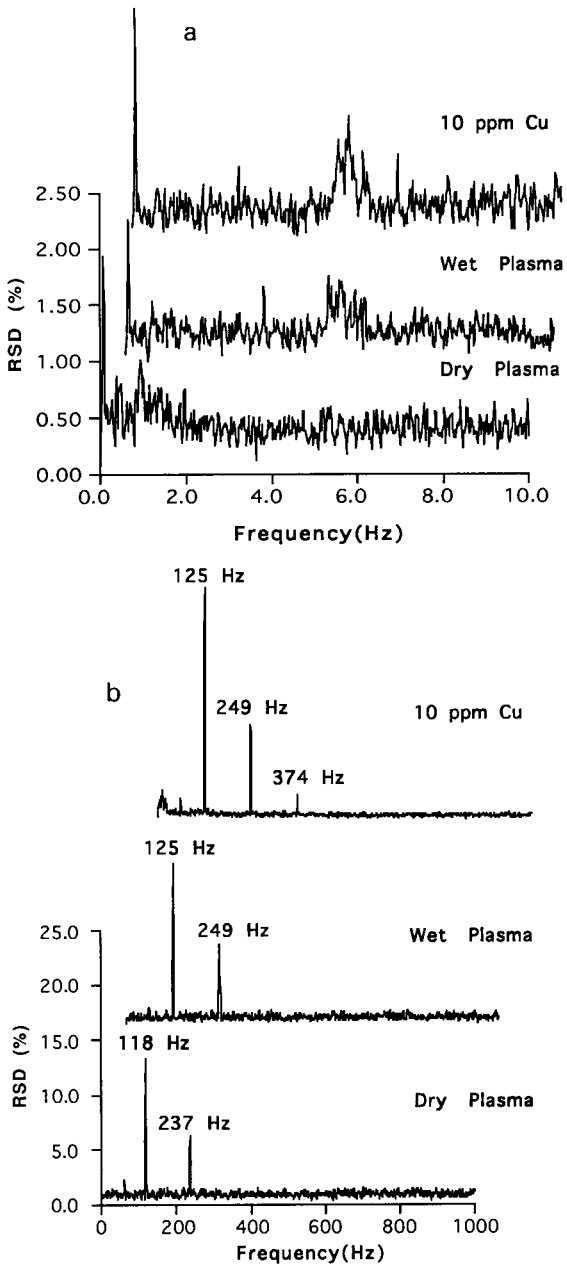

Fig. 4. Normalized noise amplitude spectra for emission from an MPT coupled with a 4-cm vertical rotary spray chamber (operating conditions as in Table 2). Spectra were normalized by dividing the ac noise amplitude at each frequency by the dc emission level and the ratio expressed as %R.S.D. All signals were monitored at 324.8 nm, corresponding to the Cu I transition. The procedures to obtain these data are described in [19]. (a) Noise frequency range 0–10 Hz, (b) noise frequency range 0–1000 Hz. "Dry Plasma" corresponds to no sample introduction; "Wet Plasma" to the introduction of an aerosol of water only. Spectra are artificially displaced with

(1.32% R.S.D.B) is obtained at an integration time of 50 s. Integration times longer than 50 s probably suffer from excessive long-term drift, possibly in the microwave supply, gas flows, or nebulizer performance.

The same sample-introduction system demonstrated comparable performance with the ICP system for continuous sample introduction. Not surprisingly, the background noise level from an ICP depends not only on integration time but also on both the observation height and carrier-gas flow rate. As shown in Fig. 6, a fixed integration time of 10 s can yield 1.9% R.S.D.B with a carrier-gas flow rate of 0.86 l min^{-1} but not with a flow rate of 0.73 l min^{-1}.

Optimization of other components

Microwave plasma torch (MPT). A 5 μg ml^{-1} Cu solution was nebulized continuously into the plasma while the Cu I 324.8 nm emission signal was recorded. Changes in microwave power between 150 to 200 W produced little change in the Cu I signal. However, at a fixed microwave power of 200 W, alterations in the carrier and support Ar gas flow rates produced a dramatic change in the emission signal (cf., Fig. 7). The maximum Cu emission was achieved at a support Ar flow rate of 0.5 l min^{-1} and a carrier Ar gas flow rate of about 0.6 l min^{-1}.

Flow-injection (FI) system. In flow injection, the dispersion coefficient D is commonly used to estimate how much the analyte is diluted on its way through the FIA network. It is common to define D as the ratio of the concentration of the originally injected sample to the concentration at the peak of an FIA signal. Usually, unity dispersion is desired in atomic spectrometry. When the injection system, flow arrangement, connection geometry and the plasma detector stay unchanged, the overall dispersion will be affected by carrier flow rate, carrier type (water or air) and spray-chamber volume [26]. The effect of these variables is examined below. In the present context, peak width is defined as the full width at half maximum.

Figure 8 shows a sequence of rapid flow-injection peaks obtained with the MPT system and a 4-cm spray chamber with a volume of 10.5 ml. In

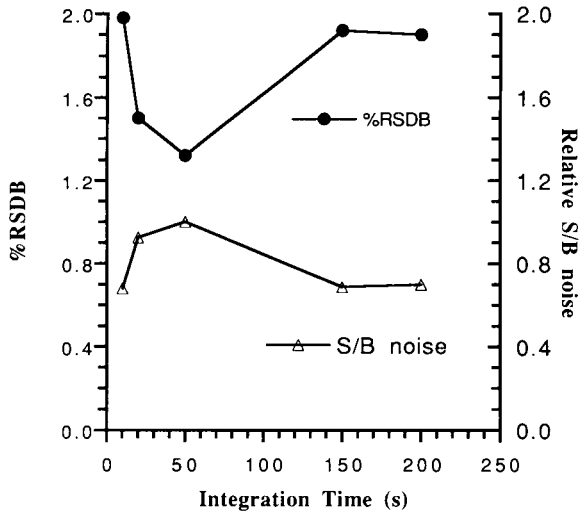

Fig. 5. The dependence of %R.S.D.B and signal to background-noise ratio on integration time in an MPT emission system operated under the conditions in Table 2 and interfaced to a 4-cm vertical rotary spray chamber. Background measured at the location of the Cu I transition at 324.8 nm.

this measurement, the sample-loop loading time was eliminated through the alternating use of two parallel injection valves. When only a single valve is used, the achievable throughput is four samples per minute or 240 samples per hour for a sample uptake rate of 2.0 ml min^{-1}.

Figure 9a displays the effect of the carrier (water) flow rate on the FI peak width for a Cu I

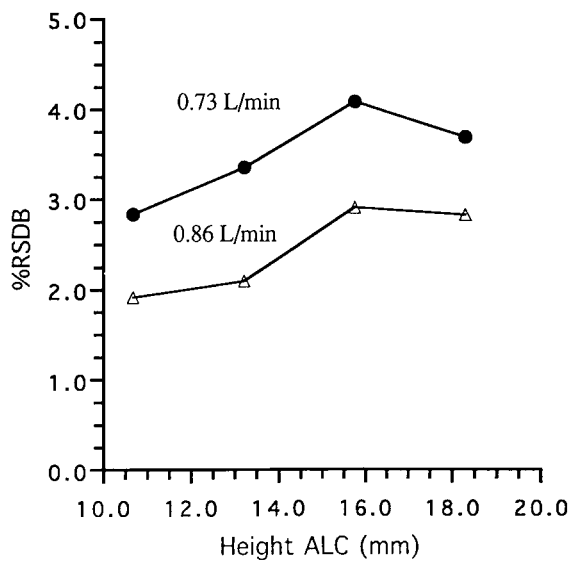

Fig. 6. Effect of carrier-gas flow rate and height above the load coil in a 27.12 MHz ICP on the relative standard of the background (%R.S.D.B). Operating conditions as in Fig. 1. Background measured at the location of the Mg II transition at 280.3 nm. Integration time: 10 s.

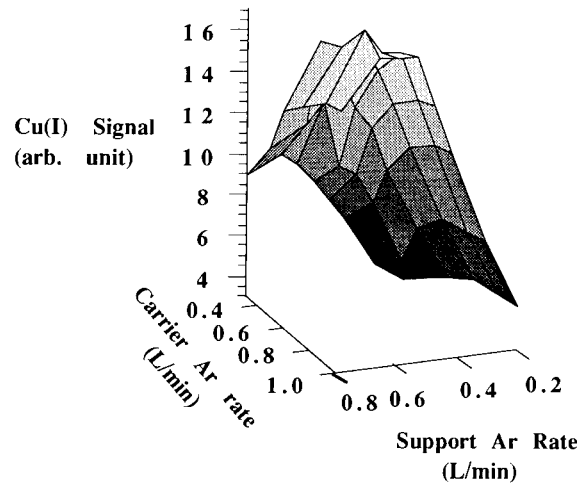

Fig. 7. Effect of carrier and support Ar gas flow rates on Cu I emission intensity from the MPT coupled to a 6-cm vertical rotary spray chamber. Other conditions as in Table 2.

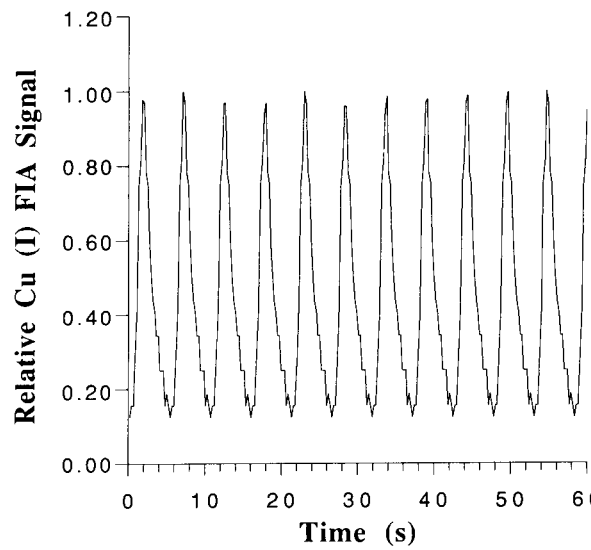

Fig. 8. Sequence of flow-injection peaks obtained with the 4-cm rotary spray chamber interfaced to the MPT. Conditions: 250 W microwave power, 2 μg ml^{-1} Cu, 324.8 nm Cu I transition, 75 μl injection volume, 1.5 ml min^{-1} solution delivery rate, 0.5 l min^{-1} support Ar gas flow rate, 0.6 l min^{-1} carrier Ar gas flow rate.

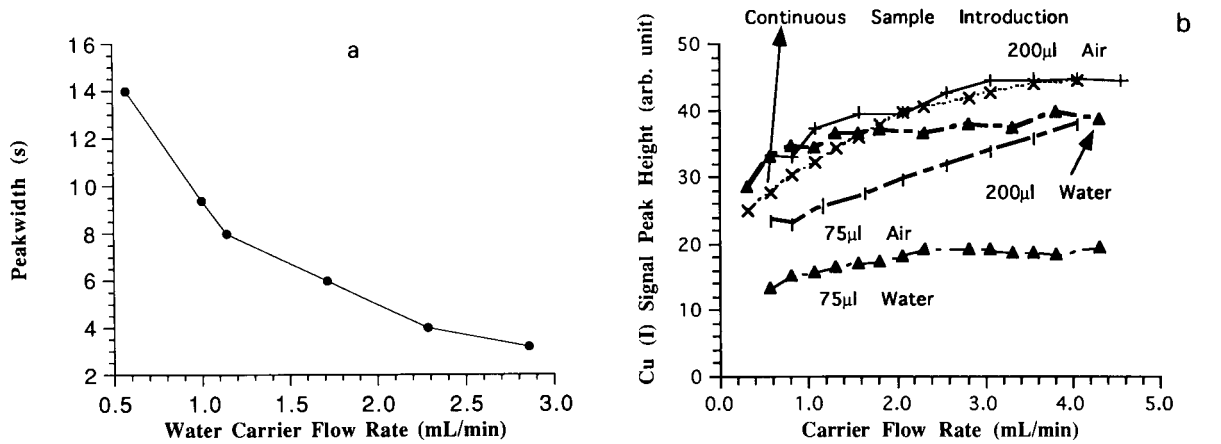

Fig. 9. (a) Effect of FI carrier (water) flow rate on FI peak width for an injected sample volume of 75 µl. (b) Effect of flow rate of two different FIA carriers (water or air) on FI peak height with injected sample volumes of 75 and 200 µl. The Cu I 324.8 nm transition was monitored from an MPT system coupled to a 4-cm vertical rotary spray chamber. Sample concentration was 5 µg ml^{-1} Cu; other experimental conditions as in Table 2.

emission signal obtained from the MPT system and a 4-cm spray chamber. The injection volume was 75 µl. The peak width drops significantly as the carrier flow rate is raised, suggesting that the width is dictated by the time required to carry the sample plug into the emission source rather than by the dead volume of the spray chamber or plasma.

Figure 9b shows the effect of the carrier flow rate on the peak height of the FI signal from Cu I, for two different injection volumes (75 and 200 µl). The effect of the carrier flow rate clearly depends not only on the carrier flow and type (air or water) but also on the injection volume.

Generally, as carrier flow rate is raised, the observed Cu I emission signal goes up. This is not surprising, since a higher carrier flow rate will sweep the sample solution more quickly into the plasma and cause a larger emission signal. Furthermore, one would expect the signals produced by an air carrier to be greater than those obtained with an aqueous carrier, since the air-carried samples cannot be diluted by dispersion and because the plasma is cooled less by introduced solvent. However, what is curious about Fig. 9b is that the water-carried FI samples generate peaks that do not increase with carrier flow as rapidly as does the continuous signal. Instead, the FI peaks obtained with the aqueous carrier level off at flows near 2 ml min^{-1}. We attribute this behavior to turbulent mixing that occurs in the FI tubing at elevated carrier velocities. Whatever the

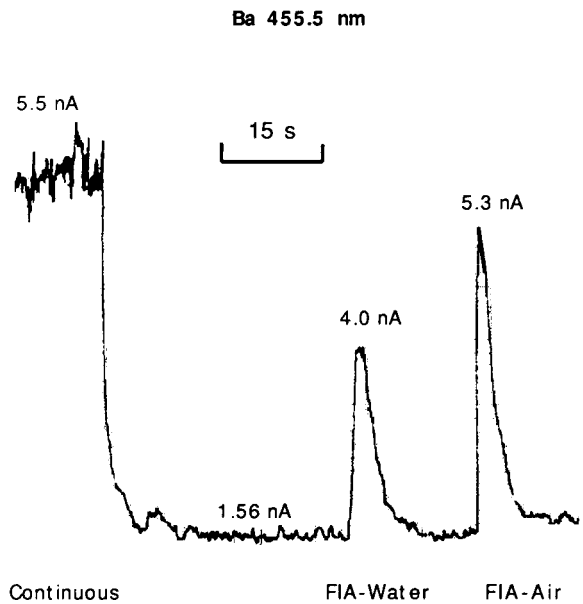

Fig. 10. Comparison of continuous-nebulization signal with FI peaks produced with air and water being employed as a sample carrier. The MPT was coupled to a 6-cm vertical rotary spray chamber. Experimental conditions: 20 µg ml^{-1} Ba, Ba II 455.5 nm transition, 75 µl injection volume, 200 W microwave power, 0.5 l min^{-1} support Ar gas flow, 0.6 l min^{-1} carrier Ar gas flow, 1.5 ml min^{-1} water elution flow.

source of this discrepancy, it is significant that the FI peak height from a 200-μl aliquot carried in air virtually matches the performance of continuous sample introduction.

The utility of air as an FI carrier is underscored by the traces in Fig. 10. Even with a 75-μl injection volume, the air carrier produces a 30% higher Ba II emission signal than does water as a carrier. The calculated flow-injection dispersion coefficients are 1.84 and 1.08, respectively, for the aqueous and air carriers. A corresponding reduction in the FI peak width can also be seen when air is used as the carrier.

As shown in Fig. 11a, the 4-cm vertical rotary spray chamber consistently produced narrower and taller FI peaks than the 6-cm chamber. In Fig. 11a, although background and noise remain about the same, the peak from the 4-cm chamber is roughly three times taller than that from the 6-cm unit.

It is useful to compare the behavior in Fig. 11a with what would be predicted theoretically. From

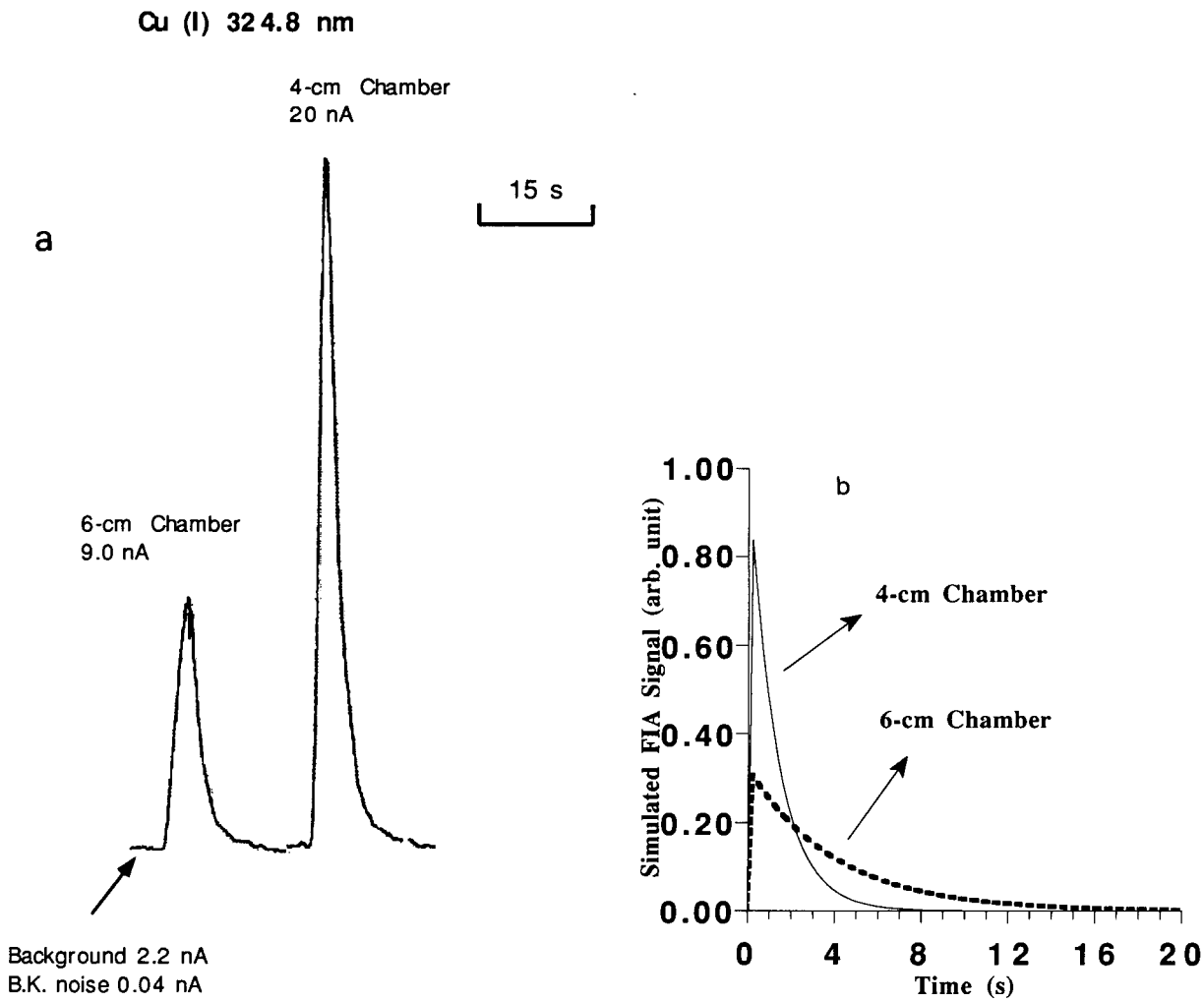

Fig. 11. (a) Comparison of FI peaks produced by the 4-cm and a 6-cm vertical rotary spray chambers, both coupled to the MPT emission system. Experimental conditions: 5 μg ml^{-1} Cu, Cu I 324.8 nm transition, other settings as in Table 2. (b) Theoretical simulation of FI signals from 4-cm and 6-cm spray chambers with volumes of 10.5 ml and 40 ml, respectively. Hypothesized experimental conditions are 75 μl sample-loop volume and others as in Table 2.

TABLE 2

Optimized operating conditions for the Ar-MPT

Forward power	200 W
Reflected power	< 5 W
Plasma viewing mode	Side-on
Plasma viewing position	6 mm above torch top [a]
Plasma support-gas flow rate	500 ml min^{-1}
Sample carrier-gas flow rate	600 ml min^{-1}
Water flow rate	1.5 ml min^{-1}
Ethanol flow rate	0.8 ml min^{-1}
Air flow rate	0.8 ml min^{-1}

[a] No attempts were made to optimize this parameter.

the single well-stirred tank model [26], the difference in the flow-injection peaks can be explained completely on the basis of the difference in volume between the 4-cm and 6-cm spray chambers, which are 10.5 ml and 40 ml, respectively. If the sample volume S_v is 75 μl, much smaller than the above spray chamber volumes V_m, and if the sample aerosol is assumed to be homogeneously and instantly mixed with the gas flowing in the spray chamber, the normalized concentration (or the FI signal profile) can be computed from the following equation:

$$C(t)/C(0) = H(t)/H(0) = (S_v/V_m) \times e^{(-t/T)}$$

where $C(t)$ is concentration measured at time t after injection has taken place, $C(0)$ the original sample concentration, $H(t)$ the flow-injection peak height at time t and $H(0)$ the measured signal level for continuous sample introduction. The mean residence time T can be calculated from the ratio of the respective spray-chamber volume to the nebulizer-gas flow rate (cf. table 2). Figure 11b displays the predicted influence of spray chamber volume on FI signals, calculated from the above equation for a nebulizer gas flow rate of 0.75 l min^{-1} and a sample injection volume of 75 μl. An enhancement of 3.2 in the FI peak signal is predicted if the 4-cm chamber is used in place of the 6-cm chamber, in very good agreement with experimental results (cf. Fig. 11a).

Table 2 summarizes the experimental parameters that were chosen on the basis of the foregoing investigations and used in the following performance studies.

Analytical performance

The above optimization studies have provided the basis for assessing the analytical performance of the new 4-cm vertical rotary spray chamber coupled to the MPT system. Under the compromise operating conditions listed in Table 2, the detection limits of ten elements were determined. The concentrations used in this determination were between 1 ppm and 20 ppm. Because the use of air as a carrier yields 90% of the continu-

TABLE 3

Detection limits of selected elements (ng ml^{-1}) obtained with the 4-cm vertical rotary spray chamber and the MPT

Element	Wavelength (nm)	ICP[a] 1.1 kW PN [b] no desolv.	He-MIP 150 W PN [10] no desolv.	MPT 200W USN [c] [11] w/desolv.	MPT 200W PN [b,d] no desolvation	MPT 200W PN [b,e] no desolvation	MPT 200W PN [b,f] no desolvation
Ag I	328.1	5	10.5	3	7.3	7.3	8.5
Ba II	455.5	1.3	–	6.8	20.3	21.4	30.5
Ca I	422.7	–	5	0.24	–	–	–
Ca II	393.4	0.1	–	0.24	6.3	8.8	11.1
Cd I	228.8	2.0	–	18	23.5	24.2	26.7
Cu I	324.8	5.4	–	1.7	4.3	5.3	8.97
Fe I	248.3	–	45	38	56	57	–
Mn II	279.5	12	17	8	12.4	14.2	–
Ni I	352.3	30	–	–	7.4	8.7	8.7
Pb I	405.8	180	–	27	72	75	–

[a] 27.12 MHz, R.K. Winge et al, Appl. Spectrosc., 33 (1979) 206. [b] PN: pneumatic nebulizer. [c] USN: ultrasonic nebulizer. [d] Continuous flow sample introduction. [e] Flow injection of 75 μl solution with air as carrier flow. [f] Flow injection of 75 μl solution with water as carrier flow. Note: detection limit is defined as 3σ.

ous-nebulization signal from a 75-μl injection volume, 75-μl sample injections were employed to measure detection limits in the FIA mode. The results, compiled in Table 3, represent the average of five replicate runs and correspond to a signal-to-background noise ratio of three (3σ). Importantly, all detection limits from the present study listed in Table 3 were determined under the same experimental conditions, so in routine determinations no re-optimization or compromise would be necessary for different elements. This feature, of course, simplifies simultaneous and sequential multielemental measurements. The detection limits are in the range of 5–50 ppb, comparable or superior to the best performance achieved by Perkins and Long [10] with a high-efficiency helium microwave-induced plasma.

Detection limits depend on element identity, transition type, and experimental parameters. The MPT system yields much poorer detection limits than an ICP for ionic transitions (e.g., Ba II 455.5 nm and Ca II 393.4 nm), similar to experience with other MIPs. Also, air as an FI carrier offers consistently better detection limits than water as a carrier, especially for transitions that overlap OH emission bands (e.g., Cu I at 324.8 nm).

Precision obtainable with the 4-cm vertical rotary spray chamber was acceptable. With water as the FIA carrier, the R.S.D. was routinely held at 2.5% for a sample at sub-ppm concentration and without resorting to use of an internal standard. No significant differences in precision were observed between results obtained with continuous nebulization and with FI sample introduction. However, this precision is slightly worse than was obtained with an ultrasonic nebulizer/desolvation sample-introduction system (USN) on a similar MPT setup (1.5–2.3%) [27].

Organic nebulization

Figure 12 shows the dependence of S/B and signal-to-background noise ratios on the percentage of ethanol in the carrier liquid (the balance of the carrier was distilled water). Not surprisingly, replacement of the aqueous carrier by ethanol introduces a large amount of hydrocarbon species into the MIP, where they consume energy. Therefore, a noticeable change in both

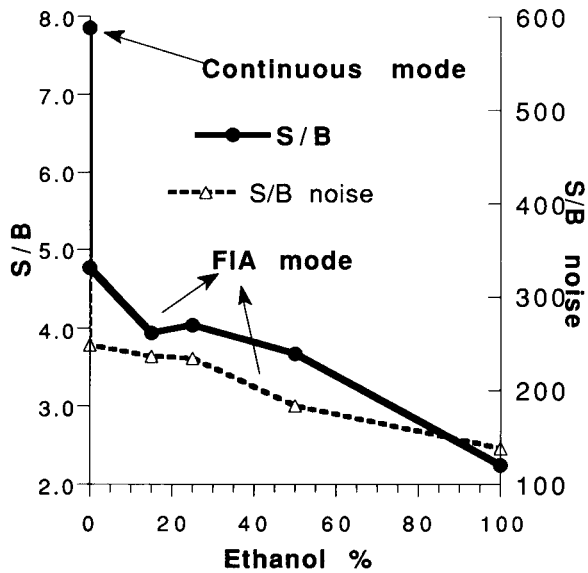

Fig. 12. Effect of ethanol concentration in the FIA carrier (the balance of the carrier is distilled water) on S/B and signal-to-background noise ratios obtained with the 4-cm vertical rotary chamber coupled to the MPT. Experimental conditions: 5 μg ml^{-1} Cu, Cu I transition at 324.8 nm, others as in Table 2.

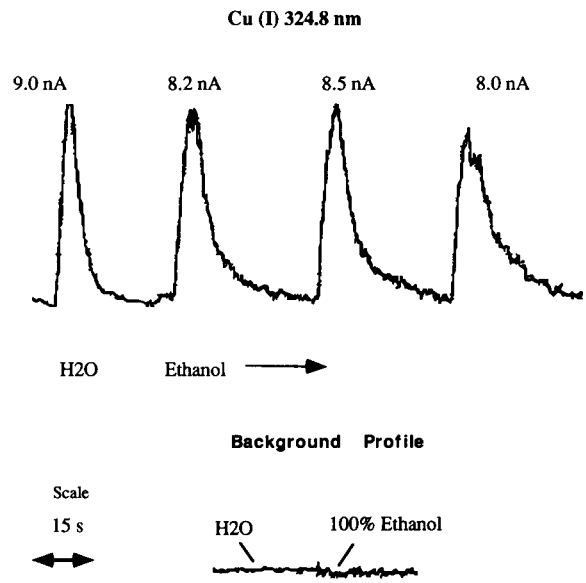

Fig. 13. Effect of undiluted ethanol on the signal from Cu I and on the corresponding background emission for a 4-cm vertical rotary chamber coupled to the MPT system. Experimental conditions: 5 μg ml^{-1} Cu, Cu I 324.8 nm transition, others as in Table 2.

the plasma background and in the analytical emission signal would be expected. Still, by adjusting the plasma support-gas and carrier-gas flow rates and tuning the plasma cavity, stable operating conditions could always be achieved.

In particular, under optimized conditions (cf. Table 2), the substitution of ethanol for water as a carrier caused only a 10–20% reduction in the FI peak height. At the same time, the background fluctuation was approximately doubled, compared to the performance with water as a carrier. This change, apparent in Fig. 13, suggests that the use of ethanol rather than water as an FI carrier would worsen detection limits by only two-fold for Cu. Similarly, 40% methanol was employed at 1.4 ml min^{-1} carrier-delivery rate and caused S/B to drop to 54% of that with water as a carrier.

The resistance of the plasma to organic solvents over a range of carrier flows from 0 to 2.0 ml min^{-1} indicates the robustness of the MPT plasma, compared with other MIPs [10].

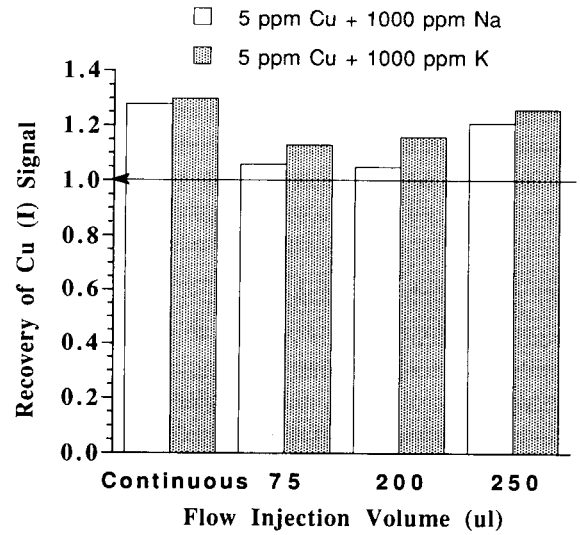

Fig. 14. Interference of Na and K (1000 $\mu g\ ml^{-1}$ each) on Cu I 324.8 nm emission for the 6-cm vertical rotary chamber coupled to the MPT system. Operating conditions: 5 $\mu g\ ml^{-1}$ Cu, others as in Table 2. When recovery is unity, interference effect is absent.

Interference effects

The effects of potassium and sodium on Cu I emission were studied for both continuous nebulization and for flow injection, with the 6-cm vertical rotary spray chamber interfaced to the MPT. As shown in Fig. 14, the addition of 1000 $\mu g\ ml^{-1}$ sodium caused only a small enhancement (less than 5%) in the copper signal for the smallest flow-injection volume (75 μl), while it showed more substantial enhancements (more than 20%) for larger flow-injection volumes. Continuous nebulization caused the largest interference effect, a 26% enhancement. The addition of 1000 $\mu g\ ml^{-1}$ potassium to the sample produces similar interference patterns to those of Na; however, the potassium-caused interference was more severe. The lower ionization potential of potassium is probably the origin of this greater enhancement; similar ionization-related effects are commonly observed in flame emission spectrometry [28].

Conclusions

Only a few studies in the past have focused on direct aerosol introduction into an MIP [10,29–32]. Generally, such attempts have met with only limited success because of the strong effect of the aerosol on the MIP stability and on its excitation capability. In contrast, the present combination of a new spray chamber with the microwave plasma torch has offered better analytical performance. The new vertical rotary spray chamber yields detection limits that are similar for continuous nebulization and for the introduction of 200-μl discrete sample volumes by flow injection. Also the FI system suffers less from interferences. The dilution factor produced by FI cannot account completely for this reduction; part is likely attributable to the new spray chamber. The smaller-volume chamber (4-cm diameter) offers lower detection limits than the larger-volume device (6-cm), possibly because of differences they cause in solvent loading. Further improvement of detection limits could probably be achieved through optimization of the spatial viewing location in the MPT. The coupling of an on-line preconcentration technique with the FI-MPT system could further improve detection limits and might simultaneously eliminate interference effects caused by easily ionized elements [24].

An earlier study that explored direct organic-solvent introduction into a microwave induced plasma utilized a rather low solution-delivery rate (0.46 ml min^{-1}) [10]. The present study reports an extension of the range of useful organic solvent loading to flows above 2.5 ml min^{-1} and offers a quantitative evaluation of the effects of an organic solvent on analytical performance.

It was one of the goals of the present study to determine whether the vertical rotary spray chamber might be an attractive alternative for use in LC—MPT studies. The flow-injection peak width produced by a 4-cm rotary chamber is typically 6 s for an organic solvent carrier at 1.5 ml min^{-1} delivery rate. The use of distilled water as a carrier offered no obvious reduction in band broadening. The band broadening observed in this study is comparable or superior to that reported for various LC—ICP interfaces investigated in [33]. In addition, the R.S.D. is slightly better.

In summary, the use of flow injection and the new vertical rotary spray chamber with the microwave plasma torch enables solutions to be nebulized directly and offers a simple, inexpensive, sensitive and stable system for elemental determinations. With some modifications, it could very well find applications in on-line process-control. Further, it serves as the first step toward application of the MPT as an element-selective detector for LC. The coupling of an LC system with the helium MPT system is being pursued in this laboratory to explore non-metal detection.

Funding for this research was provided by the National Science Foundation through grant CHE 90-20631 and by the National Institutes of Health through grant R01 GM 46853.

REFERENCES

1 M. Selby and G.M. Hieftje, Spectrochim. Acta, 42B (1987) 285.
2 C.I.M. Beenakker, Spectrochim. Acta, 31B (1976) 483.
3 M. Moisan and Z. Zakrzewski, J. Phys. D: Appl. Phys., 24 (1991) 1025.
4 P.J.W.M. Boumans, F.J. De Boer, F.J. Dahmens, H. Hoelzel and A. Myer, Spectrochim. Acta, 30B (1975) 449.
5 Q. Jin, F. Wang, C. Zhu, D.M. Chambers and G.M. Hieftje, J. Anal. At. Spectrom., 5 (1990) 487.
6 R.M. Barnes and E.R. Reszke, Anal. Chem., 62 (1990) 2650.
7 K.A. Forbes, E.R. Reszke, P.C. Uden and R.M. Barnes, J. Anal. At. Spectrom., 6 (1991) 57.
8 E. Reszke and R. Parosa, in H.V. Boenig (Ed.), Advances in Low-Temperature Plasma Chemistry, Technology, Applications, Vol. 4, Technomic Publ., Lancaster, 1992, p. 1.
9 H. Matusiewicz, Spectrochim. Acta, 47B (1992) 1221.
10 L.D. Perkins and G.L. Long, Appl. Spectrosc., 43 (1989) 499.
11 Q. Jin, C. Zhu, M.W. Borer and G.M. Hieftje, Spectrochim. Acta, 46B (1991) 417.
12 M. Morita, T. Uehiro and K. Fuwa, Anal. Chem., 52 (1980) 349.
13 P.L. Kempster, J.F. Van Staden and H.R.J. Van Vliet, J. Anal. At. Spectrom., 2 (1987) 823.
14 L.S. Dale and S.J. Buchana, J. Anal. At. Spectrom., 1 (1986) 59.
15 D.R. Luffer and E.D. Salin, Anal. Chem., 58 (1986) 654.
16 M.W. Routh, Spectrochim. Acta, 41B (1986) 39.
17 I. Hirofumi, U. Tetsuo, N. Takashi, L. Chuzo and N. Genkichi, J. Anal. At. Spectrom., 4 (1989) 351.
18 J.M. Gehlhausen and J.W. Carnahan, Anal. Chem., 61 (1989) 674.
19 M. Wu and G.M. Hieftje, Appl. Spectrosc., 12 (1992) 1261.
20 M.W. Borer, R.E. Ensman, Y. Madrid and G.M. Hieftje, Appl. Spectrosc., 46 (1992) 1162.
21 R.F. Browner, in P.W.J.M. Boumans (Ed.), Inductively Coupled Plasma Emission Spectroscopy, Part II: Applications and Fundamentals, Wiley, New York, 1987, pp. 244–288.
22 B.L. Sharp, J. Anal. At. Spectrom., 3 (1988) 939.
23 S.F. Easley, C.A. Monnig and G.M. Hieftje, Appl. Spectrosc., 45 (1991) 1368.
24 Y. Madrid, M. Wu, Q. Jin and G.M. Hieftje, Anal. Chim. Acta, 277 (1993) 1.
25 R. Pereiro, M. Wu, J.A.C. Broekaert and G.M. Hieftje, Spectrochim. Acta Rev., in press.
26 J. Ruzicka and E.H. Hansen, Anal. Chim. Acta, 99 (1978) 37.
27 Q. Jin, C. Zhu, K. Brushwyler and G.M. Hieftje, Appl. Spectrosc., 44 (1990) 183.
28 C.T.J. Alkemade, T. Hollander, W. Snelleman and P.J.T. Zeegers, Metal Vapours in Flames, Pergamon, Oxford, 1982.
29 W. Drews, G. Weber and G. Toelg, Fresenius' Z. Anal. Chem., 332 (1989) 862.
30 G.L. Long and L.D. Perkins, Appl. Spectrosc., 41 (1987) 980.
31 F. Leis and J.A.C. Broekaert, Spectrochim. Acta, 39B (1984) 1459.
32 C.I.M. Beenakker, Spectrochim. Acta, 33B (1978) 373.
33 T.J. Brotherton, P.E. Pfannerstill, J.T. Creed, D.T. Heitkemper, S.E. Pratsinis and J.A. Caruso, J. Anal. At. Spectrom., 4 (1989) 341.

Analytica Chimica Acta, 286 (1994) 169–178
Elsevier Science B.V., Amsterdam

Comparison of mixing devices for flow-injection determinations based on doublet peak formation

Roger T. Echols and Julian F. Tyson

Chemistry Department, University of Massachusetts, Amherst, MA 01003 (USA)

(Received 5th August 1993; revised manuscript received 4th October 1993)

Abstract

The well-stirred tank model accurately describes the separation (Δt) between flow-injection doublet peaks and has been found to be applicable to a variety of mixing devices that do not contain moving parts such as a magnetic follower. The reaction between lanthanum(III) and methyl thymol blue was used as a model reaction for a comparison study of mixing devices. Column and open-tubular reactors were included in the study. Mixing devices were compared on the basis of the straight line fit of Δt versus the natural logarithm of the concentration of injected La(III). The linearity of the Δt–ln[La(III)] plots was equivalent for several reactors. A mixing device composed of a column of alternating helices was selected as the best alternative mixer to the well-stirred tank when the magnitude of the slope of the plot and practicality were considered. Experiments showed that the well–stirred tank model qualitatively describes the behavior of these alternating helical reactors (AHR) in experiments designed to produce doublet peaks. The AHR was used as the mixing device in flow-injection determinations, based on doublet peaks, of zinc, hydroxide ion and of water hardness. A paired *t*-test showed that over the 16 determinations performed there was no significant bias at the 95% confidence level. Factors affecting the relative standard deviation of the concentrations measured are discussed.

Keywords: Flow injection; Double peak formation; Mixing devices

The interest over the past decade in time-based and kinetic flow-injection (FI) methods has been a natural extension of FI because of the inherent kinetic nature of such methods [1,2]. Time-based flow-injection methods of analysis have received attention as alternatives to traditional FI methods, which have relied on peak height as the quantitative analytical parameter. The increased linear range of determination of several orders of magnitude and speed of analysis have been cited as advantages of these methods [3,4].

For time-based methods an interval of time between data points on the concentration–time profile is used as the quantitative analytical parameter. Common examples of time-based FI methods are those based on a change in concentration over time under conditions of stopped-flow [1,2]. Reactions monitored in stopped-flow methods must be slow relative to the time scale of the flow system. For other time-based methods such as peak-width methods, chemical kinetics of a reaction are not considered. Reactions are sufficiently fast such that dispersion is the only phenomenon contributing to the concentration gradient of the injected sample. There has been some debate over the nomenclature used to identify these methods. In this paper, peak-width methods involving the measurement of doublet peaks will be considered a subset of time-based methods. Other time-based methods have been based upon measurement of a time interval between

Correspondence to: J.F. Tyson, Chemistry Department, University of Massachusetts, Amherst, MA 01003 (USA).

SSDI 0003-2670(93)E0577-T

points on any part of the peak profile [5]. Determinations based on the time between doublet peaks will also be referred to as "flow-injection titrations" because the term has been used previously [1–6] and is descriptive as to the kinds of chemistry [7] that can be exploited by FI time-based methods.

The use of doublet peaks as the analytical parameter of interest is in keeping with the general philosophy of FI, that of providing an easily identifiable quantitative parameter. The most common analytical parameter is peak height, for which operating conditions of the flow system are adjusted so that doublet peaks are avoided [1]. Flow-injection doublet peaks are obtained when conditions of the FI system are adjusted so that the injected sample material is in excess over the carrier stream in the center of the injected slug. Under conditions of a fast reaction and no diffusion, the product profile matches the sample profile, except in the center region. Two peaks arise from the pair of increasing and decreasing product concentration gradients. For a well-stirred tank, the gradient is exponential such that there is a semilogarithmic relationship between time and the concentration of injected analyte.

The mathematical relationship between time between doublet peaks and concentration is based on a model of plug flow of injected sample through a well-stirred mixing chamber [5]. The time interval (Δt) between doublet peaks is given by

$$\Delta t = (V/Q)\ \ln C_s + (V/Q) \times \ln[\{\exp(V_i/V) - 1\}/C_r] \quad (1)$$

in which V is the volume of the mixing chamber, Q is the flow rate, C_s is the concentration of the injected sample, C_r is the concentration of the reagent solution, and V_i is the volume of the injected sample. A plot of Δt versus ln C_s is linear with a slope of V/Q.

Two other theoretical treatments have led to the semilogarithmic relationship between time and the concentration of injected sample. Ruzicka et al. [3] used a tanks-in-series model and the concept of dispersion to derive equations relating time and analyte concentration. Points on the rise and fall curves of FI peaks were used in measuring the interval of time, which was related through a calibration plot to the logarithm of concentration. An acid–base system and a calcium–EDTA system illustrated the new method, which was termed FI titration. A complexometric titration and oxidation–reduction titration were demonstrated in a subsequent paper in which a tubular reactor was employed as the mixing device [6].

Pardue and co-workers [8–12] have derived equations that relate time intervals to analyte concentrations using a variable-time kinetic model; the last paper is a thorough overview [12]. The authors derived equations for several experimental situations and discussed using peak widths obtained from a variety of reference points on the FI concentration–time profile. Mathematical relationships between peak width and ln C_s are, in general, nonlinear. However, an approximately linear relationship is obtained for situations in which the reference point concentrations (between which the peak width is measured) are much less than injected analyte concentrations. Recent work by Jordan and Pardue [13] has shown that it is possible to obtain excellent agreement between experiment and theory for FI systems in which the dispersion behavior is dominated by the concentration gradients produced by a single well-stirred mixing chamber. They evaluated a variety of methods in which data from such FI experiments can be manipulated to give quantitative analytical parameters for the situation in which the product profile is monitored under conditions in which the reagent is always in excess [14]. An acid–base reaction, the triiodide–thiosulfate reaction and the iodate–iodide reaction were the chemical systems used in these studies [8–14].

Previous work has shown that Eqn. 1 is valid for experimental conditions that result in the formation of doublet peaks [4,5]. A well-stirred mixing chamber was used in the experiments correlating experimental data with parameters in Eqn. 1, but a gradient tube was used in the experiments designed to illustrate the linear dynamic range of FI titrations [4]. It has also been shown possible to determine stability constants from doublet peak data [15]. Recent work in our

laboratory has focused on the development of inexpensive detectors for undergraduate teaching experiments based on the measurement of time between doublet peaks [16–18]. LEDs (light-emitting diodes) and laser diodes were employed as light sources in this work; simple electronic circuitry was used to measure Δt values.

In this paper the study of practical mixing devices for FI methods based on the formation of doublet peaks is continued. Results from an investigation of a variety of FI reactors, which do not contain moving parts (such as the magnetic follower of a well-stirred tank) are presented. The linear fit of Δt–ln C_s plots and practical considerations of the application of the mixing devices are criteria for choosing one static mixer as the best mixer for further study. The applicability of Eqn. 1 to FI doublets produced under non-well-stirred tank conditions is discussed and the application of static mixers for simple determinations by FI titrations is illustrated with simple chemical systems.

EXPERIMENTAL

Apparatus

Flow-Injection System. A single-line flow-injection manifold was used in all experiments (Fig. 1). Components included a variable speed peristaltic pump (Ismatec sa), a six-port injection valve (Rheodyne, an 8-μl flow cell (Hellma), and a UV–visible detector (Novaspec). An integrator (Hewlett-Packard Model HP 3394A) was used for data collection. All flow tubing was 0.8 or 0.9 mm i.d. PTFE tubing. Slug injection was employed in all experiments; injected volume and flow rates were varied and are noted below.

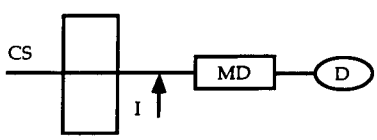

Fig. 1. Basic flow-injection manifold used in all experiments. CS, carrier stream; I, injection valve; MD, mixing device; D, detector. For the model reaction, La(III) is introduced at I into a carrier stream of methyl thymol blue. The reaction is monitored at 608 nm.

Mixing devices. Mixing devices (static mixers) were obtained from a number of sources. With the exception of the short tube and the roughened flow tubing, 0.8 mm i.d. flow tubing was used to construct the tubular reactors. A 15 cm × 2 mm i.d. PTFE tube was employed as the short tube. Roughened tubing was obtained from Lifesource Ventures (Atlanta, GA). Mixing chambers were used in previous work [4]. The empty Omni column was obtained from Omnifit. The packed reactor consisted of 250 μm glass spheres packed in a 6 cm × 2 mm i.d. PTFE tube; single-bead string reactors consisted of glass spheres of 500–600 μm diameter in 0.8 mm i.d. tubing. Alternating helical reactors (AHR) were constructed from 3/16 in. i.d. plastic helical segments inserted into lengths of 0.6 cm i.d. tubing. Flow through the reactors is disturbed by the helical segments. The helical segments are available from Cole-Parmer as "in-line static mixers." The "prototype" static mixer, also a reactor that contains segments that disturb the flow pattern, was obtained courtesy of Upchurch.

Reagents

Lanthanum–methyl thymol blue reaction. Buffered lanthanum solutions (1.13×10^{-2} M to 1.41×10^{-5} M) were prepared from a 1.8799×10^{-2} M lanthanum chloride stock solution, which was standardized against EDTA. Solutions were buffered with an acetic acid–acetate buffer that was prepared by adjusting the pH of a 0.005 M sodium acetate solution to 6.2. Methyl thymol blue (MTB) solutions were also prepared in the acetate buffer at a concentration of around 3×10^{-5} M. Preparation of MTB solutions of exactly known concentrations was difficult due to the purity of the Aldrich reagent grade MTB (95% purity).

Zinc–methyl thymol blue reaction. Zinc solutions were prepared by dilution from a standardized zinc sulfate stock solution of 4.2828×10^{-1} M. Solutions were buffered with 0.005 M acetate buffer (pH 6.0). A buffered MTB solution of 4×10^{-5} M (pH 6.0) was used as the reagent.

Hydrochloric acid–sodium hydroxide reaction. Sodium hydroxide solutions were prepared from a NaOH stock solution of 1.5512 M, which was standardized versus KHP. The carrier stream for the acid–base titration consisted of 8.9×10^{-4} M HCl and approximately 3×10^{-5} M bromothymol blue (BTB) indicator.

Magnesium / calcium–EDTA reaction. Calcium and magnesium solutions were prepared from standardized 0.2893 M and 0.3743 M stock solutions of the nitrate salts. Each solution contained about 0.1% calmagite indicator solution. The 2.030×10^{-3} M EDTA carrier stream was prepared by dissolution of the dried acid. All solutions were buffered with 10% of a pH 10.1 ammonia–ammonium buffer stock solution.

Procedures

Study of reactors used to produce doublet peaks. The colorimetric reaction between lanthanum and MTB was used in the study of mixing devices. Mixing devices were compared on the basis of the straight line fit of the plot of time between doublet peaks (Δt) versus the natural logarithm of concentration (in units of ppm) of La(III). Three or four replicate injections of each concentration were made for all mixers. In some cases a doublet peak was not produced and the data points were not used in the plot. The variance of the Δt residuals ($s^2_{y/x}$), correlation coefficient squared, intercept, slope and the confidence interval of the slope [19,20] were calculated for each mixing device using Statview (BrainPower). The goals of the study did not require that the volume injected and flow rate need be the same for all mixing devices, although reasonable values of injected volume were used and efforts were made to maintain the flow rate at approximately 27 μl/s.

Reactor volumes were obtained by acid–base titration. The mixing device was filled with a Tris solution of known concentration and eluted into an Erlenmeyer flask; standardized HCl was used as a titrant. Flow rate was determined by measuring the time required to collect 10 ml of eluent in a calibrated flask.

Characterization of alternating helical reactors. The behavior of static mixers with respect to that expected from theory [4] was investigated using the model reaction and the static mixers. Flow rate was varied from 18 μl/s to 39 μl/s for a 15 segment AHR; mixer volume was varied from 384 μl to 1860 μl for six AHRs.

TABLE 1

Experimental parameters

Carrier	Analyte	Conc. of standards (M)	V (μl)	V_i (μl)	Q (μl/s)
1 MTB	Zinc	1.03×10^{-5}–3.43×10^{-3}	1581	1494	26.0
2 HCl	NaOH	6.21×10^{-4}–3.10×10^{-1}	384	507	23.8
3 EDTA	Mg/Ca	5.99×10^{-4}–1.50×10^{-2}	1581	1211	26.2

Flow-injection titrations using alternating helical reactors. Three simple chemical systems were used to demonstrate flow-injection determinations based on doublet peaks: the complexometric reaction between zinc and MTB, the acid–base reaction between HCl and NaOH, and the traditional water-hardness titration reaction, magnesium and calcium–EDTA with calmagite indicator. Data were collected for a range of standards; calibration plots were used to determine concentration of synthetic unknowns. Conditions for these determinations are listed in Table 1. The three example reactions were chosen to illustrate different ways doublet peaks can be formed. For the Zn–MTB reaction, the product profile is monitored at 580 nm. For the acid–base reaction, the absorbance–time profile of BTB is monitored at 620 nm. For the third reaction, the absorbance of an indicator, calmagite, is monitored at 675 nm. Calmagite is participating in the ligand exchange reaction:

Mg–calmagite + EDTA $\rightleftharpoons$

Mg–EDTA + calmagite

For the latter two chemical systems, the BTB and calmagite indicators, which are the chemical species being monitored spectrophotometrically, are not the reaction products. For these reactions, it is assumed that the absorbance maxima of the indicators correspond in the time domain to the concentration maxima ("doublet peaks") of the product (see introductory part).

RESULTS AND DISCUSSION

Model reaction

Preliminary work has shown that diffusion effects are possible reasons for experimental error in acid–base doublet peak experiments; thus, a complexometric reaction rather than an acid–base reaction was selected as the model reaction. The reaction between lanthanum(III) and methyl thymol blue was chosen for the comparison study of mixing devices for the following reasons. The product of the reaction absorbs at 608 nm, a wavelength at which the molar absorptivity of the free ligand is low, the reaction is rapid and the reaction is reported to have a 1:1 stoichiometry and a conditional formation constant of 10^6 (pH 6.5) [21]; another study has reported a conditional formation constant of $10^{7.4}$ (pH 5.84) for a 2:2 reaction product [22]. The range of La(III) concentrations employed in the study was established at the low end by a concentration that yielded resolvable doublet peaks and at the high end by the concentration for which a peak maximum could be detected on the second peak of the doublet. The range of applicable solutions varied between reactors.

Comparison of mixing devices

Results from the comparison of mixing devices are enumerated in Table 2. The variance of the Δt residuals, $s^2_{y/x}$, is the parameter of merit for comparing the behavior of the mixing device to that expected from theory (i.e., a linear plot of Δt versus ln C_s). The square of the correlation coefficient is not as sensitive to differences among mixers and thus was not chosen as the parameter of merit. The scatter of Δt values from replicate injections and the non-linearity of the data is reflected in $s^2_{y/x}$. In most cases the standard deviations of replicate injections were low; thus, the data reflects deviation of Δt values from the linear least squares best-line fit. Examination of Table 2 reveals that there is little difference between the linear fit of many of the mixing devices. With the exception of the empty column reactor and the larger volume coiled reactor, all mixing devices fit the theory as well as or better than the well-stirred tanks. It should be noted

TABLE 2

Summary of results for various mixing devices

Mixing device	$s_{y/x}$	$s^2_{y/x}$	R^2	Intercept (s)	Slope (±95% CI) (s)	V (μl)	V_i (μl)	Q (μl/s)	Slope × Q V_{eff} (μl)
Well-stirred tank I	1.934	3.740	0.997	−25.83	25.67 (±0.96)	828	783	25.25	648.1
Prototype static mixer I	0.741	0.549	0.996	1.55	5.56 (±0.19)	267	374	27.17	151.0
Knotted reactor I	0.842	0.709	0.992	5.52	3.97 (±0.18)	400	374	28.46	113.0
Prototype static mixer II	0.616	0.379	0.998	15.77	6.29 (±0.16)	267	783	27.75	174.5
Coiled tubing	1.584	2.509	0.979	3.20	5.24 (±0.41)	428	374	27.73	145.3
Fat tube reactor	1.455	2.117	0.989	−0.38	5.93 (±0.30)	242	374	27.50	163.0
Uncoiled tubing	1.353	1.831	0.985	1.93	5.42 (±0.35)	428	374	28.31	153.3
Roughened tubing I	1.340	1.796	0.992	−2.57	7.25 (±0.35)	556	374	27.36	198.2
Roughened tubing II	1.616	2.611	0.977	2.93	5.33 (±0.45)	417	374	28.36	151.3
Column reactor (Omni)	2.773	7.690	0.982	−10.49	11.58 (±1.08)	748	507	27.39	317.1
Well-stirred tank II	2.270	5.153	0.993	6.84	10.82 (±0.56)	378	802	28.19	305.0
Knotted reactor II	1.206	1.454	0.989	5.60	5.60 (±0.30)	1270	507	29.01	162.4
None	0.584	0.341	0.992	7.85	2.73 (±0.15)	n/a	374	28.50	77.7
Tight coiled tubing	2.924	8.550	0.968	23.01	7.84 (±0.92)	891	802	29.03	227.6
Packed bed reactor	0.885	0.783	0.991	9.01	4.42 (±0.28)	96	374	20.82	92.0
SBSR-I	0.459	0.211	0.995	7.96	3.28 (±0.10)	192	374	25.58	84.0
SBSR-II	0.468	0.219	0.997	9.47	4.56 (±0.12)	384	507	27.28	124.4
AHR 3 segments	0.767	0.588	0.997	2.96	6.28 (±0.16)	384	507	33.23	208.7
AHR 6 segments	1.052	1.107	0.998	5.53	9.57 (±0.22)	696	783	31.21	298.8

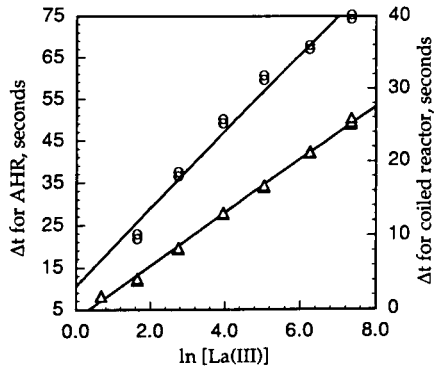

Fig. 2. Calibration plot (Δt vs. ln[La(III)]) for two static mixers: ○ = 60 cm × 0.8 mm i.d. coiled tubing reactor; △ = 3-segment alternating helical reactor. Note curvature in plot of data collected using the coiled tubing as mixing device.

that much of the error in the estimated values for the stirred tank was as a result of the large scatter of replicate Δt values around the mean Δt values. The linear fit of the mean Δt values for the well-stirred tanks was excellent.

The mixing devices with the lowest $s^2_{y/x}$ values were those reactors that were expected to enhance radial dispersion and reduce axial dispersion [1]: knotted reactors, packed reactor, single-bead string reactors and the alternating helical reactors. Surprisingly, $s^2_{y/x}$ for no mixer (absence of a mixer) was low, but it was excluded from further consideration because of the low value of the slope. Examination of plots of Δt versus the natural log of La(III) concentration indicated that there was curvature in the plots (Fig. 2) for some reactors. This has been observed in other work [14] and was expected for mixing devices such as the coiled reactor. Application of the Wald-Wolfowitz runs test [18] confirmed the curvature for these static mixers.

Perhaps the only conclusion to draw from the above discussion is that a variety of reactors, which disrupt the flow and enhance the radial dispersion, behave like well-stirred tanks for the purpose of establishing a linear relationship between the separation doublet peaks and the logarithm of injected concentration. Adherence to Eqn. 1 is limited to the linear relationship of the slope; data is not expected to validate the model to the extent that was presented earlier for a well-stirred experimental system [4]. A comparison of the actual volumes and effective volumes (V_{eff}) (Table 2) illustrates the lack of correlation between experimental and theoretical results.

The F-test (ratio of variances) was used to test for differences between $s^2_{y/x}$ of differing reactors. With the exception of the variance of the SBSRs, the variance of the packed reactor, the lowest-volume knotted reactor, prototype static mixer and AHRs were not statistically different. Given the reduced list of possible alternatives to the well-stirred tank, other criteria were imposed: the slope of the V/Q plot and practicality. The slope of the calibration plot is important in determinations based on the width of doublet peaks and will be discussed below. The prototype static reactor had a low volume, which could not be increased. Thus, only knotted reactors, single-bead string reactors, packed reactors and AHRs were considered. Increasing the volume of the knotted reactors and SBSRs did not increase the slope of the Δt vs. ln C_s plots by a significant amount. From a stand-point of practicality, the packed reactor was eliminated from considera-

TABLE 3

Results for alternating helical reactors

No. of segments	Intercept (s)	Slope (±95% CI) (s)		V (μl)	V_i (μl)	Q (μl/s)	V_{eff} (μl)
3	2.96	6.28	(±0.16)	384	507	33.23	208.7
6	5.53	9.57	(±0.22)	696	783	31.21	298.8
9	15.24	12.38	(±0.43)	966	1211	30.35	375.7
12	10.98	14.54	(±0.22)	1283	1211	30.07	437.2
15	11.51	18.03	(±0.27)	1581	1494	30.81	555.5
18	8.89	19.09	(±0.19)	1860	1494	30.89	589.8

tion because of difficulty in construction and difficulties with back-pressure. Further, construction of SBSRs was time-consuming and tedious, while the volume for AHR reactors is easily adjusted with a longer length of tubing and a greater number of helical segments. Experiments varying the volume showed that the slope of the regression plot did increase with increasing AHR volume. On the basis of this, and with consideration of the practicality, AHRs were chosen as the best alternative mixing device to well-stirred tanks.

Characterization of alternating helical reactors

Results from experiments varying the volume and flow rate of the alternating helical reactors are shown in Table 3. Adherence of the AHRs to the well-stirred tank model is indicated in Figs. 3 and 4. The slope of the plot of Δt versus ln C_s increases with reactor volume and increases as a function of the inverse flow rate ($1/Q$). It is important not to conclude that AHRs are behaving like well-stirred tanks. Significant differences exist between the volumes of the AHRs and their calculated effective volumes (product of the slope and the flow rate); further, there is little correlation between experimentally and theoretically obtained values for V_i and C_r. Figures 3 and 4 reveal that AHRs approximate the behavior of well-stirred tanks, providing sufficient mixing to allow Eqn. 1 to be used for determinations based on peak-width of doublet peaks.

The practical information derived from these results is what is important. The slopes of Δt versus ln C_s plots can be changed (typically increased) by changing the number of segments

TABLE 4

Results for flow-injection titrations

Analyte/unknown No.	Δt (s)	Analyte content (M)	Analyte found (M)	Percent difference
Zn				
1	63.78	6.852×10^{-5}	6.947×10^{-5}	1.4
2	135.97	1.713×10^{-3}	1.632×10^{-3}	−4.7
3	46.96	3.427×10^{-5}	3.330×10^{-5}	−2.8
4	121.12	8.565×10^{-4}	8.524×10^{-4}	−0.5
5	129.18	1.199×10^{-3}	1.213×10^{-3}	1.2
NaOH				
1	56.22	3.102×10^{-2}	3.223×10^{-2}	3.9
2	41.84	9.307×10^{-3}	8.979×10^{-3}	−3.5
3	17.43	9.928×10^{-4}	1.027×10^{-3}	3.4
4	34.46	4.964×10^{-3}	4.661×10^{-3}	−6.1
Mg				
1	92.50	1.123×10^{-2}	1.091×10^{-2}	−2.8
2	62.30	3.369×10^{-3}	3.153×10^{-3}	−6.4
3	33.06	8.983×10^{-4}	8.371×10^{-4}	−6.8
Mg / Ca				
1	77.76	5.888×10^{-3}	6.036×10^{-3}	2.5
2	54.32	2.158×10^{-3}	2.226×10^{-3}	3.2
3	79.54	6.941×10^{-3}	6.497×10^{-3}	−6.4
Ca				
1	63.62	3.761×10^{-3}	3.340×10^{-3}	−11.2
Calibration equations:				
Zn–MTB:		$\Delta t = 22.871 \ln[Zn] + 282.76$		
HCl–NaOH:		$\Delta t = 11.256 \ln[NaOH] + 94.883$		
Mg/Ca–EDTA:		$\Delta t = 0.892 \ln[Mg]^2 + 33.508 \ln[Mg] + 225.69$		

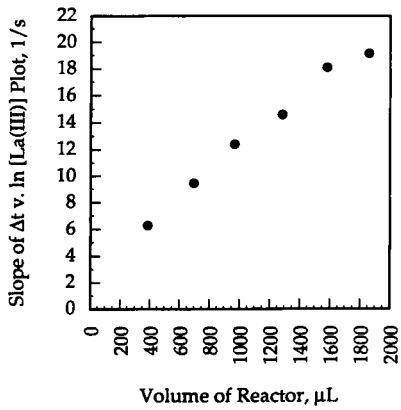

Fig. 3. Change in the slope of Δt vs. ln[La(III)] plots as a function of volume of the alternating helical reactor. The linear relationship of V/Q and V confirms the applicability of Eqn. 1 to AHRs.

placed in the reactor, or by decreasing the flow rate. An approximate value for the slope can be determined based solely on the number of segments of the alternating helical reactor; a plot of slope versus the number of reactor segments would be similar to Fig. 3.

Flow-injection titrations using alternating helical reactors

Results of FI titrations are listed in Table 4. Calibration plots were constructed from standard solutions of Zn(II), NaOH and Mg(II). Regression equations from the calibration data are noted at the bottom of the table. The results show that the doublet peak width FI method can be used quantitatively for simple determinations. Percent differences in the determined concentrations of the unknowns in Table 4 are both positive and negative. The 95% confidence interval of the mean percent difference includes zero: $-2.2 \pm 2.4\%$. Thus, there is no experimental bias in the results. Errors in determined concentrations are a result of random error and can be improved by decreasing the uncertainty in the measurement of Δt (see discussion of uncertainty below).

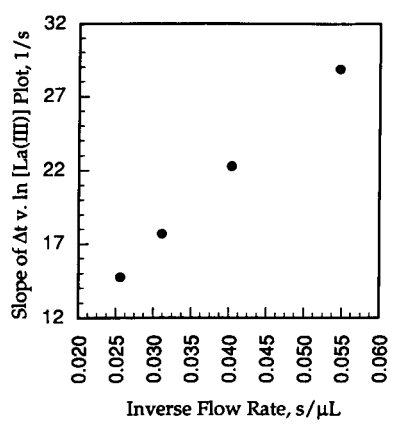

Fig. 4. Change in the slope of Δt vs. ln[La(III)] plots as a function of the inverse of the flow rate. The linear relationship of V/Q and $1/Q$ confirms the applicability of Eqn. 1 to AHRs.

The chemical systems illustrated in this work are examples of the determinations using FI titrations. As noted by Ramsing et al. [6], many titrimetric methods can be applied to FI titrations. For example, EDTA can be used as a titrant for many metals in the same manner as that described for Mg and Ca. Organic reagents such as pyrocatechol violet, xylenol orange, arsenazo III and alizarin complexone may be used in simple reactions like that described for MTB. Chemical interferents and competing side reactions can be overcome by the same procedures used in standard titrimetric methods [23].

For the Mg/Ca–EDTA system, the regression equation based on Mg standard solutions was applicable for solutions containing both Ca and Mg. The unknown solution that contained no Mg was the greatest in error. This is in keeping with the general philosophy of the water-hardness titrimetric method, that Mg is required for a sharp endpoint [23]. Other experimental similarities to the standard titrimetric method should be noted: As EDTA penetrates the injected solution slug (free Mg, free Ca and Mg–calmagite), it first reacts with the free Ca, then with the free Mg and finally with the complexonate. An alternative way to determine Mg in this FI system would be to use a buffered carrier stream of the calmagite indicator (as with the Zn–MTB method), but it would not be possible to determine the total water-hardness with such a reaction.

The indirect manner in which the Mg/Ca–EDTA reaction is monitored might be the cause of the slight nonlinearity in the regression plot. The concentration–time profile of the indicator is

not the same as that of the analyte. During the reaction EDTA displaces calmagite from the metal and the blue-colored free ligand is monitored spectrophotometrically. At the pair of points of highest EDTA penetration into the Mg/Ca injected slug, the concentration of calmagite reaches a maximum; these points are the peaks for the doublet. As was discussed above, it is assumed that the product absorbance–time profile follows that of the sample. For this reaction, it is further assumed that the indicator concentration–time profile is following the product profile. Diffusion effects and the time for the ligand exchange reaction to occur are sources of error which may lead to the nonlinearity of the plot. An advantage of this method is that broad second peaks, which are associated with the injection of high concentration sample solutions, are avoided. This is a result of adding fewer moles of indicator to the analyte solution than there are moles of metal. By adjusting the concentration of the indicator and the carrier, the working range of the method can be established at higher concentrations than those employed in this work.

Discussion of uncertainty

Discussions of the uncertainty in an instrumental procedure are often formulated in terms of a discussion of the precision of the instrument response (occasionally in terms of the uncertainty in response as a function of concentration) and usually ignore the contribution to the uncertainty caused by the need to interpolate from a calibration plot.

For methods based on a logarithmic function of concentration, an increase in the uncertainty in concentration may be expected. For Eqn. 1, the standard deviation of an Δt value, $s_{\Delta t}$ is related to the standard deviation in concentration, s_{C_s}, by the following equation [19,24]:

$$s_{\Delta t} = (\mathrm{d}[V/Q \ \ln C_s]/\mathrm{d}C_s) s_{C_s} \quad (2)$$

The relative standard deviation in concentration is expressed as

$$s_{C_s}/C_s = (Q/V) s_{\Delta t} \quad (3)$$

Q/V is the inverse of the slope for the plot of Eqn. 1. For the coiled tubing reactor, the 60 cm single-bead string reactor and the 3-segment alternating helical reactor, standard deviations in Δt are no greater than 0.3 s and thus relative standard deviations in concentration would be calculated as 5.7%, 6.6% and 4.8%. The high error in concentration is expected because the slopes of the Δt–ln C_s plots for these reactors are quite small. For the 18-segment AHR, the relative standard deviation would be 1.6%. However, this error treatment underestimates the overall uncertainty of the method as no account has been taken of the uncertainty in the slope of the calibration.

The standard deviation (s_{x_o}) of a determined concentration can be approximated using the following general equation [19,21]:

$$s_{x_o} = s_{y/x}/b\left\{1/m + 1/n + (y_o - \bar{y})^2 / b^2 \Sigma (x_i - \bar{x})^2\right\}^{1/2} \quad (4)$$

The concentration of interest (x_o) is calculated from y_o, which is a mean value based upon m replicates, $s_{y/x}$ is the standard error of the estimate, b is the slope of the calibration plot, x_i values are the individual x values obtained from a regression based on n data points, and $\bar{x}$ and $\bar{y}$ are the mean data points used in the regression. For this work, all x in Eqn. 4 represent ln C_s values and all y represent Δt values. A confidence interval (CI) can be calculated for s_{x_o} as $x_o \pm t s_{x_o}$ (t values of 95%, $n-2$ are used). Typical values for the NaOH and Zn determinations (Table 4) will be used as examples.

For NaOH Unknown 4, s_{x_o} is 0.043. The CI of ln[OH^-] is -5.369 ± 0.093, which corresponds to an OH^- concentration CI of 4.245×10^{-3} M < [OH^-] < 5.113×10^{-3} M. For Zn Unknown 4, s_{x_o} is 0.027. A ln[Zn(II)] CI of -7.067 ± 0.089 corresponds to a Zn(II) concentration CI of 7.805×10^{-4} M < [Zn(II)] < 9.318×10^{-4} M. The concentration CI is not symmetric around the determined concentration as a result of the logarithmic function. The CI of NaOH Unknown 4 encompasses percent differences of -8.9% and $+9.6\%$; the CI of Zn Unknown 4 encompasses percent differences of -8.5% and $+9.3\%$.

On the basis of the treatment of uncertainty discussed above, the FI titration results shown in

Table 4 are as good as can be expected without (a) improvements in the precision in the measurement of time, (b) an increase in the slope of the Δt–ln C_s plot and (c) improvement in the fit of the points to a straight line function, if an unweighted least squares procedure is to be used to establish the slope of the calibration function. In considering the mixing devices used in this paper, it is the magnitude of the slope, rather than the error in the Δt–ln C_s plots that is most important in reducing the error in these determinations. Several mixing devices had low $s_{y/x}$ values, but had a flat calibration plot as compared to that of the AHRs. This conclusion bolsters the argument made above for choosing the alternating helical reactor as the best static mixer. Use of slower flow rates and larger volume AHRs will result in smaller relative standard deviations in determined concentrations. Limiting the calibration range to reduce errors in locating the absorbance maxima for concentrated solutions should further reduce errors in determinations.

Conclusions

Alternating helical reactors are the mixing devices that are suitable alternatives to the well-stirred tank for FI systems designed to produce doublet peaks. The straight-line fit of the data, the relatively steep slopes of the Δt–ln C_s plots and the ease of construction of the AHRs make these reactors a practical choice for FI methods based on the time interval between doublet peaks. The slope of the calibration plots may be varied by adjustment of the reactor volume and flow rate.

The time interval between doublet peaks are accurately and easily obtained from the output of an integrator and can be used to determine metal ions in simple matrices. Three simple chemical systems illustrate the type of reactions that may be used for these FI time-based methods (FI titrations). The working range of the calibration plots are not as great as those reported previously, but are between two to three orders of magnitude. Errors in concentration that results from a calibration plot of doublet peak time intervals are reasonable. The slope of the calibration plot is important for obtaining low relative standard deviations for determined concentrations. The best experimental parameters for determinations based on doublet peak widths are large volume AHRs and relatively slow flow rates.

Financial support from Pfizer Inc. (Groton, CT) is gratefully acknowledged.

REFERENCES

1 J. Ruzicka and E.H. Hansen, Flow Injection Analysis, Wiley, New York, 2nd edn., 1988.
2 M. Valcarcel and M.D. Luque de Castro, Flow-Injection Analysis, Ellis Horwood, Chicester, 1987.
3 J. Ruzicka, E.H. Hansen and H. Mosbaek, Anal. Chim. Acta, 92 (1977) 235.
4 J.F. Tyson, Analyst, 112 (1987) 523.
5 J.F. Tyson, Anal. Chim. Acta, 179 (1986) 131.
6 A.U. Ramsing, J. Ruzicka and E.H. Hansen, Anal. Chim. Acta, 129 (1981) 1.
7 J. Bassett, R.C. Denney, G.H. Jeffrey and J. Mendham, Vogel's Textbook of Quantitative Inorganic Analysis, Longman, New York, 2nd edn., 1978.
8 H.L. Pardue and B. Fields, Anal. Chim. Acta, 124 (1981) 39.
9 H.L. Pardue and B. Fields, Anal. Chim. Acta, 124 (1981) 65.
10 H.L. Pardue and P. Jager, Anal. Chim. Acta, 179 (1986) 343.
11 P. Jager and H.L. Pardue, Anal. Chim. Acta, 187 (1986) 343.
12 H.L. Pardue, Anal. Chim. Acta, 220 (1989) 23.
13 J.M. Jordan and H.L. Pardue, Anal. Chim. Acta, 270 (1992) 204.
14 J.M. Jordan, S.H. Hoke and H.L. Pardue, Anal. Chim. Acta, 272 (1993) 115.
15 J.F. Tyson, Analyst, 112 (1987) 527.
16 M.K. Carroll and J.F. Tyson, J. Chem. Educ., 70 (1993) A210.
17 M.K. Carroll, A. Murfin and J.F. Tyson, Anal. Chim. Acta, submitted for publication.
18 M.K. Carroll and J.F. Tyson, Appl. Spectrosc., in press.
19 A. Wynne, personal communication.
20 J.C. Miller and J.N. Miller, Statistics for Analytical Chemistry, Ellis Horwood, Chichester, 3rd edn., 1993.
21 L.S. Serdyuk and V.S. Smirnaya, Zh. Anal. Khim., 20 (1965) 161.
22 B. Budesinsky and E. Antonescu, Collect. Czech. Chem. Commun., 28 (1963) 3264.
23 A. Ringbom, Complexation in Analytical Chemistry, Robert E. Krieger Publishing Co., New York, 1979.

Analytica Chimica Acta, 286 (1994) 179–187
Elsevier Science B.V., Amsterdam

Ion chromatography for monitoring biotechnological processes

Part II. Applications for industrial cultivation media

Ute Scheller, Detlef Siedenberg, Uwe Hübner, Michael Siebold, Gerlinde Kretzmer and Karl Schügerl

Institut für technische Chemie der Universität Hannover, Callinstr. 3, D-30167 Hannover (FRG)

(Received 10th September 1993)

Abstract

Ion-exchange chromatography was applied for off-line and on-line monitoring of chloride, phosphate and sulfate anions during the production of alkaline protease by *Bacillus licheniformis* and during the cultivation of *Cephalosporium acremonium*. Ion-exclusion chromatography was used for off-line and on-line monitoring of acetic, citric and lactic acid anions as well as glucose during the production of lactic acid by *Lactobacillus salivarius* subsp. *salivarius*. The problems of sampling and sample pretreatment and optimization of the chromatographic analysis and enrichment of the analytes after dialysis are discussed.

Keywords: Ion chromatography; Industrial cultivation media; Sample pretreatment

On-line monitoring of medium components during biotechnological production processes is still exceptional in industry. In few research laboratories, on-line monitoring of medium components are performed by flow-injection analysis (FIA) and liquid chromatography (LC). Ion chromatography (IC) has not been used yet for this purpose.

In a preceding paper, the development of ion chromatographic systems for monitoring biological processes was considered [1]. The aim of the present contribution is to show that the analyser system developed and discussed in the preceding paper is suitable for on-line process analysis in biotechnological practice.

Correspondence to: K. Schügerl, Institut für technische Chemie der Universität Hannover, Callinstr. 3, D-30167 Hannover (FRG).

On-line monitoring of chloride, phosphate and sulfate by ion-exchange chromatography during the production of alkaline protease by Bacillus licheniformis

Bacillus licheniformis (DSM 641) was cultivated and alkaline protease (washing enzyme) was produced on a complex industrial medium (Table 1) in a stirred tank reactor at temperature $T = 39.5°C$, stirrer speed $N = 940$ rpm, specific volumetric aeration rate with respect to the medium volume (vvm) $= 1\ min^{-1}$. The duration of the batch production process was about 36 h [2]. Table 1 shows that the cultivation medium had a complex composition. During enzyme production, high amounts of protein (up to 20 g l^{-1}), were excreeted into the medium. Sampling was done either with cross flow filtration modules integrated into a medium recycle loop (Biopem, B. Braun Melsungen [3]; Separation cell, Amafilter

SSDI 0003-2670(93)E0566

TABLE 1

Composition of the cultivation medium of *Bacillus licheniformis* [2]

Medium components	Concentration ($g\ l^{-1}$)
Corn starch	100.0
Amylase Thermamyl L 120	0.4
Sodium caseinate	27.0
Soy flour	23.0
$(NH_4)_2HPO_4$	0.5
$Na_2HPO_4 \cdot 12H_2O$	0.5
Corn steep liquor	7.0
Antifoam Ke 2111	4.0
KH_2PO_4	0.3
$MnSO_4 \cdot H_2O$	0.02
$FeSO_4 \cdot 7H_2O$	0.05
$MgSO_4 \cdot 7H_2O$ dissolved in tap water	0.05

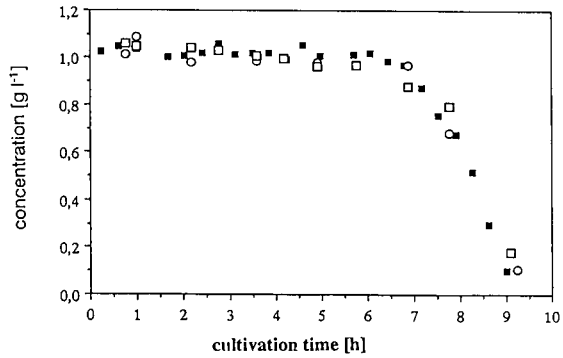

Fig. 2. Comparison of phosphate concentrations measured (■) on-line, (○) off-line with ion exchange chromatography and (□) off-line with an UV photometer during batch cultivation of *Bacillus licheniformis* and production of alkaline protease.

[2]; cross-flow module, Waters-Millipore [2]) or with an in situ tubular filter (ABC Bioverfahrentechnik [4]).

As was reported in the preceding paper, samples were prepared with ultrafiltration using 20-kD membranes as well as by dialysis. Their chromatograms indicated that the peaks of the samples processed by ultrafiltration were improperly evaluated at the position of the phosphate peak (at wavelength 280 nm) due to simultaneously occurring negative peaks caused by the protein content. Also, proteins bound on the column material irreversibly reduced the retention time of the inorganic ions and hindered the separation of their peaks. Protein adsorption did increase the pressure drop across the column as well. It was not possible to regenerate these column materials.

The phosphate was consumed by the cells within 10 h, but sulfate and chloride concentrations changed only slightly during batch cultivation (Fig. 1). The on-line and off-line measured phosphate concentrations agree well, as indicated by Fig. 2.

During fed-batch cultivations, the phosphate was consumed faster by the cells (Fig. 3) than during batch cultivations (Fig. 1). Again, the on-line and off-line measurements agree well (Fig. 4).

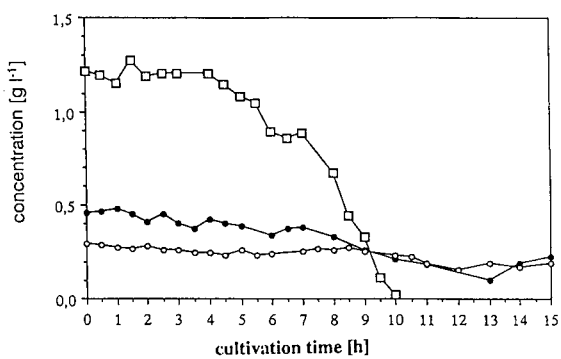

Fig. 1. Concentrations of (□) phosphate, (●) sulfate and (○) chloride during batch cultivation of *Bacillus licheniformis* and production of alkaline protease.

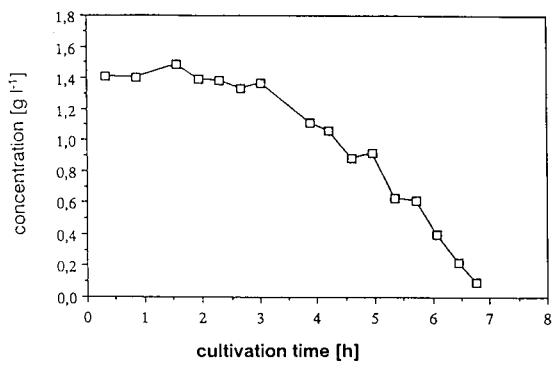

Fig. 3. On-line monitored phosphate concentration during fed-batch cultivation of *Bacillus licheniformis* and production of alkaline protease.

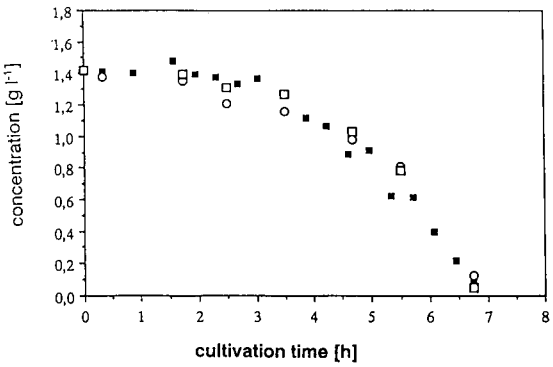

Fig. 4. Comparison of phosphate concentrations measured (■) on-line, (○) off-line with ion-exchange chromatography and (□) off-line with an UV photometer.

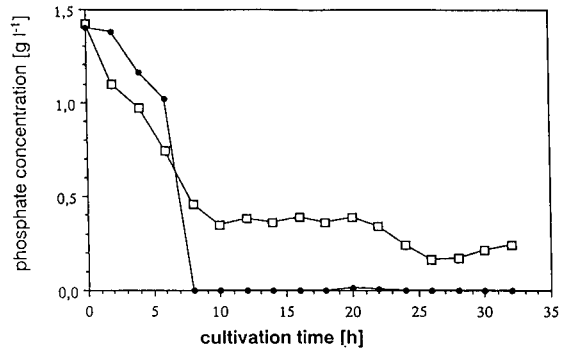

Fig. 5. Extracellular (●) and intracellular (□) phosphate concentrations measured with ion-exchange chromatography during batch cultivation of *Bacillus licheniformis* and production of alkaline protease.

In Fig. 5, the intracellular and extracellular phosphate concentrations are shown during batch cultivation. After 8 h, no phosphate could be detected in the medium, but after 10 h, the intracellular phosphate concentration approached a constant value (initially at 3.4 g l^{-1} and at the end of the cultivation at 1.5 g l^{-1}).

Phosphate consumption was related to the cell growth during batch culture. Exponential growth started at about 6 h. At the same time, the phosphate concentration began to diminish (Fig. 6). This figure shows the culture fluorescence. Its initial constant value was due to the fluorescence active casein peptone in the medium, which decreased due to its consumption during the first 6 h, and increased with increasing cell mass. After the casein peptone was consumed, the NADH-

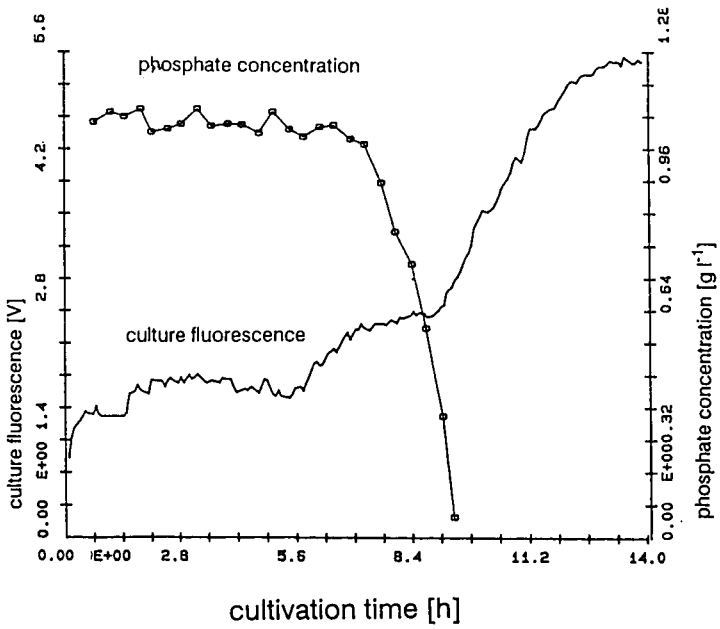

Fig. 6. Phosphate concentration and culture fluorescence as a function of the time during batch cultivation of *Bacillus licheniformis* and production of alkaline protease.

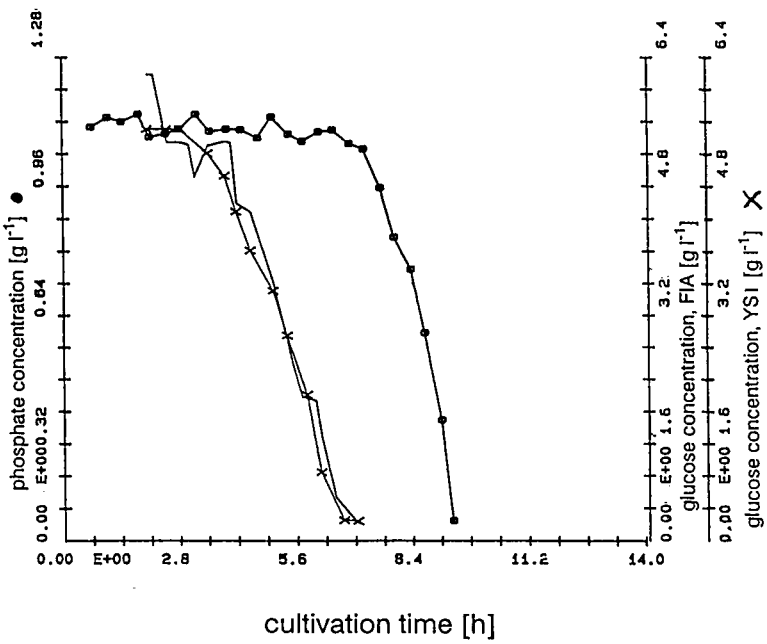

Fig. 7. Phosphate concentration monitored by ion-exchange chromatography and glucose concentration measured by the YSI analyser off-line and enzyme FIA system on-line during fed-batch cultivation of *Bacillus licheniformis* and production of alkaline protease.

dependent fluorescence intensity increased and the cell mass concentration and the fluorescence intensity were well correlated [5].

In Fig. 7, the phosphate concentration course is compared with that of the glucose concentration. The latter was measured, off-line with the Yellow Spring Instrument (YSI) analyser as well as on-line with an enzyme FIA system (immobilized glucose oxidase (GOD) and amperometric oxygen detector). Phosphate concentration started to diminish after the glucose has been consumed.

The initial concentration of phosphate was for the fed-batch cultivation only 85% of that of the batch cultivation. 15% was fed later to the culture medium. In the fed-batch process phosphate was consumed faster than in batch cultivation. As soon as the medium feeding started, the extracellular and intracellular phosphate concentrations increased and passed a maximum (Fig. 8). Again, the intracellular concentration was considerably higher than the extracellular one. In Fig. 9, the concentrations of glucose and phosphate as well the culture fluorescence intensity are shown as a function of the time for another fed-batch culture. Once more, extracellular phosphate concentration started to diminish as soon as the glucose has been consumed.

High glucose and phosphate consumption rates are indicators for high cell growth rate. As long

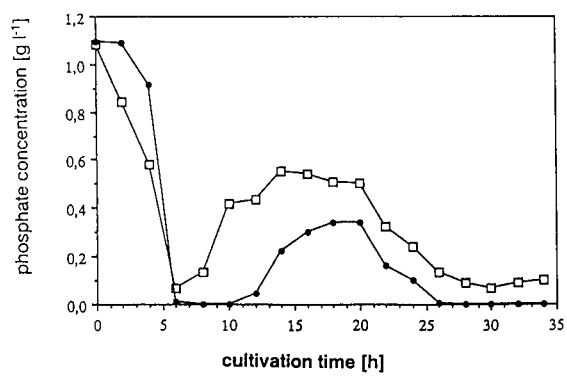

Fig. 8. Extracellular (●) and intracellular (□) phosphate concentrations measured during fed-batch cultivation of *Bacillus licheniformis* and production of alkaline protease.

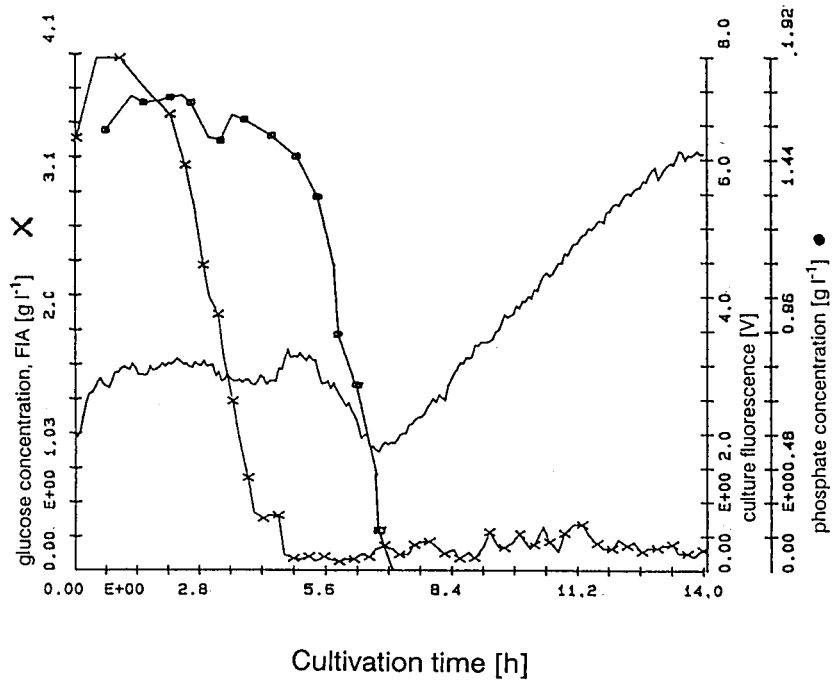

Fig. 9. Glucose and phosphate concentrations as well as culture fluorescence intensity during fed-batch cultivation of *Bacillus licheniformis* and production of alkaline protease.

as they are present in the medium, the cells keep growing. In case of *Bacillus licheniformis*, growth stopped and enzyme production started after the glucose and phosphate concentrations dropped below a critical value. Thus, they are important key components for process control [5].

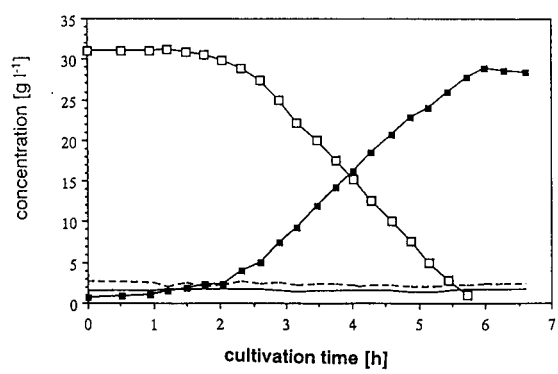

Fig. 10. Glucose (□), lactic (■), acetic (— — —) and citric (———) acid concentrations monitored by ion-exclusion chromatography during batch cultivation of *Lactobacillus salivarius* subsp. *salivarius* and production of lactic acid.

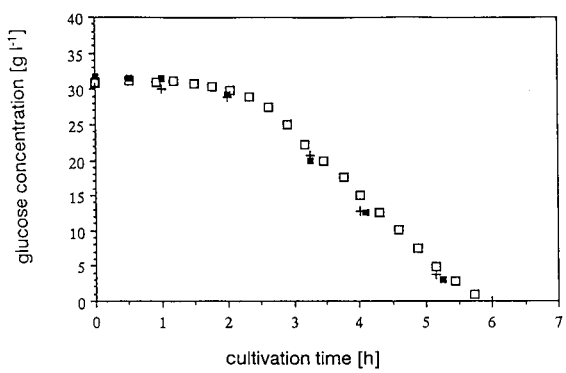

Fig. 11. Comparison of glucose concentration monitored by ion chromatography on-line (□) and off-line (■) as well as by enzyme FIA system (+) during batch cultivation of *Lactobacillus salivarius* subsp. *salivarius* and production of lactic acid.

TABLE 2

Composition of the cultivation MRS medium of *Lactobacillus salivarius* subsp. *salivarius* [3]

Components	Concentration ($g\ l^{-1}$)
Casein	10.0
Meet extract	10.0
Yeast extract	5.0
Glucose	30.0
Tween 80	1.0
K_2HPO_4	2.0
Sodium acetate	3.0
$(NH_4)_2$citrate	2.0
$MgSO_4 \cdot H_2O$	0.2
$MnSO_4 \cdot H_2O$	0.05

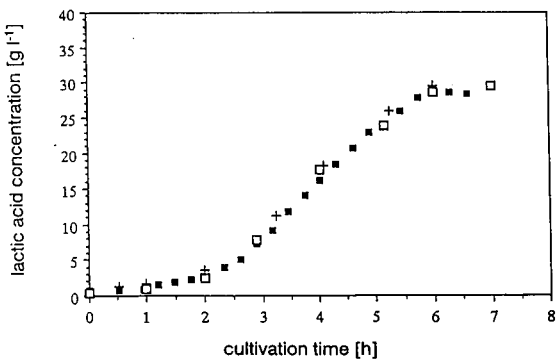

Fig. 12. Comparison of lactic acid concentrations measured with YSI analyser off-line (+), enzyme FIA system on-line (■) and ion chromatography off-line (□) during batch cultivation of *Lactobacillus salivarius* subsp. *salivarius*.

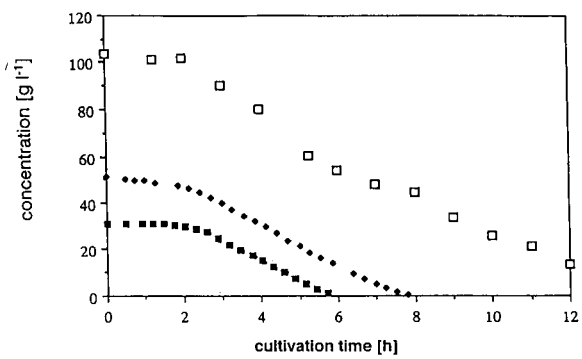

Fig. 13. Glucose concentrations monitored by ion chromatography during batch cultivation of *Lactobacillus salivarius* subsp. *salivarius* and production of lactic acid at different initial glucose concentrations. (■) LS 12, 3% glucose; (◆) LS 10, 5% glucose and (□) LS 9, 10% glucose.

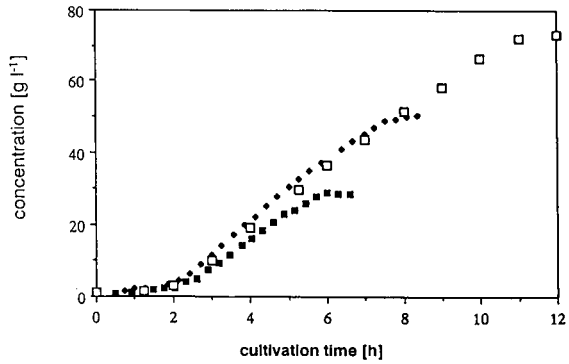

Fig. 14. Lactic acid concentrations monitored by ion chromatography during batch cultivation of *Lactobacillus salivarius* subsp. *salivarius* and production of lactic acid at different initial glucose concentrations. For symbols see Fig. 13.

On-line monitoring of lactic, acetic and citric acid and glucose by ion-exclusion chromatography during the production of lactic acid by Lactobacillus salivarius subsp. salivarius

Lacobacillus salivarius subsp. *salivarius* (DSM 20492) was cultivated and lactic acid was produced on a complex industrial medium (Table 2) in a stirred tank reactor at $T = 45°C$, pH 7. The duration of the anaerobic batch production process was about 7 h [6].

The formation of lactic acid from glucose is a homofermentative process. The lactic acid yield is close to 100%. Glucose and lactic acid concentra-

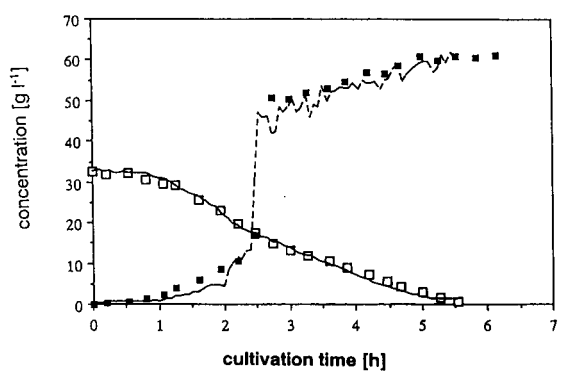

Fig. 15. Glucose and lactic acid concentrations monitored by ion chromatography during batch cultivation of *Lactobacillus salivarius* subsp. *salivarius* and production of lactic acid and stepwise increase of the lactic acid concentration. □ = Glucose, IC; ■ = lactic acid, IC; ——— = glucose, FIA; — — — = lactic acid, FIA.

tion courses were mirror images in batch cultures (Fig. 10). Low-level acetic and citric acid supplements caused the cell growth and lactic acid production rate to increase [7]. They were not consumed by the cells. Therefore, their concentrations were constant (Fig. 10).

The glucose concentrations measured on-line by IC and off-line by IC and by the yellow spring instrument analyser agreed well (Fig. 11). The same holds true for the lactic acid concentration (Fig. 12). When varying the initial glucose concentrations, the glucose consumption rates (Fig. 13) and lactic acid production rates (Fig. 14) were nearly the same, but the cultivation time was longer and the final lactic acid concentrations were much higher.

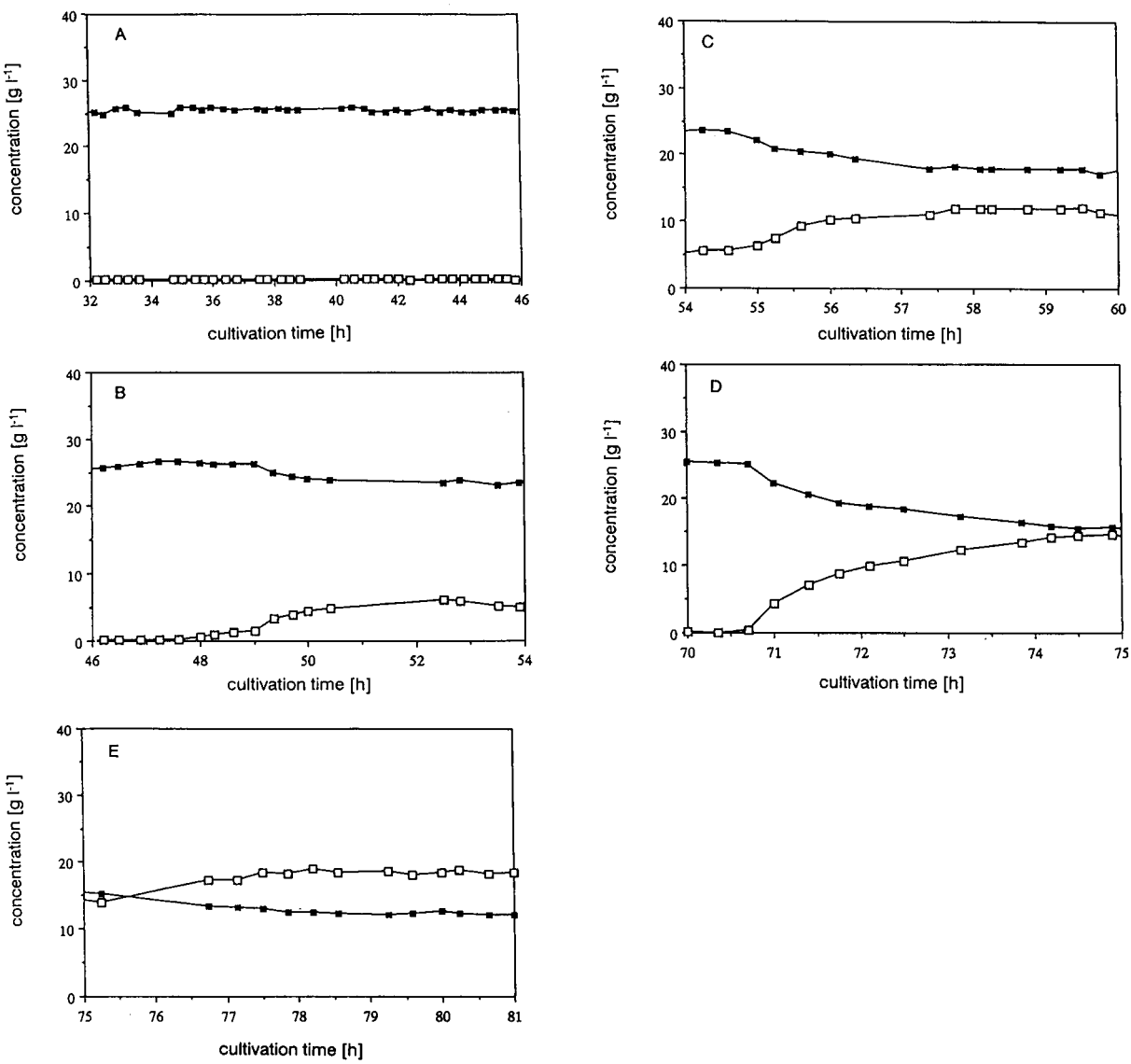

Fig. 16. Glucose (□) and lactic acid (■) concentrations during continuous cultivation of *Lactobacillus salivarius* subsp. *salivarius* and production of lactic acid at different dilution rates. (A) $D = 0.61\ h^{-1}$, (B) $D = 0.8\ h^{-1}$, (C) $D = 1.03\ h^{-1}$, (D) $D = 1.21\ h^{-1}$, (E) $D = 1.43\ h^{-1}$.

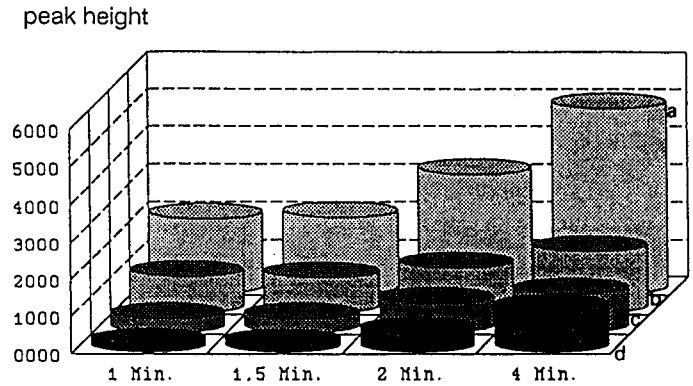

Fig. 17. Peak height at different enrichment times of (a) acetate, (b) chloride, (c) phosphate and (d) sulfate using ion chromatography (with precolumn).

In order to test the product inhibition, the lactic acid concentration was increased to 60 g l^{-1} in a batch culture by adding lactic acid to the medium (Fig. 15); growth rate, glucose consumption rate and lactic acid production rate were not influenced by it. Again, the glucose and lactic acid concentrations measured by IC and the enzyme FIA system (glucose by immobilised GOD and L(+)-lactic acid by immobilised lactate oxidase (LOD) and amperometric dissolved oxygen detector) agreed well. When the lactobacilli produced L(+)- and D(−)-lactic acids, the comparison of FIA and IC analysis allowed the evaluation of the ratio L(+)- to D(−)-lactic acid.

Continuous cultivation of *Lactobacillus salivarius* subsp. *salivarius* was carried out at different dilution rates (D = 0.31, 0.42, 0.61, 0.8, 1.03, 1.21 and 1.43 h^{-1}) and glucose concentrations (up to 30 g l^{-1}) in feed. Glucose and lactic acid concentrations were monitored during the initial batch phase and during continuous operation. On account of the substrate limited (chemostate) operation up to D = 0.61 h^{-1}, the glucose concentration was very low, and the lactic acid concentration varied, depending on the glucose concentration in the feed. Above this dilution rate only a part of the glucose was converted into lactic acid. With increasing dilution rate, the glucose conversion and lactic acid concentration diminished and the glucose concentration increased (Fig. 16). During a two-week period of the continuous cultivation 800 IC measurements were carried out without any breakdown of the IC analysis system.

Monitoring of phosphate concentration during the cultivation of Cephalosporium acremonium and production of cephalosporin C

Sulfate, chloride, phosphate and acetate were determined by ion-exchange chromatography (with a Hamilton PRP-X 100 column) and the RI detector (ERC-7515 A) in the model medium. The phosphate in the cultivation medium (Table 3) of *Cephalosporium acremonium* was measured by using a dialysis membrane for sample preparation [1]. By applying the dialyser, the sample was strongly diluted, and by using a refractive index (RI) detector, which has a rather low sensitivity,

TABLE 3

Composition of the cultivation medium of *Cephalosporium acremonium*

Components	Concentration (g l^{-1})
Peanut flour	100
Ammonium acetate	3.0
Soy oil	1.75
D,L-Methionine	3.0
Glucose monohydrate	5.0
$CaSO_4 \cdot 2H_2O$	1.25
$MgSO_4 \cdot 7H_2O$	1.25
$CaCO_3$	2.5
SAG 471 (antifoam agent)	1.5

it was difficult to analyse medium components with low concentrations. To increase the sensitivity, the analytes were enriched by a precolumn (Hamilton PRX-X100) [8–10]. Elution liquid was 2 mmol l^{-1} potassium hydrogen phthalate. In Fig. 17, the influence of the enrichment time on the peak heights of sulfate, phosphate, chloride and acetate in model medium are shown. Sulfate and phosphate enrichments were rather low, the ones for chloride and acetate fairly satisfactory. Further investigations are necessary to improve the enrichments.

Conclusion

Sampling pretreatment techniques and ion chromatographic analyses were developed and successfully applied for off-line and on-line monitoring of inorganic an ions and carboxylic acids in complex industrial cultivation media for alkaline protease production by *Bacillus licheniformis*, lactic acid production by *Lactobacillus salivarius* subsp. *salivarius* and cephalosporin C production by *Cephalosporium acremonium*. High precision and long range analysis is only possible if the proteins are removed from the sample by dialysis. On account of the diminution of the analyte concentrations due to the dialysis, enrichment of low concentations of analytes is necessary. Suitable enrichment techniques are not yet available and have to be developed.

REFERENCES

1 U. Scheller, D. Siedenberg and K. Schügerl, Anal. Chim. Acta, 285 (1994) 169.
2 U. Hübner, Dissertation, Universität Hannover, 1991.
3 B. Braun Melsungen, Operation Manual.
4 H. Graf, D. Wentz and K. Schügerl, Biotechnol. Techniques, 5 (1991) 183.
5 U. Hübner, U. Bock and K. Schügerl, Appl. Microbiol. Biotechnol., 40 (1993) 182.
6 M. Siebold, Dissertation, Universität Hannover, 1991.
7 M. Siebold, P. v. Frieling, R. Joppien, D. Rindfleisch, K. Schügerl and H. Röper, Proc. Biochem., in press.
8 J.D.H. Cooper, D.C. Turnell and B. Green, J. Chromatogr., 456 (1988) 53.
9 B. Green, J.D.H. Cooper and D.C. Turnell, Ann. Clin. Biochem., 26 (1989) 361.
10 F. Verillon and F. Quian, Analusis, 19 (1991) 271.

Analytica Chimica Acta, 286 (1994) 189–195
Elsevier Science B.V., Amsterdam

Stripping potentiometric measurements of copper in blood using gold microelectrodes

Joseph Wang, Emanuel Sucman [1] and Baomin Tian [2]

Department of Chemistry and Biochemistry, New Mexico State University, Las Cruces, NM 88003 (USA)

(Received 7th July 1993; revised manuscript received 28th September 1993)

Abstract

A rapid, reliable, sensitive and simple stripping potentiometric method for the determination of copper in blood samples, based on a bare (mercury-free) gold fiber microelectrode is described. The method involved a 1:40 dilution of the 50 μl whole blood sample with 0.8 M hydrochloric acid, a short (60 s) deposition at -0.40 V, and a constant stripping current of 0.5 μA. The analytical performance is not compromised by replacing the traditional mercury electrodes with the gold microsensor. The detection limit is 1.5 μg/l (1 min deposition) and the relative standard deviation for 80 repetitive blood assays is 4.1%. Good agreement with target reference values and flame atomic absorption measurements is reported for both whole blood and blood serum samples, indicating that the total copper content is being monitored. By obviating the needs for mercury plating or disposal, solution stirring, oxygen removal or sample pretreatment, the prospects for on-site monitoring of blood copper levels are greatly improved.

Keywords: Potentiometry; Blood; Copper; Gold microelectrode; Serum

Because of the important role of copper in various metabolic processes [1], its reliable determination in biological fluids (such as serum, plasma or whole blood) is of great clinical and nutritional significance. Procedures for the determination of whole blood or blood serum copper levels are often used in the diagnosis of Wilson's disease, inborn error of metabolism and various kinds of anemias. Such procedures usually rely on atomic absorption spectroscopy [2] or colorimetric methods [3]. Several papers reported the utility of the most sensitive electrochemical technique, stripping analysis, for determining copper in biological fluids [4–7]. Such procedures rely on voltammetric and potentiometric stripping schemes at various mercury (drop or film) electrodes. However, the growing concerns about the toxicity of mercury, coupled with the needs for decentralized clinical monitoring of copper, have led us to explore alternative (mercury-free) stripping electrodes for trace copper.

This paper describes a rapid stripping potentiometric procedure, based on a plain gold fiber microelectrode, for reliable assays of copper in blood and serum samples. We have demonstrated recently that convenient quantitation of trace lead can be accomplished by replacing the traditional mercury electrodes with plain gold surfaces [8,9]. In particular, the coupling of computerized stripping potentiometry with gold-coated screen-printed sensors [8] or gold fiber microelectrodes [9] offers reproducible results for μg/l (ppb) concentrations of lead following short deposition periods. Upon applying the gold microelectrode for blood lead assays we observed a separated, well-

Correspondence to: J. Wang, Department of Chemistry and Biochemistry, New Mexico State University, Las Cruces, NM 88003 (USA).

[1] On leave from University Veterinary Medicine, Brno (Czech Republic).

[2] On leave from Sichuan University, Chengdu (China).

SSDI 0003-2670(93)E0583-S

defined and reproducible copper peak. Such finding prompted the present investigation, which led to an easy-to-use and reliable approach for blood copper measurements. The new procedure eliminates the hazards of mercury, and obviates the needs for sample pretreatment or solution stirring. Such features and advantages are reported in the following sections.

EXPERIMENTAL

Apparatus

Potentiometric stripping experiments were carried out with the TraceLab potentiometric stripping unit (PSU 20, Radiometer, Copenhagen), in connection with a SAM sample station (Radiometer) and an IBM PS/55SX. Blood analyses were performed in a 2-ml cell, while synthetic samples employed 10 ml solutions. A two-electrode system was used, with the gold fiber and Ag/AgCl reference (BAS, Model RE-1) being introduced through holes in the cover. A BAS-100A electrochemical analyzer was used in the voltammetric stripping experiments. Flame atomic absorption spectroscopy was performed using an IL 551 instrument (with air-acetylene flame, lamp current of 5 mA and wavelength of 324.7 nm).

The microcylinder electrodes were fabricated by inserting a single gold wire (25 μm diameter, Goodfellow Metals) into a 100-μl Eppendorf plastic pipette tip. The wire was sealed into the narrow end by gently and carefully melting the plastic tip in heat produced by a nearby Bunsen burner. Electrical contact was made by back filling the tip with carbon paste (made of 65:35% graphite powder–mineral oil) and inserting a copper wire. Microcylinders of 8 mm length were used in most experiments.

Reagents

All solutions were prepared with double-distilled water and analytical grade chemicals. The copper stock solution (1000 ppm, atomic absorption standard, Aldrich) was diluted daily as required. A 0.8 M hydrochloric acid solution served as the supporting electrolyte. This solution was prepared from the concentrated acid (EM Science). The sheep blood was obtained from the College of Agriculture at the New Mexico State University, and stored in venoject sterile ampules; the U.S. Centers for Disease Control (Atlanta, GA) provided the bovine blood (BL-LRS Pool Sample-Base Pool 8/90) and the human serum (Standard Reference Materials, R467, and R676). Whole blood and blood serum samples were stored at 4°C.

Procedure

Potentiometric stripping assays were performed in the following manner. A 50-μl aliquot of the blood or serum sample was pipetted into a stirred 1820-μl double-distilled water solution (in the electrochemical cell). Subsequently, a 130-μl aliquot of a concentrated hydrochloric acid solution was added slowly into the mixture; stirring proceeded for additional 3 or 10 min (for serum or whole blood samples, respectively). The deposition potential (-0.40 V) was then imposed for a 1 min period while the solution was kept quiescent. At the end of the deposition period, the potentiogram was recorded by applying a constant current of $+0.5$ μA; the BASE 5 command was used for the base line treatment. Stripping was terminated when the electrode had reached a potential of $+0.8$ V. A 60-s conditioning period at this potential was used prior to the next potentiometric stripping cycle. The square wave stripping voltammetric experiments were carried out with a 120-s deposition period; the voltammograms were recorded by scanning the potential from -0.4 to 0.8 V with a 30 Hz frequency, 40 mV amplitude and a 6 mV step. The standard addition method was used for evaluating the sample concentration (and addressing matrix effects); a 1-min stirring was used after each addition. Failure of the electrode, e.g. due to blockage by a blood particle, can be rapidly corrected by removing it from the sample and rinsing it with double-distilled water.

RESULTS AND DISCUSSION

Figure 1 compares stripping potentiograms for a diluted blood sample, obtained at the plain gold

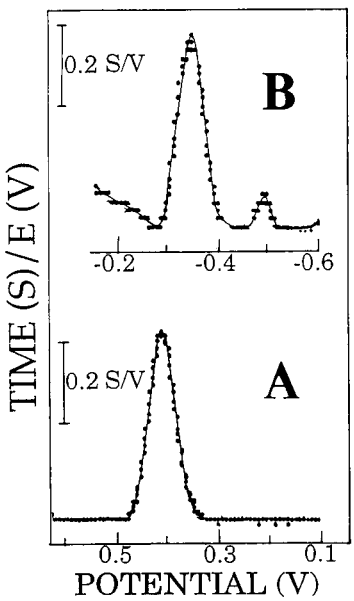

Fig. 1. Potentiograms for a diluted (1:40) sheep blood at the gold- (A) and mercury-coated glassy carbon (B) electrodes. One min deposition at −0.4 (A) and −0.7 (B) V, with 0 (A) and 300 (B) rpm stirring. Stripping current, 0.5 (A) and 5 (B) μA. Dilution solution, 0.8 M HCl (A) and 0.6 M HCl containing 18 mg/l mercury (B).

fiber (A) and mercury-coated glassy carbon (B) electrodes. Both electrodes exhibit a well-defined copper peak following a short (1-min) deposition period. A peak potential of +0.40 V and width (at half height) of 58 mV characterize the copper peak at the gold surface, as compared to −0.35 V and 61 mV, respectively, at the mercury-coated electrode. Unlike the rising mercury-oxidation background contribution at the coated glassy carbon surface, the gold microelectrode offers a flat background response, and overall improved signal-to-background characteristics. Note also that other components of the blood matrix do not contribute to the response of the gold sensor, while a lead peak (at −0.50 V), accompanies the copper one at the mercury surface. (The lead peak potential at the gold microelectrode is around 0.0 V.) The relatively high blood copper level (ca. 0.8 mg/l) and the inherent sensitivity of the method allow significant (1:40) sample dilution and the use of short deposition periods. While the mercury film disk electrode required a stirred solution (to facilitate the copper deposition), a quiescent solution was employed in the case of the gold fiber. The similar peak intensities thus reflect the efficient non-linear diffusional properties inherent to the ultramicro-electrode. The stripping potentiometric mode eliminates the need for oxygen removal, and hence further simplifies the analytical procedure. Another important factor, relevant to the simplified operation, is the fact that the gold sensor does not require any preplating (of a film) or conditioning.

Experimental variables affecting the copper response of the gold fiber electrode were charac-

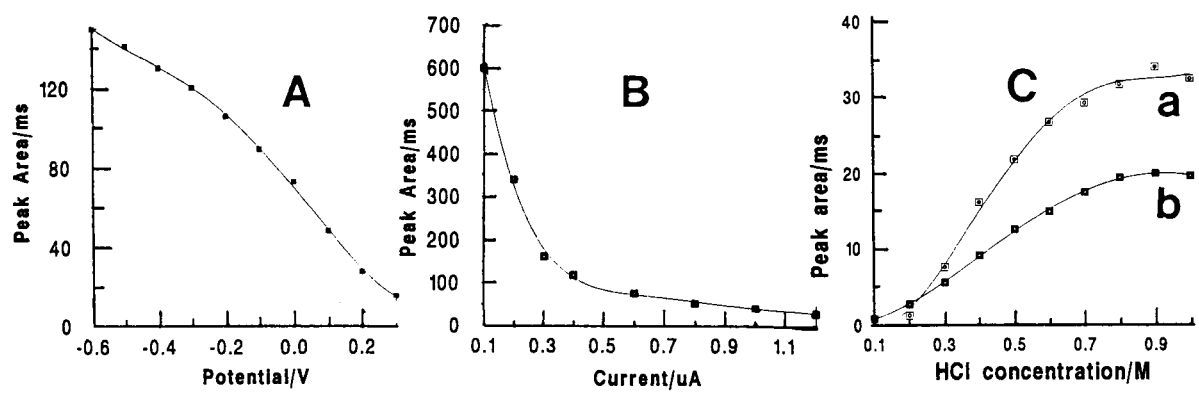

Fig. 2. Effect of deposition potential (A), stripping current (B) and HCl concentration (C) upon the response to a 10 μg/l copper (A, B) and sheep blood (C) solutions. Deposition for 2 (A, B) and 1 (C) min at −0.4 V (B,C). Dilution factor, 40 (A,B,C(b)); 20 (C(a)). Other conditions, as in Fig. 1A.

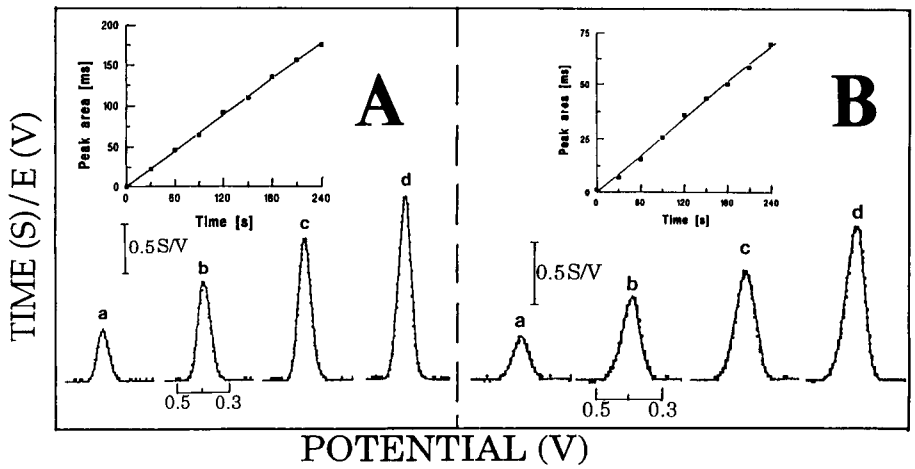

Fig. 3. Potentiograms for a 10 μg/l copper solution (A) and a diluted sheep blood sample (B) following different deposition times: 1(a), 2 (b), 3 (c), and 4 (d) min. Other conditions, as in Fig. 1A.

terized and optimized. Figure 2 examines the influence of the deposition potential (A), stripping current (B) and the concentration of the hydrochloric acid (C). The copper peak decreases slowly upon changing the deposition potential between -0.6 and -0.4 V, and more rapidly at more positive potentials. A value of -0.4 V was used in all subsequent work, as a compromise between high sensitivity and hydrogen evolution problems (in the acidic medium used). Such potential is 0.8 V more negative than the copper stripping potential. The stripping current controls the rate of copper dissolution and hence has a profound effect on the response (B). A very sharp

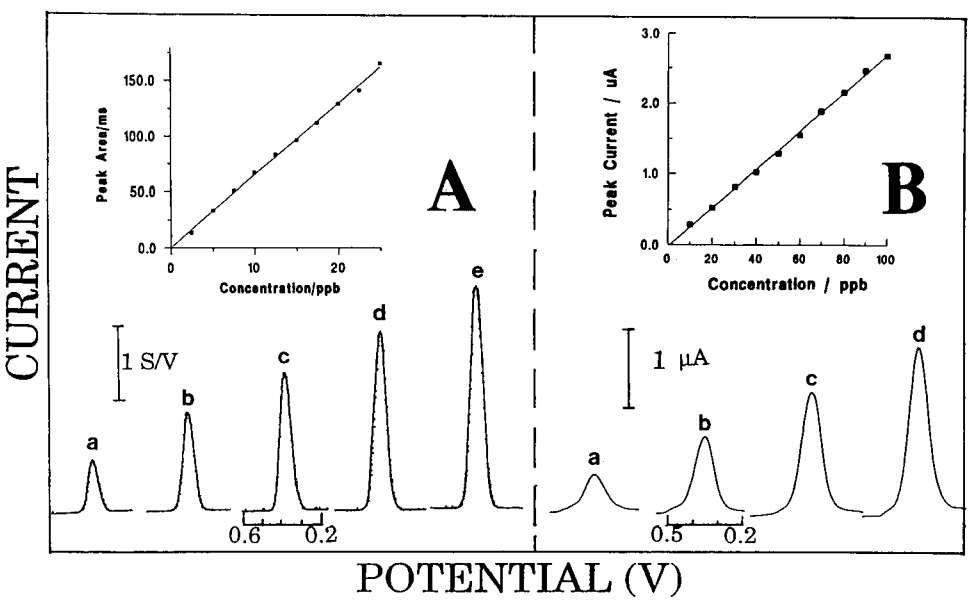

Fig. 4. Potentiograms (A) and voltammograms (B) for copper solutions of increasing concentrations in 5 and 20 μg/l steps, respectively. Two min deposition at -0.40 V. Square-wave conditions (B), amplitude, 40 mV, frequency, 30 Hz; step, 6 mV. Other conditions, as in Fig. 1A.

(nearly exponential) decrease of the copper peak is observed upon increasing the current between 0.1 and 0.5 μA, with a slower one for higher currents. However, low stripping currents are characterized by higher background noise levels. The most favorable signal-to-noise characteristics were observed with 0.5 μA, a value used in all subsequent work. Various acids, including HNO_3, H_2SO_4, HCl, and CCl_3COOH were tested in connection with sample preparation step, with HCl yielding most favorable results. The concentration of the hydrochloric acid also influences the copper peak. Such effect was tested using different blood dilutions (20 and 40 fold). In both cases, the response increases rapidly upon increasing the acid concentration between 0.2 and 0.8 M, and levels off for higher concentrations. All subsequent work was carried out in 0.8 M hydrochloric acid. The suitability of stripping potentiometry for monitoring the total content of various metals in whole blood following similar sample pretreatments has been established recently [10].

The influence of another important experimental parameter, the deposition time, is evaluated in Fig. 3. For both the synthetic (A) and blood (B) samples examined, the copper peak increases rapidly and linearly upon extending the deposition period (between 0 and 240 s). Slightly sharper peaks are observed using the synthetic sample. The well-defined peaks observed for this 10 μg/l solution following short deposition times indicate again the inherent sensitivity of the gold microsensor. For example, a detection limit of ca. 1.5 μg/l copper can be estimated based on the signal-to-noise characteristics ($S/N = 3$) of the response following a 1-min deposition (Fig. 3A (b)). Even a lower detection limit of 0.3 μg/l (3.1×10^{-9} M) was calculated from analogous measurements of 0.5 μg/l copper (5 min deposition; not shown).

Various stripping modes can be used to measure the copper deposit on the gold fiber. Figure 4 shows stripping potentiograms (A) and voltammograms (B) for solutions of increasing copper levels [5–25 μg/l (A(a–e)), 20–80 μg/l (B (a–d))], following 2 min accumulation. These data clearly illustrate the advantage of the potentiometric stripping scheme over the square-wave mode when gold surfaces are concerned. Apparently, the extensive software of computerized stripping potentiometry offers a very effective background correction. Hence, its detection limit (1 μg/l) is an order of magnitude lower than the corresponding value (10 μg/l) estimated for the square-wave operation. The peaks displayed in

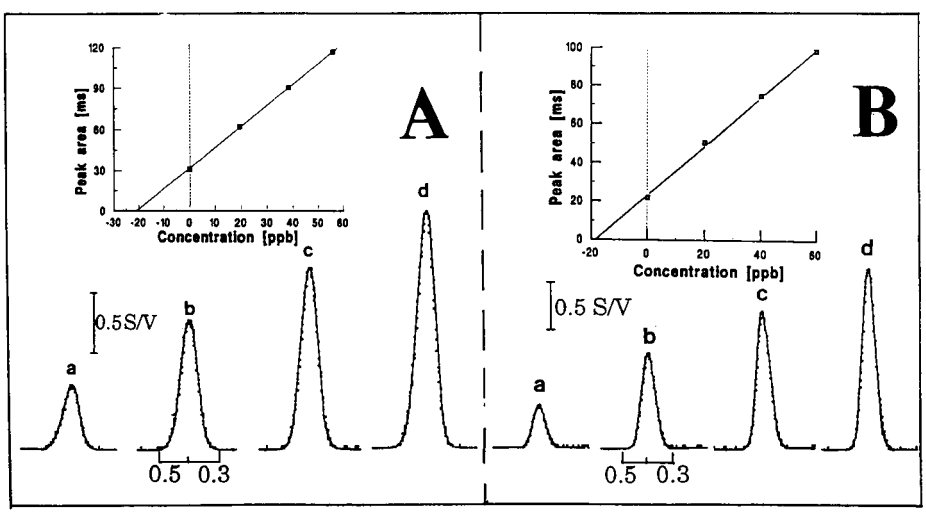

Fig. 5. Determination of copper in diluted bovine (A) and sheep (B) blood samples. Potentiograms for the sample (a) and subsequent concentration increments of 20 μg/l (b–d). Conditions, as in Fig. 1A.

Fig. 4 are part of series of ten concentration increments. The resulting calibration plots at both electrodes (shown as insets) are highly linear (slopes, 6.48 ms l/μg (A) and 27.1 nA l/μg (B); correlation coefficients, 0.999).

Figure 5 demonstrates the suitability of the gold microsensor stripping procedure for assays of bovine (A) and sheep (B) blood samples. With simple dilution and a short (1 min) preconcentration time, the method yields a well-defined copper peak for these samples (a). This peak can be easily quantified following three standard additions (b–d). Copper levels of 0.902 (A) and 0.745 (B) mg/l were thus calculated from the resulting standard addition plots (also shown). The electrochemical data were verified by a flame atomic absorption spectroscopic-based method. The optical results (1.033 and 0.875 mg/l, respectively) show a relatively good correlation between the two techniques. Many diagnostic observations rely on the determination of copper in serum. Human serum (CDC reference material) samples were thus analyzed in a similar fashion (e.g. Fig. 6). The data, summarized in Table 1, indicate that

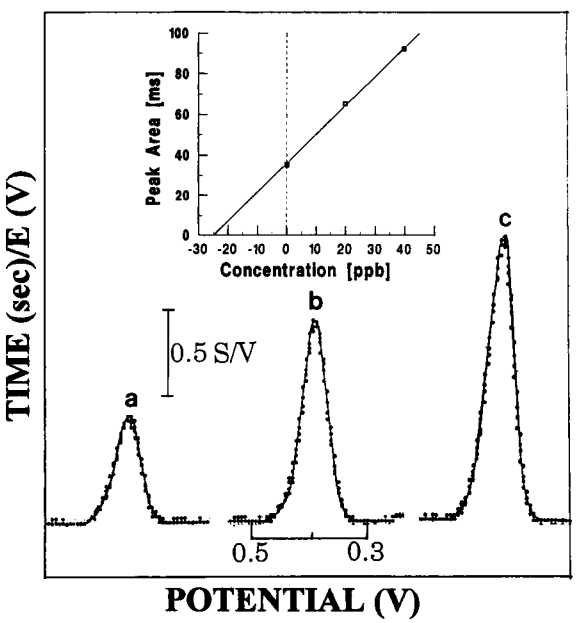

Fig. 6. Determination of copper in diluted serum sample. Potentiograms for the sample (a) and subsequent concentration increments of 20 μg/l (b,c). Conditions, as in Fig. 1A.

TABLE 1

Application of the stripping procedure to the determination of copper in human serum reference materials [a]

Sample	95% Confidence limits (mg/l)	99% Confidence limits (mg/l)
CDC Pool 476	0.85–1.00 (0.71–0.94)	0.80–1.06 (0.67–0.98)
CDC Pool 676	1.92–2.13 (1.88–2.08)	1.83–2.22 (1.85–2.11)

[a] Target reference values are given in parenthesis.

there is a good agreement between the target values and the confidence intervals obtained by the stripping procedure. It should be pointed out that the serum samples required a shorter (3 min) acidification period to liberate the electrolabile copper species. This step may be further shortened by adding appropriate metals that facilitates the decomplexation process.

A somewhat surprising and important finding is the inherent stability of the response of the gold sensor in the biological fluid. While originally designed as disposable electrodes, the new microelectrodes hold a great promise for use as reusable devices. Such operation requires a short "cleaning" period (1 min at +0.8 V) between successive runs. The performance of the gold fiber under continuous use was examined for 80 repetitive runs in the diluted blood during a prolonged (4 h) period (conditions, as in Fig. 1A; not shown). The copper stripping peak remains unchanged throughout this entire operation. The relative standard deviation for the complete series is 4.1%. Apparently, the coupling of the gold surface with the potentiometric stripping operation greatly reduces the susceptibility to surfactant adsorption problems. Such stability data indicate many potential applications, including automated (continuous or flow injection) analysis. In addition, considering the small dimension of the fiber electrodes, one may envision their potential application as implantable in vivo monitoring devices. The elimination of mercury surfaces may further facilitate such a possibility. Such operation will measure the labile copper species, and will require use of protective coatings.

In conclusion, this study has demonstrated that the coupling of gold microelectrodes with stripping potentiometry represents an accurate, sensi-

tive, rapid and simple avenue for clinical monitoring of copper in various biological fluids. The analytical performance is not compromised by the use of mercury-free sensors or by the greatly simplified sample pretreatment and stripping operation. The good agreement with target reference values and spectroscopic procedures indicate reliable monitoring of the total copper content. Matrix effects are minimized through the substantial sample dilution. Such use of mercury-free sensors for trace copper opens the door for decentralized clinical screening of this metal. Computerized stripping potentiometry is particularly attractive for such an operation due to the use of nondeaerated samples and its efficient baseline correction capability. Automation (for centralized operations) can be accomplished via autosamplers or flow injection manifolds. Such automated systems (available commercially from Radiometer A/S) should prove economical not only in manpower but also in time (as time-consuming sample preparations can be carried out simultaneously for numerous samples). Applicability to other trace elements is anticipated. Such an operation will result in a viable alternative to atomic absorption spectroscopic procedures currently being used for routine analysis of blood samples.

This publication was supported by a grant from the Centers for Disease Control (CDC) (contract number CCR608615-01). Its contents are solely the responsibility of the authors and do not represent the official views of CDC.

REFERENCES

1 G. Davis and W. Mertz, in W. Mertz (Ed.), Trace Elements in Human and Animal Nutrition, Vol. 1, Academic Press, San Diego, CA, 1987, Chap. 10.
2 M.A. Evensen and B.L. Waren, Clin. Chem., 21 (1975) 619.
3 A. Abe, S. Yamashita and A. Noma, Clin. Chem., 35 (1989) 552.
4 J. Wang, Stripping Analysis: Principles, Instrumentation and Applications, VCH, New York, 1985.
5 M. Oehme and W. Lund, Fresenius' Z. Anal. Chem., 298 (1979) 260.
6 J. Tahán and R.A. Romero, Anal. Chim. Acta, 273 (1993) 53.
7 J. Wang, J. Electroanal. Chem., 139 (1982) 225.
8 J. Wang and B. Tian, Anal. Chem., 65 (1993) 1529.
9 J. Wang and B. Tian, Electroanalysis, 5 (1993) 809.
10 P. Ostapczuk, Clin. Chem., 38 (1992) 1995.

Analytica Chimica Acta, 286 (1994) 197–203
Elsevier Science B.V., Amsterdam

Piezoelectric sensor sensitive to nitrobenzene based on a cyclohexanone–formaldehyde coating

Krzysztof Ren

Department of Instrumental Analysis, Faculty of Chemistry, Adam Mickiewicz University, 60 780 Poznan (Poland)

(Received 15th June 1993; revised manuscript received 22nd September 1993)

Abstract

This paper presents the construction and analytic properties of a piezoelectric sensor with a cyclohexanone–formaldehyde polymer coating. The sensor was constructed on the basis of a quartz resonator with a resonance frequency of 9 MHz by coating its surface with polymer layers changing the resonance frequency by 10 kHz. The sensor is highly sensitive to aromatic nitro-compounds. Its sensitivity to nitrobenzene vapour is 0.73 Hz/μg l^{-1} (4 Hz/ppm). An attempt was made to assess the type of intermolecular interactions which determine the sensitivity of the sensor. The sensor was used to determine nitrobenzene in air and results were compared to those obtained from measurements performed by gas chromatography.

Keywords: Piezoelectric sensors; Cyclohexanone–formaldehyde coating; Nitrobenzene

Among the well-known sensors there is a group of piezoelectric sensors (quartz crystal microbalances) which are attractive because of the simplicity of their structure. A quartz resonator which is the main part of the piezoelectric sensor, responds to small variations of mass with changes in resonance frequency.

By coating the surface of quartz resonator with a substance capable of absorbing selectively a component from the surrounding environment, a sensor sensitive to this component can be constructed. Different chemical substances, mostly liquids, were used as coatings. As a consequence, the sensor thus formed featured limited stability and low mechanical durability. Polymers share some qualities with liquids, which permit diffusion and sorption of the component to be determined for the bulk of polymer layer.

Correspondence to: K. Ren, Department of Instrumental Analysis, Faculty of Chemistry, Adam Mickiewicz University, 60 780 Poznan (Poland).

The present paper reports results of studies on the application of a cyclohexane–formaldehyde polymer (see Scheme 1) as a coating in a piezoelectric sensor sensitive to aromatic nitro-compounds.

EXPERIMENTAL

Coating

As a coating, a cyclohexane–formaldehyde copolymer of the following formula was used:

The polymer was obtained by condensation of formaldehyde with cyclohexanone in alkaline medium [1]. The reaction was carried out at 30°C

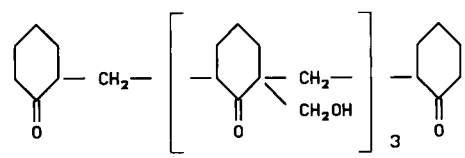

Scheme 1.

SSDI 0003-2670(93)E0546-J

by adding formaldehyde to an alkaline solution of cyclohexanone.

For the studies, the copolymer fraction precipitated from alcohol solution by means of diethyl ether, was employed. The melting point of the copolymer fraction used was in the range of 128–132°C and the average molecular weight determined by the osmometric method, was equal to 645.

The polymer structure was confirmed by elemental analysis as well as by infrared (IR) and nuclear magnetic resonance (NMR) spectroscopic measurements.

Structure of the piezoelectric sensor

The sensor consisted of a quartz plate (AT-cut, 0.3 mm thickness, 12 mm diameter), with two nickel electrodes (5.5 mm diameter) in the middle of its surfaces. This plate surface was coated with polymer layers. The quartz plate with the electrodes was taken from a commercial quartz resonator of the 1011 type made by OMIG-Poland, whose resonance frequency was 9 MHz.

Coating of the plate surface with the polymer layer was performed by the immersion method. The thickness of the polymer layer was controlled by the concentration of the polymer solution in which the resonator was immersed. The quartz resonator was immersed in 2.5% polymer solution in chloroform, taken out and dried in a drier at 60°C. A layer of the coating polymer brought a decrease in resonance frequency by about 10 kHz.

The polymer layer of a desired thickness can be also deposited by repeated immersion and drying procedure using a polymer solution of a lower concentration. However, the decrease in the resonance frequency obtained after each procedure is not the same as the thickness of polymer layers deposited in each procedure is not equal.

Frequency measurement

The quartz resonator used in the piezoelectric sensor was an element stabilizing the frequency of a generator described earlier [2]. Frequency was measured by a PFL-28 type counter made by Zopan (Poland). This instrument was connected with a personal computer to monitor the experiment and to collect the measurement results.

Characteristics of the sensor under static and dynamic conditions were obtained using measuring cells, whose constructions were described elsewhere [2].

The experiments were performed at 25°C ± 0.2.

Determination of nitrobenzene in air by gas chromatography

The determination was performed on a GCHF 18.3 type gas chromatograph made by Chromatron (Germany) equipped with a flame ionization detector (FID) and a 1 m column packed with WHP-Chromosorb (Manville, Denver, CO) containing 3% OV1 (Pye-Unicam). The air was supplied through a gas loop of 2 cm^3 volume. Solutions of nitrobenzene in hexane were used as standards.

RESULTS AND DISCUSSION

Characteristic of the quartz resonator used in the sensor

The main element of piezoelectric sensor is a quartz resonator. In order to provide more detailed information about its properties, its sensitivity to the mass of cyclohexanone–formaldehyde copolymer deposited on its surfaces was determined. This was achieved by coating the surface of the quartz resonator with a solution of polymer, determining the mass of the deposited solution by a gravimetric method, evaporating the solvent and measuring changes in resonance frequency.

The determined sensitivity to mass was 37 $Hz/\mu g$ in terms of the whole surface of the resonator, and 150 $Hz/\mu g$ when expressed in terms of surface area occupied by the electrodes (the electrodes took about 21% of the surface of the quartz plate).

The determined sensitivity to mass was by about 60% lower than theoretically predicted by Mierzwinski and Witkiewicz [3] for a resonator of this type.

The reason for such a low mass sensitivity may be its high dependence on the location on the

surface of the resonator, and the physical properties of the coating applied.

As follows from this experiment, change in frequency of the sensor by 1 Hz must be accompanied by a deposition of 2.7×10^{-8} g of mass on its surfaces.

Selection of the conditions of sensor preparation

Three ways of applying the coating material were tested:

(i) application of a defined volume of the solution to the center of resonator plate by a microsyringe;

(ii) application of coating by spray-method, in flux of copolymer solution aerosol;

(iii) immersion in solution of polymer.

The statistical assessment of the reproducibility of polymer coatings prepared by the three different methods is presented in Table 1. It shows the superiority of the third method, which is used in further experiments.

As it is shown in Fig. 1, there is a linear dependence of the sensor sensitivity on the mass of coating deposited on quartz resonator surfaces within quite a wide range of mass.

Increase in the coating mass is accompanied by an increase in sensitivity, and also by a rise in the response time of the sensor, which is related to the mass transfer into the bulk of the coating layer.

In the presented sensor, resonator surfaces were coated with a polymer layer whose mass corresponded to a decrease in resonance frequency by about 10 kHz. Such a polymer layer was a compromise between the sensor sensitivity and the response time.

TABLE 1

Statistical assessment of the reproducibility of polymer layers introduced by three different methods (for 10 samples)

Method of coating	Coating mass expressed by changes in resonance frequency [kHz]	
	Mean value	Standard deviation for one result
Syringe	11	1.2
Aerosol	13.6	4.4
Immersion	9.6	0.3

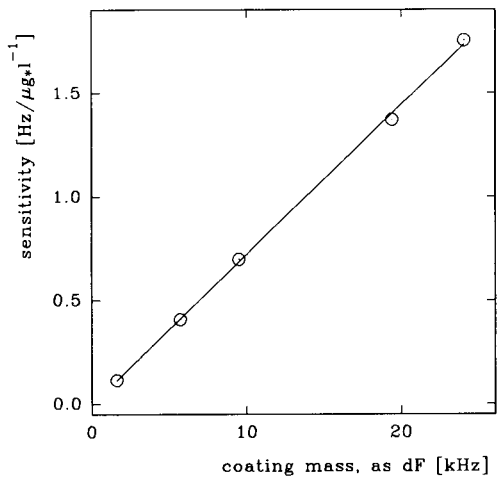

Fig. 1. Dependence of sensor sensitivity to nitrobenzene on coating mass (as frequency change).

Sensitivity order of the sensor

Table 2 lists values of the sensor sensitivity to vapours of different organic compounds. The presented values correspond to coating mass which cause 1 kHz frequency change.

The sensitivity order reflects the degree of interaction between polymer molecules and molecules of the studied chemical compounds. The compounds under study, shown in Table 2, may be subdivided into those showing weaker or stronger interaction.

Of interest is a mechanism of those interactions, in particular with aromatic nitro-compounds to which the sensor is the most sensitive. It is worth mentioning here that its sensitivity to aromatic nitro-compounds is by almost 100 times higher than to the aliphatic ones.

Compounds which interact stronger with the polymer have high dipole moments and high polarity (high values of Onsager polarity function [4,5], expressed as $2(\epsilon - 1)/(2\epsilon + 1)$; ϵ = dielectric constant). Among the compounds which show low sensitivity, there are some with a high dipole moment and polarity. Therefore we cannot consider these properties as exerting a decisive influence on the mechanism of the interaction.

As coating mass, a polymer consisting of functional groups showing donor properties (–OH, =CO groups, cycloalkyl ring) was chosen. Thanks

TABLE 2

Sensitivity order of piezoelectric sensor (for coating mass causing a 1 kHz frequency change, quartz resonator of 9 MHz resonance frequency, operating at 25°C)

Compound	Sensitivity S_{1kHz} (Hz/μg l^{-1})	Dipole moment (D)	Onsager polarity function
Diethyl ether	0.000024	1.17	0.68
n-Octane	0.000059	0	0.39
Tetrachloromethane	0.000077	0	0.45
Ethanol	0.000087	1.68	0.94
Chloroform	0.000095	1.06	0.75
Acetone	0.000096	2.85	0.93
Benzene	0.00011	0	0.46
Tetrahydrofuran	0.00040	1.7	0.81
Toluene	0.00054	0.37	0.49
Propanol	0.00060	1.64	0.93
Water	0.00075	1.84	0.98
Nitromethane	0.00088	3.54	0.96
Nitroethane	0.00096	3.58	0.95
Butanol	0.0017	1.63	0.92
Methanol	0.0021	1.7	0.95
Chlorobenzene	0.0032	1.69	0.76
o-Dichlorobenzene	0.0037	2.16	0.85
1,4-Dioxane	0.0043	0	0.45
1,1′,2,2′-Tetrachlorethane	0.0089	1.36	0.83
Nitropropane	0.0096	2.98	0.94
o-Nitrophenetole	0.021	–	–
2,3-Dimethylnitrobenzene	0.037	–	–
o-Nitrotoluene	0.047	4.4	0.95
2,4-Dimethylnitrobenzene	0.057	4.4	–
Nitrobenzene	0.073	4.2	0.96

to the presence of –OH groups in the polymer, the interactions in question may occur through hydrogen bonds, provided that the studied compounds have atoms which permit formation of such bonds.

In the case of nitrobenzene, whose interaction with polymer is the strongest, hydrogen bonds can be formed between the $-NO_2$ group and the –OH groups of the polymer. Yet, no changes in polymer IR spectrum in the absorption region of –OH and =CO groups were observed (the examination was performed for a solution of polymer and nitrobenzene and for a film of polymer subjected to the influence of nitrobenzene vapour). However, in the polymer molecules intramolecular hydrogen bonds between –OH and =CO groups were found to occur (a broad absorption bond at 3500 cm^{-1}). It is probably the presence of that intramolecular hydrogen bond that accounts for the low probability of appearance of other weaker intermolecular hydrogen bonds.

Interactions of the electron donor–acceptor type (EDA) may occur, between the polymer and the compounds under study, which are favoured by the donor character of the functional groups present in the polymer. Low sensitivity of the sensor to compounds which belong to weaker acceptors, such for example, aromatic hydrocarbons (benzene, toluene) and aromatic chloro-derivatives (chloro- and dichlorobenzene), and high sensitivity of the sensor to compounds of high acceptor properties, such as for example aromatic nitro-compounds seem to corroborate the above hypothesis.

In the case of nitrobenzene no changes in the UV spectrum were observed, in the presence of both polymer and cyclohexanone.

The absence of C–T band, which may result from a too high ionization potential of =CO polymer group, certifies a low contribution of EDA type interactions.

The big difference in the sensor sensitivity to aliphatic and aromatic nitro compounds may be caused by effective interactions with an aromatic ring (of Π-complex types).

Calibration curve

The presented sensor is most sensitive to nitrobenzene. Figure 2 shows calibration curves for nitrobenzene determined by the static and dynamic method. The calibration curve for low nitrobenzene concentrations, determined by the dynamic method, is presented in Fig. 3.

Response time and reversibility

Analytical usefulness of a sensor depends to a high degree on the time it needs to respond to concentration changes.

A number of experiments have been performed to determine the period of time needed for the estabilishment of the sensor frequency. The following conclusions can be drawn:

(i) the response time is the longer, the greater is the change in nitrobenzene concentration, (ii) this time is longer for measurements carried out by static method, and (iii) the response time is

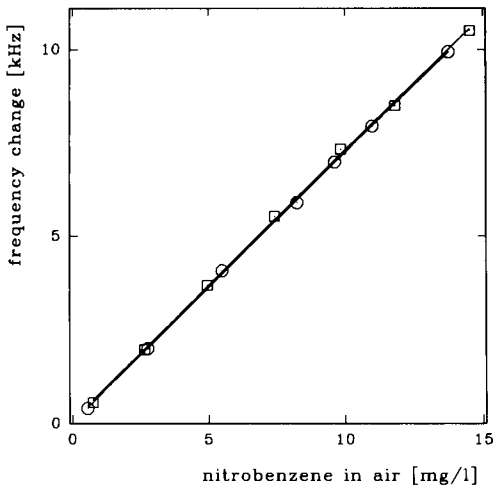

Fig. 2. Calibration curves of the nitrobenzene sensor. □ = flow-through method; ○ = statical method.

almost twice as long during nitrobenzene desorption than during its sorption.

When the measurements are carried out by the flow-through method the response time of a sensor depends on the air flow rate through a measuring cell. Some curves illustrating the sensor frequency estabilishment for different air flow rates are shown in Fig. 4.

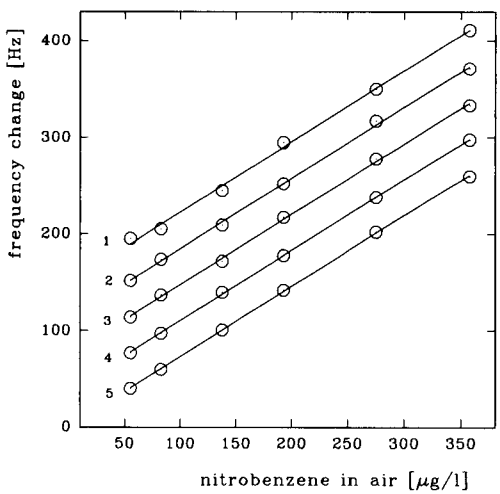

Fig. 3. Calibration curves of the nitrobenzene sensor in air with different water contents (a flow-through method). Water concentration: 1 = 20 mg l^{-1}; 2 = 15 mg l^{-1}; 3 = 10 mg l^{-1}; 4 = 5 mg l^{-1}; 5 = no water.

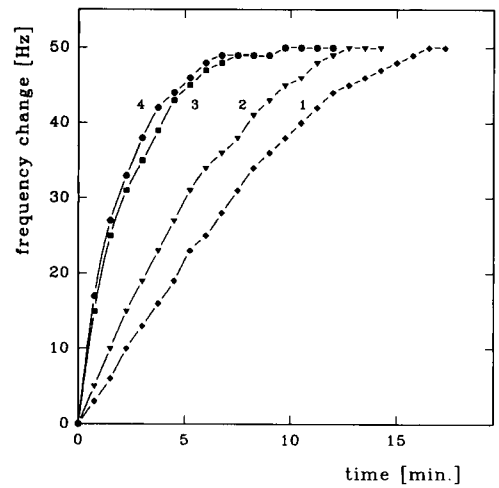

Fig. 4. Response time of the nitrobenzene sensor (concentration change 0–71 mg l^{-1}) for the flow-through method at different flow rates. Flow rates: 1 = 50 l h^{-1}; 2 = 100 l h^{-1}; 3 = 150 l h^{-1}; 4 = 200 l h^{-1}.

The reproducibility of measured frequency of the sensor depend on concentration of nitrobenzene. For low nitrobenzene concentrations, in sorption–desorption cycles, under flow-through conditions, reproducibility is ±5 Hz. After long use of the sensor slow changes in its frequency are observed, of an order of 10 Hz per 24 h, up and down the scale.

Effect of water

Water is the main of the possible interferents in the determination of nitrobenzene. Its concentration in atmospheric air varies considerably (8–25 mg l^{-1}). So far no method for the selective removal of water from air that would not induce changes in nitrobenzene concentration has been reported. Therefore, the analytical procedure for the determination of nitrobenzene by a piezoelectric sensor must take into account the influence of water. In order to investigate the influence of water on the performance of the sensor, calibration curves for nitrobenzene in air containing different amounts of water have been determined. The curves, obtained by the flow-through method, are shown in Fig. 3.

Parallel course of the calibration curves and their shift proportional to water concentration in

air prove that the effect of water is additive, which permits easy error correction.

Sensor calibration

The analytical properties described above refer to a sensor made of a quartz resonator with a resonance frequency of 9 MHz, whose surfaces were coated with polymer layer of mass which causes 10 kHz frequency change, and which operated at 25°C. As follows from a relation given by Sauerbrey [6], the sensitivity of quartz resonator to mass changes depends mainly on its resonance frequency. The resonance frequency of quartz resonators used in the construction of piezoelectric sensors and the temperature of their operation may be selected freely. The only parameter that we cannot select freely is the mass of the coating substance. In practice, although the way of applying a polymer layer guaranteed a good repeatability, coatings of different mass were obtained, which naturally affects the sensitivity of the constructed piezoelectric sensor.

Prior to the analytical use of a sensor, it is necessary to calibrate it. The results of the studies presented in Fig. 1 suggest that sensitivity is proportional to the coating mass. Figure 5 shows a curve illustrating the ratio of the analytical signal to coating mass as a function of nitrobenzene concentration for sensors with polymer layers of different thickness. The fact that for different sensors the relations were identical enabled us to develop the following formula to calculate nitrobenzene concentration in air:

$$c_{\text{nitrob}} = \frac{\Delta F}{\text{CM} \times S_{1\text{kHz}}^{\text{nitrob}}}$$

where ΔF = analytical signal, the measured changes of sensor frequency caused by nitrobenzene vapour (Hz); CM = coating mass equivalent to changes of resonance frequency (kHz); and $S_{1\text{kHz}}^{\text{nitrob}}$ = sensor sensitivity to nitrobenzene expressed in terms of coating mass equivalent to 1 kHz frequency change.

As the calibration curves in the presence of water are parallel, it is possible to introduce a correction for the water content in air. Then the equation assumes the following form:

$$c_{\text{nitrob}} = \frac{\Delta F}{\text{CM} \times S_{1\text{kHz}}^{\text{nitrob}}} - \frac{S_{1\text{kHz}}^{\text{H}_2\text{O}}}{S_{1\text{kHz}}^{\text{nitrob}}} \times c_{\text{H}_2\text{O}}$$

where $C_{\text{H}_2\text{O}}$ = water concentration in air (μg l^{-1}); $S_{1\text{kHz}}^{\text{H}_2\text{O}}$ = sensor sensitivity to water expressed in terms of coating mass equivalent to 1 kHz frequency change; and $(S_{1\text{kHz}}^{\text{H}_2\text{O}})/(S_{1\text{kHz}}^{\text{nitrob}})$ = the selectivity of nitrobenzene sensor to water.

As follows from the equation presented above, the only sensor's parameter to be determined is CM, the resonance frequency change equivalent to mass of coating deposited on resonator's surfaces.

Analytical application

The sensor presented was applied to the determination of the nitrobenzene concentration in air. Measurements were carried out by a flow-through method, using a home made measuring cell [2].

The main element of the measuring cell was a rectangular PTFE block, with a cavity hosting a piezoelectric sensor. The air to be analyzed entered the measuring cell through two inlets lying on opposite planes of the resonator.

The air was sucked inwards through channels milled on the surface of the PTFE body. The

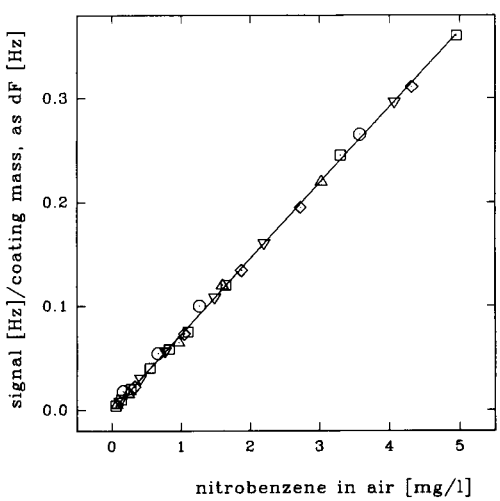

Fig. 5. Calibration curves of sensors with different coating mass (under flow-through conditions). Coating mass equivalent to resonance frequency change: ○ = 1.8 kHz; ▽ = 6 kHz; □ = 10 kHz; △ = 19 kHz; ◇ = 24 kHz.

TABLE 3

Results of the determination of the nitrobenzene concentration in air obtained by using the piezoelectric sensor and by a gas chromatographic method

Nitrobenzene concentration in air ($\mu g \times l^{-1}$)	
Piezoelectric sensor	Gas chromatography
189	191
524	540
442	420
389	396
324	300

channels were covered with PTFE foil and metal plates which stabilized the temperature of the air sucked and the whole PTFE body. The metal plates were electrically heated, and their temperature was electrically controlled. The construction of the measuring cell assured a temperature stability of the air under study with an accuracy better than ± 0.2°C.

At the outlet of the measuring cell, a system was placed for measuring the water concentration in air, consisting of two thermoresistors (wet and dry) in a bridge circuit. The signal (via an A/D converter) along with the value of the measured frequency were transmitted to a computer enabling a continuous calculation of the nitrobenzene content in air with a correction for the presence of water taken into account.

The system was connected in series with a gas loop of a gas chromatograph which permitted, at any moment, the performance of an independent determination of the nitrobenzene content in air.

The nitrobenzene concentration was measured in a room with nitrobenzene kept in an open vessel.

Table 3 shows the results obtained by using the presented piezoelectric sensor as well as by the gas chromatographic method.

A good agreement proves the analytical usefulness of the presented piezoelectric sensor.

REFERENCES

1 M.N. Tilichenko and L. V Zykova, J. Appl. Chem. USSR, 25 (1952) 62.
2 K. Ren, Chem. Anal. (Warsaw), 38 (1993) 589.
3 A. Mierzwinski and Z. Witkiewicz, Chem. Anal. (Warsaw), 30 (1985) 429.
4 M.F. Nicol, Appl. Spectrosc. Rev., 8 (1974) 183.
5 N.S. Bayliss, Adv. Quantum Chem., 1 (1964) 145.
6 G.Z. Sauerbrey, Z. Phys., 155 (1959) 206.

Analytica Chimica Acta, 286 (1994) 205–212
Elsevier Science B.V., Amsterdam

Adsorption of metal ions from solutions on the quartz plate of an electrode-separated piezoelectric quartz crystal

Toshiaki Nomura, Mie Isawa, Hiromi Matsuzawa and Yoko Shibukawa

Department of Chemistry, Faculty of Science, Shinshu University, Asahi, Matsumoto 390 (Japan)

(Received 8th February 1993)

Abstract

Metal ions were adsorbed on the quartz plate of an electrode-separated piezoelectric quartz crystal in solution. The substances adsorbed were hydroxides. Only a few metal ions adsorbed in solutions of higher ionic strength, but a quartz plate coated with Teflon adsorbed many metal ions and had a higher sensitivity, that is, it could be used for the determination of small amounts of metal ions.

Keywords: Piezoelectric sensors; Adsorption; Metal ions

A piezoelectric quartz crystal in contact with a solution on one side is able to oscillate [1]. A crystal connected to the oscillator linked to another condenser oscillates when the whole crystal is immersed in the solution [2]. The frequency shifts with temperature, density, viscosity and conductivity of the solution [1,3]. The frequency change caused by the mass change on the crystal surface, caused by, e.g., adsorption, desorption or electrodeposition, can be measured in solution when the temperature and these properties are controlled by a water-bath and buffer solutions. Therefore, some species in the solution can be determined in situ [4]. The piezoelectric quartz crystal in solution is negatively charged, so that positively charged substances in the solution adhere spontaneously, especially metal ions, which adhere to the crystal as hydroxo metal ions [5]. If the frequency behaviour of the quartz crystal is to be used for the investigation of adsorption, electrodeposition, desorption, etc., this spontaneous adsorption of positively charged substances, such as metal ions and surfactants, should be removed by using a controlled pH, a masking reagent or separation.

An electrodeless piezoelectric quartz crystal (electrodeless PQC) is constructed with no electrode attached to either side of the quartz plate, but electrodes are inserted in the separate electrolyte solutions on both sides of the quartz plate, and are connected to an oscillator. (In this work the crystal is placed horizontally on a platinum plate, solution is placed on the crystal and a platinum wire electrode is inserted in the solution.) The frequency shifts due to the solution properties and the mass change on the quartz plate is just the same as for a normal piezoelectric quartz crystal (normal PQC) having two electrodes [6]. The electrodeless PQC will be more useful than the normal PQC because the elec-

Correspondence to: T. Nomura, Department of Chemistry, Faculty of Science, Shinshu University, Asahi, Matsumoto 390 (Japan).

SSDI 0003-2670(93)E0558-O

trodeless PQC can be made smaller and it thus as a much higher frequency, and then quartz plate is cheaper [7].

The electrode-separated piezoelectric quartz crystal (electrode-separated PQC) is constructed with a quartz plate and with platinum plate electrodes on each side of the quartz plate but separated from it, instead of the evaporated metal electrodes on the quartz plate as in a normal PQC. The electrode-separated PQC oscillates in solution, and the frequency shifts due to the solution properties are just same as for the normal PQC except that there is a higher dependence on the conductivity and permittivity. The frequency of the electrode-separated PQC shifts with the mass change on the quartz plate in the same way as an electrodeless PQC if the temperature and the properties of the solution are controlled using a water-bath and pH buffer solution. The electrode-separated PQC will also be more useful than the electrodeless PQC because the only the quartz plate need be placed in the solution [8]. The quartz plate of the electrodeless PQC or the electrode-separated PQC, on which the adsorbing mass results in a frequency change, is not connected to the oscillator directly and hence has no charge, in contrast to the normal PQC. To use the electrode-separated PQC, the frequency behaviour caused by the adsorption of some species from solution must be examined. In this paper, the adsorption of metal ions from solution and application to the determination of these metal ions are discussed.

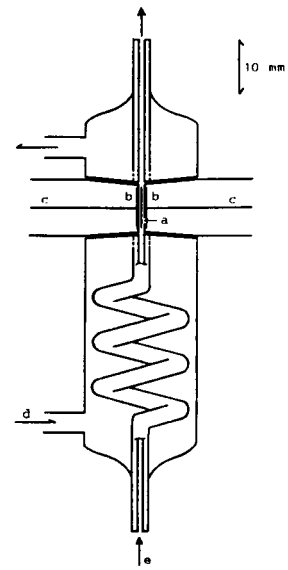

Fig. 1. Vertical section of the electrode-separated PQC in a flow cell. a = Quartz plate; b = electrodes; c = lead wires; d = thermostated water; e = reagent blank or metal ion solution.

EXPERIMENTAL

Apparatus and reagents

A piezoelectric quartz crystal plate, which was AT-cut, 9 MHz, circular and with no electrode, was obtained from Kyushu Dentsu. The quartz plate was set in a flow cell having a cooler to control the solution temperature followed by degreasing with 2 M sodium hydroxide (Fig. 1). Platinum plate electrodes were connected with lead wires to a transistorized oscillator, to which was applied 6.0 V by a Metronix 521C supplier. The cooler was connected to a water-bath (Taiyo Kagaku Thermo Unit C650) to control the temperature of the solution at 25.0 ± 0.1°C. The length of the coiled tube in the cooler was about 25 cm. The frequency was measured with an Advantest, TR5822 frequency counter and a Toa Denpa FBR-252A recorder. A metal ion sample solution containing pH buffer, a reagent blank (pH buffer) solution or an eluent to desorb the adsorbed metal ions was selected with a Teflon tap and sent to the flow cell by a peristaltic pump (Yamato, Cole-Parmer Masterflex PA-26A). The experiments with the electrodeless PQC were carried out as in the previous system [7].

All chemicals were of analytical-reagent grade from Wako. Stock standard solutions (0.1 M) of metal ions were prepared by dissolving the nitrates or sulphates in water, but iron(III) and aluminium(III) solutions were in 0.1 mM nitric acid. These solutions were diluted with water as required when they were used. Buffer solutions were prepared from acetic acid, sodium acetate,

boric acid and sodium hydroxide, and diluted with water as required when they were used. pH values were measured with a Toa Denpa HM-5EST pH meter. Deionized water prepared with an autostill (Yamato WG-25) was used throughout. The eluent to desorb the adsorbed metal ions was 10 mM nitric acid.

Adsorption of metal ions on the quartz plate in the electrode-separated PQC

Pass a reagent blank (pH buffer) solution to the flow cell at a constant flow-rate and read off the frequency when it becomes constant (F_1). Pass the metal ion sample solution, which was allowed to stand for 5 min after preparation with a buffer solution, for exactly 5 min. Pass the reagent blank solution again. Read off the frequency (F_2) 10 min after changing the stream from the sample solution to the reagent blank solution. Calculate the frequency changes caused by the adsorption of metal ions ($F_1 - F_2$). Elute the adsorbed metal ions with 10 mM nitric acid for 5 min and then with deionized water. Pass the reagent blank solution through the flow cell for the next experiment.

Adsorption of metal ions on the quartz plate of the electrodeless PQC

Place the quartz plate, treated with a Teflon spray, on the horizontal platinum plate in the cell. Place 5 μl of 1 M potassium chloride solution containing 0.1 M buffer reagent along with a platinum wire as a lead wire on the centre of the quartz plate. Record the frequency. Place 5 μl of metal ion solution containing 1 M potassium chloride on the 1 M potassium chloride solution when the frequency becomes constant. Examine the adsorption behaviour from the frequency shift just after the metal ion solution has dropped in. Remove the quartz plate from the cell. Immerse the plate in 10 mM EDTA solution for 10 min to remove the adsorbed metal ions. Rinse with water and then ethanol and dry for the next experiment. Wipe the platinum plate and wire in the cell with water and acetone. For the determination of metal ions, use the difference in the frequency at the time the metal ion solution dropped in and that 3 min later.

RESULTS AND DISCUSSION

Effect of concentration of reagent blank (pH buffer) solution on adsorption

The optimum conditions for metal ion adsorption on the quartz plate were investigated with a nickel(II) solution. The frequency change, depending on the adsorption of nickel(II), decreased with increasing concentration of borate buffer (Fig. 2) and increasing concentration of potassium chloride solution added to a constant concentration of the buffer. This frequency behaviour was observed when other metal ions were used. It was assumed that the adsorption of metal

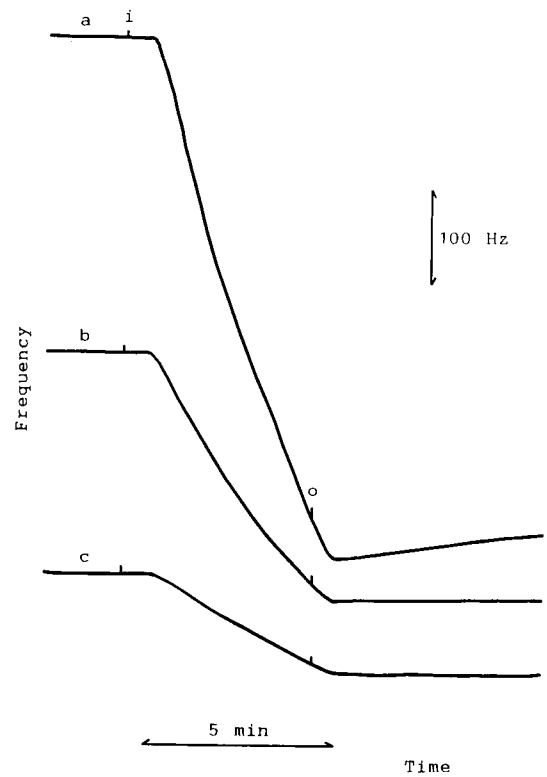

Fig. 2. Dependence of frequency shifts of the quartz plate in the nickel(II) solution (100 μM) on the concentration of borate buffer solution (pH 9.2). Concentration of the buffer solution, (a) 1, (b) 5 mM and (c) 10 mM; flow-rate, 4.0 ml min^{-1}; temperature, 25.0 ± 0.1°C. Readings begin at the left-hand side and the nickel(II) solution was passed through the flow cell at the first mark (i) and changed to the reagent blank solution at the second mark (o) after 5 min.

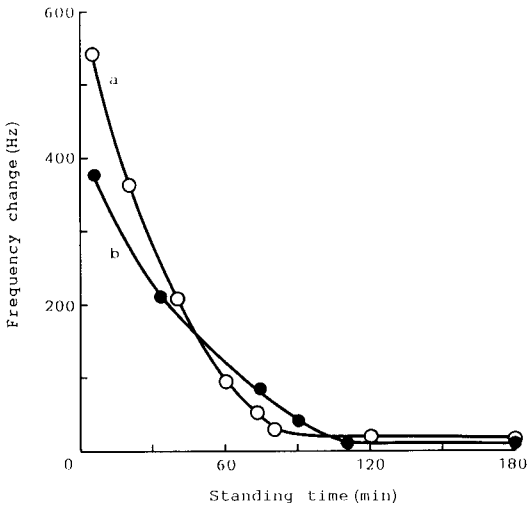

Fig. 3. Dependence of frequency changes of the electrode-separated PQC on the standing time after the preparation of nickel(II) solution. pH of the buffer solution (1 mM): (a) 9.12; (b) 9.05. Other conditions as in Fig. 2.

ions on the quartz plate depended on the ionic strength.

In order to detect the frequency change caused by the adsorption of metal ions, a 1 mM reagent blank solution (pH buffer solution) was used, in which many metal ions adsorbed on the quartz plate and a large frequency change was obtained. In 10 mM buffer, only aluminium(III), cadmium(II), nickel(II) and zinc(II) produced the frequency change caused by adsorption.

Effect of standing time after preparation of metal ion solution on frequency change

The standing time was the period between the time when the metal ion solution was mixed with the pH buffer solution (preparation of the sample solution) and the time when the sample solution was passed into the flow line. A frequency change occurred about 40 s after turning the Teflon tap to initiate sample flow. The frequency changes decreased with increasing standing time, as shown in Fig. 3. It seems that any precipitate formed aged and grew into larger particles during the standing time and brought about the lower adsorption. In subsequent experiments a 5 min standing time was adopted.

Dependence of adsorption of metal ions on flow-rate

The frequency change caused by the adsorption of nickel(II) increased with increasing flow-rate of the nickel(II) solution up to 4.2 ml min^{-1}, but then decreased.

Dependence of adsorption of metal ions on pH

The pH dependence of the frequency change of the quartz plate with a flow of nickel(II) solution was investigated under the following conditions: buffer solution, 1 mM; concentration of nickel(II), 100 μM; flow-rate, 4.0 ml min^{-1}; standing time, 5 min; and sampling time [period for passing the nickel(II) solution through the flow cell], 5 min. As shown in Fig. 4, the maximum frequency change was recorded at ca. pH 9.2 and a constant frequency was observed after changing the flow from the nickel(II) solution to

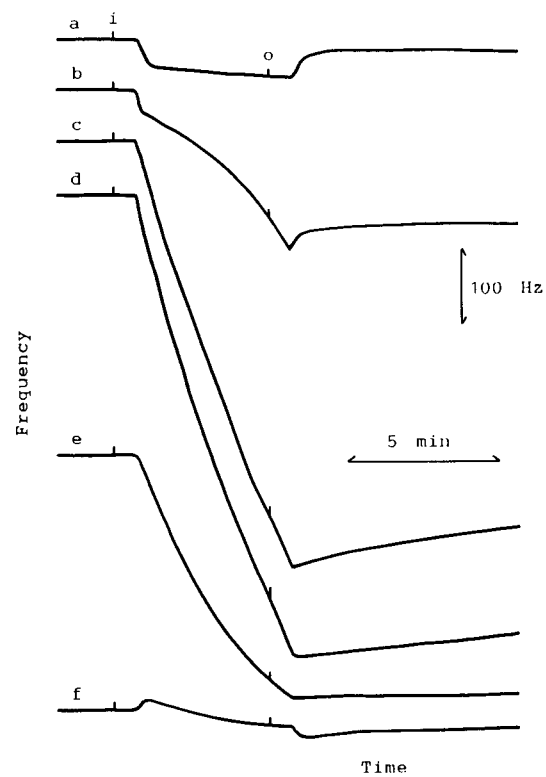

Fig. 4. Dependence of frequency shifts on pH: (a) 8.86; (b) 8.97; (c) 9.03; (d) 9.23; (e) 9.52; (f) 10.08. Other conditions as in Fig. 3.

the reagent blank solution at higher pH. From the facts that frequency changes were observed around pH 8 and above and the quartz plate in the electrode-separated PQC was electrically neutral, it was assumed that the precipitate would be a nickel(II) hydroxide [9]. The frequency change decreased with increasing pH because the precipitate of nickel(II) hydroxide would more readily change to larger, more stable particles at pH > 9.2, and so did not adhere to the quartz plate. The frequency changes (ΔF, Hz) caused by the adsorption of nickel(II) was proportional to concentration (c, μM) in the range 10–120 μM, and at pH 9.2, $c = \Delta F/4.27$.

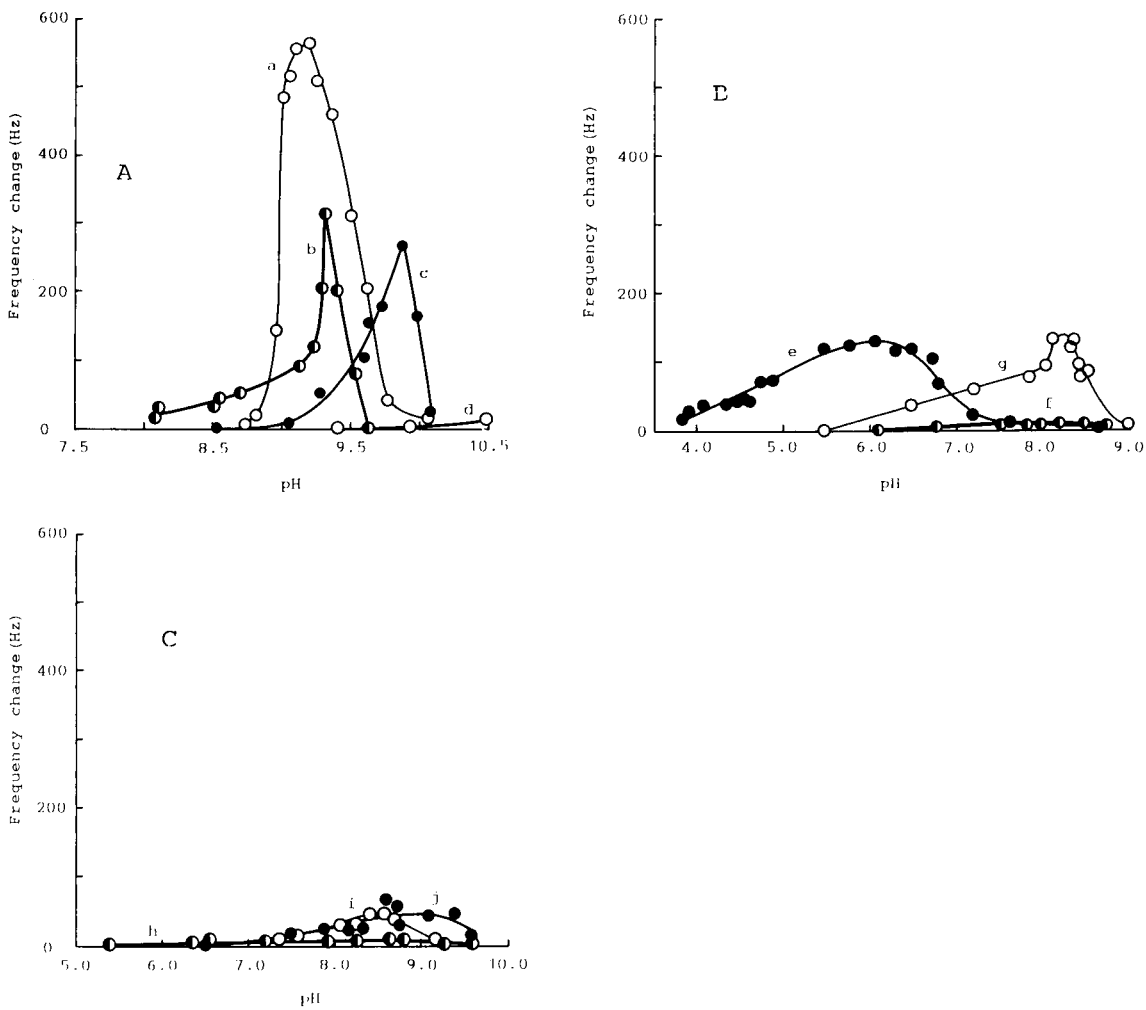

Fig. 5. Dependence of frequency changes on pH in various metal ion solutions. (A) (a) nickel(II); (b) cobalt(II); (c) manganese(II); (d) magnesium(II); (B) (e) iron(III); (f) aluminum(III); (g) copper(II); (C) (h) lead(II); (i) zinc(II); (j) cadmium(II). Other conditions as in Fig. 3.

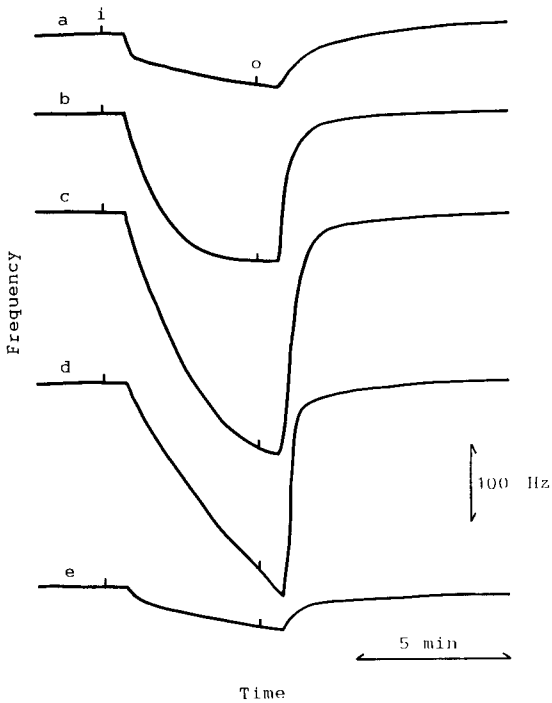

Fig. 6. Dependence of frequency shifts on pH in aluminum(III) solutions: (a) 6.10; (b) 7.50; (c) 7.80; (d) 8.19; (e) 8.46. Other conditions as in Fig. 3.

The same procedure as for nickel(II) was applied to other metal ions to study the dependence of pH on the frequency change. These results are shown in Fig. 5.

Zinc(II) solutions of pH $\geq$ 7 gave a suspension of white particles in a 10 mM buffer solution and a slight suspension in 1 mM buffer solution. Only a small frequency change caused by the adsorption of zinc(II) was observed, however. No aluminium(III) hydroxide adsorbed on the quartz plate over the pH range considered, as shown in Fig. 5B. Figure 6, however, shows that the aluminium(III) hydroxide may be adsorbed on the quartz plate but is rapidly removed when the buffer solution only is passed through. The behaviour of aluminium(III) on the quartz plate was not observed with other metal ions Cadmium(II) adsorbed slightly at ca. pH 8.5, but with poor reproducibility. The frequency of the quartz plate in cobalt(II) solution shifted with adsorption of cobalt(II) hydroxide, but it was removed gradually when the flow was changed to the reagent blank solution, that is, the adsorbed precipitate adhered weakly on the quartz plate. Copper(II) in the buffered solution adsorbed at lower pH. However, the surface of the glassware containing the copper(II) solution of ca. pH 9.0 and above had a precipitate on it. The iron(III) precipitate adsorbed on the quartz plate was held strongly when the iron(II) solution was changed to the reagent blank solution.

Magnesium(II) did not adsorb and no frequency change was observed.

Above pH 10.5, the metal ion solutions had higher conductivities caused by the higher content of sodium hydroxide, and then the quartz plate of the electrode-separated PQC did not oscillate stably. Magnesium(II) in this higher pH solution would adsorb on the quartz plate as the hydroxide if the measurements could be made in that pH range. The precipitate of manganese(II) in the higher pH range was not removed from the quartz plate, that is, the frequency was constant when the reagent blank solution was passed instead of the metal ion solution, and manganese(II) in the higher pH solution adhered to the wall of the glassware.

Lead(II) solution formed a suspension just after the preparation of the sample solution with the buffer solution, but did not change the frequency of the quartz plate.

Adsorption of metal ions on the quartz plate of the electrodeless PQC [7]

No adsorption of hydroxide precipitates on the quartz plate in the electrode-separated PQC just after the preparation of the metal ion solution (sample solution) could be observed because the preparation of the sample solution and the system of the flow cell needed times of at least several minutes. The frequency behaviour of the hydroxides of metal ions just after the preparation using the electrodeless PQC has already been discussed [7]. The frequency behaviour of the quartz plate of the electrodeless PQC in the sample solution having a pH > 9 was not investigated because the solution dissolved the Teflon spread on the quartz plate.

Only nickel(II) and lead(II) produced frequency changes due to the adsorption of hydroxides. The former adsorbed in the same pH range as above and the latter above pH 7.6. A high concentration (1 M) of potassium chloride solution was needed to oscillate the electrodeless PQC. Only lead(II) adsorbed on the quartz plate of the electrodeless PQC in the pH range 7.6–8.5, and then could be determined without the separation of other metal ions. The frequency changes (ΔF, Hz) caused by the adsorption of lead(II) hydroxide in a time interval of 3 min and at pH 8.1 depended on the concentration (c, mM) according to $c = (\Delta F - 46)/486$, and the relative standard deviation of five runs using 2 mM lead(II) solution was 8.21%.

Adsorption of metal ions on the quartz plate treated with Teflon in the electrode-separated PQC

Method of Teflon coating. A quartz plate having no electrode was layed horizontally on a filter-paper, sprayed with a Teflon spray (Iuchi Seiei Do), at a distance of ca. 50 cm from the top and at a constant blowing rate, and left for about 10 min. The quartz plate was turned over, sprayed on the other side by the same method and left to dry. The platinum electrode of the electrode-separated PQC was coated with Teflon by the same method as for the quartz plate. The quartz plate and the glass tubes containing the electrodes were set in the flow cell.

Method of the measurement. The frequency was measured in the same way as in the preceding procedure.

Frequency behaviour of electrode-separated PQC coated with Teflon

The electrode-separated PQCs, which had an uncoated quartz plate and platinum electrodes coated with Teflon one or four times, a quartz plate coated with Teflon twice on both sides and uncoated electrodes, and a coated quartz plate and coated electrodes, were used to investigate the frequency behaviour with respect to the conductivity in the potassium chloride solution and the density and viscosity in the sucrose solution. The frequency behaviour of the electrode-separated PQC coated with Teflon on the electrodes and/or quartz plate was the same as for that without Teflon treatment [8].

The adsorption behaviour of metal ions on the quartz plate coated with Teflon was studied under the following conditions: metal ion solution, 25 μM zinc(II) nitrate; sampling time, 10 min; and borate buffer solution (pH 8.8), 10 mM. First, the dependence on the flow-rate of the frequency change caused by the adsorption of zinc(II) was almost the same as for the electrode-separated PQC not treated with Teflon except that larger frequency changes were observed and the maximum frequency change occurred at a flow-rate of ca. 4.5 ml min^{-1}. The frequency change increased with increase in sampling time up to about 18 min and then remained almost constant. The sensitivity for the adsorption of the metal ion on the quartz plate coated with Teflon was much greater than that on the uncoated quartz plate, so the dependence on pH of the frequency change caused by the adsorption was studied using 25 μM zinc(II) solution. The frequency changes due to the adsorption of metal ions were observed in almost the same pH ranges as for the uncoated quartz plate (Fig. 7). Although the concentration of the buffer solution was 10 mM, manganese(II) and cobalt(II), in addition to the metal ions ad-

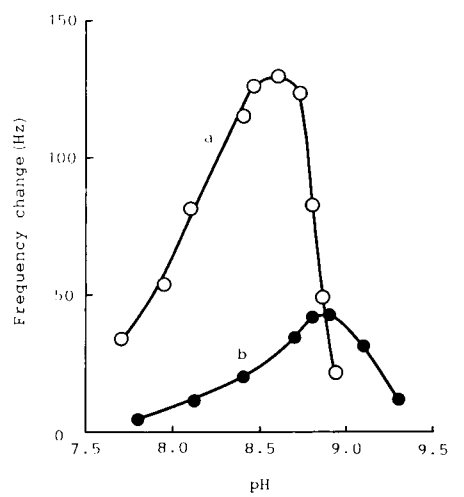

Fig. 7. Frequency change of the quartz plate (a) coated with Teflon or (b) uncoated on pH in (a) 25 μM or (b) 100 μM zinc(II) solution. Concentration of buffer solution, 10 mM; flow-rate, 4.5 ml min^{-1}; sampling time, 10 min.

sorbed on the uncoated quartz plate, shifted the frequency resulting from adsorption of the precipitates. It seems that the precipitates were easily adsorbed on the Teflon because the surface became much more hydrophobic than the uncoated quartz plate. The pH ranges of adsorption of the metal ions were almost the same as those at the concentration of 1 mM described above. The frequency changes (ΔF, Hz) of the quartz plate coated with Teflon in the zinc(II) solution containing 10 mM buffer (pH 8.5) were proportional to concentration (c, μM) in the range 2.5–30 μM according to $c = \Delta F/5.40$, under the following conditions: sampling time, 10 min; and flow-rate, 4.5 ml min^{-1}. Nitric acid (10 mM) or alkaline EDTA solution (10 mM EDTA solution in 1 mM sodium hydroxide) as the eluent dissolved or removed in the Teflon coating, so it could not be used for a long period. Disodium EDTA solution (10 mM) as the eluate could be used about 40 times. However, in the experiments at pH > 9, the frequency change decreased gradually as the Teflon coating was perhaps removed. The removal increased at higher pH.

Conclusion

Adsorption of metal ions as their hydroxides on the quartz plate in the electrode-separated PQC depended on the pH, ionic strength, flow-rate to the quartz plate and standing (ageing) time of the metal ion solutions. The adsorption behaviour of the hydroxides varied among the metal ions. No frequency change was observed when the metal ion solutions were suspended with a precipitate, or formed a precipitate at higher pH. However, the quartz plate in the metal ion solution at the beginning of the precipitation adsorbed an unstable, tiny precipitate. The frequency behaviour of the quartz plate coated with Teflon in the metal ion solutions was very subject to this adsorption process, and the frequency change and the maximum frequency change caused by the adsorption occurred at a lower pH than for the uncoated quartz plate. As the surface of the quartz plate coated with Teflon was much more hydrophobic than the uncoated plate, the metal ions, which did not adsorb on the uncoated plate, adhered and then changed the frequency. Further, the metal ions at lower concentration adsorbed and then gave a frequency change that could be used for the determination of smaller amounts of metal ions. The electrode-separated PQC could be used for the determination of metal ions as hydroxides, with control of the pH and ionic strength and using a masking agent if necessary. Further, various chemical species could be determined as precipitates if a suitable precipitating reagent is used.

The authors gratefully acknowledge financial support by research grants from Asama–Polis Development Organization.

REFERENCES

1 T. Nomura and A. Minemura, Nihon Kagaku Kaishi, (1980) 1621.
2 T. Nomura and M. Okuhara, Anal. Chim. Acta, 142 (1982) 281.
3 T. Nomura, M. Watanabe and T.S. West, Anal. Chim. Acta, 175 (1985) 107.
4 T. Nomura, Bunseki, 1989 (1989) 104.
5 T. Nomura and T. Kanazawa, Anal. Chim. Acta, 245 (1991) 71.
6 T. Nomura, F. Tanaka, T. Yamada and H. Itoh, Anal. Chim. Acta, 243 (1991) 273.
7 T. Nomura, Yu. Ohno and Yu. Takaji, Anal. Chim. Acta, 272 (1993) 187.
8 T. Nomura, T. Yanagihara and T. Mitsui, Anal. Chim. Acta, 248 (1991) 329.
9 L. Erdey, Gravimetric Analysis, Vol. 1, Pergamon, Oxford 1963, p. 189.

Analytica Chimica Acta, 286 (1994) 213–218
Elsevier Science B.V., Amsterdam

Permeability controllable overoxidised polypyrrole film modified glassy carbon electrodes

Zhiqiang Gao [a], Minxian Zi and Beshen Chen

Department of Chemistry, Henan University, Kaifeng, Henan 475001 (China)

(Received 21st June 1993; revised manuscript received 30th September 1993)

Abstract

A voltammetric study on overoxidised polypyrrole (PPy) film modified electrodes is reported. These electrodes show permselective and accumulative properties towards cationic dopamine (DA). The exclusion of anionic ascorbate offers substantial improvement in the selectivity of DA determination. Differences in voltammetric responses of DA and ascorbate are attributed to the charge and porosity of the film. The volume of doping ions used for PPy preparation takes an important role in the film permeability. Other factors such as film thickness and preconcentration time are also investigated.

Keywords: Voltammetry; Polypyrrole film modified glassy carbon electrodes

In the last decade conducting polymers have become one of the most active fields in electrochemistry and a range of possible applications has been studied [1–3]. Polypyrrole (PPy), in particular, has shown great promise because, besides exhibiting desirable electrochemical and optical properties, it is easily polymerised in an aqueous solution. Most of the applications of PPy arise from its reversible switching between the doped and undoped states. During switching, both electron and ion transports take place in the polymer film which are directly related to the fundamental properties [1–3]. Only a little attention has been paid, however, to the overoxidised PPy films [4,5]. This is probably due to the loss of what many see as its desirable properties after overoxidation. More recently Witkowski et al. [6,7] demonstrated that a deliberate overoxidation of PPy films can be advantageous. It was found that the electrode substrate plays a definite role in the permselectivity of the polymer films. However, the practical usefulness of their electrodes is limited by the low sensitivity. We have shown that the overoxidised PPy films, prepared in bulky anion solutions, can be used for voltammetric determination of cationic species in the presence of large excesses of anions [8,9]. The current sensitivity for cations is enhanced and selectivity against anions is greatly improved.

In this study, PPy films prepared in different electrolyte solutions are overoxidised in 0.1 M NaOH solution and the voltammetric responses of dopamine and ascorbic acid are evaluated.

EXPERIMENTAL

Reagents and apparatus

Dopamine (DA) (Aldrich), L-ascorbic acid (AA) (Merck), sodium dodecyl sulphate (DS) (Fluka), sodium *p*-toluensulfonate (TS) (Aldrich)

Correspondence to: Z. Gao, Department of Chemistry, Henan University, Kaifeng, Henan 475001 (China).
[a] Present address: Department of Materials and Interfaces, Weizmann Institute of Science, Rehovot 76100 (Israel).

SSDI 0003-2670(93)E0555-L

and sodium salicylate (SC) (Baker) were used as received. Pyrrole (Merck) was purified by double distillation and stored in a refrigerator. All other chemicals were of certified analytical grade. Solutions of DA and AA were prepared daily with degassed Millipore-purified water. Dissolved oxygen in the solution was removed by bubbling with high purity nitrogen and a nitrogen atmosphere was kept throughout experiments.

Voltammetric experiments were performed with a Metrohm Polarecord E506 Polarograph. A conventional three-electrode system equipped with a modified glassy carbon electrode, a platinum wire counter electrode and a saturated calomel reference electrode (SCE) was used throughout. All potentials given in this paper were referred to the SCE. Experiments were performed at room temperature. A 2000 Potentiostat/Galvanostat (NF Circuit Design Block, Japan) was employed for the PPy film preparation.

Preparation of overoxidised PPy film modified glassy carbon electrodes

A clean and polished glassy carbon electrode (0.2 cm^2) was pretreated according the procedure described by Anjo et al. [10]. It was then placed in a degassed 0.1 M pyrrole–0.1 M electrolyte solution, and a constant current (1–2 mA/cm^2) was applied to the glassy carbon electrode. The film thickness was controlled based on the amount of charge passed [11]. For the same polymerisation charge the variation of film thickness was found in the range 10–20% (by scanning electron microscopy). The PPy film doped with anion A was denoted as PPy/A. The PPy film was overoxidised in 0.1 M NaOH by potential cycling between −1.0 and 0.4 V with a scan rate of 20–50 mV/s. The electrode was then ready for use after the final wash with water.

Voltammetry with overoxidised PPy film modified electrodes

All voltammetric experiments were performed in a consistent manner in 0.1 M degassed phosphate buffer (pH 7.4). The modified electrode was immersed under open-circuit conditions in 20 ml of phosphate buffer containing the analytes. After a given period of time the voltammetry was conducted and the electrode was then kept at 0.4 V for 60 s to ensure complete oxidation of the preconcentrated analyte prior to the next measurement.

RESULTS AND DISCUSSION

Voltammetry of solutes at the overoxidised PPy film coated electrodes

When a PPy film modified electrode is subjected to potential cycling between −1.0 and 0.4 V in 0.1 M NaOH, the conducting state of the

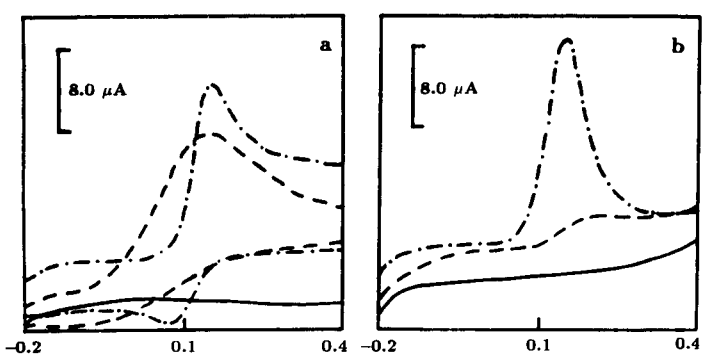

Fig. 1. Voltammograms of DA and AA at the bare (a) and the overoxidised PPy/TS modified electrodes (b). Film thickness 0.1 μm, 0.1 M phosphate buffer (pH 7.4), potential scan rate 40 mV/s, preconcentration time 60 s. (a) Background current (———), 0.4 mM AA (------) and 0.2 mM DA (·–·–·–). (b) Background current (———), 1.0 mM AA (------) and 10 μM DA (·–·–·–).

polymer is destroyed by nucleophilic attack of hydroxide ions on pyrrole units and further oxidised to carbonyl groups, which results in the loss of conjugated structure and hence the loss of conductivity [4]. The polymer is converted from an electronic/ionic conducting polymer to a purely ionic conducting polymer and the large charging current observed in the electronic conducting state is greatly reduced [6–9]. Voltammetric responses of DA and AA were examined at the resulting modified electrodes because of their analytical interest to neurochemists. At a bare electrode the oxidation of DA exhibits a diffusion-controlled quasi-reversible behaviour (Fig. 1a). The anodic peak potential is about 0.17 V, which is practical constant from electrode to electrode. On the other hand, the oxidation of AA is both chemically and electrochemically irreversible (Fig. 1a). Although the thermodynamic redox potential of AA is more negative than 0 V, the anodic peak potential at the bare electrode is ca. 0.16 V, which strongly depends on the history of the electrode surface. A peak potential variation of 150 mV in positive direction is observable during the experiments. Because of the overlapping of the oxidation potentials of these two species it is extremely difficult to selectively determine either of them in a mixture solution. However, at the modified electrode, the oxidation of these species shows dramatically improved selectivity. The anodic current of DA at the modified electrodes is enhanced over 20 times, while that of AA is greatly suppressed (Fig. 1b). This is contrary to those obtained by Witkowski et al. [6,7] although some differences were observed by changing the substrate electrode. The sensitivity for DA at their electrodes was never higher than that at the bare electrodes.

The ability to vary the permeability of overoxidised PPy films via control of the molecular volume of doping ions is illustrated in Fig. 2. A facile transport of the positively charged DA through all films is observed and all films exhibit a preconcentration property for DA (see below), confirming that the PPy film is negatively charged after overoxidation [7,8]. On the contrary, the oxidation of mM AA is almost completely excluded (Fig. 2b). Furthermore the peak potentials of DA and AA at the modified electrode are practically the same as those at the bare electrode, which suggests that the electron-exchange process occurs at the substrate electrode. Similar permeabilities are observed for PPy films treated by constant potential electrolysis and constant

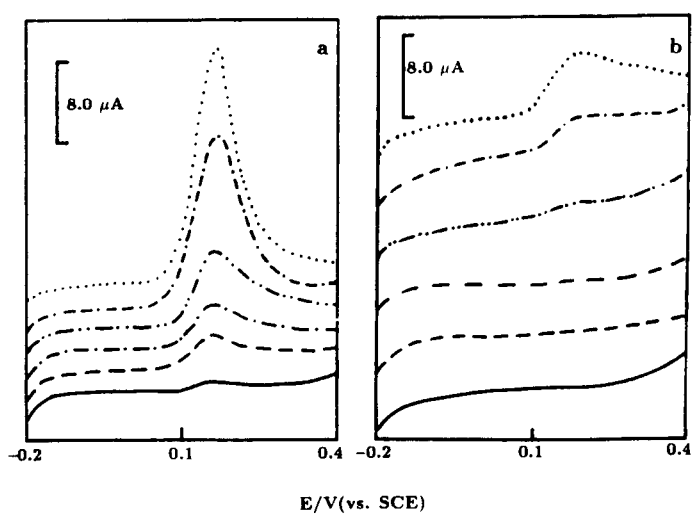

Fig. 2. Linear sweep voltammograms of DA (a) and AA (b) at overoxidised PPy film modified electrodes. Experimental conditions as for Fig. 1(b). PPy/F (———), PPy/Cl (------), PPy/BF_4 (·–·–·–), PPy/ClO_4 (–··–··), PPy/SC (-- ·--) and PPy/DS (·····).

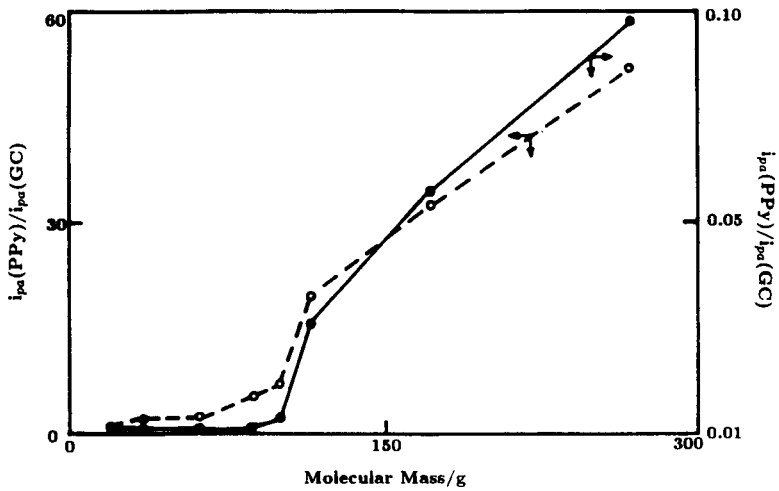

Fig. 3. Dependence of the permeability of overoxidised PPy films on the molecular mass of doping ions. Film thickness 0.3 μm, preconcentration time 2 min, other conditions as for Fig. 1b doping ions used are F^-, Cl^-, NO_3^-, BF_4^-, ClO_4^- SC^-, TS^- and DS^-. ———, AA; — — —, DA.

current electrolysis in 0.1 M NaOH. However, incomplete surface coverage is often observed following these treatments, which is probably due to the high overoxidation rate, resulting in the formation of pinholes or even large defects. It may also be attributed to the evolution of oxygen at the electrode substrate due to the high electrode potential [12], which leads to the poor adherence of the film on the electrode surface. This effect is more obvious when thick films are used. It was found that the best film is obtained by potential cycling between −1.0 and 0.4 V. In addition, no obvious differences are observed when changing electrode substrate, polymerisation current density and pyrrole concentration. However, the overoxidation rate is increased by increasing the pH of the overoxidation solution. It seems that the permeability of the film is directly related to the molecular volume of doping ion used for PPy preparation. As been well-known, the doping ion has a profound effect on the properties of the conducting polymers [1,13]. Dramatic changes in the voltammogram of PPy film doped by different anions are observed in our experiments, which are similar to those reported by Walton et al. [13]. After overoxidation the doping ions are expelled from the film [9], which leads to a porous structure of the film.The larger the doping ion used for PPy preparation the higher the porosity of the film and therefore the higher the permeability (Fig. 3). Since the film thickness is controlled by controlling the charge passed during electropolymerisation, it is expected that for the same polymerisation charge the same amount of negative charge should be formed in the film during overoxidation treat-

TABLE 1

Voltammetric selectivity (response ratios) of DA against AA at the overoxidised PPy film modified electrode [a]

Thickness (μm)	PPy/BF_4	PPy/ClO_4	PPy/SC	PPy/TS	PPy/DS
0.0	3.23	3.22	3.25	3.19	3.21
0.1	450	460	480	370	320
0.3	520	550	710	570	540
0.5	680	700	810	730	720

[a] Experimental conditions as for Fig. 3. The uncertainties of the selectivity are less than 10%.

ment. As a result the ion-exchange capacity should be equal for all films. This is confirmed by the chronocoulometry of DA loaded films in blank electrolyte solution. For 30-min preconcentration in 2 mM DA solution, the charge for the complete oxidation was found to be 4.8 ± 0.5 mC for 0.5 μm thick films doped with SC, TS or DS.

Varying the film thickness shows a pronounced effect on the film permeability. Thickening the film results in a more effectively excluding AA. For example, 90 and 97% attenuations of the oxidation current of 1.0 mM AA are observed at 0.3 μm PPy/DS and PPy/ClO_4 films respectively. Less than 1% of the signal can be detected at 1.0 μm thick film modified electrodes. The oxidation of DA also shows a strong dependence on the film thickness. For a 2-min preconcentration time in a 10 μM DA solution, the highest sensitivity is observed at 0.1 μm PPy/Cl and 0.3 μm PPy/DS films, respectively. At much lower concentrations of DA the highest sensitivity is obtained at PPy/DS films thinner than 0.3 μm.

The selectivities of the electrodes for DA against AA are shown in Table 1. Owing to the difficulty of measuring the oxidation of AA at PPy/F and PPy/Cl electrodes, only five films have been examined. The results clearly indicate that the modified electrodes are from 100 to 250 times more selective to DA than AA, mainly depending on the film thickness. This could be of analytical importance in neurochemistry because the large excess of AA in mammalian brain [14].

The effect of preconcentration time on the current sensitivity is illustrated in Fig. 4. Prolonged preconcentration increases the sensitivity. This is not surprising because prolonged preconcentration allows a large amount of analyte partition into the film. The rate of DA uptake is dependent on DA concentration and doping ion used for PPy film preparation. The preconcentration rate is increased by increasing DA concentration or/and the molecular volume of doping ion. For PPy/DS films, more than 60% of the final response is generated within the first minutes of preconcentration. In contrast, a linear relationship exists with PPy/Cl films. On the other hand, no obvious preconcentration effect is observed in AA solutions. Consequently better selectivity would be expected when a longer preconcentration time is used. Such profiles obtained at different films appear to represent the kinetics of the cation uptake, which is in good agreement with common models for ion exchangers [15].

The above results indicate that the experimental variables are all interrelated. This makes de-

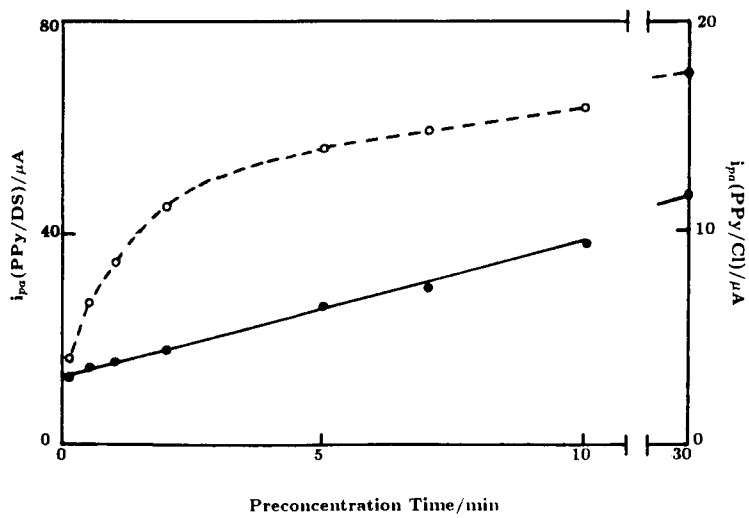

Fig. 4. Dependence of the anodic peak current of DA on the preconcentration time at PPy/Cl (———) and PPy/DS (------) electrodes. Experimental conditions as for Fig. 3.

lineation of optimising experimental conditions difficult for practical analysis, since optimisation would require a prior knowledge of the analyte concentration. Fortunately, this caveat is not significant for in vivo study where the concentration range of DA is already known.

The modified electrode is not entirely stable upon repeated voltammetric determinations. For example after 2 h running, a ca. 10% decrease of the current sensitivity is observed in 1.0 μM DA. This deterioration appears to be worse when high concentrations of DA or multicomponent solutions are examined. The lack of stability might be due to the changes of the film structure over long-term use, not due to the poisoning by the oxidised product of DA since much worse voltammetric responses are observed at the bare electrode.

Practical applications

Voltammetric determination of DA in a mixed solution of 0.1 mM AA and 0.1 mM uric acid is used to evaluate the significance of the controlled permeability and sensitivity with regard to in vivo sensor development. A linear calibration graph between 0.1 and 10 μM with a detection limit of ca. 50 nM is obtained with 0.1–0.5 μm PPy/DS and PPy/TS films. The detection limit with inorganic anion-doped PPy films is much higher (ca. 1.0 μM), but the selectivity is also fairly good for DA analysis. In contrast, detection is not feasible with the bare electrode. The utility of the overoxidised PPy films as anti-fouling layers in the presence of protein, such as albumin, has also been studied. Stable oxidation currents are obtained at the modified electrode in 5.0 μM DA solution containing 1 mg/ml albumin. Six voltammetric runs yield a relative error of ca. 5% (2 min preconcentration). On the contrary, a rapid loss in voltammetric activity (32–38%) is observed at the bare electrode.

Conclusions

The concept of using different experimental conditions to control the permeability of overoxidised PPy films has been demonstrated. The most serious shortcoming of these films is their instability. This, however, may be overshadowed by their excellent sensitivity and selectivity toward organic cations. The film shows good adherence and perfect covering of the substrate electrode owing to the use of electropolymerisation method. It seems likely that the good permeability afforded by such films might be of general utility in in vivo electrochemistry.

REFERENCES

1 T.A. Skotheim, Handbook of Conducting Polymers, Marcel Dekker, New York, 1986.
2 A. Ivaska, Electroanalysis, 3 (1991) 247.
3 A.F. Diaz, J.F. Rubinson and H.B. Mark, Adv. Polymer Sci., 84 (1988) 113.
4 F. Beck, P. Braun and M. Oberst, Ber. Bunsenges. Phys. Chem., 91 (1987) 967.
5 A.F. Diaz, J.I. Castillo, J.O. Logan and W-Y. Lee, J. Electroanal. Chem., 129 (1981) 115.
6 A. Witkowski, M.S. Freund and A. Brajter-Toth, Anal. Chem., 63 (1991) 622.
7 A. Witkowski and A. Brajter-Toth, Anal. Chem., 64 (1992) 635.
8 Z. Gao, M. Zi and B. Chen, J. Electroanal. Chem., in press.
9 Z. Gao, M. Zi and B. Chen, Analyst, in press.
10 D.M. Anjo, M. kahr, M.M. Khodabakhsh, S. Nowinski and M. Wanger, Anal. Chem., 61 (1989) 2603.
11 A.F. Daiz and J.I. Castillo, J. Chem. Soc., Chem. Commun., (1980) 397.
12 R.A. Bull, R.F. Fan and A.J. Bard, J. Electrochem. Soc., 129 (1982) 1009.
13 D.J. Walton, C.E. Hall and A. Chyla, Analyst, 117 (1992) 1305.
14 R.N. Adams, Anal. Chem., 48 (1976) 1126A.
15 T. Qian, Ion-Exchanger and Its Applications, Sci. and Tech. Press, Tianjing, 1984, p. 84.

Analytica Chimica Acta, 286 (1994) 219–224
Elsevier Science B.V., Amsterdam

Novel DNA sensor for electrochemical gene detection

Koji Hashimoto, Keiko Ito and Yoshio Ishimori

Materials and Devices Research Laboratories, Research and Development Center, Toshiba Corporation, 1, Komukai Toshiba-cho, Saiwai-ku, Kawasaki 210 (Japan)

(Received 12th May 1993; revised manuscript received 6th October 1993)

Abstract

Some commercially available intercalators have been found to be electrochemically active through voltammetric experiments. For example, daunomycin was oxidized at a low potential (446 mV) with a high current density (6.5 $\mu A/cm^2$ in a 10 μM solution) on a basal plane pyrolytic graphite electrode with an adsorbed DNA probe. Daunomycin was able to electrochemically distinguish between double and single stranded DNAs using linear sweep voltammetry. After the hybridization reaction of a model targeted gene with DNA probes adsorbed on the electrode, the electrochemical signal of daunomycin intercalated between base pairs of the formed hybrids on the electrode was measured. The use of daunomycin resulted in the detection of the targeted gene of 10^{-8} g/ml in the buffer solution.

Keywords: Voltammetry; Sensors; DNA; Gene detection

A growing interest has arisen in gene diagnoses using nucleic acid hybridization techniques for infectious diseases. Recently, various novel techniques have been developed to replace a traditional method using radioactive substances [1]. Biotin [2], digoxigenin [3], and fluorescent dyes [4] have become popular reagents for labeling. Furthermore, the polymerase chain reaction (PCR), which is a major advancement in molecular biology, has become widely used to detect gene deletions and point mutations [5].

However, all these conventional methods need labelled probes, take at least 10 h for detection and ask for skilled personnel to perform the complicated operations. In these methods, gene detection is performed at different places from the hybridization reaction. Recently, Hashimoto et al. [6] devised a unique and electrochemical gene detection method named the "DNA sensor", which was based on a graphite electrode supporting the DNA probes without labeling. In the DNA sensor hybridization reaction and gene detection proceed at the same place. It detects a specific gene by measuring the electrochemical signals derived from an intercalator (acridine orange) bound to the specific hybrids formed on the DNA probe-adsorbed-electrode. However, the electrochemical signals derived from acridine orange were small, and acridine orange bound not only to the formed hybrids (double stranded DNAs; dsDNAs) but also to the probes on the electrode (single stranded DNAs; ssDNAs) or to the surface of the electrode directly through physical adsorption. These non-specific bindings are considered to decrease the sensitivity of the DNA sensor. Thus, the properties of the intercalators are very important for the DNA sensor to detect a gene specifically with high sensitivity.

The electrochemical properties of commercially available intercalators is reported in this

Correspondence to: K. Hashimoto, Materials and Devices Research Laboratories, Research and Development Center, Toshiba Corporation, 1, Komukai Toshiba-cho, Saiwai-ku, Kawasaki 210 (Japan).

SSDI 0003-2670(93)E0565-O

article in order to select an optimum intercalator for the DNA sensor.

EXPERIMENTAL

Materials

Acridine orange hydrochloride, 7-aminoactinomycin D, and ethidium homodimer were purchased from Molecular Probe Inc. Vinblastine sulfate, minocycline hydrochloride, doxycycline hydrochloride, daunomycin hydrochloride, tetracycline hydrochloride, chlortetracycline hydrochloride, doxorubicin hydrochloride, pirarubicin, aclarubicin hydrochloride, chromomycin A_3, rifampicin, quinacrine mustard dihydrochloride, bleomycin hydrochloride, and 4′,6-diamidino-2-phenylindole dihydrochloride (DAPI) were purchased from Wako. Propidium iodide, ethidium monoazide bromide, 2′-(4-ethoxyphenyl)-5-(4-methyl-1-piperazinyl)-2,5′-bi-1*H*-benzimidazole trihydrochloride (Hoechst 33342), and 2′-(4-hydroxyphenyl)-5-(4-methyl-1-piperazinyl)-2,5′-bi-1*H*-benzimidazole trihydrochloride (Hoechst 33258) were obtained from Funakoshi. Tris(phenanthrolin)rutenium [$Ru(phen)_3$] and tris(phenanthrolin)iron [$Fe(phen)_3$] were obtained from Aldrich. 1-Ethyl-2-[3-(ethylnaphtho[1,2-*d*]thiazolin-2-ylidene)-2-methylpropenyl]naphthol[1,2-*d*]-thiazolium bromide (stains-all), 9-aminoacridine hydrochloride, olivomycin and mithramycin A were purchased from Sigma. Ethidium bromide was obtained from Bio-Rad Labs. Reagents for oligonucleotide syntheses were all purchased from Applied Biosystems. Other reagents were commercially available or laboratory grade ones. These solutions were prepared with high-purity water ($\rho = 18$ MΩ cm).

Procedure

The electrochemical analyses were performed using an electrochemical analyzer manufactured by Bioanalytical Systems (Model BAS-100B) and a TOSHIBA J-3100 computer system with data storage. All voltammetric experiments were carried out in a double-compartment cell of 500 ml at 25°C [supporting electrolyte; 1/15 M sodium phosphate buffer (pH 7.0), reference electrode; Ag/AgCl (Toa Electronics, Tokyo), counter electrode; Pt flag (4.9 cm^2)]. Linear sweep voltammetry (LSV), and cyclic voltammetry (CV) were examined at a sweep rate of 25 mV/s.

DNA preparation

A model targeted gene, pVM623 containing the Pst I fragment of 1.5-kilobase pair (kbp) of oncogene v-myc, was prepared as described previously [6]. pVM623 was linearized with endonuclease Hin dIII. Both a DNA probe A (5′-TGCA-GTTCCGGTGGCTGATC-3′), which was complementary to the 3′ end of v-myc, and a DNA probe B (5′-GATCGCCACCGGAACTGCA-3′), which was complementary to probe A, were synthesized with a DNA synthesizer (Applied Biosystems; Model 391 PCR-MATE EP), and purified with NAP columns (Pharmacia). The concentrated stock solutions were stored in a 10 mM Tris–HCl (pH 8.0)–1 mM EDTA solution denoted as TE buffer at 4°C.

Preparation of the DNA sensor

The synthesized probe A was adsorbed on a polished basal plane pyrolytic graphite (BPPG) electrode (0.2 cm^2) in a solution [10 μg/ml in 100 mM sodium chloride] for 30 min at 100°C. Then, the electrode was washed with distilled water at 100°C to remove any non-adsorbed probes. The details of the experiments for the preparation of the DNA sensor are referred to in a previous paper [6]. The electrodes were stored in the TE buffer at 4°C before use.

Characterization of the intercalators

Individual intercalator solutions (10 μM) were prepared with 1/15 M phosphate buffer (pH 7.0), respectively. Voltammetric experiments were examined using a bare BPPG electrode, the probe A-adsorbed-electrode (ssDNA electrode), and a double stranded DNA-adsorbed-electrode (ds-DNA electrode). The dsDNA electrode was prepared by the following procedure; the ssDNA electrode was immersed into a hybridization buffer [300 mM sodium chloride–30 mM sodium citrate (pH 7.0), denoted as 2 × SSC buffer] containing 1 μg/ml probe B for 1 h at 40°C with

shaking. The specific hybrids (dsDNAs) were formed on the ssDNA electrode.

Gene detection with the DNA sensor

The ssDNA electrode (DNA sensor) was immersed into a 2 × SSC buffer containing heat denatured pVM623. The hybridization reaction was carried out for 1 h at 40°C with shaking (150 rpm). After the reaction, the electrode was washed with distilled water to remove DNAs bound non-specifically. Then, the electrode was immersed into an intercalator solution [10 μM in 10 mM Tris–HCl (pH 8.5)] containing 100 mM sodium chloride in a plastic vessel for 5 min at room temperature under a dark condition, and washed with a 1/15 M phosphate buffer (pH 7.0) for 5 min. The electrochemical signals from the intercalator bound to the hybrids formed on the electrode obtained by LSV were used for the determination of the concentration of pVM623.

TABLE 1

Screening of intercalators[a]

Intercalators [b]	E_{pa} (mV)	i_{pa} (μA)	E_{pc} (mV)	i_{pc} (μA)
Acridine dyes				
9-Aminoacridine	854	1.75	–	–
Acridine orange	830, 96	6.28, 0.52	67	0.70
Anthracycline antibiotics				
Aclarubicin	774, 1049	0.56, 1.94	–	–
Daunomycin	446	2.06	394	0.34
Doxorubicin	440, 711	3.81, 1.29	391	0.41
Pirarubicin	446	1.47	389	0.26
Ethidium dyes				
Ethidium bromide	678, 61	3.39, 0.48	29	0.90
Ethidium homodimer	699	2.97	29	0.28
Ethidium monoazide	563	0.79	−2	0.10
Tetracycline antibiotics				
Chlortetracycline	650, 850	–	–	–
Tetracycline	674	1.88	–	–
Doxycycline	663, 763, 874	2.79, 1.81, 0.35	–	–
Minocycline	385	3.58	155, −85	0.42, 6.40
Bisbenzimide dyes				
Hoechst 33258	586	9.50	–	–
Hoechst 33342	571	3.52	–	–
Others				
7-Aminoactinomycin D	651	1.34	376	0.51
Chromomycin A_3	550	–	–	–
Mithramycin A	510	0.36	–	–
Olivomycin	900	–	–	–
Vinblastine	522, 741	2.30, 4.21	–	–
Propidium iodide	631	4.84	494, 44	1.03, 0.48
Quinacrine mustard	688, 796, 1020	2.54, 0.37, 0.78	−73	0.32
DAPI	806, 45	0.48, 0.12	533, 29	0.17, 0.18
Rifampicin	103, 718	1.20, 3.49	44	0.57
Stains-all	–	–	–	–
Fe $(phen)_3$	–	–	–	–
Ru $(phen)_3$	–	–	–	–

[a] Working electrode, BPPG 0.2 cm^2. Reference electrode, Ag/AgCl. Sweep rate, 25 mV/s. [b] 10 μM in 1/15 M phosphate buffer (pH 7.0).

RESULTS

Characterization of the intercalators

The voltammetric characteristics of the intercalators are summarized in Table 1. Some were electrochemically active when a bare BPPG electrode is used. Daunomycin, doxorubicin, minocycline, vinblastine, propidium iodide, Hoechst 33258 and 33342, which were oxidized at a lower potential, showed high current densities. These intercalators can be expected to amplify signals from a small amount of formed hybrids on the electrode, because oxidation waves from both water and oligonucleotide adsorbed do not affect the signals of the intercalators.

A DNA sensor recognizes the hybrids (dsDNAs) formed on the electrode using an intercalator as an electrochemical probe. Thus, sensitivity depends on the intercalators. The authors consider that an intercalator should be bound to dsDNAs (formed hybrids) more specifically than ssDNAs (adsorbed probes) in order to detect a specific gene with high sensitivity. Bard et al. [7] reported that positive shifts in the peak potential of intercalators were observed in the case of intercalation which was specifically bound to dsDNAs. Thus, the selectivity of the intercalators to dsDNAs was estimated by measuring the difference between the anodic peak potential of the dsDNA-electrode and that of the ssDNA electrode (Table 2). Anodic waves were not observed using minocycline and vinblastine. The peak potentials of Hoechst 33258 and propidium iodide

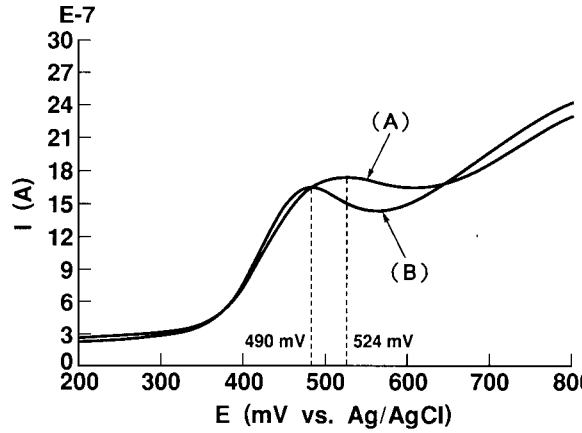

Fig. 1. Linear sweep voltammograms of daunomycin on (A) dsDNAs and (B) ssDNAs adsorbed BPPG electrodes. Sweep rate, 25 mV/s. Daunomycin concentration, 10 μM.

shifted very little. On the other hand, the anodic peak potentials of daunomycin shifted to more positive values in the case of the dsDNA electrode compared with the ssDNA electrode (495 → 529 mV) (Fig. 1). Daunomycin is considered to distinguish between probes and hybrids on the electrode. So, daunomycin was used as the optimal intercalator for the DNA sensor.

Voltammetric experiments on both ssDNAs and dsDNAs electrodes coated with or without stearylamine (1 mM) in ethanol showed that a small amount of daunomycin was adsorbed on the electrode (Table 3). It was not necessary to coat the electrode surface with a lipid to prevent any non-specific adsorption of daunomycin.

TABLE 2

Voltammetric behaviour of intercalators

Intercalator [a]	BPPG [b] E_{pa} (mV)	ssDNA–BPPG [c]		dsDNA–BPPG [d]		ΔE (mV)	Δi (μA)
		E_{pa} (mV)	i_{pa} (μA)	E_{pa} (mV)	i_{pa} (μA)		
Acridine orange	821	–	–	–	–	–	–
Daunomycin	446	490	1.28	524	1.31	34	0.03
Vinblastine	522	–	–	–	–	–	–
Hoechst 33258	576	549	7.43	547	8.4	−2	0.97
Minocycline	385	–	–	–	–	–	–
Propidium iodide	631	544	0.30	548	0.35	4	0.05

[a] Each electrode was immersed into a 10 μM intercalator solution and washed with a phosphate buffer. Voltammetric experiments were examined in a 1/15 M phospate buffer. [b] Bare BPPG electrode. [c] ssDNA (20-mer)-adsorbed BPPG electrode. [d] dsDNA (20-mer)-adsorbed-BPPG electrode.

TABLE 3

Effect of stearylamine coating [a] on non-specific adsorption of daunomycin

Treatment	ssDNA–BPPG [b]		dsDNA–BPPG [c]		ΔE (mV)	Δi (μA)
	E_{pa} (mV)	i_{pa} (μA)	E_{pa} (mV)	i_{pa} (μA)		
Non-coating	490	1.28	524	1.31	34	0.03
Coating	471	0.95	508	1.06	37	0.11

[a] Each electrode was immersed into a stearylamine solution (1 mM in ethanol). [b] ssDNA (20-mer)-adsorbed-BPPG electrode. [c] dsDNA (20-mer)-adsorbed-BPPG electrode.

Gene detection with the DNA sensor

After hybridization, the sensor was immersed into a daunomycin solution, and washed with a phosphate buffer. Linear sweep voltammetry showed that the electric capacity derived from daunomycin increased and the anodic peak potential shifted to more positive values when the DNA sensor was reacted with pVM623 (1 μg/ml), compared with the data in a solution without pVM623. On the other hand, the peak potential hardly shifted when the DNA sensor had reacted with pUC118 (1 μg/ml). The differences in the anodic peak potentials (ΔE_{pa}) were 18 mV (with pVM623) and 3 mV (with pUC118), respectively. ΔE_{pa} was related to the concentration of the targeted DNA (pVM623) in the hybridization reactions ranging from 10^{-8} to 10^{-6} g/ml (Fig. 2).

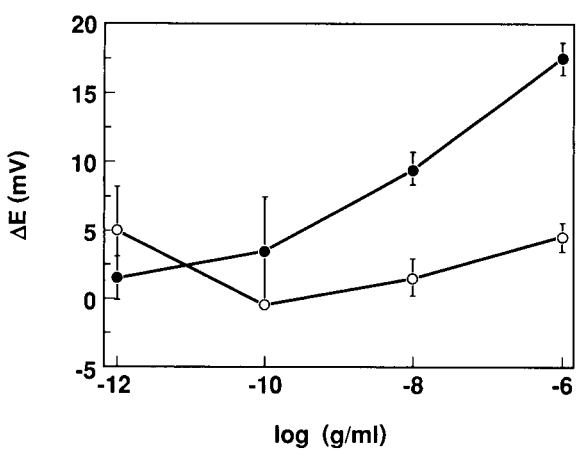

Fig. 2. Calibration curve for (●) targeted DNA pVM623 and (○) pUC118. Hybridization condition; in 2×SSC buffer (see Experimental for detail), 1 h, 40°C.

DISCUSSION

Voltammetric experiments showed that some intercalators were electrochemically active and could distinguish between dsDNAs and ssDNAs. Using daunomycin as an intercalator in the DNA sensor had three merits. First, a small amount of daunomycin was directly adsorbed on the surface of the DNA sensor through physical adsorption. Gene detection could proceed without any coating with a lipid (stearylamine) to prevent the non-specific adsorption of intercalators. Secondly, daunomycin was oxidized on the DNA probe-adsorbed-graphite electrode with a higher current density (6.5 μA/cm^2) than acridine orange (below 1 μA/cm^2). Therefore, the electrochemical signals derived from daunomycin bound to the formed hybrids were easily detected by LSV instead of by more time-consuming differential pulse voltammetry. Thirdly, the electrochemical signals of daunomycin (peak potential ca. 0.5 V) were not influenced by the oxidation waves derived from oxygen and oligonucleotide probes (peak potential ca. 1.0 V) adsorbed on the BPPG electrode. There was no need to oxidize the adsorbed oligonucleotide on the electrode in advance in order to measure clear electrochemical signals from the intercalators. The procedure for the DNA sensor became easier and more convenient by using daunomycin as an intercalator.

The data of the voltammetric experiments using both the ssDNA and dsDNA electrode showed the type of binding of the intercalators. Bard and co-workers [7–9] reported that positive shifts of the peak potential were observed in the binding form via hydrophobic interactions (intercalation) while electrostatic interactions led to negative shifts. Vinblastine and minocycline are considered not to combine either to dsDNAs or to ssDNAs. Hoechst 33258 is considered to attach more specifically to dsDNAs than ssDNAs, because the anodic peak current of Hoechst 33258 in the dsDNA electrode was larger than that of the ssDNA electrode. On the other hand, the anodic peak potentials shifted very little. In recent studies, some workers have reported that Hoechst 33258 recognized adenine–thymine rich sequences of double-stranded DNAs within the

minor groove of the helix [10]. In the case of daunomycin and propidium iodide, they were bound both to dsDNAs by intercalation and to ssDNAs by electrostatic interactions [11–13]. However, the shift value of the peak potential derived from daunomycin bound to dsDNAs was larger than that of propidium iodide. The reason for the larger values of daunomycin is unclear.

The peak potential shifts of the intercalators bound to DNAs via hydrophobic interactions (intercalation) were also examined. The peak potential shifts of the examined intercalators were considered to reflect the selectivity to dsDNAs except for Hoechst 33258. Therefore, the selectivity of intercalators to dsDNAs was estimated indirectly by measuring their anodic peak potential shifts. Hoechst 33258 did not influence the peak potential. The selectivity of Hoechst 33258 to dsDNAs must be estimated by measuring the anodic peak current instead of the peak potential shift.

Daunomycin, which was oxidized at a low potential and showed a high current density, was not related to high-sensitivity. Better intercalators suitable for the DNA sensor to detect specific genes with high-sensitivity are being looked for.

Using daunomycin as electrochemical probe, the DNA sensor can become a quick and convenient use for determining genes specifically. The successful development of this sensor for detecting genes may markedly facilitate the understanding of human pathological conditions.

REFERENCES

1 K. Jacobs, S.F. Wolf, L. Haines, J. Fisch, J.N. Kremsky and J.P. Dougherty, Nucleic Acid Res., 15 (1987) 2911.
2 R.H. Symons, N. Habili and J.L. McInnes, J. Virol. Methods, 23 (1989) 299.
3 G. Gentilomi, E. Ferri and S. Girotti, Anal. Chim. Acta, 255 (1991) 387.
4 Y.W. Kan and F.F. Chehab, Proc. Natl. Acad. Sci. USA, 86 (1989) 9178.
5 H.A. Erlich, R.K. Saiki, P.S. Walsh and C.H. Levenson, Proc. Natl. Acad. Sci. USA, 86 (1989) 6230.
6 K. Hashimoto, K. Miwa and Y. Ishimori, Supramol. Chem., 2 (1993) 265.
7 A.J. Bard, M.T. Cater and M. Rodoriguez, J. Am. Chem. Soc., 111 (1989) 8901.
8 A.J. Bard and M.T. Cater, J. Am. Chem. Soc., 109 (1987) 7528.
9 A.J. Bard and M. Rodoriguez, Anal. Chem., 62 (1990) 2658.
10 J. Portugal and M.J. Waring, Biochim. Biophys. Acta, 949 (1988) 158.
11 G.J. Quigley, A.H.-J. Wang, G. Ughetto, G. van der Marel, J.H. van Boom and A. Rich, Proc. Natl. Acad. Sci. USA, 77 (1980) 7204.
12 E.J. Gabbay, D. Grier, R.E. Fingerle, R. Reimer, R. Levy, S.W. Pearce and W.D. Wilson, Biochemistry, 15 (1976) 2062
13 K.H. Jones and J.A. Senft, J. Histochem. Cytochem., 33 (1985) 77.

Analytica Chimica Acta, 286 (1994) 225–232
Elsevier Science B.V., Amsterdam

Construction and design of a gas-sensing detector capable of handling and determining sulphur- and phosphorus-containing gaseous samples

M. Pakniat, N. Maleki and A. Safavi

Department of Chemistry, Faculty of Sciences, Shiraz University, Shiraz (Iran)

(Received 25th March 1993; revised manuscript received 16th May 1993)

Abstract

A gas-sensing detector based on molecular emission cavity analysis employing a flame-containing cavity was devised. The requirements for handling, reproducible sampling and continuous monitoring of air were investigated. SO_2 and PH_3 were selected as representative sulphur and phosphorus compounds. As little as 24 ng of sulphur and 0.1 ng of phosphorus in gaseous samples (7 ml) can be detected.

Keywords: Sensors; Air; Emission spectrometry; Gas-sensing detector; Molecular emission cavity analysis; Phosphorus; Sulphur

Numerous methods have been developed for determining sulphur and phosphorus compounds in various samples [1–9], but there is still a great need for rapid detection, handling, standardization, quantification and continuous monitoring of gaseous samples or aerosols containing sulphur and phosphorus compounds. Sulphur dioxide and phosphine gases were selected as representative sulphur and phosphorus compounds. Molecular emission cavity analysis (MECA) using a flame-containing cavity was utilized. S_2 and HPO emissions were measured at 384 and 528 nm, respectively. Some parameters such as hydrogen, air, nitrogen and water flow-rates affect the emission intensity and should be optimized for efficient performance of the device.

Correspondence to: A. Safavi, Department of Chemistry, Faculty of Sciences, Shiraz University, Shiraz (Iran).

EXPERIMENTAL

Reagents

Unless stated otherwise, all solutions were prepared from analytical-reagent grade chemicals and triply distilled water.

A stock standard solution (0.1 mg ml^{-1}) of sulphur as sulphite was prepared daily by dissolving 0.0197 g of anhydrous sodium sulphite in water. After addition of 0.0184 g of EDTA and 0.0200 g of NaOH, the solution was diluted to 50 ml with water. This solution was standardized by iodimetric titration. A stock standard solution of potassium permanganate (0.02 M) was prepared by dissolving 0.8180 g of $KMnO_4$ in water and diluting to 250 ml. A stock standard solution of oxalic acid was prepared by dissolving 1.5758 g of $C_2H_4O_4 \cdot 2H_2O$ in water. After addition of 60 ml of sulphuric acid (1 + 1), the solution was diluted to 250 ml.

Sulphur dioxide was purchased from Fluka (5-l

SSDI 0003-2670(93)E0556-M

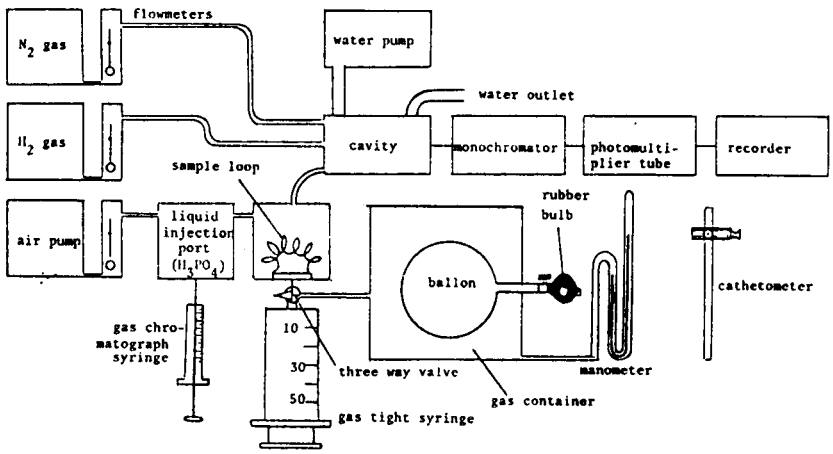

Fig. 1. Assembly for monitoring SO_2 samples.

cylinder of pure SO_2). Phosphine was generated by treatment of aluminium phosphide with water. Aluminium phosphide was obtained from commercial tablets containing 56% (w/w) aluminium phosphide (Celphos, Excel Industries, India). Pure, dry phosphine is spontaneously flammable in air. Moist but otherwise pure phosphine does not ignite when mixed with air at atmospheric pressure and temperature; if the pressure is reduced, the mixture explodes. Phosphine that contains a small percentage ($> 0.2\%$) of P_2H_4 is spontaneously flammable and this is the reason for self-ignition of the gas prepared by the action of water on commercial metallic phosphides. Phosphine is a highly toxic gas and special care is needed in handling zinc, calcium, magnesium,

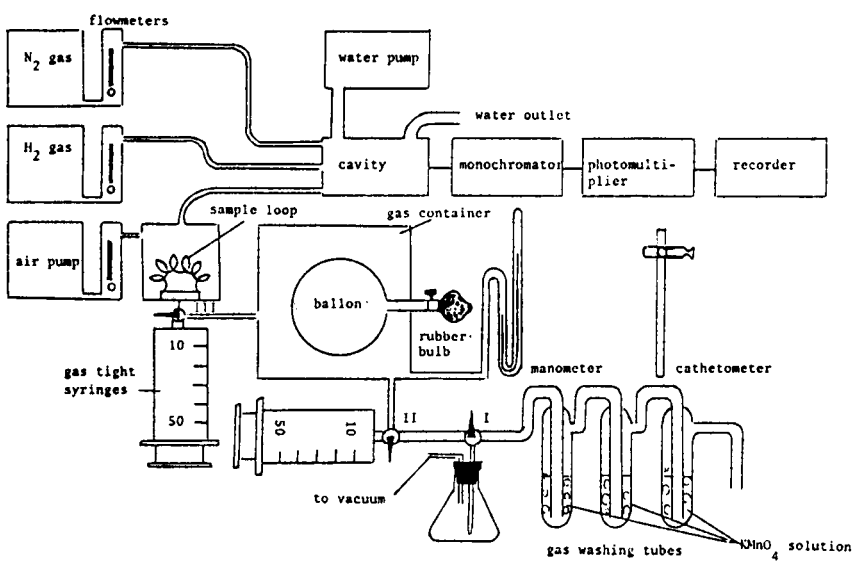

Fig. 2. Assembly for monitoring PH_3 samples.

aluminium and sodium phosphides, which react with moisture and evolve phosphine.

Apparatus

Schematic diagrams of the present version of the instrument for measurements of SO_2 and PH_3 are shown in Figs. 1 and 2. The cavity used for these studies was a flame-containing type [1,10,11], the structure of which is shown in Fig. 3. The cavity was made from stainless steel; a water cooling section surrounded the cavity and three stainless-steel gas tubes were introduced tangentially into the cavity. The diameter of the cavity was 0.25 in and its depth was 0.5 in. The length and diameter of the cylindrical stainless steel for making all of these compartments were each 1 in. The volume of the sample loop was 7 ml.

For SO_2 measurements, SO_2–air samples were injected into the cavity. The S_2 emission was viewed through the slit of an optical part of a Beckman Model B UV–visible spectrophotometer that included the following: replacement of the standard phototube with a circular-cage multiplier structure in a side-on photomultiplier tube (American Instrument, Silver Spring, MD) (700 V operating voltage) and replacement of the lamp housing with the flame-containing cavity compartment. The slit width was 15 nm for intensity measurements and 1 nm for obtaining S_2 and HPO spectra. The emission peaks were recorded on a Shimadzu Chromatopack C-R3A connected to the output of the photomultiplier tube. A cathetometer (Precision Tool and Instrument, Surrey) was used for the precise control of the pressure inside the standard SO_2–air gaseous sample container. For standardizing the gaseous samples, standard sample solutions of sodium sulphite (5–50 μl) were injected into 3 M orthophosphoric acid through a rubber septum in the liquid injection port.

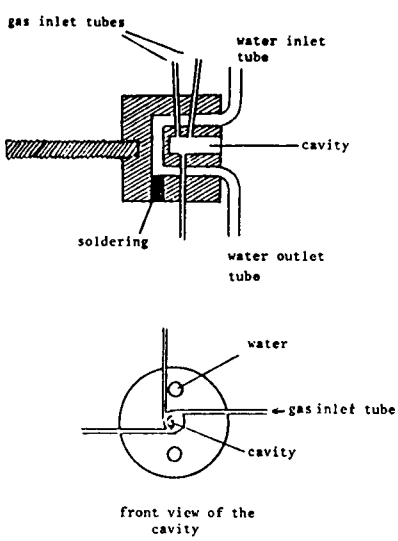

Fig. 3. Flame-containing cavity.

For PH_3 measurement the instrument was mainly that which was used for SO_2, except that the liquid injection port was omitted and a series of gas washing tubes for standardizing the PH_3 content of the sample were added.

Recommended procedure

Figure 1 shows schematically the design used for standardization and subsequently the investigation of S_2 emission. The liquid injection port contains 3 M orthophosphoric acid. Injection of a known volume of standard sulphite solution into this part generates an equivalent amount of SO_2 gas which was swept by a stream of air into the cavity and the resulting emission was recorded. For standardizing an SO_2–air sample, about 3–5 times the volume of the sample loop was taken by means of a gas-tight syringe and at the same time the pressure inside the container was adjusted utilizing the rubber bulb. Expansion of the balloon inside the container compensates for the pressure drop (2 mmHg) resulting from taking samples. By utilizing the cathetometer the pressure can be readjusted with a precision of about 0.01 mmHg. After passing the contents of the syringe through the loop while the rotary valve was in the loading state, the sample was injected into the air stream by means of the latter. The whole process was repeated several times and by comparing the average peak area resulting from the SO_2–air samples the concentration of the sample was established. Figure 4 shows the MECA responses for such a standardization.

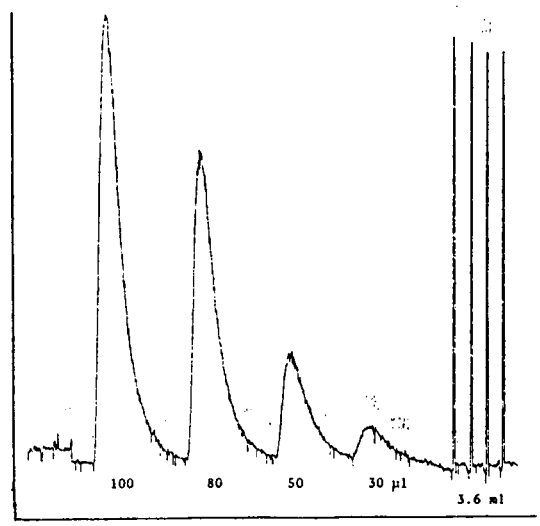

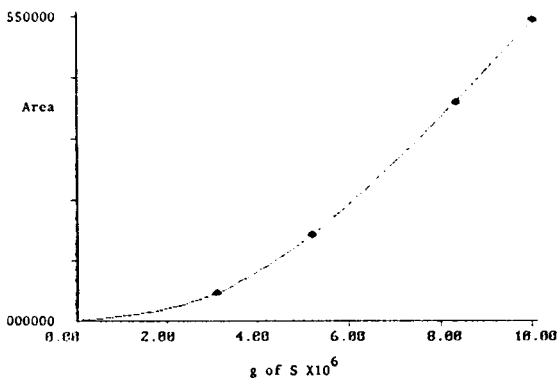

Fig. 4. MECA responses and calibration graph for SO_2 in gaseous SO_2–air samples. Flow-rates: air, 54.5; H_2, 280; N_2, 129; H_2O, 4.8 ml min^{-1}.

To determine the amount of PH_3 in a gaseous sample, two methods were used. The first method was based on the procedure presented by the ISI (Indian Standard Institution) [12]. A known volume of standard potassium permanganate solution (20 ml of 0.02 M $KMnO_4$) was added to three absorption tubes (Fig. 2). By the gas-tight syringe (1) and employing valves I and II appropriately, 50 ml gaseous samples were successively injected through the absorption tubes until a change was observed in the colour of the potassium permanganate solution. The pressure of the container was readjusted to the laboratory pressure simultaneously within the injections. The solution in the absorption tubes was then sucked into a conical flask. A known volume of standard oxalic acid solution was added to the absorption tubes. After shaking the tubes to dissolve all the manganese dioxide, the washing solution was added to the conical flask. This step was repeated using water, and the latter was also added to the conical flask. The contents of the flask were heated to ca. 60°C and the excess oxalic acid was titrated with standard potassium permanganate solution.

As the standardization step for gaseous phosphine samples was time consuming, a second method for generating phosphine from aqueous solutions [6,7] was selected. Here an appropriate amount of phosphate was placed in a sample

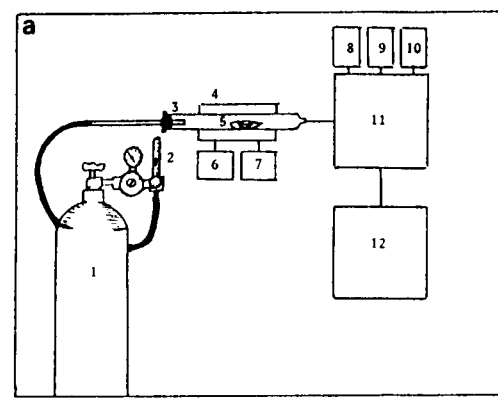

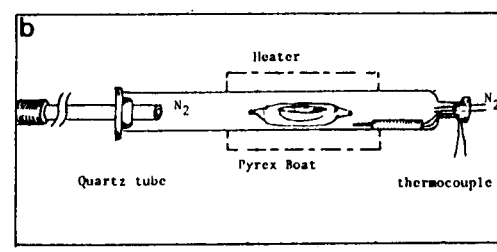

Fig. 5. Phosphine generation system. (a) Diagram of hydride generation system followed by MECA detection. 1 = N_2 cylinder; 2 = flow meter; 3 = reaction tube; 4 = heater; 5 = Pyrex boat; 6 = slide transformer; 7 = thermocouple; 8 = hydrogen gas cylinder; 9 = air pump; 10 = water peristaltic pump; 11 = MECA assembly; 12 = recorder. (b) Design of reaction tube and boat.

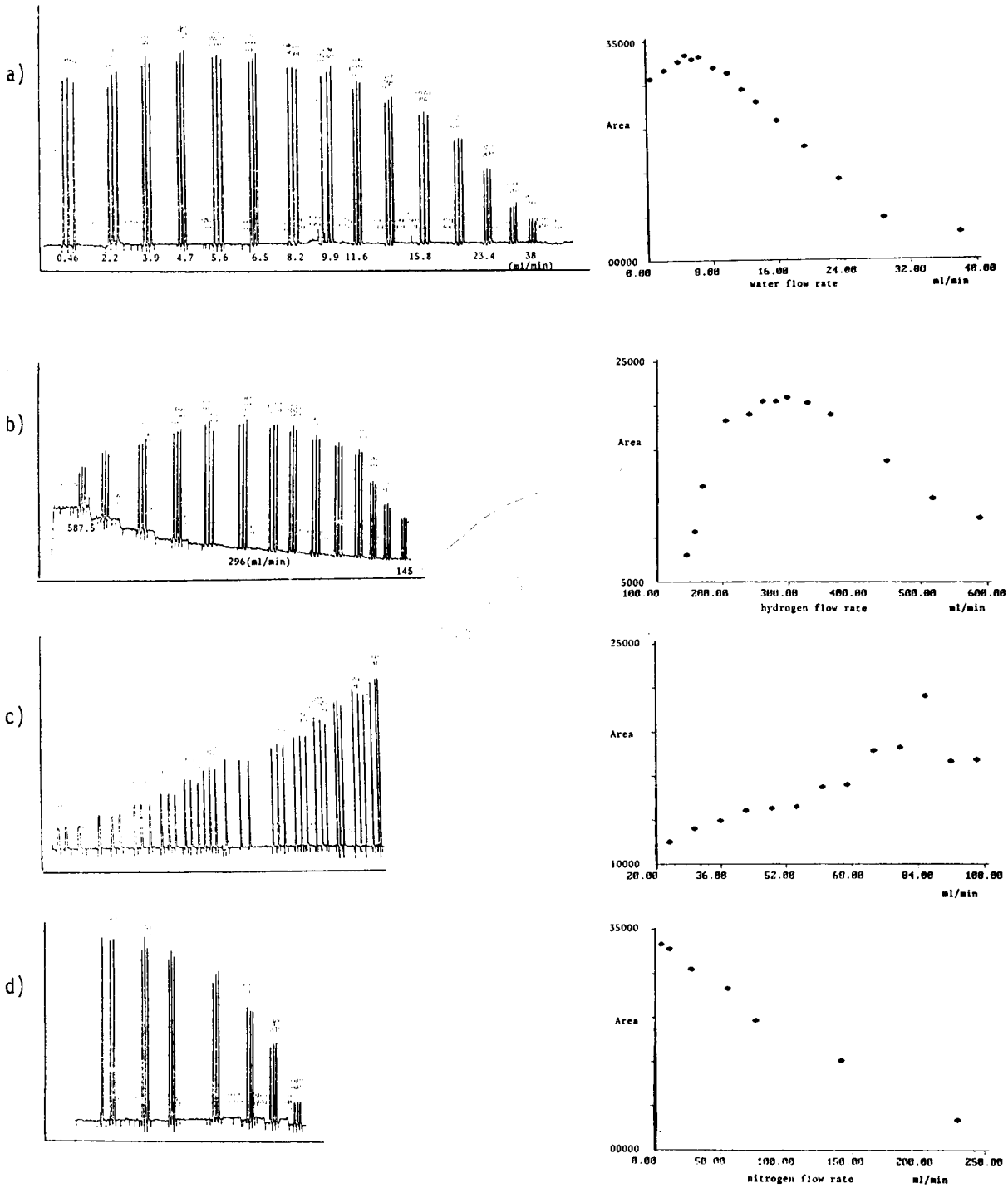

Fig. 6. Effects of (a) water, (b) hydrogen, (c) air and (d) nitrogen flow-rates on S_2 emission. Air flow-rate: (a), (b) 54.5; (c) variable; (d) 86 ml min^{-1}. H_2 flow-rate: (a) 280; (b) variable; (c), (d) 296 ml min^{-1}. N_2 flow-rate: (a)–(c) 129 ml min^{-1}; (a) variable. Water flow-rate: (a) variable; (b)–(d) 4.8 ml min^{-1}.

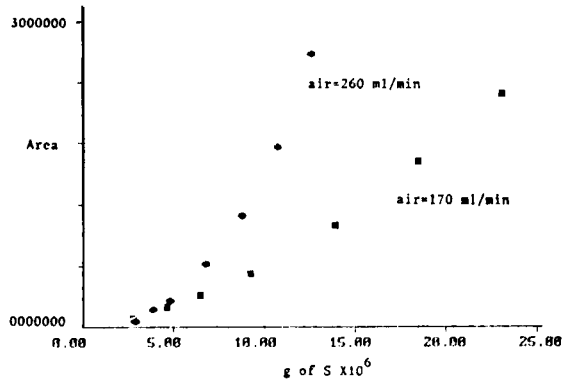

Fig. 7. Effect of air flow-rate on calibration graph.

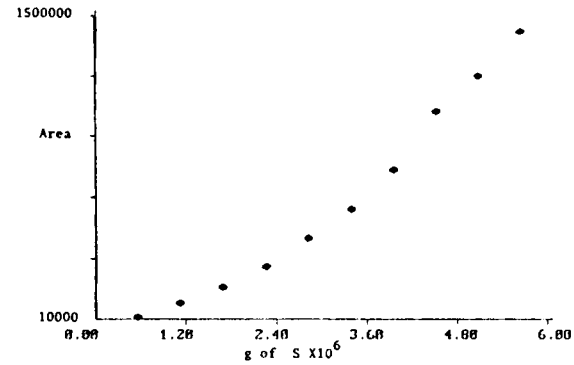

Fig. 8. Calibration graph for SO_2 at high sensitivity. Flow-rates: air, 353; H_2, 517; H_2O, 8.2 ml min^{-1}.

vessel and completely dried, then 100 μl of 6% sodium tetrahydroborate solution were added and the mixture was again dried below 45°C in an oven for 2 h or alternatively under an incandescent light. The dried mixture was inserted into a phosphine generation tube made of quartz (Fig. 5), heated to 480–500°C by a cylindrical Nichrome heater whose temperature was controlled and monitored by a thermocouple connected to a digital voltmeter. Nitrogen was used as the carrier gas for the generated phosphine.

RESULTS AND DISCUSSION

The emission spectra of S_2 and HPO obtained by successive injection of gaseous SO_2 and PH_3 samples and measuring the emissions at different wavelength were in good agreement with the spectra reported in other studies [2]. The optimum wavelengths for measurements of S_2 and HPO emissions, were chosen as 384 and 528 nm, respectively.

Figure 6 shows the effect of water and gas flow-rates on S_2 emission in the operational limits of the design. During exploration of the optimum conditions, it was observed that at high flow-rates of water, some deposition of sulphur compounds occurred at the cavity wall. This caused the appearance of a high response when the water flow-rate was decreased. This was not unexpected, because at high water flow-rates the cold cavity wall facilitates the deposition of some sulphur compounds inside the cavity. On the other hand, when the water flow-rate is decreased and the cavity wall becomes hotter, evaporation of the deposited sulphur becomes feasible and thus an abnormally high response is observed.

The results show that at optimum water, hydrogen and air flow-rates the presence of nitrogen in the flame greatly suppressed the emission. Figure 7 shows the effect of changes in the air flow-rate on the calibration graph at constant water and hydrogen flow-rates. It can be concluded that increasing the air flow-rate increases the rate of introduction of the SO_2 sample into the cavity and thus higher sensitivity is obtained. Some operational difficulties restrict an unlimited increase in the air flow-rate, e.g., splashing of acid solution through the liquid injection port and the great difference between the air flow-rates when the rotary valve is in the injection position and when it is in the loading position, which causes a great pressure drop between the loading and injection steps, in some cases extinguishing the flame inside the cavity. Considering

Fig. 9. Effects of (a) water, (b) air, (c) hydrogen and (d) nitrogen flow-rates on HPO emission. Air flow-rate: (a), (c), (d) 160 ml min^{-1}; (b) variable. H_2 flow-rate: (a), (b) 312; (c) variable; (d) 222 ml min^{-1}. N_2 flow-rate: (a)–(c) 113 ml min^{-1}; (d) variable. H_2O flow-rate: (a) variable, (b)–(d) 17 ml min^{-1}.

a)

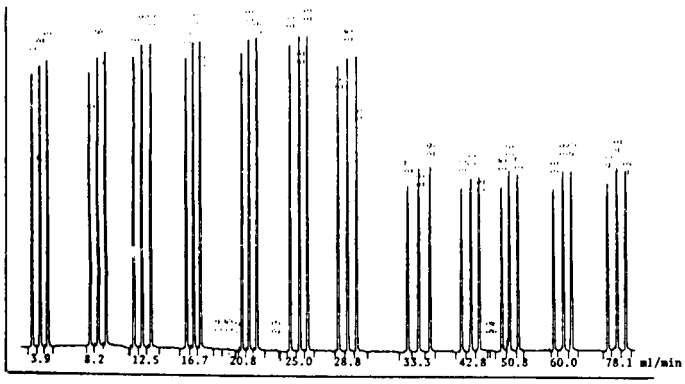
3.9
8.2
12.5
16.7
20.8
25.0
28.8
33.5
42.8
50.8
60.0
78.1 ml/min

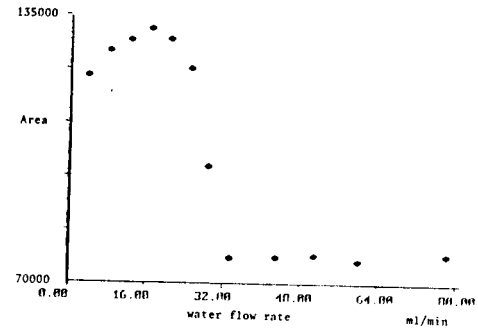
135000
Area
70000
0.00
16.00
32.00
40.00
64.00
80.00
water flow rate
ml/min

b)

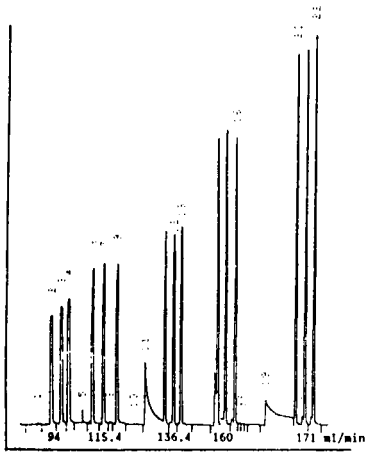
94
115.4
136.4
160
171 ml/min

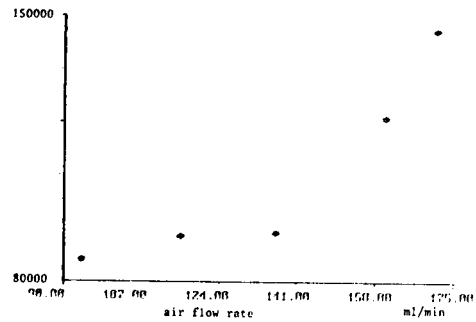
150000
80000
107.00
124.00
141.00
158.00
air flow rate
ml/min

c)

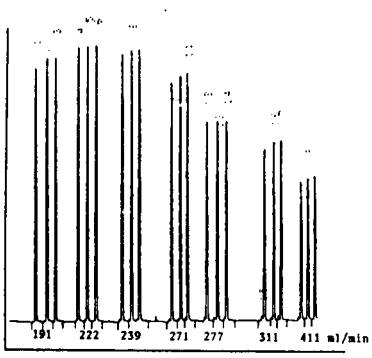
191
222
239
271
277
311
411 ml/min

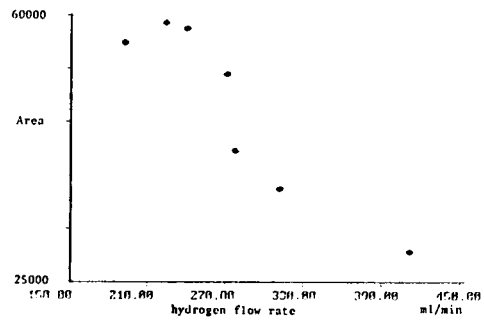
60000
Area
25000
210.00
270.00
330.00
390.00
hydrogen flow rate
ml/min

d)

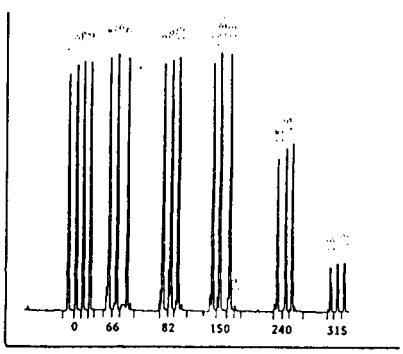
0
66
82
150
240
315

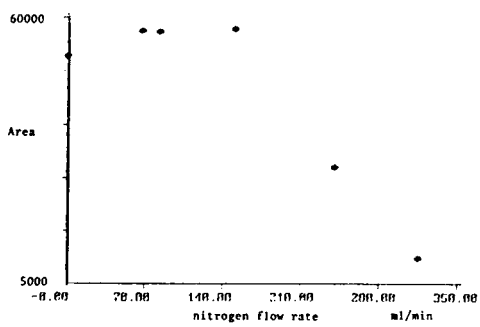
60000
Area
5000
-8.00
78.00
148.00
218.00
288.00
nitrogen flow rate
ml/min

the points discussed above the conditions for obtaining the highest sensitivity at the maximum air flow-rate were optimized. Figure 8 shows the calibration graph obtained at the optimized water and gas flow-rates.

Under the optimum conditions with respect to air, hydrogen and water flow-rates, the reproducibility of successive injection of a gaseous SO_2 sample (7 ml of 0.775 μg ml^{-1} S) was investigated. The relative standard deviation for twelve successive injections was 0.71%.

Defining the detection limit as the amount of sulphur which gives a signal equal to $X + 3s$, where X is the average of the background signal and s is the standard deviation of the background, the detection limit of the method was 24 ng of sulphur in gaseous samples (7 ml).

Figure 9 shows the effect of water and gas flow-rates on the HPO emission. The water flow-rate has a slight enhancing effect on the HPO emission at lower flow-rates but suppresses the emission at higher flow-rates. The intensity of the emission increased as the rate of introduction of air into the cavity was increased. The hydrogen flow-rate shows an optimum and the nitrogen flow-rate suppresses the emission at high flow-rates. As with sulphur dioxide, increasing the rate of introduction of gaseous samples into the cavity increases the concentration of the emitting species and intensifies the emission. The calibration graph obtained was linear.

The relative standard deviation of twelve successive injections of 20 ng ml^{-1} P was 1.3% and the detection limit of the method was 0.112 ng P in gaseous samples (7 ml).

The above results together with the rapid response time of the method, which is characteristic of MECA systems, make the method potentially useful in various industrial fields.

The authors are indebted to Shiraz University Research Council for support of this work.

REFERENCES

1 M. Burguera, S.L. Bogdanski and A. Townshend, CRC Crit. Rev. Anal. Chem., 10 (1980) 185.
2 S.L. Bogdanski, Ph.D. Thesis, Birmingham University, Birmingham (1973).
3 M.C. Bowman and M. Beroza, Anal. Chem., 40 (1968) 1448.
4 R.K. Stevens and A.E. O'Keefe, Anal. Chem., 42 (1970) 143A.
5 Th.A. Kouimtzis, Anal. Chim. Acta, 88 (1977) 303.
6 S. Hashimoto, K. Fujiwara, K. Fuwa, Anal. Chem., 57 (1985) 1305.
7 K. Fujiwara, T. Kanchi, S.I. Tsunura and T. Kumamaru, Anal. Chem., 61 (1989) 2699.
8 N. Grekas and A.C. Calokerinos, Anal. Chim. Acta, 173 (1985) 311.
9 N. Grekas and A.C. Calokerinos, Analyst, 110 (1985) 335.
10 S.L. Bogdanski, E. Henden and A. Townshend, Anal. Chim. Acta, 116 (1980) 93.
11 A. Celik and E. Henden, Analyst, 114 (1989) 563.
12 Indian Standard Institution IS, 6438 (1972) CM/L-5067.

Analytica Chimica Acta, 286 (1994) 233–239
Elsevier Science B.V., Amsterdam

Hexadecylpyridinium chloride micelles for the kinetic determination of sulphur-containing compounds by their induction of the iodine–azide reaction

M.L. Lunar, S. Rubio and D. Pérez-Bendito

Department of Analytical Chemistry, Faculty of Sciences, University of Córdoba, 14004 Córdoba (Spain)

(Received 13th April 1993; revised manuscript received 8th October 1993)

Abstract

The potential use of the association formed by triiodide ion and hexadecylpyridinium chloride (cetylpyridinium chloride, CPC) for the determination of sulphur-containing compounds, which act as inductors for the iodine–azide reaction was investigated. Triiodide ion interacts with CPC cationic micelles, which results in maximum absorption at 500 nm in addition to a substantially increased absorptivity and stability constant of the triiodide complex. The micellar medium allows the determination of reduced glutathione, tetramethylthiuram disulphide and ethylenebisdithiocarbamic acid (zineb) in the ranges $(2–10) \times 10^{-7}$ M, $(8–63) \times 10^{-9}$ M and 40–450 ng ml^{-1}, respectively, with detection limits (3σ) for the three inductors of 0.7×10^{-7} M, 5.4×10^{-9} M and 32 ng ml^{-1}, respectively. The presence of the surfactant allows one to determine lower concentrations of tetramethylthiuram disulphide, reduced glutathione and zineb by factors of 51, 32 and 2.5 respectively, relative to the aqueous medium. The proposed method has been applied to the determination of reduced glutathione in whole blood samples and to the fungicide tetramethylthiuram disulphide present in a commercial formulation used in agriculture.

Keywords: Kinetic methods; Blood; Hexadecyl pyridinium chloride; Iodine; Micelles; Sodium azide; Sulphur

The reaction between sodium azide and iodine, $2NaN_3 + I_2 \rightarrow 3N_2 + 2NaI$, is induced by substances containing sulphur in oxidation state $-II$ and has been extensively used for the determination of inorganic anions (e.g., sulphide [1], thiocyanate [2] and thiosulphate [3]), dithiocarbamates [4], thiolamino acids (e.g., cysteine [5] and reduced glutathione [6]), thioureas [7], thiuram disulphides [8] and thiophosphoryl compounds [9]. For quantitative purposes, the reaction is usually monitored by measuring the iodine consumed photometrically at 350 nm [1,9]. Alternatively, it can be followed by direct-injection enthalpimetry [11], dual photometric–thermometric detection [12] or biamperometry [13].

Applications based on the photometric detection of triiodide, though very simple and rapid, have certain drawbacks stemming from the poor spectral features of the triiodide complex in aqueous media (viz. maximum absorbance at 350 mn and a relatively low absorptivity). Measurements at such a short wavelength pose serious problems in analysing many samples which absorb significantly in this spectral region. Extraction of excess unreacted iodine into carbon tetrachloride and photometric measurement of this solution (maximum absorbance at 525 nm) avoids this problem, but the procedure involved is rather cumbersome and results in poor sensitivity (the molar absorptivity of iodine in carbon tetrachlo-

Correspondence to: D. Pérez-Bendito, Department of Analytical Chemistry, Faculty of Sciences, University of Córdoba, 14004 Córdoba (Spain).

SSDI 0003-2670(93)E0564-N

ride is 895 l mol^{-1} cm^{-1}) [5]. Therefore, developing improved methods for the spectrophotometric monitoring of the triiodide ion could be of interest to the determination of divalent sulphur-containing compounds.

In this work, cetylpyridinium chloride (CPC) micelles were used as simple means of enhancing the sensitivity and selectivity of determinations based on the reaction between iodine and azide. It has been found [14] that, at CPC surfactant concentrations slightly above its critical micellar concentration, triiodide ion undergoes a bathochromic shift from 350 to 500–530 nm, depending on the experimental conditions used, in addition to a substantial increase in its stability constant [$(5.4 \pm 0.2) \times 10^4$ mol^{-1} l, i.e., ca. 50 times that in water] and absorptivity (molar absorptivity values of ca. 6.51×10^4 l mol^{-1} cm^{-1}, i.e., ca. 3 times that in water have been found by us in the determination of hydroperoxides). These effects may allow one to minimize the selectivity and sensitivity problems which confront many of the original photometric procedures involving aqueous media for monitoring iodine.

In order to check the use of the triiodide–CPC system for the determination of divalent sulphur compounds based on their induction of the reaction between iodine and azide, reduced glutathione, tetramethylthiuram disulphide (used as a fungicide, pesticide, antioxidant and medical drug) and zineb (a dithiocarbamate used as pesticide) were chosen as test materials. The triiodide–CPC association permitted us to develop a straightforward, fast kinetic method for determining low concentrations of the tested analytes.

EXPERIMENTAL

Apparatus and reagents

Spectrophotometric measurements were performed on a Hitachi U-2000 spectrophotometer fitted with cells of 1-cm pathlength. The spectrophotometer cell compartment was thermostated by circulating water from a Neslab RTE bath with a temperature stability of ± 0.1°C.

All reagents used were of analytical grade and used as received. Bidistilled water was used throughout. A stock solution of glutathione (5×10^{-4} M) was prepared by dissolving 0.0154 g of reduced glutathione (Sigma) in 100 ml of bidistilled water. A 150 μg ml^{-1} stock solution of zineb was made by dissolving 0.0150 g of ethylenebis dithiocarbamic acid as zinc salt (Chem Service) in 100 ml of 0.12 M hydrochloric acid. A tetramethylthiuram disulphide stock solution (6.41×10^{-4} M) was made by dissolving 0.0154 g of this compound (Aldrich) in 100 ml of ethanol. These solutions were prepared weekly. Solutions of lower concentration were prepared by appropriate dilution in bidistilled water. The sodium azide solution (0.5 M) was made from sodium azide (Merck) and adjusted to pH 6 with hydrochloric acid. A 0.4 M aqueous solution of potassium iodide (Merck) was prepared and stored in the dark as usual to avoid photochemical reaction. Aqueous solutions of potassium iodate (9.2×10^{-4} M, Fluka), CPC (1.4×10^{-3} M, Serva), sulphuric acid (0.5 M), and sodium hydroxide (0.5 M) were also prepared. The deproteinization of human blood samples was carried out with a precipitating solution made by mixing 4.014 g of trichloroacetic acid with 20.0 g of sodium chloride and bringing to 100 ml with bidistilled water.

Procedure for the kinetic photometric determination of reduced glutathione, zineb or tetramethylthiuram disulphide

To a 10-ml standard flask were added, in sequence, 1 ml of CPC (1.4×10^{-3} M), 0.1 ml of potassium iodate (9.2×10^{-4} M), 0.4 ml of sulphuric acid (0.5 M), 4.5 ml of bidistilled water and 40 μl of potassium iodide (0.4 M). The mixture was kept at 20°C for 2 min in order to permit complete generation of triiodide ion, which associates to CPC micelles. Then, 0.8 ml of sodium hydroxide (0.5 M) (final pH 6.4), 2.8 ml of sodium azide (0.5 M) and appropriate volumes of the analyte solution were added. The final analyte concentration was comprised between 2×10^{-7} M and 1×10^{-6} M glutathione, 40 and 450 ng ml^{-1} zineb or 8.1×10^{-9} and 6.3×10^{-8} M tetramethylthiuram disulfide. The stop-clock was started and the solution was diluted to the mark with water. An aliquot of the reaction mixture was transferred to a thermostated cell at 20 ±

0.1°C and the absorbance at 500 nm was recorded as a function of time. Measurements were made exactly 45 s after addition of glutathione or zineb, and 105 s after addition of tetramethylthiuram disulphide. A standard blank containing no analyte was prepared similarly for each series of samples and the resulting absorbance was subtracted from that yielded by the samples.

Determination of reduced glutathione in human blood samples

To 0.2 ml of whole blood, anticoagulated with disodium EDTA, were added 1.8 ml of bidistilled water and 3.0 ml of precipitating solution. The mixture was allowed to stand for 5 min at room temperature and then filtered through coarse-grade filter paper. Aliquots of the filtrate (50–100 μl) were then used for the kinetic spectrophotometric determination of glutathione by using the procedure described above. In order to remove the interference due to iodine reductants of blood samples (e.g., glucose), blank determinations in the absence of azide (blood blank), by using the same volume of blood as in samples (50–100 μl), were made. The absorbance signal corresponding to the inductor effect of the glutathione (GSH) present in the blood samples was calculated from the equation:

$$A(\mathrm{GSH}) = \Delta A_{\text{blood sample}} - \Delta A_{\text{blood blank}} - \Delta A_{\text{standard blank}}$$

where $\Delta A_{\text{blood sample}}$, $\Delta A_{\text{blood blank}}$ and $\Delta A_{\text{standard blank}}$ were obtained by subtracting the resulting absorbance yielded by a solution containing triiodide ion and CPC in sulphuric acid medium (prepared according to the procedure specified for the kinetic photometric determination of glutathione) from those yielded by the blood sample, blood blank and standard blank, respectively. The GSH concentration of the blood sample was determined by interpolation of this absorbance signal in the glutathione calibration graph.

Determination of tetramethylthiuram disulphide (thiram) in commercial formulations

An amount of commercial formulation (containing 80% of active ingredient) of at least 20 mg, in order to give assurance that the sample taken is representative of the whole, was weighed accurately into a beaker. The thiram content of the sample was dissolved in about 80 ml of ethanol using a magnetic stirrer for 15 min to aid dissolution. The sample was filtered to remove insoluble material and diluted to 100 ml with ethanol in a volumetric flask. About 0.2 ml of this solution were diluted to 25 ml with bidistilled water before the analysis. 20–40 μl aliquots of this diluted solution were analysed as described in the procedure for the kinetic spectrophotometric determination of thiram.

RESULTS AND DISCUSSION

The reaction between iodine and azide hardly develops in the absence of an inductor. When a sulphur(−II) compound is added, two competitive reactions take place: iodometric and induced. The induced reaction is faster than the iodometric reaction, in which the sulphur(−II) compound is oxidized to a higher oxidation state of sulphur, usually ultimately to sulphonic acid or sulphate, and removed from the cycle of the induced reaction [8].

Conventional analytical determinations based on the oxidative properties of iodine have certain drawbacks stemming from the instability of its solutions (a high volatility, low solubility in aqueous media, photosensitivity, etc.). One potential solution (e.g., in the determination of ascorbic acid [15]) is generating triiodide ion in the reaction medium by using iodate to oxidize iodide. In this work we describe the in situ generation of triiodide for the determination of reduced glutathione, tetramethylthiuram disulphide and zineb by their induction of the reaction between iodine and azide.

Taking into account the overall procedure for the determination of these sulphur(−II) compounds in the presence of CPC micelles, one should consider two steps in optimizing the reaction conditions: generation of triiodide/formation of the triiodide–CPC association, and induction of the triiodide–azide system by sulphur(−II) compounds.

Generation and stability of the triiodide–CPC association

Production of triiodide and simultaneous formation of the triiodide–CPC association was essentially affected by such parameters as pH and the iodide, iodate and CPC concentrations. Figure 1 shows three representative absorbance–time kinetic curves obtained at significant pH values by measuring the absorbance at 500 nm. The pH affected the time at which maximum absorbance was reached (the rate of production of triiodide from iodate and iodide increased with increasing acidity) and the stability of the triiodide–CPC association (it was previously found [10]) that the optimum pH for the formation and stabilization of the triiodide–CPC association is comprised between 2 and 10, whereas a pH of ca. 1 causes it to rapidly degrade). Therefore, the net value of the maximum absorbance signal obtained at 500 nm as a function of pH (Fig. 2A) depended on the rate of production of triiodide ion and on that of the triiodide–CPC association. A pH of 1.4 was chosen as optimal because it allowed rapid obtainment of the maximum absorbance signal, which remained stable long enough to perform reproducible measurements.

The effect of the potassium iodate concentration on the production of triiodide ion was investigated over the range 7.0×10^{-6}–3.0×10^{-5} M. The maximum absorbance obtained varied linearly with the iodate concentration in this interval. The rate of production of triiodide increased with increase in the iodate concentration up to 1.3×10^{-5} M, above which it remained constant. Under these conditions, the reaction completed in 2 min. Iodate concentrations above 2×10^{-5} M resulted in absorbance values greater than 2.0, in addition to precipitation of a cetylpyridinium iodate salt and degradation of the triiodide–CPC association. Therefore, an iodate concentration of 1.5×10^{-5} M in the reaction medium was chosen as optimal.

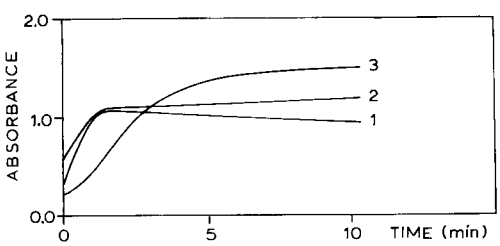

Fig. 1. Kinetic curves for the production of triiodide ion at different pH values. (1) pH 1.0, (2) 1.4, (3) 2.3. Solutions were prepared as described under Experimental.

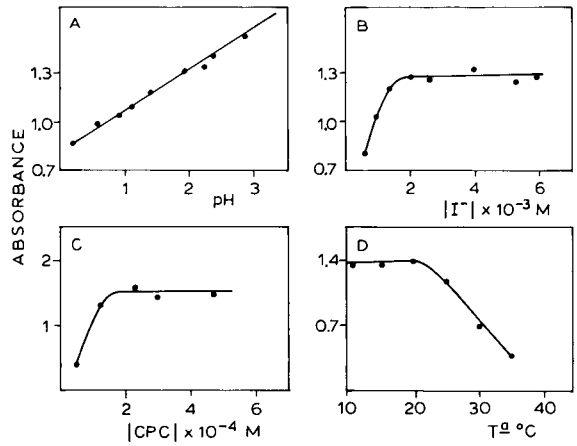

Fig. 2. Influence of (A) pH, (B) the iodide concentration, (C) the CPC concentration and (D) temperature on the maximum absorbance obtained in the production of triiodide ion.

The effect of the iodide concentration on the production of triiodide ion was studied in the range $(0.5\text{–}6) \times 10^{-3}$ M. The results obtained showed (Fig. 2B) the concentration of triiodide produced to increase sharply with iodide concentration up to about 1.5×10^{-3} M, above which it remained virtually constant. The stability of the triiodide–CPC association was greater at iodide concentrations above 2×10^{-3} M. Therefore, an iodide concentration of 2.6×10^{-3} M was chosen as optimal.

The concentration of CPC in the reaction medium should be high enough to ensure complete formation of the triiodide–CPC association. This occurred at CPC concentrations greater than 1.5×10^{-4} M (Fig. 2C). The surfactant concentration did not affect the stability of the association compound. The critical micellization concentration (cmc) of CPC in the reaction medium was calcutated from surface tension measurements performed with a stalagmometer (Brand, Germany). A value of 3.2×10^{-5} M CPC was found. The concentration is lower than the cmc calcu-

tated for distilled water (1.2×10^{-4} M) and the analytical concentration used (2.3×10^{-4} M), wich suggests that micelles are indeed formed under the experimental conditions used.

Increased temperatures had an adverse effect on the absorbance of the triiodide–CPC association owing to its rapid degradation (Fig. 2D), even though the absorbance values obtained between 10 and 20°C were virtually the same. A temperature of 20°C was chosen as optimal; in order to obtain maximum precision, the reactants were kept in a water bath at 20 ± 0.1°C when used.

Under the selected experimental conditions, production of triiodide ion was maximal within 2 min and the triiodide–CPC association was stable for at least 10 min.

Optimization of the experimental conditions for the reaction between triiodide–CPC and azide induced by sulphur(−II) compounds

The effect of different variables affecting the reaction between triiodide ion and azide in a CPC cationic micellar medium was studied in order to find the optimal experimental conditions for the determination of tetramethylthiuram disulphide, zineb and reduced glutathione. Conditions were optimized for maximum sensitivity and minimum variations in the measured parameter (decreasing in absorbance at 500 nm and a fixed time) with the assayed concentration. Blank reactions involving no inductors were also studied. Induced reactions gave rise to a first, quick stage up to about 30 s, followed by a lower stage. The fixed time used to measure the absorbance (45 s for the glutathione and zineb-induced reactions and 105 s for the tetramethylthiuram disulfide-induced reaction) was a compromise between maximum sensitivity, a wide linear range and expeditious measurements.

Development of the induced reactions was essentially affected by the azide concentration and pH. The absorbance at a fixed time was constant for azide concentrations over the range 1.2–1.8 M for the three induced reactions studied. The pH range of primary interest was 5.5–6.7. Above pH 6.7, the contribution of the blank reaction started to be significant, particularly at pH > 9. On the other hand, low pH values resulted in the release of the toxic hydrogen azide ($pK_a = 4.72$).

Analytical features

Calibration graphs for the determinations of zineb, reduced glutathione and tetrametylthiuram disulphide in the CPC micellar medium were run under the optimal conditions given in the Experimental section. Their figures of merit are summarized in Table 1, which also shows the detection limit and precision. Based on these features, the selected inductors can be determined with a high sensitivity in the CPC micellar medium. Compared to existing methods for the determination of these analytes by their inducing effect on the iodine–azide system developed in aqueous me-

TABLE 1
Analytical figures of merit of the determination of zineb, reduced glutathione and tetramethylthiuram disulphide by their inducing effect on the iodine–azide reaction in the presence of CPC

Parameter	Zineb	Reduced glutathione	Tetramethylthiuram disulphide
Linear range	40–450 ng ml^{-1}	$(2–10) \times 10^{-7}$ M	$(8–63) \times 10^{-9}$ M
Slope ± S.D.	$(1.7 \pm 0.1) \times 10^{3}$ ng^{-1} ml	$(3.5 \pm 0.1) \times 10^{5}$ M^{-1}	$(8.5 \pm 0.2) \times 10^{6}$ M^{-1}
Intercept ± S.D. (absorbance)	0.080 ± 0.009	0.001 ± 0.003	0.003 ± 0.009
Standard error of the estimate (absorbance)	1.36×10^{-2}	1.17×10^{-2}	1.45×10^{-2}
Correlation coefficient ($n = 7$)	0.994	0.998	0.998
Detection limit [a]	32 ng ml^{-1}	0.7×10^{-7} M	5.4×10^{-9} M
R.S.D (%) [b]	3.4	5.0	3.8

[a] 3σ. [b] $n = 11$, for 175 ng ml^{-1} zineb, 5×10^{-7} M reduced glutathione and 2.5×10^{-9} M tetramethylthiuram disulphide.

dia, those using CPC are more sensitive [8,16–18]. Thus, the surfactant allows one to determine lower concentrations of tetramethylthiuram, reduced glutathione and zineb by a factor of 51, 32 and 2.5 respectively, relative to those achieved in the aqueous medium.

On the other hand, although CPC micelles do not provide significantly increased selectivity towards substances which induce the iodine–azide system relative to the aqueous medium, they do increase selectivity to some extent judging the batochromic shift in the maximum absorbance of the triiodide ion.

Applications

The applicability of the triiodide–CPC association for the determination of divalent sulphur compounds based on their induction of the reaction between iodine and azide was tested by choosing two different kinds of samples of analytical interest. In the first sample, determination of erythrocyte glutathione concentration was carried out. As it is known [19], this parameter is of clinical significance because the erythrocyte glutathione concentration is diminished in many persons who have defects in the hexose monophosphate or glutathione synthesis pathways. Since virtually all of the non-protein sulphydryl groups of erythrocytes are in the form of reduced glutathione, the main interferences in the determination of glutathione in whole blood by using the triiodide–CPC method came from iodine reductants in blood, such as glucose. These types of interferences, characteristic of the iodine–azide reaction, may usually be overcome by means of blank determinations in the absence of azide [20,21], and we checked that this correction was sufficient to obtain accurate results in the determination of erythrocyte glutathione concentrations. Table 2 summarizes the results obtained in the determination of glutathione in four whole blood samples by the triiodide–CPC method and shows excellent agreement with those provided by the classical DTNB [5,5′-dithiobis(2-nitrobenzoic acid)] method [19].

Since zineb and thiram are widely used in agriculture as active ingredients in various formulations utilized to control leaf diseases in vegetables, the second type of sample selected to test the applicability of the triiodide–CPC proposed method was a commercial formulation. The chosen formulation (ZZ-Fernide, ICI-Zeltia) contained 80% thiram and the results obtained for this sample (79.0 ± 0.9%) were consistent with those claimed by the manufacturer.

TABLE 2
Determination of glutathione in human blood samples

Sample	Glutathione content (μg ml^{-1})	
	Triiodide–CPC method [a]	DTNB method
A	221 ± 7	218
B	267 ± 8	260
C	241 ± 3	252
D	175 ± 9	180

[a] Mean of four determinations ± S.D.

In conclusion, CPC micelles are useful for the determination of reduced glutathione, zineb and tetramethylthiuram disulphide by their inducing effect on the iodine–azide system. The proposed method is very sensitive, inexpensive and rapid.

The authors gratefully acknowledge financial support from the CICyT (Project no. PB91-0840).

REFERENCES

1 A. Sakuragawa, T. Harada, T. Okutani and S. Utsumi, Bunseki Kagaku, 29 (1980) 264.
2 S. Utsumi, T. Okutani and T. Yamada, Bunseki Kagaku, 24 (1975) 799.
3 S. Utsumi and T. Okutani, Nippon Kagaku Kaishi, (1973) 75.
4 W. Ciesielski and W. Jedrzejewski, Mikrochim. Acta, Part. III, (1984) 177.
5 R.D. Strickland, P.A. Mack and V.A. Childs, Anal. Chem., 32 (1960) 430.
6 W. Ciesielski, Chem. Anal. (Warsaw), 31 (1986) 39 and 469.
7 N. Kiba and M. Furusawa, Talanta, 28 (1981) 601.
8 Z. Kurzawa, K. Janowicz and J. Kurzawa, Anal. Chim. Acta, 243 (1991) 201.
9 W. Ciesielski, W. Jedrzejewski, Z.H. Hudzin, P. Kielbasinski and M. Mikolajczyk, Analyst, 116 (1991) 85.
10 L.P. Atkinson and J.G. Natoli, Anal. Chem., 46 (1974) 1316.
11 N. Kiba, M. Nishijima and F. Furusawa, Talanta, 27 (1980) 1090.

12 H. Weisz, W. Meiners and G. Fritz, Anal. Chim. Acta, 107 (1979) 301.
13 S. Pantel, Anal. Chim. Acta, 152 (1983) 215.
14 M.L. Lunar, S. Rubio and D. Pérez-Bendito, Anal. Chim. Acta, 268 (1992) 145.
15 J. Hernández-Méndez, A. Alonso Mateos, M.J. Almendral Parra and C. García de María, Anal. Chim. Acta, 184 (1986) 243.
16 Z. Kurzawa and E. Kubaszewski, Chem, Anal., 19 (1974) 263.
17 Z. Kurzawa and J. Kurzawa, Chem. Anal., 19 (1974) 775.
18 Z. Kurzawa and A. Krzyminska, Chem. Anal., 22 (1977) 671.
19 V.F. Fairbanks and G.G. Klee, in N.W. Tietz (Ed.), Fundamentals of Clinical Chemistry, Saunders, London, 1987, pp. 794–795.
20 Z. Kurzawa, Chem. Anal., 5 (1960) 555.
21 T. Pérez Ruiz, C. Martínez Lozano and M. Hernández Lozano, Ann., Quim., 78B (1982) 241.

Analytica Chimica Acta, 286 (1994) 241–246
Elsevier Science B.V., Amsterdam

Fluorescence lifetimes of metal(III) chelates of 5-sulphoquinolin-8-ol and their modification by the internal heavy atom effect

K. Hoffmann

Zentrum für Heterogene Katalyse, Rudower Chaussee 5, 12489 Berlin (Germany)

U. Stahl and S. Dähne

Bundesanstalt für Materialforschung und -prüfung, Laboratorium für zeitaufgelöste Spektroskopie, Rudower Chaussee 5, 12489 Berlin (Germany)

(Received 5th May 1993; revised manuscript received 22nd September 1993)

Abstract

For metal(III) [M(III)] 5-sulphoquinolin-8-olates, systematic studies of the atomic number effect in complexes exhibiting ligand fluorescence were carried out in aqueous solution. The fluorescence lifetimes of various chelates were investigated as a function of complexed metal ion, pH and metal-to-ligand ratio. The reported data for M(III) 5-sulphoquinolin-8-olates in aqueous solution include absorption and emission maxima, fluorescence quantum yields and fluorescence lifetimes, in addition to calculated rate constants of fluorescence and intersystem crossing. It was found that the internal atomic number effect is sufficient to distinguish between different M(III) chelates in aqueous media on the basis of their fluorescence lifetimes. The analytical applicability is limited, however, by the influence of the metal-to-ligand ratio and pH sensitivity.

Keywords: Fluorimetry; Sulphoquinolin-8-ol metal chelates

The analytical application of luminescence techniques with laser sources, including pulsed lasers, is one of the growing topics in analytical chemistry [1], especially since laser optics are essential for miniaturized instruments. As laser technology continues to develop, its use in analytical luminescence studies has become increasingly realistic. New technologies such as the manufacture and use of semiconductors are expected to increase the emission of metal compounds, e.g., gallium, into the environment. Also, for the detection of metal compounds, fluorescence procedures, with their advantages of high selectivity and sensitivity, are a promising field of application in miniaturized chromatographic devices.

However, most metal ions are non-luminescent in aqueous solution, but many of them can be determined fluorimetrically via the formation of fluorescent complexes with various organic multidentate ligands. In general, metal chelates exhibit ligand fluorescence, that is, the absorption and fluorescence spectra correspond to those of the ligand perturbed by the presence of the metal ion [2,3]. Therefore, the simultaneous determination of different metal chelates by steady-state fluorescence spectroscopy is often impossible without

Correspondence to: K. Hoffman, Zentrum für Heterogene Katalyse (Institut für Angewandte Chemie), Rudower Chaussee 5, 12489 Berlin (Germany).

SSDI 0003-2670(93)E0547-K

metal ion separation. Lytle et al. [4] predicted that chelates of the same ligand containing various metals should have different fluorescence decay times owing to the heavy atom effect [5], which produces a systematic increase in the rate constant of intersystem crossing caused by spin–orbit coupling.

The possibility of the application of phase [6,7] and pulse fluorimetry [4,8–10] for the discrimination of metal chelates showing ligand fluorescence has already been studied. A strong pH dependence of fluorescence lifetimes was reported [6,10]. In the present work the effect of pH and metal-to-ligand ratio on the fluorescence decay times of Al, Ga and In 5-sulphoquinolin-8-olates in aqueous solution was systematically studied with respect to the application of time-resolved fluorescence detection in the chromatography of inorganic species.

Metal(III) [M(III)] 5-sulphoquinolin-8-olates are suitable for studies of internal heavy atom effects within aqueous systems because of their similar steady-state fluorescence properties, with the exception of the non-fluorescent thallium(III) chelate [11].

EXPERIMENTAL

Reagents

All the chemicals used were of analytical-reagent grade. Quinolin-8-ol-5-sulphonic acid monohydrate (8-HQS) from Merck was recrystallized twice from a large volume of water. Standard solutions of metal ions containing $M(NO_3)_3 \cdot xH_2O$ in dilute HNO_3 were purchased from Merck ($c_M = 1$ g l^{-1}). For pH studies of fluorescence, the pH was adjusted with dilute hydrochloric acid, ammonia or sodium hydroxide. In other experiments acetate (pH 4.66) and phosphate (pH 6.88) buffer solutions from Merck were used. Distilled, deionized water was used for all solution preparations.

General procedure for preparing the sample solution

Stock standard solutions of metals were prepared by dilution of Merck standard solutions with deionized water. Aqueous ligand stock solutions containing 4×10^{-3} mol l^{-1} 8-HQS were used for all the experiments. As the order in which the reagents were added to the sample was found to be very important [6], the following procedure was adhered to for all preparations: to 3 ml of acetate or phosphate buffer solution an appropriate amount of stock standard solution of 8-HQS was added, then an appropriate volume of stock standard solution of metal was added and the mixture was diluted to 10 ml with buffer solution. The stock standard solutions were prepared freshly every day. Each sample contained 4×10^{-4} mol l^{-1} of metal, with the exception of solutions prepared for the determination of fluorescence quantum yields.

Apparatus

Static spectra were recorded with a Perkin-Elmer LS-50 spectrofluorimeter and a Specord M400 photometer from Carl Zeiss (Jena). Fluorescence decay curves were measured with a unique laser pulse fluorimeter. Fluorescence was excited with a nitrogen laser-pumped dye laser at 395 nm (pulse duration 0.5 ns, repetition rate 20 pulses s^{-1}, spectral half-width 0.5 nm). The detector system consisted of a compact monochromator (registration wavelength 505 nm, band width 2.5 nm), a fast photomultiplier (Hamamatsu R4703) and a digital sampling oscilloscope (MFA 105, manufactured by the Centre of Scientific Devices, Berlin). The pulse duration (FWHM) of the system response was 1.45 ns. Decay curves were recorded within a temporal range of about 24 ns with a step width of 46 ps. By averaging eight samples per step it took about 200 s to obtain one decay curve. For analytical applications it would be possible to decrease the time to measure one decay curve to 1 s using newly developed digitizing real-time oscilloscopes such as the Tektronix TDS 620.

Fluorescence quantum yield

Fluorescence quantum yields of the chelates were determined relative to quinine sulphate in 0.25 M sulphuric acid both excited at 365 nm near of their absorption maxima. The room-temperature fluorescence quantum yield of quinine

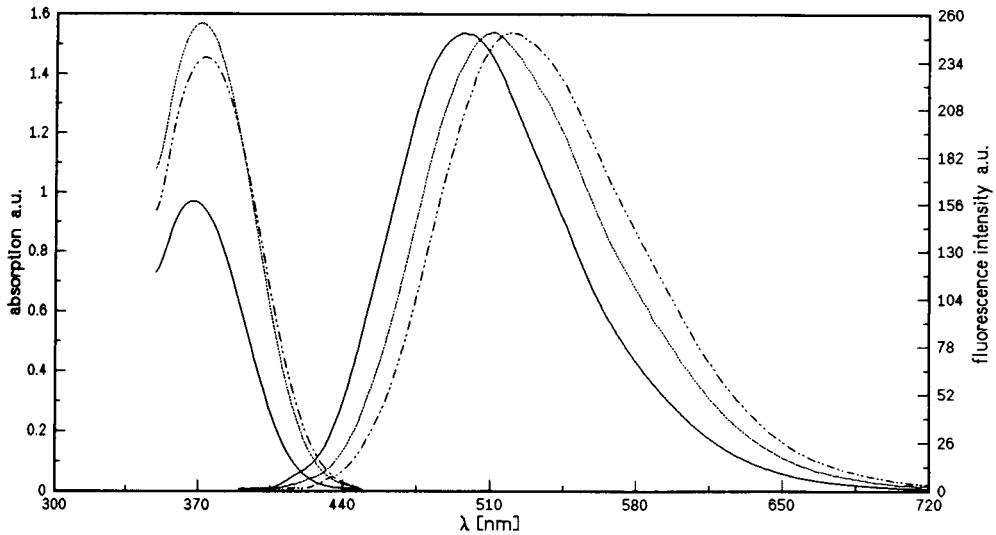

Fig. 1. Long-wavelength absorption and emission spectra of M(III) chelates. Key: ———, Al; - - - - - -, Ga; — - - —, In.

sulphate is taken to be 0.546 [12]. Emission spectra were corrected with respect to background emission and photomultiplier sensitivity. For minimizing reabsorption effects the absorbances of all samples were adjusted to ca. 0.05.

Fluorescence lifetimes

Fluorescence decay curves were analysed with a numerical deconvolution procedure (DecaMax) allowing multi-exponential fits and automated compensation for effects of colour-shifted system response curves. All decay curves were found to be significantly biexponential. The short decay time 0.9 ± 0.2 ns was independent of the metal, metal-to-ligand-ratio and pH. This decay time was not an artifact but cannot be explained. Subsequently in this paper, only data for the longer fluorescence lifetimes are given and discussed.

RESULTS AND DISCUSSION

Steady-state and time-resolved fluorescence measurements

An example of the long-wavelength part of the absorption spectra and steady-state emission spectra of the M(III) 8-HQS chelates is given in Fig. 1. The spectra are broad and very similar for the different metals. The absorption and emission

TABLE 1
Spectral maxima and lifetimes of M(III) chelates in aqueous solution (excitation at 395 nm)

pH	M:L	Long-wavelength absorption (nm)			Emission (nm)			Fluorescence decay time (ns)		
		Al	Ga	In	Al	Ga	In	Al	Ga	In
4.66	1:1	359.0	367.5	366.0	499.5	511.5	524.5	8.8 ± 0.2	4.6 ± 0.5	3.1 ± 0.1
	1:3	358.0	368.0	366.0	503.0	515.0	519.5	7.3 ± 0.1	2.5 ± 0.2	2.8 ± 0.2
	1:10	359.0	368.0	366.0	503.0	514.0	519.5	5.1 ± 0.2	3.2 ± 0.3	2.2 ± 0.1
6.88	1:1	360.0	367.0	368.5	500.5	510.0	519.5	7.5 ± 0.4	2.2 ± 0.1	3.4 ± 0.1
	1:3	360.0	367.0	368.5	496.5	510.0	518.5	5.3 ± 0.1	2.6 ± 0.1	2.0 ± 0.1
	1:10	362.0	366.0	368.0	506.5	510.0	513.0	6.5 ± 0.8	5.2 ± 0.1	3.7 ± 0.2
	1:20	365.0	366.0	368.0	506.5	510.0	513.0	7.8 ± 0.8	4.9 ± 0.1	6.5 ± 0.2

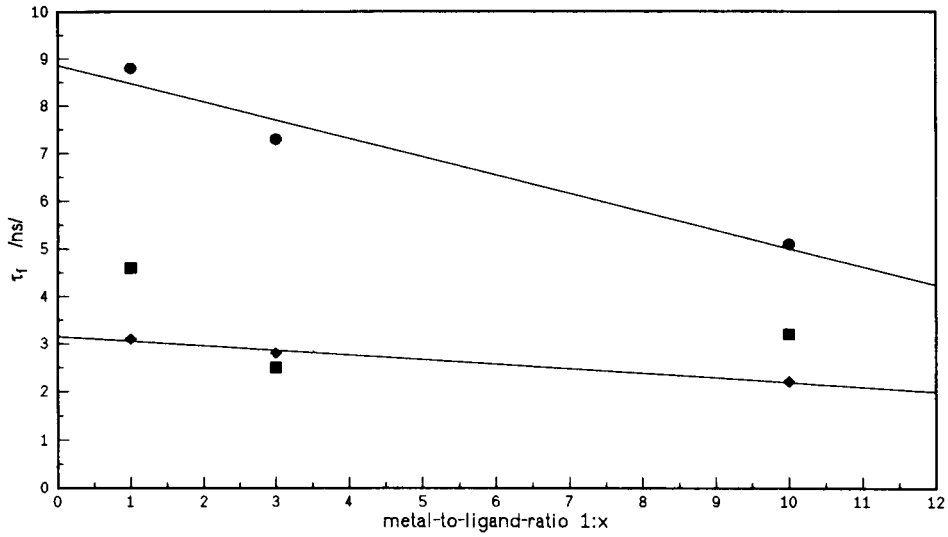

Fig. 2. Fluorescence lifetimes, τ_f, of M(III) chelates as a function of metal-to-ligand-ratio. • = Al; ■ = Ga; ◆ = In.

maxima of M(III) chelates obtained at different pH values and metal-to-ligand ratios are given in Table 1. In contrast to the nearly equal steady-state spectra, the fluorescence lifetimes of the chelates differ significantly (Table 1). A shortening of the observed fluorescence decay times with increasing atomic number is evident. The trend is in accordance with [10].

From pH studies, optimum differences in fluorescence lifetimes between M(III) chelates were found at about pH 5. Therefore, the fluorescence decay times were determined as a function of metal-to-ligand ratio at pH 4.66 and pH 6.88. A plot of fluorescence decay times, τ_f, versus metal-to-ligand ratio shows a decrease in the differences of τ_f with increasing excess of ligand (Fig. 2). Nevertheless, from Fig. 2 it follows that it should be possible to discriminate the Al chelate from Ga and In chelates down to a metal-to-ligand ratio of about 1 : 10 at pH 4.66 and 6.88 by means of their fluorescence lifetimes. In contrast, discrimination between Ga and In 5-sulphoquinolin-8-olates was found to be impossible.

Quantification of heavy atom effect

From the fluorescence decay time, τ_f, and the fluorescence quantum yield, ϕ_f, it is possible to calculate the rate constant of fluorescence, k_f.

TABLE 2
Parameters for M(III) 8-HQS chelates in aqueous solution, where $\lambda(em)_{max}$ is the maximum of fluorescence emission, ϕ_f the fluorescence quantum yield, τ_f the fluorescence lifetime, k_f the rate constant of fluorescence, k_{ISC} the rate constant of intersystem crossing, n the main quantum number and Z the atomic number

Parameter	pH 4.66			pH 6.88		
	Al	Ga	In	Al	Ga	In
$\lambda(em)_{max}$ (nm)	499.5	511.5	524.5	500.5	510.0	519.5
ϕ_f	0.125 ± 0.004	0.029 ± 0.003	0.063 ± 0.001	0.138 ± 0.005	0.032 ± 0.004	0.045 ± 0.005
τ_f (ns)	8.8	4.6	3.1	7.5	2.2	3.4
k_f (s^{-1})	1.42×10^7	6.30×10^6	2.23×10^7	1.84×10^7	1.46×10^7	1.32×10^7
k_{ISC} (s^{-1})	9.94×10^7	2.11×10^8	3.02×10^8	1.15×10^8	4.40×10^8	2.81×10^7
n	3	4	5	3	4	5
Z	13	31	49	13	31	49
Log k_{ISC} + 6 log n	10.86	11.94	12.67	10.92	12.26	12.64

TABLE 3
Excited-state parameters in aqueous solution as a function of pH and metal-to-ligand ratio (M:L)

pH	M:L	k_{ISC} (10^8 s^{-1})			k_f (10^8 s^{-1})		
		Al	Ga	In	Al	Ga	In
4.66	1:1	0.99	2.11	3.02	1.42	0.63	2.23
	1:3	1.20	3.88	3.35	1.71	1.16	2.46
	1:10	1.68	3.03	4.26	2.40	0.91	3.14
6.88	1:1	1.15	4.40	2.81	1.84	1.46	1.32
	1:3	1.63	3.72	4.78	2.60	1.23	2.25
	1:10	1.33	1.83	2.58	2.12	0.65	1.22
	1:20	1.09	1.98	1.47	1.75	0.65	0.69

Assuming that the singlet–singlet radiationless processes are negligible, the rate constant of intersystem crossing is given by $k_{ISC} = (1 - \phi_f)/\tau_f$.

From the data in Table 1, the rate constants of intersystem crossing, k_{ISC}, and fluorescence decay, k_f, were calculated at both pH 4.66 and 6.88 and are given in Table 2. Table 3 gives the rate constants of intersystem crossing and fluorescence as a function of pH and metal-to-ligand ratio, and show a general tendency for an increase in the intersystem crossing rate constant with increasing atomic number.

The observed increase is in accordance with the theory of the internal heavy atom effect, which is caused by enhanced spin–orbit coupling. Using a central field single electron approximation, the relationship between ISC rate constant and spin–orbit coupling constant, ξ, is described by

$$k_{ISC} \propto \xi_{nl}^2 = c^2 \left[\frac{z^4}{n^3(l+1)(l+\frac{1}{2})l} \right]^2 \quad (1)$$

where n and l are the usual quantum numbers, C is a constant and Z is the atomic number. Therefore, the heavy atom effect shows a Z^8 dependence, modified by the screening of nucleus (n^6) and the orbital penetration, $[(l+1)(l+\frac{1}{2})l]^2$. Correspondingly, the term $\log k_{ISC} + 6 \log n$ was used for quantifying the heavy atom effect (see Table 2). For chelates of metals from a given main group with the same ligand, Lytle *et al.* [4] suggested that the slope S of $\log k_{ISC} + 6 \log n = f(\log Z)$ correlates with the extent of atomic number perturbation of ligand fluorescence. The example in Fig. 3 for M(III) 5-sulphoquinolin-8-olates in aqueous solution at pH 4.66 with M:L = 1:1 shows that the observed variation of fluorescence lifetimes of the M(III) chelates in aqueous solution is really due to the internal atomic number effect. All the plots with slopes S given in Table 4 indicate that a systematic atomic number effect is present and that this effect depends

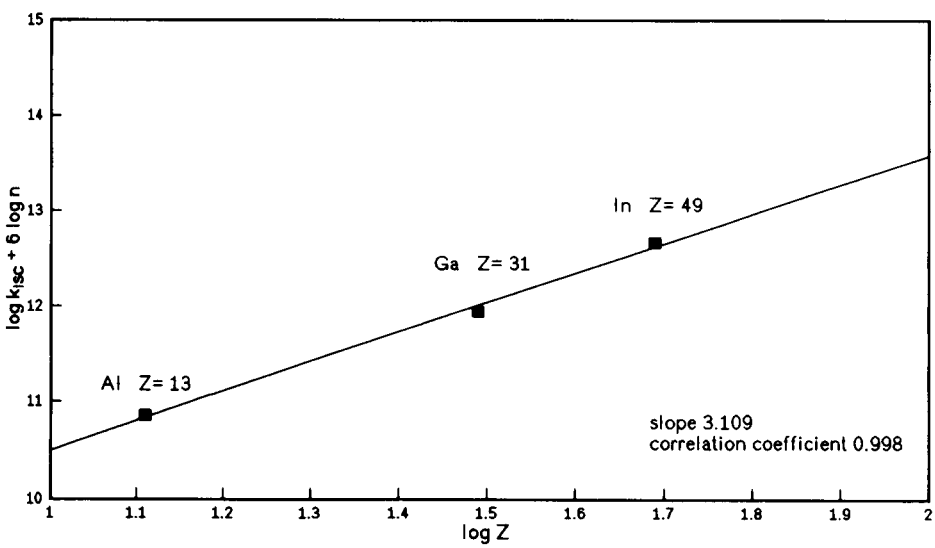

Fig. 3. Heavy atom effect of M(III) chelates in water, according to Lytle et al. [4]. Z = atomic number; n = quantum number.

TABLE 4
Slopes S from plot of log $k_{ISC} + 6$ log n vs. log Z as a function of pH and metal-to-ligand ratio (M:L)

pH	M:L	S
4.66	1:1	3.11
	1:3	3.12
	1:10	2.96
6.88	1:1	3.06
	1:3	3.10
	1:10	2.91
	1:20	2.68

slightly on the pH and metal-to-ligand ratio. The atomic number effect in M(III) 8-HQS chelates in dimethylformamide (DMF) has already been reported [4]. This work shows evidence of lifetime shortening owing to the internal heavy atom effect also in the aqueous system.

The present results should offer the possibility of time-resolved fluorescence analysis of these chelates without further extraction, e.g., in water analysis. It follows that the simultaneous determination of Al and In chelates should be possible in the same way as the reported discrimination between Al and Ga chelates [10]. The analytical application of fluorescence lifetime shortening with the studied system was found to be limited by the influence of the metal-to-ligand ratio and pH sensitivity. Taking into consideration this limitation, it should be possible to discriminate the Al from Ga and In 5-sulphoquinolin-8-olates in aqueous solution on the basis of their fluorescence lifetimes as shown in Fig. 2 and Table 1.

The work was supported by the Federal Ministry of Science and Technology and the Fonds der chemischen Industrie, Germany.

REFERENCES

1 I.M. Warner and L.B. McGown, Anal. Chem., 64 (1992) 343R.
2 G.G. Guilbault, Practical Fluorescence, Dekker, New York, 1988.
3 St.G. Schulman, Molecular Luminescence Spectroscopy, Part 1 (Chemical Analysis, Vol. 77), Wiley, New York, 1985.
4 F.E. Lytle, D.R. Storey and M.E. Juricich, Spectrochim. Acta, Part A, 29 (1973) 1357.
5 D.S. McClure, J. Chem. Phys., 17 (1949) 905.
6 K.R. Vitense and L.B. McGown, Anal. Chim. Acta, 193 (1987) 119.
7 K.R. Vitense and L.B. McGown, Analyst, 112 (1987) 1273.
8 T.L. Craven and F.E. Lytle, Anal. Chim. Acta, 107 (1979) 273.
9 T.L. Craven and F.E. Lytle, Spectrosc. Lett., 12 (1979) 559.
10 Y. Nishikawa, K. Hiraki and K. Morishige, Anal. Chim. Acta, 97 (1978) 121.
11 K. Soroka, R.S. Vithanage, D.A. Philips, B. Walker and P.K. Dasgupta, Anal. Chem., 69 (1987) 629.
12 W.H. Melhuish, J. Phys. Chem., 65 (1961) 229.

Analytica Chimica Acta, 286 (1994) 247–251
Elsevier Science B.V., Amsterdam

Titrations in non-aqueous media: Conductimetric and spectrophotometric investigation of reactions between iodine and aliphatic amines in acetonitrile

Turgut Gündüz and Mustafa Taştekin

Department of Chemistry, Faculty of Science, University of Ankara, Ankara (Turkey)

(Received 27th July 1993; revised manuscript received 22nd September 1993)

Abstract

The reactions between iodine and methyl-, ethyl-, *n*-propyl- and *n*-butylamines were investigated conductimetrically and spectrophotometrically in acetonitrile. The mole ratios of iodine to the amines titrated are 1:2, 2:2, 3:2 and 4:2, respectively, indicating strongly the formation of anionic species of the types I^-, I_3^-, I_5^- and I_7^- and cationic species of the type $[R_3N{-}I{-}NR_3]^+$. Although the conductivities of the primary amines do not show a regular order, the secondary and tertiary amines show orders at least at the first end-points. The order for secondary amines is $Me_2NH > Et_2NH > n\text{-}Pr_2NH > n\text{-}Bu_2NH$ and for tertiary amines $n\text{-}Bu_3N > n\text{-}Pr_3N > Et_3N > Me_3N$. The end-points of the conductimetric titrations are fairly sharp and can be used in the determination of these amines.

Keywords: Conductimetry; Titrimetry; UV–Visible spectrophotometry; Amines; Iodine complexes

The reactions between iodine and aliphatic amines in different solvents have been known for a long time, but unfortunately these reactions are not fully understood yet, and there is considerable controversy [1–16]. In order to eliminate this controversy at least partly, this work has been undertaken. To do this, twelve methyl-, ethyl-, *n*-propyl- and *n*-butylamines were titrated conductimetrically in acetonitrile with standard iodine solution in *n*-heptane. In these titrations, ca. 0.01 M iodine and ca. 5×10^{-4} M amine solutions were used in order to avoid the formation of ion pairs or aggregates. Conductimetry allows the detection of ions which are formed in the media [17–19]. The reason for choosing acetonitrile as the solvent is also to prevent the ions from forming ion pairs. As a result it may be possible to differentiate between inner and outer complex species [2,3,7].

Spectrophotometry was also used in order to identify the ionic species formed during the conductimetric titrations. This was of great help in elucidating the conductimetric titration curves.

Correspondence to: T. Gündüz, Department of Chemistry, Faculty of Science, University of Ankara, Ankara (Turkey).

EXPERIMENTAL

Apparatus

For conductimetric titrations, an Orion Model 101 conductivity meter equipped with an Orion 99-01-01 conductivity cell (with a cell constant of 1.04 cm^{-1}) was used. All conductimetric titrations were performed in a thermostated cell in a nitrogen atmosphere.

For the spectrophotometric investigations a Hitachi Model 200-20 UV–visible spectrophotometer was used.

SSDI 0003-2670(93)E0545-I

Chemicals

Acetonitrile and *n*-heptane (Merck, 99.7% and 99%, respectively) were purified according to [20].

Methyl-, dimethyl- and trimethylamine hydrochloride (each 97%, BDH) and ethylamine hydrochloride (98%, BDH) were used as received. Free amines were obtained by treating the amine hydrochlorides with sodium hydroxide. They were dissolved in acetonitrile and standardized against standard hydrochloric acid. Diethylamine (98%, Riedel-de Haën), triethylamine (98%, Fluka), *n*-propyl- and *n*-butylamine (98%, BDH) and di-*n*-propyl-, tri-*n*-propyl-, di-*n*-butyl- and tributylamine (each 99%, BDH) were purified according to [20]. Standard solutions of the amines of ca. 5×10^{-4} M were prepared in acetonitrile.

Iodine (Chemie Farma, Maarssen, Netherlands) was purified by sublimation. Throughout this study a 0.01 M solution of iodine in *n*-heptane was used.

Hydriodic acid was prepared as described in [21]. A 0.001 M solution in acetonitrile was used.

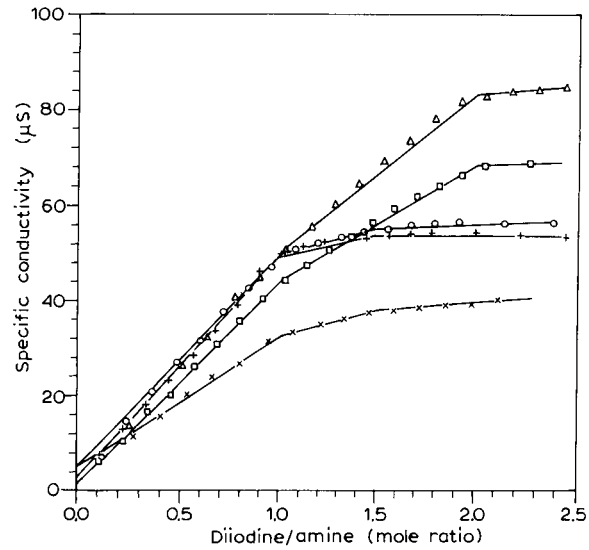

Fig. 1. Conductimetric titration curves of primary aliphatic amines (5×10^{-4} M) with iodine solution (0.010 M) in acetonitrile under a nitrogen atmosphere at 25°C. × = Ammonia; ○ = methylamine; + = ethylamine; □ = *n*-propylamine; △ = *n*-butylamine.

RESULTS AND DISCUSSION

The initial conductivities of the amines in acetonitrile are low, ca. 5 μS (5 μmho). However, the conductivities increase rapidly on addition of iodine solution. The conductivity curves of the amines are fairly well shaped and have more than one end-point. As the curves of the primary, secondary and tertiary amine series show somehow different characteristics, they will be considered separately.

Primary amines

The titration curves of the primary amines including ammonia are shown in Fig. 1.

The sharp increase in the conductivity until the first end-point indicates the formation of ionic species in the medium:

$$2CH_3NH_2 + 2I_2 \rightarrow [CH_3NH_2\text{–}I\text{–}NH_2CH_3]^+ + I_3^- \quad (1)$$

The mole ratio of iodine to the methyl amine is 2:2. At this stage one can consider another set of reactions, such as

$$B + H_2O \rightleftharpoons BH^+ + OH^-$$

$$OH^- + I_2 \rightleftharpoons HOI + I^- \quad (2)$$

If the initial increase in conductivity were due to such reactions, no end-point of the reaction would be observed, because, it is well known that there is not much difference between the mobilities of the anions in non-aqueous media [22]. Therefore, it is believed that reaction 1 is the correct one.

In order to confirm this view, we also recorded the spectra of the solution before and after the end-point and observed the characteristic absorption peaks of I_3^- ion at 362 and 292 nm (Fig. 2). At the second end-point the mole ratio of the iodine to methylamine is 3:2. This ratio suggests the following reaction [17–19]:

$$[CH_3NH_2\text{–}I\text{–}NH_2CH_3]^+ I_3^- + I_2 \rightarrow [CH_3NH_2\text{–}I\text{–}NH_2CH_3]^+ I_5^- \quad (3)$$

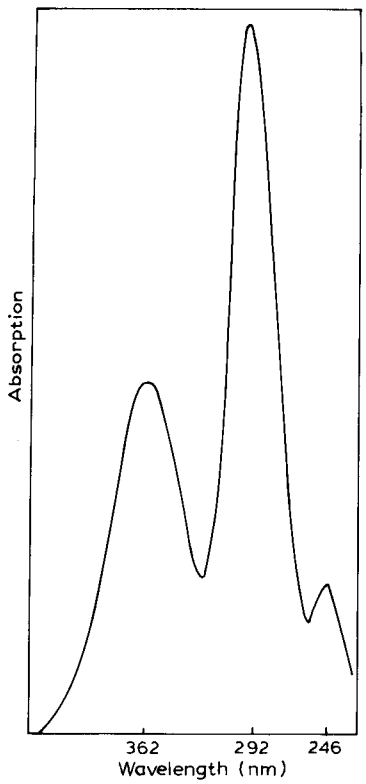

Fig. 2. UV spectrum of polyiodide ions.

The increase in the conductivity of the solution after the first end-point can be explained by the charge distribution in the larger ionic species. Thus, the charge distribution is better in the I_5^- ion than is in the I_3^- ion. As a result of such a charge distribution, the concentration of ion pairs decreases from I_3^- to I_5^-, which results in an increase in the conductivity of the solution. However, one might say that the mobility of the heavier ion is slower than that at the lighter ion, but this is not always correct, especially in non-aqueous media [22]. Both complexes have positively charged iodonium ions in common [15,16]. Unfortunately, we could not find a direct means to show the presence of this ion.

The titration curve of ammonia is given as a standard in all figures.

There are several reasons to believe that reactions, (1) and (3) are correct, as follows. The iodine molecule is very prone to undergo heterolytic splitting reaction:

$$I_2 \rightleftharpoons I^+ + I^-$$

The iodide ion readily forms homonuclear complexes such as

$$I^- + I_2 \rightleftharpoons I_3^-$$

$$I_3^- + I_2 \rightleftharpoons I_5^-$$

$$I_5^- + I_2 \rightleftharpoons I_7^-$$

Finally, iodine can easily violate the octet rule and can accommodate ten electrons in the valence shell.

The behaviour of ethylamine towards iodine is the same as that of methylamine (Fig. 1), whereas the behaviour of the *n*-propyl- and *n*-butylamines differs. They also give two stochiometric end-points, but the mole ratios of iodine to the amines at the end-points are 2:2 and 4:2 (Fig. 1). The ionic species at these end-points can be written as follows:

$$2RNH_2 + 2I_2 \rightarrow [RNH_2\text{–}I\text{–}NH_2R]^+ + I_3^-$$

$$[RNH_2\text{–}I\text{–}NH_2R]^+ + I_3^- + 2I_2 \rightarrow$$

$$[RNH_2\text{–}I\text{–}NH_2R]^+ + I_7^-$$

(R = *n*-propyl and *n*-butyl).

Secondary amines

The conductivity of the solutions of secondary amines is also very low, which indicates the absence of ions in appreciable concentration in solutions. However, the conductivity increases linearly and rapidly on addition of the iodine solution to the amine solutions (Fig. 3).

It is clear from Fig. 3 that the titration curves of the secondary amines follow a more regular pattern than those of the primary amines. Each amine shows two end-points. The mole ratio of iodine to the amine at the first end-point is 1:2, which indicates that until the first end-point the following reaction proceeds:

$$2R_2NH + I_2 \rightarrow [R_2NH\text{–}I\text{–}NHR_2]^+ + I^-$$

(R = methyl, ethyl, *n*-propyl and *n*-butyl). This view was supported by UV spectra of the solutions until the first end-point. An absorption peak

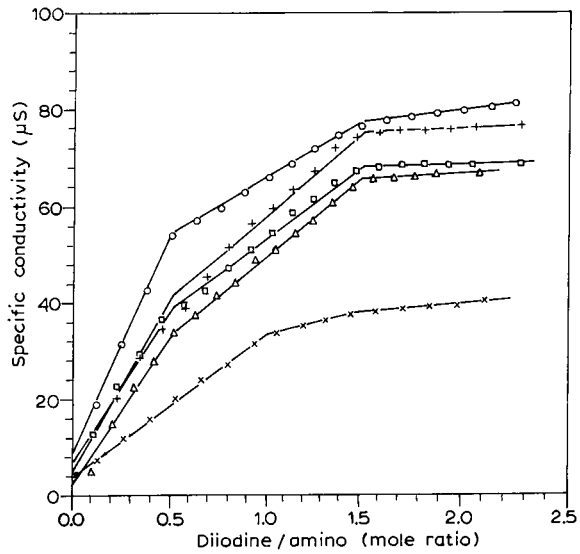

Fig. 3. Conductimetric titration curves of secondary aliphatic amines (5×10^{-4} M) with iodine solution (0.010 M) in acetonitrile under a nitrogen atmosphere at 25°C. × = Ammonia; ○ = dimethylamine; + = diethylamine; □ = di-*n*-propylamine; △ = di-*n*-butylamine.

at about 246 nm was observed. At the second end-point the mole ratio of iodine to amine is 3:2, which implies the following reaction:

$$2R_2NH + 3I_2 \rightarrow [R_2NH\text{–}I\text{–}NHR_2]^+ + I_5^-$$

The presence of the I_5^- ion in solution is also supported by UV data for the solutions (Fig. 2).

Another interesting result in the titration of the secondary amine solution is the conductivity order of the amine solutions at the first and second end-points, i.e., $Me_2NH > Et_2NH > n\text{-}Pr_2NH > n\text{-}Bu_2NH > NH_3$.

Tertiary amines

The titration curves of the tertiary amines with iodine are shown in Fig. 4. The initial conductivities of the tertiary amines are also very low, but increase linearly with additions of iodine. This is again a strong indication of the formation of ions in the medium. They all show breaks at a ratio of iodine to amines of 1:2. This ratio suggests the following reaction:

$$2R_3N + I_2 \rightarrow [R_3N\text{–}I\text{–}NR_3]^+ + I^-$$

(R = methyl, ethyl, *n*-propyl and *n*-butyl).

Trimethyl- and triethylamines give fairly sharp second end-points. At this point, the mole ratio of iodine to the trimethylamine is 2:2. The reaction corresponding to this ratio can be written as

$$2Me_3N + 2I_2 \rightarrow [Me_3N\text{–}I\text{–}NMe_3]^+ + I_3^-$$

The mole ratio of iodine to the triethylamine at the second end-point is 3:2 and the reaction corresponding to this ratio can be given as

$$2Et_3N + 3I_2 \rightarrow [Et_3N\text{–}I\text{–}NEt_3]^+ + I_5^-$$

In contrast, the *n*-propyl- and *n*-butylamines both show end-points at the same place, the mole ratio of iodine to amines being 2:2.

The conductivity order of these amines at the first end-point is $n\text{-}Bu_3N > n\text{-}Pr_3N > Et_3N > Me_3N$, which is exactly reverse of that for the secondary amines. This difference cannot be explained. We also carried out a blank test by titrating the solvent (acetonitrile) with standard iodine solution, but did not obtain a meaningful titration curve.

We also titrated the aliphatic amines with hydriodic acid in acetonitrile solvent. They all

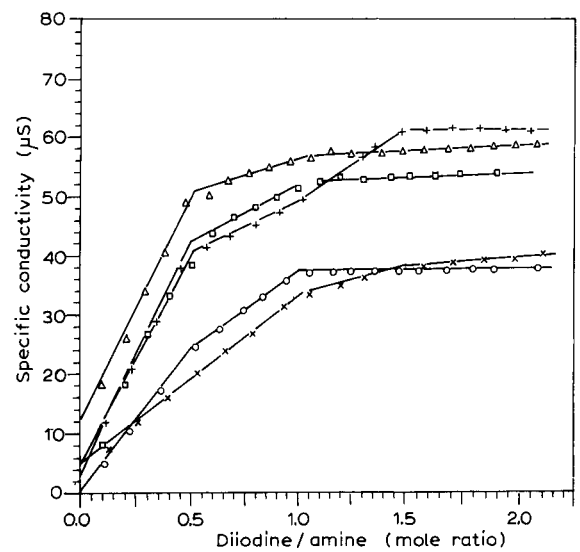

Fig. 4. Conductimetric titration curves of tertiary aliphatic amines (5×10^{-4} M) with iodine solution (0.010 M) in acetonitrile under a nitrogen atmosphere at 25°C. × = Ammonia; ○ = trimethylamine; + = triethylamine; □ = tri-*n*-propylamine; △ = tri-*n*-butylamine.

showed only one end-point. The end-points are stoichiometric but rather poor. The UV–visible spectra of the amine solutions titrated with hydriodic acid did not show absorption peaks at 362 and 292 nm. The reason why hydriodic acid is not a good titrant for aliphatic amines is that the mobilities of the ions in non-aqueous media are nearly identical [22].

Conclusions

The iodine molecule undergoes heterolytic splitting reactions to give positively and negatively charged ions of the types I^+ and I^-. Of these, the positively charged ion forms iodonium complexes with aliphatic primary, secondary and tertiary amines of the types $[RNH_2–I–NH_2R]^+$, $[R_2NH–I–NHR_2]^+$ and $[R_3N–I–NR_3]^+$ (R = methyl, ethyl, *n*-propyl and *n*-butyl), whereas the iodide ion remains in solution either as I^- or as polyiodide ions (I_3^-, I_5^- or I_7^-), depending on the species of the amine that is titrated.

A characteristic absorption band originating from the iodonium ions could not be observed in the UV–visible spectra. Their absorptions are probably at the far end of the UV region.

Iodide ion gives an absorption band at ca. 246 nm, depending on its cation, in acetonitrile solvent.

All the polyiodide ions (I_3^-, I_5^- and I_7^-) observed in this work give absorption peaks at ca. 362 and 292 nm in acetonitrile. These absorption wavelengths do not change appreciably with the number of iodine atoms in the polyiodide ions.

It has also been shown that the aliphatic amines can be determined with iodine solution in acetonitrile. For the determination of these amines hydriodic acid (a strong acid in non-aqueous media) is not suitable because of the poor end-points obtained.

REFERENCES

1 R. Faster, Organic Charge Transfer Complexes, Academic, New York, 1969.
2 R.S. Mulliken, J. Chem. Phys., 56 (1952) 801.
3 S. Nagakura, J. Am. Chem. Soc., 80 (1958) 520.
4 K. Toyoda and W.B. Person, J. Am. Chem. Soc., 88 (1966) 1629.
5 S. Kobinata and S. Nagakura, J. Am. Chem. Soc., 88 (1966) 3905.
6 P. Klaboe, J. Am. Chem. Soc., 89 (1967) 3667.
7 C.D. Schlumbach and D.M. Hart, J. Am. Chem. Soc., 86 (1967) 2347.
8 C. Yokayama, T. Fujita and M. Nakajima, J. Org. Chem., 44 (1979) 2871.
9 S.G.W. Ginn and J.L. Wood, Trans. Faraday Soc., 62 (1966) 777.
10 V. Jander and U. Engelhardt, Z. Anorg. Allg. Chem., 225 (1965) 312, 339.
11 T. Gündüz, H. Yîlmaz, E. Kîîç, O. Atakol and M. Tastekin, in Ş, Kunç et al. (Eds.), IV Chemistry and Chemical Engineering Symposium, Fîrat University Press, Elaziğ, Turkey, 1987, p. 43.
12 C. Reid and R.S. Mulliken, J. Am. Chem. Soc., 76 (1954) 3869.
13 R.S. Drago and N.J. Rose, J. Am. Chem. Soc., 81 (1959) 6141.
14 A.J. Hamilton and L.E. Sutton, Chem. Commun. (1968) 460.
15 I.I. Schuster and J.D. Roberts, J. Org. Chem., 44 (1979) 2658.
16 H. Handel, P. Labbé R. Le Goaller and J.L. Pierre, J. Chim. Phys., 78 (1981) 421.
17 R. Ding, J.L. Grant, R.M. Metzger and L.D. Kisperty, J. Phys. Chem., 92 (1988) 4600.
18 T. Yokota and Y. Kimura, Makromol. Chem., 190 (1989) 939.
19 S.K. Das, T. Gündüz, R.A. Show and B.C. Smith, J. Chem. Soc. A, (1969) 524.
20 D.D. Perrin, W.L.F. Armarego and D.R. Perrin, Purification of Laboratory Chemicals, Pergamon, Oxford, 1966.
21 U. Hofmann and W. Rüdorff, Anorganische Chemie, Viewag Verlag, Braunschweig, 1966, 19th edn., p. 245.
22 J.H. Exner and E.C. Steiner, J. Am. Chem., Soc., 96 (1974) 1782.

Analytica Chimica Acta, 286 (1994) 253–263
Elsevier Science B.V., Amsterdam

New methodology for calculation of acid–base dissociation constants of monoprotic and diprotic acids with close pK values from absorptiometric data and pH measurements

A. Cladera, C. Tomás, J.M. Estela and V. Cerdà

Department of Chemistry, Faculty of Sciences, University of the Balearic Islands, E-7071 Palma de Mallorca (Spain)

(Received 19th July 1993; revised manuscript received 28th September 1993)

Abstract

A new methodology for calculation of acid–base dissociation constants of monoprotic and diprotic compounds from absorptiometric data and pH measurements was developed. The equations derived for monoprotic compounds enable calculation of their pK values even in those cases where the molar absorptivities of the acid or basic species involved are unknown; those for diprotic compounds allow the easy calculation of acid–base dissociation constants however similar they may be. The applicability and limitations of the proposed methodology were studied in simulated processes. Finally, the new methodology was used to calculate the acid–base dissociation constant for maleimide dioxime at several wavelengths and with good results.

Keywords: Acid–base constants; pH

There are several straightforward available methods for calculation of similar acid–base dissociation constants by use of potentiometric methods including the Speakman linear extrapolation method [1] and the Prytz elimination method [2]. However, there are rather few choices for determining such constants spectrophotometrically, most of which involve labour-intensive and often rather limited iterative methods. Thus, the method of Albert and Serjeant [3] entails a long series or laborious approximations. Other iterative methods for this purpose [4–6] rely on complex matrix computations. Non-iterative methods used in this context include those of Robinson and Biggs [7], Thamer and Voigt [8], Ang [9] and Albelda et al. [10]. Robinson and Biggs [7] determined acid-base dissociation constants from three absorbance measurements at three different pH values by solving a system of three equations with three unknowns; the experimental measurements required must be made very accurately. The method of Thamer and Voigt [8] is only applicable if the variation of the absorbance at a given wavelength with pH has a maximum or minimum. This method requires the absorbance and pH at the maximum or minimum in question to be accurately known, which is not always easy. The Ang method [9] is also only applicable to $A = f(\text{pH})$ graphs including a maximum or minimum, but is simpler and can use intermediate points on the graph. Finally, the method of Albelda et al. [10] enables calculations at wavelengths where the $A = f(\text{pH})$ graph has no maximum or minimum; this requires the prior determination of a

Correspondence to: Dr. V. Cerdà, Department of Chemistry, Faculty of Sciences, University of the Balearic Islands, E-7071 Palma de Mallorca (Spain).

SSDI 0003-2670(93)E0554-K

fitting parameter at a wavelength where the graph does include a maximum or minimum, so this method is actually a variant of the Ang method. Other references of interest for the mathematical treatment of spectrophotometric data values are those of Asuero et al. [11–12]

MATHEMATICAL FOUNDATION

Monoprotic compounds

The law of additivity of absorbances establishes that the absorption A_i of a dissolved monoprotic compound at a given wavelength can be expressed as the summation of the individual absorptions of its protonated (A_{HL}) and unprotonated form (A_L) at the wavelength in question, i.e.

$$A_i = A_{HL} + A_L = \epsilon_{HL} c_{HL} + \epsilon_L c_L \quad (1)$$

where ϵ_{HL} and ϵ_L are the molar absorptivity, and c_{HL} and c_L the concentration of the protonated and unprotonated species, respectively.

Concentrations c_{HL} and c_L can be substituted by an expression including the proton concentration (h), protonation constant (β_1^H) and analytical concentration (c_t) of the compound:

$$A_i = \epsilon_{HL} c_t \frac{\beta_1^H h}{1+\beta_1^H h} + \epsilon_L c_t \frac{1}{1+\beta_1^H h} \quad (2)$$

which can be simplified to

$$A_i + A_i \beta_1^H h = A_{HL}^0 \beta_1^H h + A_L^0 \quad (3)$$

Hence,

$$\beta_1^H = \frac{1}{h} \frac{A_L^0 - A_i}{A_i - A_{HL}^0} \quad (4)$$

where A_{HL}^0 and A_L^0 are the absorbances of the solutions containing the protonated or unprotonated species alone, respectively.

Taking logarithms in Eqn. 4 yields

$$\log \beta_1^H = \mathrm{pH} + \log\left(\frac{A_L^0 - A_i}{A_i - A_{HL}^0}\right) \quad (5)$$

a widely known and used equation that is representative of a straight line and allows constant β_1^H to be graphically or analytically calculated from values of the logarithmic absorption term and pH measurements. However, Eqn. 5 requires A_{HL}^0 and A_L^0 to be known beforehand. This is not always the case (e.g., when either or both cannot be determined owing to insolubility or decomposition of the compound concerned, limiting conditions on the pH scale, etc.); under such circumstances, Eqn. 3 allows two new equations to be derived for calculation of these parameters. Thus, if A_H^0 cannot be determined directly,

$$A_i = (A_{HL}^0 - A_i)\beta_1^H h + A_L^0 \quad (6)$$

and hence

$$A_i = A_L^0 + \beta_1^H (A_{HL}^0 - A_i) h \quad (7)$$

On the other hand, if A_{HL}^0 cannot be determined directly,

$$\frac{A_i - A_L^0}{\beta_1^H h} = A_{HL}^0 \quad (8)$$

so

$$A_i = A_{HL}^0 + \frac{A_L^0 - A_i}{h} \frac{1}{\beta_1^H} \quad (9)$$

Both Eqns. 7 and 9 represent straight lines that allow β_1^H to be graphically or analytically calculated (e.g., by using a linear regression method). Once this parameter is known, the maximum absorption of the species that precludes calculation from Eqn. 5 can also be determined. These two equations are similar to those used by Sommer [13] in similar situations.

Diprotic compounds with close pK values

Diprotic compounds (H_2L) with distant pK values can be processed as if they were monoprotic compounds. The problem arises when the pK values of the compound concerned are too close for the absorption of the intermediate species, HL, to be readily determined. This frequently precludes determination of the pK values concerned. The problem can be solved by using a similar reasoning to that exposed above for monoprotic substances. From the law of additivity

TABLE 1

Effect of imprecision in absorbance and/or pH measurements on the calculation of pK for a monoprotic compound using Eqn. 9 [a]

pH imprecision	Absorbance imprecision	pK (%R.S.D.)	K (%R.S.D.) ± st (%R.S.D.)	A^0_{HL} (%R.S.D.) ± st(%rsd)	r (%R.S.D.)	E% (R.S.D.)
±0.001	±0.000	10.000 (0.00)	1.00×10^{-10} (0.07) ± 1.06×10^{-13} (11.79)	0.635 (0.00) ± 0.000 (0.00)	1.0000 (0.00)	0.0001 (0.00)
±0.002	±0.000	10.000 (0.01)	1.00×10^{-10} (0.10) ± 2.35×10^{-13} (18.03)	0.635 (0.00) ± 0.000 (0.00)	1.0000 (0.00)	0.0002 (38.49)
±0.010	±0.000	10.001 (0.01)	9.98×10^{-11} (0.12) ± 9.62×10^{-13} (11.03)	0.635 (0.00) ± 0.001 (0.00)	0.9998 (0.00)	0.0008 (31.74)
±0.020	±0.000	9.998 (0.04)	1.00×10^{-10} (0.94) ± 1.71×10^{-12} (26.27)	0.635 (0.08) ± 0.001 (0.00)	0.9992 (0.02)	0.0016 (15.36)
±0.100	±0.000	10.029 (0.27)	9.37×10^{-11} (6.14) ± 7.51×10^{-12} (17.85)	0.632 (0.42) ± 0.007 (16.50)	0.9801 (0.70)	0.0089 (30.40)
±0.000	±0.001	10.001 (0.01)	9.97×10^{-11} (0.26) ± 8.04×10^{-13} (16.70)	0.635 (0.00) ± 0.001 (0.00)	0.9999 (0.00)	0.0006 (30.29)
±0.000	±0.003	9.995 (0.08)	1.02×10^{-10} (1.74) ± 2.26×10^{-12} (10.33)	0.636 (0.20) ± 0.002 (28.57)	0.9986 (0.04)	0.0022 (37.23)
±0.000	±0.005	9.998 (0.13)	1.01×10^{-10} (3.05) ± 3.44×10^{-12} (20.32)	0.635 (0.24) ± 0.004 (16.50)	0.9958 (0.17)	0.0046 (21.22)
±0.000	±0.010	10.013 (0.14)	9.71×10^{-11} (3.25) ± 6.36×10^{-12} (22.91)	0.634 (0.46) ± 0.006 (8.70)	0.9873 (0.26)	0.0054 (18.43)
±0.001	±0.001	9.999 (0.02)	1.00×10^{-10} (0.41) ± 8.66×10^{-13} (16.16)	0.635 (0.00) ± 0.001 (0.00)	0.9998 (0.00)	0.0010 (18.23)
±0.001	±0.003	10.004 (0.12)	9.92×10^{-11} (2.69) ± 2.04×10^{-12} (15.96)	0.634 (0.20) ± 0.002 (28.57)	0.9989 (0.01)	0.0019 (29.80)
±0.010	±0.003	9.997 (0.07)	1.01×10^{-10} (1.59) ± 2.16×10^{-12} (14.45)	0.636 (0.09) ± 0.002 (40.82)	0.9984 (0.05)	0.0028 (34.23)
±0.001	±0.005	10.002 (0.15)	9.95×10^{-11} (3.38) ± 3.38×10^{-12} (32.00)	0.634 (0.27) ± 0.003 (18.18)	0.9965 (0.14)	0.0036 (14.87)
±0.010	±0.010	10.003 (0.03)	9.93×10^{-11} (0.85) ± 7.37×10^{-12} (9.57)	0.634 (0.33) ± 0.008 (7.70)	0.9813 (0.37)	0.0097 (9.41)

[a] $A^0_L = 0.406$, $A^0_{HL} = 0.635$, p$K = 10.000$. Data can be acquired up to pH = p$K - 1$. R.S.D. = relative standard deviation, s = standard deviation, t = Student's t, E = error of fit.

of absorbances for a dissolved diprotic compound it follows that

$$A_i = A_{H_2L} + A_{HL} + A_L$$
$$= \epsilon_{H_2L} c_{H_2L} + \epsilon_{HL} c_{HL} + \epsilon_L c_L \quad (10)$$

Substitution of the concentrations of dissolved species by expressions including the overall concentration of compound (c_t), the overall protonation constants (β_1^H and β_2^H) and the proton concentration (h) yields

$$A_i = \epsilon_{H_2L} c_t \frac{\beta_2^H h^2}{1 + \beta_1^H h + \beta_2^H h^2} + \epsilon_{HL} c_t \frac{\beta_1^H h}{1 + \beta_1^H h + \beta_2^H h^2} + \epsilon_L c_t \frac{1}{1 + \beta_1^H h + \beta_2^H h^2} \quad (11)$$

where the overall protonation constants β_2^H and β_1^H are represented by $1/K_1K_2$ and $1/K_2$, respectively, K_1 and K_2 being the successive dissociation constants of the compound.

Rearranging Eqn. 11 yields

$$A_i = A_{HL}^0 - \frac{A_i - A_L^0}{h} \frac{1}{\beta_1} + \left(A_{H_2L}^0 - A_i\right) h \frac{\beta_2}{\beta_1} \quad (12)$$

which is the equation of a plane [$y = A_{HL}^0 - (1/\beta_1^H)X_1 + (\beta_2^H/\beta_1^H)X_2$] and can be solved by multiple linear regression from experimental y, X_1 and X_2 values to obtain pK_1, pK_2 and the maximum absorption of the intermediate species, A_{HL}^0.

Budesinsky [14] proposed a similar equation for diprotic acids.

EXPERIMENTAL

In order to validate the above equations and study the effect of imprecisions in absorbance and pH values as well as other factors such as the difference between the molar absorptivities of the different species, the closeness of pK values, the usable pH range, etc., (A_i, pH_i) data were simulated with the aid of two programmes, GENMONOP and GENSIMOP, written by the authors in QuickBasic for running on IBM PC and compatible computers. In both programmes, the simulated imprecision in the absorption and/or pH values is assigned to each data by a random process involving calculation of the average of 10 randomly generated numbers between +1 and −1 in order to obtain a normal distribution, and multiplying the result by its corresponding imprecision.

The real experimental values used to calculate the dissociation constants for maleimide dioxime were reported elsewhere [10].

RESULTS AND DISCUSSION

Simulated data

The results given below are the average of four simulations.

TABLE 2

Results obtained by studying the acquirability of experimental data over different working pH ranges in calculating pK for a monoprotic compound using Eqn. 9 [a]

Acquisition up to pH =	pK (%R.S.D.)	K (%R.S.D.) ± st (%R.S.D.)	A_{HL}^0 (R.S.D.%) ± st (%R.S.D.)	r (%R.S.D.)	E (%R.S.D.)
$pK - 2$	10.000 (0.08)	9.99×10^{-11}(1.90) ± 1.22×10^{-12}(15.12)	0.635(0.13) ± 0.001(0.00)	0.9992 (0.01)	0.0018 (23.17)
$pK - 1$	10.004 (0.12)	9.92×10^{-11}(2.69) ± 2.04×10^{-12}(15.96)	0.634(0.20) ± 0.002(28.57)	0.9989 (0.01)	0.0019 (29.80)
$pK - 0.5$	10.006 (0.13)	9.87×10^{-11}(2.90) ± 4.40×10^{-12}(26.89)	0.634(0.26) ± 0.004(12.83)	0.9974 (0.06)	0.0022 (37.23)
pK	10.012 (0.03)	9.72×10^{-11}(0.79) ± 1.34×10^{-11}(23.77)	0.631(0.15) ± 0.020(24.93)	0.9831 (0.80)	0.0038 (24.10)
$pK + 0.5$	10.252 (0.89)	5.69×10^{-11}(21.09) ± 3.51×10^{-11}(22.97)	0.551(4.35) ± 0.070(20.53)	0.7326 (10.88)	0.0088 (25.94)

[a] $A = 0.406$, $A_{HL}^0 = 0.635$, $pK = 10.000$. pH imprecision = ±0.001, absorbance imprecision = ±0.003. For other symbols, see footnote to Table 1.

Calculation of pK values for monoprotic compounds

Table 1 shows the results obtained by using Eqn. 9 with various imprecisions in the pH and/or absorbance values in order to calculate a pK of 10 in a hypothetical case where data could only be acquired up to pH = pK − 1. As can be seen, both the pK values and the fitting correlations were quite good in every instance. As expected, errors and standard deviations increased with increasing imprecision, the effect of absorbance imprecisions being more marked than that of pH imprecisions on pK values.

The effect of the working pH range used to obtain the experimental values is shown in Table 2. The values in this table were obtained at a constant imprecision in pH and absorbance of ±0.001 and ±0.003, respectively; data were as-

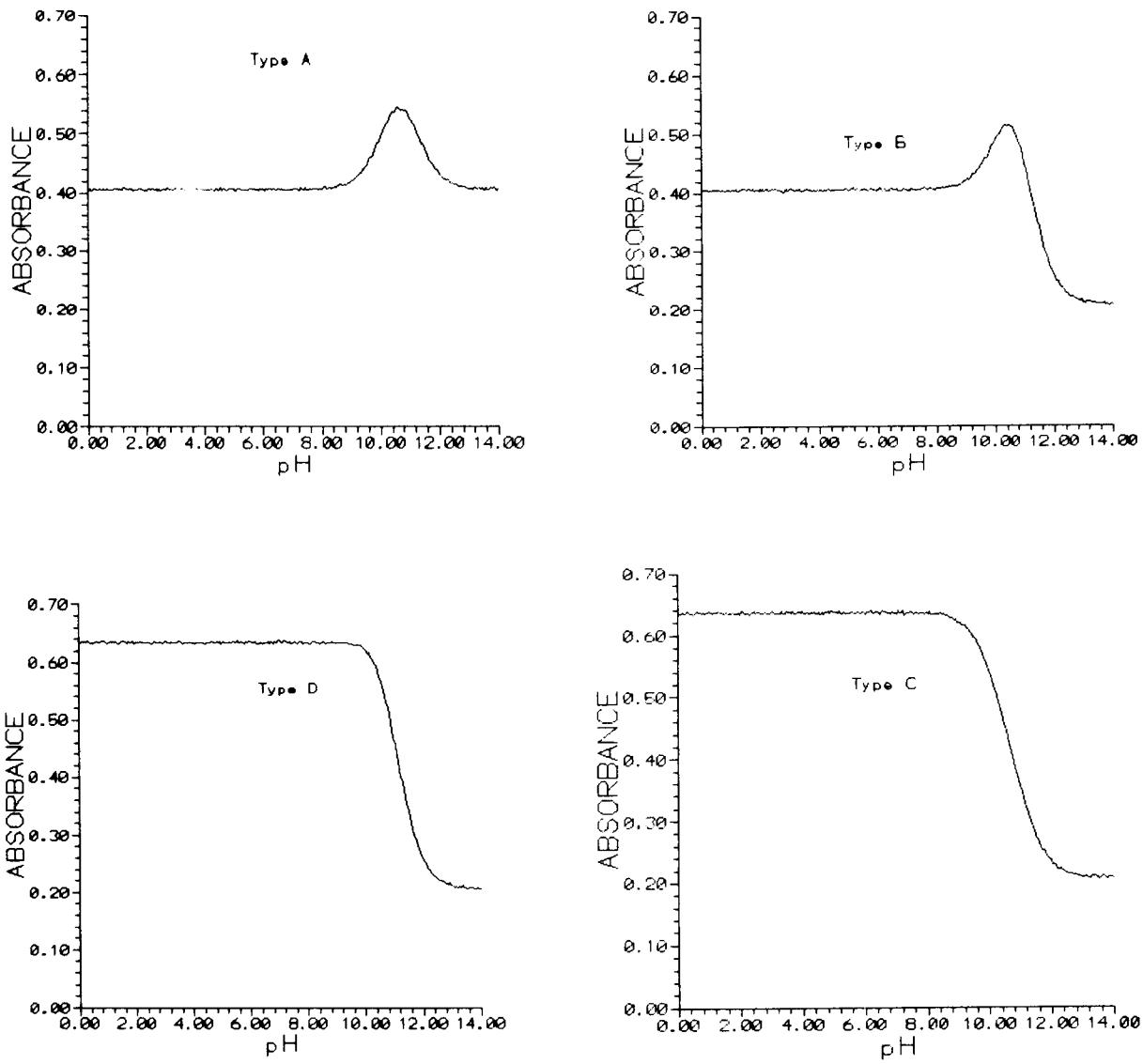

Fig. 1. Types of $A = f(\mathrm{pH})$ curves obtained for diprotic compounds as a function of the working wavelength. Simulated data. pH imprecision = ±0.001. A imprecision = ±0.003. pK_1 = 10.19. pK_2 = 11.14.

TABLE 3

Effect of pH and absorbance imprecisions on the pK values obtained by applying Eqn. 12 to type A curves for diprotic compounds [a]

pH imprecision	Absorption imprecision	pK_1 (%R.S.D.)	E (%)	pK_2 (%R.S.D)	E (%)	A^0_{HL} (%R.S.D.)	sm (%R.S.D.)	r^2 (%R.S.D.)
±0.000	±0.0005	10.190 (0.02)	0.00	11.139 (0.01)	−0.01	0.635 (0.00)	0.001 (10.50)	0.9997 (0.01)
±0.000	±0.001	10.189 (0.05)	−0.01	11.141 (0.03)	0.01	0.635 (0.15)	0.001 (8.91)	0.9987 (0.03)
±0.000	±0.002	10.182 (0.20)	−0.08	11.146 (0.14)	0.05	0.633 (0.64)	0.002 (13.82)	0.9951 (0.09)
±0.000	±0.003	10.186 (0.31)	−0.04	11.136 (0.12)	−0.04	0.636 (0.68)	0.003 (24.94)	0.9909 (0.53)
±0.000	±0.005	10.147 (0.2)	−0.42	11.168 (0.11)	0.25	0.626 (0.46)	0.006 (26.09)	0.9687 (1.01)
±0.000	±0.010	9.844 (1.23)	−3.40	11.306 (0.87)	1.49	0.587 (3.90)	0.013 (29.23)	0.8736 (3.60)
±0.001	±0.000	10.190 (0.00)	0.00	11.140 (0.00)	0.00	0.635 (0.00)	0.00 (0.00)	1.0000 (0.00)
±0.002	±0.000	10.190 (0.09)	0.00	11.140 (0.01)	0.00	0.635 (0.00)	0.000 (0.00)	1.0000 (0.00)
±0.010	±0.000	10.193 (0.09)	0.03	11.139 (0.05)	−0.01	0.636 (0.30)	0.001 (18.00)	0.9992 (0.03)
±0.020	±0.000	10.191 (0.13)	0.01	11.140 (0.08)	0.00	0.635 (0.41)	0.002 (10.58)	0.9963 (0.06)
±0.050	±0.000	10.183 (0.41)	−0.07	11.142 (0.23)	0.02	0.634 (1.20)	0.005 (43.19)	0.9793 (0.47)
±0.100	±0.000	10.059 (0.88)	−1.28	11.217 (0.44)	−0.69	0.613 (1.49)	0.010 (22.12)	0.9227 (3.00)
±0.001	±0.001	10.187 (0.08)	−0.03	11.141 (0.04)	0.01	0.635 (0.20)	0.001 (8.70)	0.9988 (0.01)
±0.001	±0.003	10.179 (0.17)	−0.11	11.150 (0.14)	0.09	0.632 (0.62)	0.004 (18.16)	0.9882 (0.35)
±0.010	±0.003	10.186 (0.15)	−0.04	11.145 (0.14)	0.05	0.634 (0.64)	0.003 (36.35)	0.9876 (0.58)
±0.005	±0.001	10.188 (0.07)	−2.04	11.143 (0.05)	0.03	0.634 (0.27)	0.001 (14.18)	0.9984 (0.03)
±0.001	±0.0005	10.189 (0.01)	−0.01	11.142 (0.00)	0.02	0.635 (0.09)	0.001 (18.24)	0.9997 (0.02)
±0.010	±0.005	10.172 (0.21)	−0.18	11.154 (0.19)	0.13	0.631 (0.93)	0.005 (14.09)	0.9696 (0.41)

[a] $A^0_{H_2L} = 0.406$, $A^0_{HL} = 0.635$, $A^0_L = 0.406$, p$K_1 = 10.19$, p$K_2 = 11.14$. sm = mean standard deviation of fit, r = correlation coefficient of fit.

TABLE 4

Effect of pH and absorbance imprecisions on the pK values obtained by applying Eqn. 12 to type B curves for diprotic compounds [a]

pH imprecision	Absorption imprecision	pK_1 (%R.S.D.)	E (%)	pK_2 (%R.S.D.)	E (%)	A^0_{HL} (%R.S.D.)	sm (%R.S.D.)	r^2 (%R.S.D.)
±0.000	±0.0005	10.190 (0.01)	0.00	11.141 (0.01)	0.01	0.635 (0.08)	0.001 (8.70)	1.0000 (0.01)
±0.000	±0.001	10.189 (0.02)	−0.01	11.141 (0.01)	0.01	0.635 (0.08)	0.001 (8.70)	0.9998 (0.00)
±0.000	±0.002	10.186 (0.06)	−0.04	11.141 (0.00)	0.01	0.634 (0.24)	0.002 (30.99)	0.9994 (0.04)
±0.000	±0.003	10.194 (0.03)	0.04	11.137 (0.01)	−0.03	0.636 (0.08)	0.003 (11.74)	0.9982 (0.06)
±0.000	±0.005	10.176 (0.21)	−0.14	11.145 (0.05)	0.05	0.633 (0.52)	0.004 (9.32)	0.9966 (0.12)
±0.000	±0.010	10.181 (0.17)	−0.09	11.145 (0.08)	0.05	0.632 (0.43)	0.010 (21.02)	0.9808 (0.55)
±0.001	±0.000	10.190 (0.01)	0.00	11.140 (0.00)	0.00	0.635 (0.00)	0.000 (40.83)	1.0000 (0.00)
±0.002	±0.000	10.190 (0.01)	0.00	11.140 (0.00)	0.00	0.635 (0.00)	0.000 (35.36)	1.0000 (0.00)
±0.010	±0.000	10.196 (0.02)	0.06	11.137 (0.02)	−0.03	0.637 (0.09)	0.002 (26.43)	0.9996 (0.01)
±0.020	±0.000	10.179 (0.16)	−0.11	11.146 (0.08)	0.05	0.632 (0.60)	0.005 (27.83)	0.9976 (0.04)
±0.050	±0.000	10.181 (0.40)	−0.09	11.141 (0.17)	0.01	0.633 (1.51)	0.011 (10.61)	0.9871 (0.18)
±0.100	±0.000	9.994 (1.14)	−1.92	11.214 (0.41)	0.66	0.601 (2.02)	0.020 (36.21)	0.9416 (0.77)
±0.001	±0.001	10.189 (0.03)	−0.01	11.141 (0.02)	0.01	0.635 (0.09)	0.001 (9.34)	0.9998 (0.01)
±0.001	±0.003	10.180 (0.06)	−0.10	11.144 (0.04)	0.04	0.633 (0.32)	0.003 (5.89)	0.9983 (0.01)
±0.010	±0.003	10.188 (0.12)	−0.02	11.141 (0.06)	0.01	0.635 (0.54)	0.004 (22.20)	0.9975 (0.08)
±0.005	±0.001	10.190 (0.05)	0.00	11.139 (0.01)	−0.01	0.636 (0.09)	0.002 (11.41)	0.9996 (0.01)
±0.001	±0.0005	10.190 (0.02)	0.00	11.140 (0.00)	0.00	0.635 (0.08)	0.001 (18.64)	0.9999 (0.00)
±0.010	±0.005	10.149 (0.40)	−0.40	11.151 (0.15)	0.10	0.629 (1.05)	0.006 (11.06)	0.9940 (0.08)

[a] $A^0_{H_2L} = 0.406$, $A^0_{HL} = 0.635$, $A^0_L = 0.206$, p$K_1 = 10.19$, p$K_2 = 11.14$.

TABLE 5

Effect of pH and absorbance imprecisions on the pK values obtained by applying Eqn. 12 to type C curves for diprotic compounds [a]

pH imprecision	Absorption imprecision	pK_1 (%R.S.D.)	E (%)	pK_2 (%R.S.D.)	E (%)	A^0_{HL} (%R.S.D.)	sm (%R.S.D.)	r^2 (%R.S.D.)
±0.000	±0.0005	10.192 (0.02)	0.02	11.143 (0.01)	0.03	0.419 (0.20)	0.001 (9.52)	1.0000 (0.00)
±0.000	±0.001	10.191 (0.09)	0.01	11.139 (0.09)	−0.01	0.420 (0.78)	0.001 (21.14)	0.9999 (0.01)
±0.000	±0.002	10.189 (0.09)	−0.01	11.141 (0.07)	0.01	0.420 (0.70)	0.002 (7.51)	0.9995 (0.00)
±0.000	±0.003	10.187 (0.23)	−0.03	11.138 (0.22)	−0.02	0.421 (2.08)	0.003 (15.36)	0.9993 (0.02)
±0.000	±0.005	10.191 (0.35)	0.01	11.152 (0.33)	0.11	0.417 (3.21)	0.005 (20.99)	0.9974 (0.09)
±0.000	±0.010	10.146 (0.40)	−0.43	11.108 (0.24)	−0.29	0.432 (2.24)	0.010 (7.11)	0.9899 (0.11)
±0.001	±0.000	10.190 (0.01)	0.00	11.140 (0.01)	0.00	0.420 (0.19)	0.00 (0.00)	1.0000 (0.00)
±0.002	±0.000	10.190 (0.01)	0.00	11.140 (0.01)	0.00	0.420 (0.00)	0.000 (16.50)	1.0000 (0.00)
±0.010	±0.000	10.193 (0.09)	0.03	11.143 (0.07)	0.03	0.419 (0.70)	0.002 (2.90)	0.9997 (0.00)
±0.020	±0.000	10.195 (0.13)	0.05	11.144 (0.15)	0.04	0.419 (1.06)	0.003 (14.41)	0.9992 (0.03)
±0.050	±0.000	10.188 (0.37)	−0.02	11.139 (0.36)	−0.01	0.421 (3.48)	0.009 (10.48)	0.9953 (0.12)
±0.100	±0.000	10.193 (0.56)	0.03	11.175 (0.39)	0.31	0.416 (4.58)	0.018 (10.80)	0.9840 (0.34)
±0.001	±0.001	10.190 (0.02)	0.00	11.139 (0.03)	−0.01	0.420 (0.23)	0.001 (19.83)	0.9999 (0.01)
±0.001	±0.003	10.177 (0.36)	−0.13	11.126 (0.30)	−0.13	0.425 (2.91)	0.003 (4.38)	0.9990 (0.01)
±0.010	±0.003	10.205 (0.28)	0.15	11.154 (0.19)	0.13	0.415 (1.99)	0.003 (11.92)	0.9989 (0.03)
±0.005	±0.001	10.182 (0.14)	−0.08	11.132 (0.09)	−0.07	0.423 (0.97)	0.001 (7.23)	0.9998 (0.01)
±0.001	±0.0005	10.194 (0.05)	0.04	11.145 (0.04)	0.05	0.418 (0.30)	0.001 (16.65)	1.0000 (0.00)
±0.010	±0.005	10.214 (0.42)	0.24	11.164 (0.39)	0.22	0.412 (3.69)	0.005 (13.50)	0.9977 (0.06)

[a] $A^0_{H_2L} = 0.635$, $A^0_{HL} = 0.420$, $A^0_L = 0.206$, p$K_1 = 10.19$, p$K_2 = 11.14$.

TABLE 6

Effect of pH and absorbance imprecisions on the pK values obtained by applying Eqn. 12 to type D curves for diprotic compounds [a]

pH imprecision	Absorption imprecision	pK_1 (%R.S.D.)	E (%)	pK_2 (%R.S.D.)	E (%)	A^0_{HL} (%R.S.D.)	sm (%R.S.D.)	r^2 (%R.S.D.)
±0.000	±0.0005	10.185 (0.04)	−0.05	11.140 (0.01)	0.00	0.635 (0.08)	0.000 (20.16)	1.0000 (0.00)
±0.000	±0.001	10.176 (0.04)	−0.14	11.140 (0.01)	0.00	0.636 (0.00)	0.001 (15.22)	0.9999 (0.00)
±0.000	±0.002	10.197 (0.18)	0.07	11.139 (0.01)	−0.01	0.635 (0.13)	0.002 (17.76)	0.9996 (0.01)
±0.000	±0.003	10.210 (0.81)	0.20	11.140 (0.04)	0.00	0.634 (0.96)	0.003 (18.68)	0.9992 (0.02)
±0.000	±0.005	10.127 (0.84)	−0.62	11.138 (0.04)	−0.02	0.638 (0.69)	0.005 (11.74)	0.9979 (0.03)
±0.000	±0.010	9.616 (4.28)	−5.63	11.137 (0.11)	−0.03	0.653 (1.58)	0.009 (33.10)	0.9929 (0.29)
±0.001	±0.000	10.187 (0.02)	−0.03	11.140 (0.00)	0.00	0.635 (0.00)	0.000 (0.00)	1.0000 (0.00)
±0.002	±0.000	10.186 (0.04)	−0.04	11.140 (0.00)	0.00	0.635 (0.00)	0.00 (22.22)	1.0000 (0.00)
±0.010	±0.000	10.174 (0.14)	−0.16	11.141 (0.01)	0.01	0.636 (0.09)	0.002 (11.66)	0.9996 (0.01)
±0.020	±0.000	10.164 (0.42)	−0.30	11.142 (0.05)	0.02	0.635 (0.15)	0.003 (28.25)	0.9991 (0.01)
±0.050	±0.000	10.122 (0.69)	−0.67	11.147 (0.09)	0.06	0.637 (0.27)	0.007 (14.41)	0.9965 (0.10)
±0.100	±0.000	9.540 (4.55)	−6.38	11.172 (0.21)	0.29	0.644 (0.82)	0.012 (39.44)	0.9803 (1.10)
±0.001	±0.001	10.170 (0.12)	−0.20	11.141 (0.01)	0.01	0.636 (0.15)	0.001 (11.23)	0.9999 (0.00)
±0.001	±0.003	10.096 (0.22)	−0.92	11.139 (0.00)	−0.01	0.640 (0.27)	0.003 (13.46)	0.9990 (0.02)
±0.010	±0.003	10.125 (0.81)	−0.64	11.140 (0.02)	0.00	0.638 (0.78)	0.005 (7.65)	0.9985 (0.02)
±0.005	±0.001	10.185 (0.10)	−0.05	11.140 (0.01)	0.00	0.635 (0.13)	0.001 (7.41)	0.9999 (0.01)
±0.001	±0.0005	10.176 (0.07)	−0.14	11.140 (0.01)	0.00	0.636 (0.08)	0.001 (8.70)	1.0000 (0.00)
±0.010	±0.005	10.143 (0.94)	−0.46	11.138 (0.04)	−0.02	0.637 (0.97)	0.006 (17.45)	0.9976 (0.07)

[a] $A^0_{H_2L} = 0.635$, $A^0_{HL} = 0.635$, $A^0_L = 0.206$, p$K_1 = 10.19$, p$K_2 = 11.14$.

sumed to be acquirable from pH 14 to pH = pK − 2, pK − 1, pK − 0.5, pK and pK + 0.5, with pK = 10. As can be seen, imprecisions and errors increased with decreasing width of the working pH range; the limit for application of this methodology to obtaining experimental data is pH = pK − 0.5.

Calculation of close pK values for diprotic compounds

Figure 1 shows typical $A = f(\mathrm{pH})$ curves for diprotic compounds with similar dissociation constants at various wavelengths. Curve A corresponds to a hypothetical case where $A^0_{H_2L} = A^0_L \neq A^0_{HL}$; curve B to one where $A^0_{H_2L} \neq A^0_L$ and both parameters are greater than or less than A^0_{HL}; curve C to $A_{H_2L} > A^0_{HL} > A^0_L$ or $A^0_{H_2L} < A^0_L < A^0_L$; and curve D to $A^0_{H_2L} \neq A^0_{HL} = A^0_L$ or $A^0_{H_2L} = A^0_{HL} \neq A^0_L$. Each of these four types of curve was studied in terms of the effect of imprecisions in the pH and/or absorbance values and the effect of the similarity between dissociation constants on their calculation from Eqn. 12.

Tables 3–6 show the effect of imprecisions in pH and/or absorbance measurements. As can be seen, the type of curve considered had little influence on the calculations performed with Eqn. 12. As a rule, both errors in the pK values and correlations from the fitting parameters were quite good. However, absorbance imprecisions resulted in larger errors in pK values than did similar pH imprecisions. This is clearly reflected in Fig. 2, which shows the variation of errors in the pK_1 and pK_2 values as a function of imprecisions in pH or absorbance for a type A curve; the other curves behaved similarly in this respect.

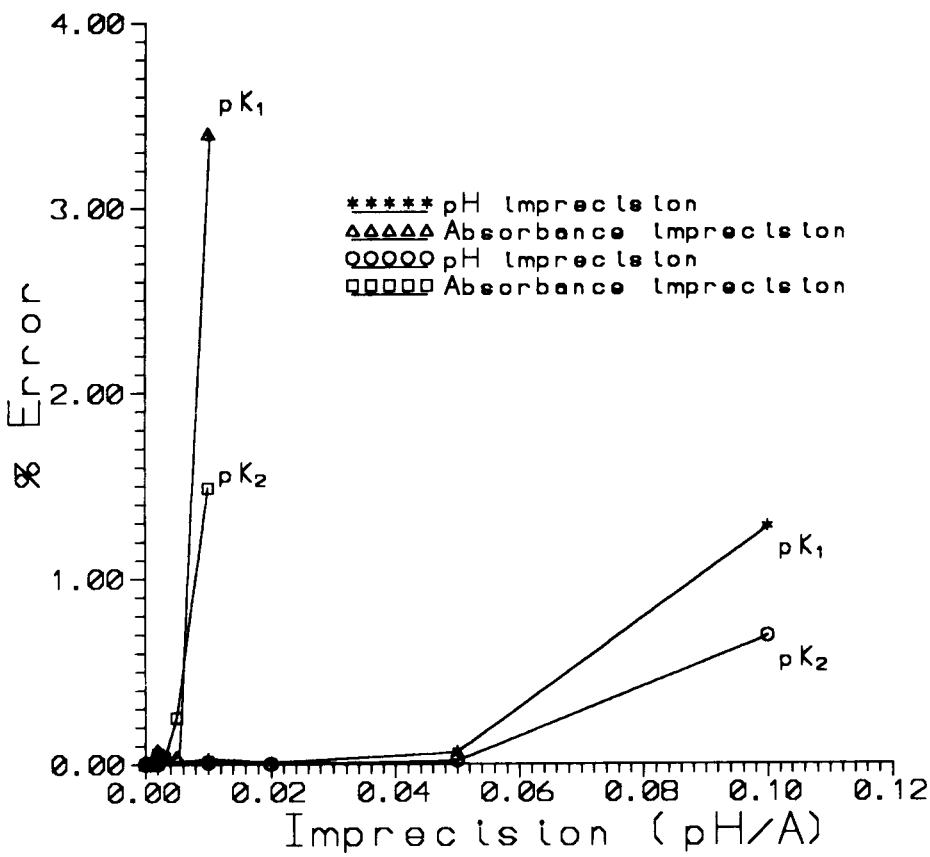

Fig. 2. Errors obtained as a function of absorbance or pH imprecision in the calculation of pK values for diprotic compounds by application of Eqn. 12 to $A = f(\mathrm{pH})$ curves of type A.

TABLE 7

Effect of the similarity of pK values on the calculation of the pKs for a diprotic compound by applying Eqn. 12 to various types of $A = f(\text{pH})$ curves at a pH imprecision of ± 0.001 and an absorbance imprecision of ±0.003 [a]

Curve type	$pK_{1(theo)}$	$pK_{2(theo)}$	ΔpK	pK_1 (%R.S.D.)	E (%)	pK_2 (%R.S.D.)	E (%)	$A^0_{HL(theo)}$	A^0_{HL} (%R.S.D.)	sm (%R.S.D.)	r^2 (% R.S.D.)
A	9.140	11.140	2.000	9.143 (0.07)	0.03	11.138 (0.04)	−0.02	0.635	0.636 (0.09)	0.003 (13.01)	0.9967 (0.06)
A	10.140	11.140	1.000	10.138 (0.11)	−0.02	11.143 (0.04)	0.03	0.635	0.635 (0.38)	0.004 (17.22)	0.9870 (0.39)
A	10.640	11.140	0.500	10.602 (0.71)	−0.36	11.171 (0.46)	0.28	0.635	0.625 (2.68)	0.005 (23.43)	0.9641 (0.97)
A	10.690	10.690	0.000	10.573 (0.83)	−1.09	10.782 (0.55)	0.86	0.635	0.601 (3.57)	0.006 (37.39)	0.9035 (3.92)
B	9.140	11.140	2.000	9.135 (0.15)	−0.06	11.141 (0.02)	0.01	0.635	0.635 (0.20)	0.003 (11.31)	0.9993 (0.01)
B	10.140	11.140	1.000	10.147 (0.09)	0.07	11.140 (0.04)	0.00	0.635	0.636 (0.41)	0.004 (26.66)	0.9978 (0.10)
B	10.640	11.140	0.500	10.634 (0.09)	−0.06	11.143 (0.06)	0.03	0.635	0.633 (0.56)	0.004 (28.57)	0.9970 (0.13)
B	10.690	10.690	0.000	10.649 (0.27)	−0.38	10.710 (0.14)	0.19	0.635	0.622 (1.45)	0.006 (11.75)	0.9923 (0.24)
C	9.140	11.140	2.000	9.139 (0.07)	−0.01	11.140 (0.04)	0.00	0.420	0.420 (0.23)	0.003 (9.65)	0.9991 (0.03)
C	10.140	11.140	1.000	10.131 (0.19)	−0.09	11.130 (0.21)	−0.09	0.420	0.423 (1.77)	0.003 (26.08)	0.9991 (0.02)
C	10.640	11.140	0.500	10.597 (1.16)	−0.40	11.117 (0.86)	−0.21	0.420	0.436 (13.08)	0.004 (21.52)	0.9987 (0.04)
C	10.690	10.690	0.000	10.687 (0.11)	−0.03	10.689 (0.10)	−0.01	0.420	0.422 (2.36)	0.006 (8.00)	0.9980 (0.04)
D	9.140	11.140	2.000	8.201 (9.16)	−10.27	11.137 (0.02)	−0.03	0.635	0.639 (0.00)	0.002 (12.35)	0.9995 (0.01)
D	10.140	11.140	1.000	10.064 (0.49)	−0.75	11.140 (0.01)	0.00	0.635	0.639 (0.37)	0.003 (14.49)	0.9992 (0.02)
D	10.640	11.140	0.500	10.629 (0.15)	−0.10	11.140 (0.03)	0.00	0.635	0.636 (0.27)	0.004 (14.26)	0.9988 (0.01)
D	10.690	10.690	0.000	10.694 (0.29)	0.04	10.691 (0.04)	0.01	0.635	0.633 (0.97)	0.007 (24.16)	0.9975 (0.08)

[a] E = error of fit, sm = mean standard deviation of fit, r = correlation coefficient of fit.

Table 7 shows the effect of similarity in the pK values for the different types of curve considered at an imprecision of ±0.001 in pH and ±0.003 in the absorbance. As can be seen, the calculated pK_2 values were scarcely influenced by the type of curve or the similarity between pK values, the errors being quite small except for those resulting from curve A and identical pK values. On the other hand, pK_1 was markedly influenced by these two variables (e.g., with type D curve and pK values differing by 2 and 1 units, respectively). These observations can be interpreted in the light

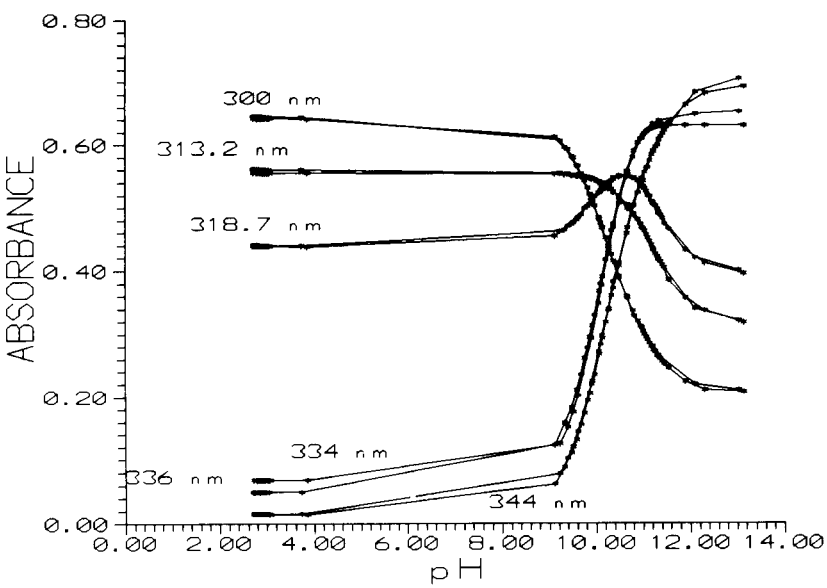

Fig. 3. $A = f(\text{pH})$ curves obtained for 3.74×10^{-5} M maleimide dioxime at various wavelengths.

of Fig. 1 taking into account the pK values to be determined. Since a type D curve is obtained when A^0_{HL} and A^0_L (case 1) or A^0_{HL} and $A^0_{H_2L}$ (case 2) are identical or very similar, the absorbance cannot be substantially altered by approaching a pH close to the pK, so such a pK cannot be determined accurately from measurable data. At a given wavelength where A^0_{HL} is very similar to A^0_L, pK_2 cannot be resolved; in addition, if A^0_{HL} is very similar to $A^0_{H_2L}$, pK_1 cannot be resolved either. As pK_2 approaches pK_1 (case 1) or pK_1 approaches pK_2 (case 2), the resolvable range increases and allows more accurate calculation of both pK values.

Experimental data

Figure 3 shows the $A = f(\text{pH})$ curves obtained at various wavelengths from 3.74×10^{-5} M solutions of maleimide dioxime (pK_1 = 10.12 and pK_2 = 11.11) in butylamine buffer of ionic strength 0.5 M adjusted with KCl. The figure shows some cases of the above-described types of curve for diprotic compounds, the shape of which is a function of the wavelength at which data are acquired. Thus, a wavelength of 318.7 nm gives rise to a type B (nearly type A) curve, while those of 313.2, 334.2 and 336 nm result in a type D curve and those of 344 and 300 nm in a type C curve. Based on previous results obtained with simulated data, type D curves should provide the worst calculated pK values since their actual values differ by only ca. 1 unit. As can be seen in Table 8, the calculated pK values obtained from Eqn. 12 were quite consistent with one another and their theoretical counterparts [10] except for those obtained at 336 and 334 nm, where the calculated pK_1 value was correct, whereas pK_2 was subjected to a large error; on the other hand, at 313.2 nm, the calculated pK_1 was subjected to a major error whereas pK_2 was correct. These findings can be explained in the light of Fig. 3 by taking into account the pK values to be determined and the above reasoning for type D curves. At 336 or 334 nm, A^0_{HL} is very similar to A^0_L, so

TABLE 9

Results obtained by applying the multiple linear regression method to experimental data obtained at 318.7 nm [a]

X_1	X_2	Y_{exp}	Y_{cal}	D
$0.952\times10^{+10}$	-16.916×10^{-13}	0.547	0.549	−0.002
$0.110\times10^{+11}$	-13.438×10^{-13}	0.542	0.543	−0.001
$0.123\times10^{+11}$	-11.266×10^{-13}	0.538	0.537	0.001
$0.134\times10^{+11}$	-94.577×10^{-14}	0.533	0.531	0.002
$0.141\times10^{+11}$	-85.387×10^{-14}	0.530	0.528	0.002
$0.149\times10^{+11}$	-74.545×10^{-14}	0.526	0.523	0.003
$0.153\times10^{+11}$	-63.255×10^{-14}	0.519	0.522	−0.003
$0.163\times10^{+11}$	-58.008×10^{-14}	0.518	0.516	0.002
$0.169\times10^{+11}$	-46.865×10^{-14}	0.510	0.513	−0.003
$0.178\times10^{+11}$	-39.553×10^{-14}	0.505	0.508	−0.003
$0.189\times10^{+11}$	-34.461×10^{-14}	0.502	0.500	0.002
$0.198\times10^{+11}$	-28.853×10^{-14}	0.497	0.495	0.002
$0.204\times10^{+11}$	-24.298×10^{-14}	0.492	0.491	0.001
$0.214\times10^{+11}$	-20.469×10^{-14}	0.488	0.485	0.003
$0.220\times10^{+11}$	-16.798×10^{-14}	0.483	0.481	0.002
$0.218\times10^{+11}$	-11.954×10^{-14}	0.474	0.483	−0.009
$0.246\times10^{+11}$	-72.267×10^{-15}	0.466	0.464	0.002
$0.291\times10^{+11}$	11.462×10^{-15}	0.432	0.433	−0.001
$0.320\times10^{+11}$	15.001×10^{-15}	0.411	0.411	−0.000

[a] $Y_{cal} = 0.641 - 0.72\times10^{-11}X_1 + 0.14\times10^{-11}X_2$. p$K_{2(exp)}$ = 11.143, p$K_{1(exp)}$ = 10.150, A = 0.641, S = 0.0031, r^2 = 0.9925.

TABLE 8

pK values for maleimide dioxime calculated by applying Eqn. 12 to experimental data obtained at various wavelengths

λ (nm)	pK_1	pK_2	A^0_{HL}	$1/\beta^H_1$	β^H_2/β^H_1	s	r^2	A^0_L	$A^0_{H_2L}$
300.0	10.095	11.205	0.319	0.62×10^{-11}	0.12×10^{11}	0.0026	0.9994	0.210	0.646
300.0	10.136	11.283	0.303	0.52×10^{-11}	0.14×10^{11}	0.0023	0.9994	0.207	0.642
313.2	9.559	11.176	0.563	0.67×10^{-11}	0.36×10^{10}	0.0023	0.9971	0.318	0.556
313.2	8.587	11.173	0.555	0.67×10^{-11}	0.39×10^{9}	0.0014	0.9986	0.321	0.562
318.7	10.085	11.291	0.621	0.51×10^{-11}	0.12×10^{11}	0.0021	0.9957	0.400	0.440
318.7	10.150	11.143	0.641	0.72×10^{-11}	0.14×10^{11}	0.0031	0.9925	0.395	0.441
334.2	10.100	11.017	0.668	0.96×10^{-11}	0.13×10^{11}	0.0028	0.9996	0.630	0.069
336	10.083	11.046	0.649	0.90×10^{-11}	0.12×10^{11}	0.0042	0.9994	0.652	0.050
344	10.097	11.251	0.533	0.56×10^{-11}	0.13×10^{11}	0.0057	0.9991	0.705	0.016
344	10.115	11.189	0.527	0.65×10^{-11}	0.13×10^{11}	0.0061	0.9990	0.692	0.016

pK_2 cannot be correctly resolved. At 313.2 nm, A^0_{HL} is very similar to $A^0_{H_2L}$, so pK_1 cannot be correctly resolved. By way of example, Table 9 shows one of the result listings provided by the multilinear regression programme applied to experimental data measured at 318.7 nm.

Conclusions

The new methodology, of general use for calculation of acid–base dissociation constants of monoprotic and diprotic compounds by absorptiometric and pH measurements allows, the pK of monoprotic substances to be accurately determined from equations similar to those previously derived by Sommer. With diprotic substances, the proposed methodology allows similar dissociation constants to be determined without the need an for $A = f(pH)$ curve of a given shape by using quite straightforward calculations. Simulated processes subsequently validated with experimental data showed the methodology to be much more markedly influenced by imprecisions in absorbance than in pH values; also, with the different possible $A = f(pH)$ curves one can obtain, only if the intermediate species has a similar absorptivity to that of the protonated or deprotonated species are the pK values obtained (one or both) incorrect.

The authors wish to thank the Spanish DGICyT for financial support received for the realization of Project PB90-0359.

REFERENCES

1 J.C. Speakman, J. Chem. Soc., (1940) 855.
2 M. Prytz, Z. Anorg. Allg. Chem., 172 (1928) 147.
3 A. Albert and E.P. Serjeant, The Determination of Ionization Constants, Chapman and Hall, London, 1971.
4 E.W. Wentworth and W. Hirsch, J. Phys. Chem., 71 (1967) 218.
5 G. Heys, H. Kinns and D.D. Perrin, Analyst, 97 (1972) 52.
6 R. Hanus, Anal. Chim. Acta, 90 (1977) 167.
7 R.A. Robinson and A.I. Biggs, Aust. J. Chem., 10 (1957) 128.
8 B.J. Thamer and A.F. Voigt, J. Phys. Chem., 56 (1952) 225.
9 K.P. Ang, J. Phys. Chem., 62 (1958) 1109.
10 M.L. Albelda, V. Cerdà and C. Mongay, Bull. Soc. Chim. Fr., 1 (1982) 19.
11 A.G. Asuero, J.L. Jiménez-Trillo and M.J. Navas, Talanta, 33 (1986) 531.
12 A.G. Asuero, J.L. Jiménez-Trillo and M.J. Navas, Talanta, 33 (1986) 929.
13 L. Sommer, Folia Fac. Sci. Nat. Univ. Purkynianae Brun., 5 (1964) 1.
14 B. Budensinsky, Talanta, 16 (1969) 1277.

Analytica Chimica Acta, 286 (1994) 265–270
Elsevier Science B.V., Amsterdam

Synthesis of bisthiacrown ethers and their liquid–liquid extraction of copper(I)

Yong Qin and Jiqiu Yang

Chengdu Institute of Organic Chemistry, Academia Sinica, P.O. Box 415, Chengdu 610015 (China)

(Received 27th April 1993; revised manuscript received 16th September 1993)

Abstract

Five new bisthiacrown ethers bearing 7-aza-1,4,10,13-tetrathiacyclohexadecane were succesfully synthesized. A study of the extraction equilibria for copper(I) in the presence of picrate shows that copper(I) is extracted in the form of a 1:1 ion-pair $[ML]^+pic^-$ complex. The extraction constants, log K_{ex}, for copper(I) with these thiacrown ethers are in the range 6.46–8.05. The extractabilities of the thiacrown ethers with respect to class a, b and ab metals were examined. Class b metals except cadmium(II) could be well extracted. The relationship between the structure of bisthiacrown ethers and their complexing ability is discussed in detail.

Keywords: Bisthiacrown ethers; Copper; Extraction

It is well known that some transitional metals and heavy metals form complexes with thiacrown ethers [1,2]. The complexing properties of thiacrown ethers with respect to transitional metal cations have been studied in recent years and some of these complexes have been isolated and characterized [3–8]. In addition, studies of extraction equilibria for silver(I), mercury(II) and copper(I) with monothiacrown ethers have been reported [2,9–13]. However, few studies of extraction equilibria for transitional metal cations with bisthiacrown ethers have been published [14–16]. These facts stimulated interest in the examination of the complexing properties of bisthiacrown ethers with respect to transitional metals by liquid–liquid extraction.

This paper reports the syntheses of some new bisthiacrown ethers (**2–6**) bearing 7-aza-1,4,10,13-tetrathiacyclohexadecane (**1**) moieties, their extraction equilibria for copper(I) and the results of complexing with some transition metals such as Cu^+, Ag^+, Pd^{2+}, Cd^{2+}, Au^{3+}, Co^{2+}, Ni^{2+}, Zn^{2+} and Cu^{2+} and with the alkali metal Cs^+. The differences in extractability between **1** and **2–6** are discussed.

The monothiacrown ether 7-aza-1,4,10,13-tetrathiacyclohexadecane (**1**) and its derivatives **2–6** were synthesized according to Scheme 1.

Correspondence to: Jiqiu Yang, Chengdu Institute of Organic Chemistry, Academia Sinica, P.O. Box 415, Chengdu 610015 (China).

EXPERIMENTAL

Reagents

Reagents for synthesis were commercially available. Metal sulphates and metals of quaranteed reagent grade were used to prepare 1×10^{-2} M stock solutions, which then were standardized by EDTA titration. Other reagents used in extraction were of analytical-reagent grade. Picric acid was dried with P_2O_5 before use. Analytical-reagent grade chloroform was shaken with concentrated sulphuric acid followed by water three

SSDI 0003-2670(93)E0562-L

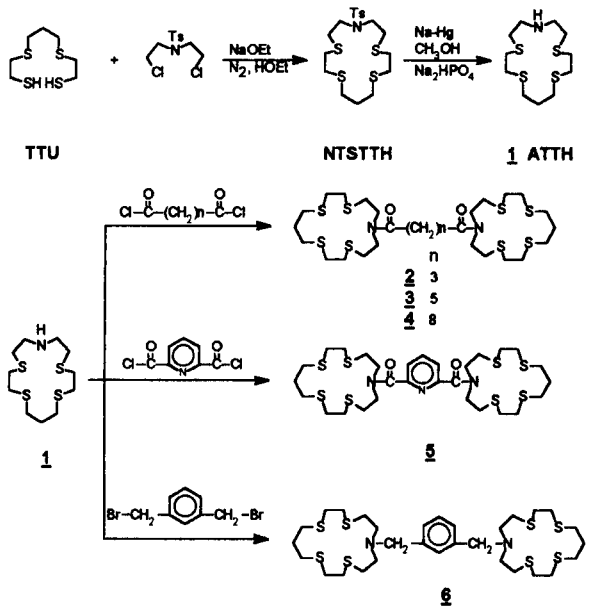

Scheme 1. Synthetic routes.

times, then dried over anhydrous calcium chloride and distilled, the b.p. 61°C fraction being collected. Ligand solutions were prepared just before use.

Apparatus

Melting points were uncorrected. IR spectra were measured with a Nicolet MX-1, ^{1}H NMR spectra with a Varian FT-80A and mass spectra with a Finnigan MAT 4510 spectrometer. Elemental analyses were performed with a Carlo Erba Model 1106 instrument. Extraction was done using a JingHua SHZ-82 shaker at 20°C. A ShengYang WYZ-402 atomic absorption spectrometer was used to determine the concentrations of transition metals. The pH of the aqueous phase was measured with a ShangHai pH29-C pH meter.

Syntheses

1,4,8,11-Tetrathiaundecane (TTU) was prepared by the general procedure described by Rosen and Bush [1].

N-Tosylamido-7-aza-1,4,10,13-tetrathiacyclohexadecane (NTSTTH). TTU (10 g, 0.044 mol) was added to absolute ethanol (500 ml) in which sodium metal (2.50 g, 0.1 mol) had been dissolved. *N*-Tosylamido-β,β'-dichloroethylamine (15 g, 0.05 mol) was dissolved in 500 ml of absolute ethanol. These two solutions were simultaneously added dropwise to hot absolute ethanol (500 ml, 65–75°C) under N_2 over 3 h, during which period a white precipitate formed. Reaction was continued for a further 1 h at this temperature and then the volume was concentrated to about 300 ml and filtered at once. On cooling, a white solid was deposited, which was filtered and recrystallized from ethanol to give the product (5.6 g, 27.0%), m.p. 104.5–105.5°C. Elemental analysis: found, C 48.44, H 6.45, N 3.39, S 35.02; $C_{18}H_{29}NO_2S_5$ requires C 47.86, H 6.47, N 3.10, S 35.49%. IR (KBr, cm^{-1}): 2930(m), 2900(m), 2840(w), 1594(w), 1450(m), 1340(s), 1150(s). ^{1}H NMR ($CDCl_3$, TMS): 1.90 (m, 2H, $SCH_2CH_2CH_2S$), 2.35–2.80 (m, 19H, SCH_2, $ArCH_2$), 3.30 (tri, 4H, NCH_2), 7.50 (m, 4H, Ar-H). MS (*m/z*): 451 (M^+).

7-Aza-1,4,10,13-tetrathiacyclohexadecane (1). Under N_2, NTSTTH (29.0 g, 0.064 mol) and Na_2HPO_4 (10.0 g, 0.134 mol) were added to 200 ml of methanol. While the mixture slowly refluxed, 110 g of 10% sodium amalgam were added over 24 h. The mercury was separated out after reaction. The solution was evaporated under reduced pressure to give a colourless oil, which slowly solidified when washed with water. The solid was recrystallized from Et_2O. The pure product (16.2 g, 84.8%) was obtained, m.p. 31–32°C. Elemental analysis: found, C 44.72, H 7.93, N 4.57, S 41.32; $C_{11}H_{23}NS_4$ requires C 44.40, H 7.76, N 4.70, S 43.10%. IR (KBr, cm^{-1}): 3265(w), 2902(s), 2814(s), 1437(s). ^{1}H NMR ($CDCl_3$, TMS): 1.80 (m, 2H, $SCH_2CH_2CH_2S$), 1.98 (s, 1H, absent on adding D_2O), 2.72 (m, 20H, SCH_2). MS (*m/z*): 298 (M + 1).

Bisthiacrown ethers (2–6). The following representative procedure was used in the syntheses of bisthiacrown ethers. The reagents used in the syntheses of **2–6** were glutaryl chloride, pimelyl chloride, sebacyl chloride, dipicolinyl chloride and 1,3-dibromoxylene, respectively.

Bis(7-aza-1,4,10,13-tetrathiacyclohexadecane)-glutaric amide (2). To a mixture of 1.188 g (4

mmol) of **1** and 0.80 g (8 mmol) of triethylamine dissolved in 15 ml of dry benzene was added dropwisely 10 ml of a solution containing 0.338 g of glutaryl chloride at room temperature over 1 h. The mixture was refluxed for 4 h and then benzene was evaporated under reduced pressure and the residue was dissolved in 50 ml of chloroform. The solution was washed with 7% HCl, water and dilute ammonia solution and then again with water to neutrality and dried over anhydrous $MgSO_4$. After the solution had been filtered and evaporated, a reddish oil is remained. The residue was purified by chromatography on silica gel with $CHCl_3$–5% CH_3OH to give the crude product. Further purification was done by recrystallization from Et_2O very slowly, giving a white solid (0.635 g, 46.0%), m.p. 80–82°C. Elemental analysis: found, C 47.33, H 7.32; N 3.88; $C_{27}H_{50}N_2O_2S_8$ requires C 46.92, H 7.29, N 4.05%. IR (KBr, cm^{-1}): 2990(m), 2920(s), 2850(m), 1640(s), 1420(s), 1360(m), 1200(m), 1150(m). ^1H NMR ($CDCl_3$, TMS): 1.70–2.00 (m, 6H, $COCH_2CH_2CH_2CO$, $SCH_2CH_2CH_3S$), 2.35 (m, 4H, $COCH_2$), 2.50–2.85 (m, 32H, CH_2S), 3.25–3.65 (m, 8H, NCH_2). MS (*m/z*, field desorption (FD)): 691 (M^+).

Bis(7-aza-1,4,10,13-tetrathiacyclohexadecane)-pemelic amide (3). The residue was purified by recrystallization from acetone–diethyl ether to give 1.018 g (70.7%) of white solid, m.p. 97–98°C. Elemental analysis: found, C 48.64, H 7.67, N 3.84; $C_{29}H_{54}N_2O_2S_8$ requires C 48.43, H 7.57, N 3.90%. IR (KBr, cm^{-1}): 2950(m), 2920(s), 2850(m), 1649(s), 1465(m), 1450(s), 1430(s), 1360(m), 1285(m), 1170(s), 1146(m). ^1H NMR ($CDCl_3$, TMS): 1.35–2.00 (m, 10H, $-SCH_2CH_2CH_2S$, $COCH_2(CH_2)_3CH_2CO$), 2.25 (tri, 4H, $COCH_2$), 2.50–290 (m, 32H, CH_2S), 3.45 (m, 8H, $CONCH_2$). MS (*m/z*, FD): 719 (M^+).

Bis(7-aza-1,4,10,13-tetrathiacyclohexadecane)-sebacic amide (4). The residue was purified by chromatography on silica gel with $CHCl_3$–2% CH_3OH to give crude product, which was further purified by very slow recrystallization from Et_2O, giving a white solid (0.775 g, 50.9%), m.p. 88–90°C. Elemental analysis: found, C 50.51, H 8.42, N 3.57, S 32.42; $C_{32}H_{60}N_2O_2S_8$ requires C 50.48, H 7.94, N 3.68, S 33.69%. IR (KBr, cm^{-1}); 2900(m), 2830(s), 1640(s), 1440(s), 1420(s), 1360(m), 1280(m), 1250(m), 1200(s), 1750(s). ^1H NMR ($CDCl_3$, TMS): 1.25 (m, 8H, $COCH_2(CH_2)_6CH_2CO$), 155 (m, 4H, $COCH_2CH_2$), 1.85 (m, 4H, $SCH_2CH_2CH_2S$), 2.25 (tri, 4H, $COCH_2$), 3.00–3.30 (m, 32H, CH_2S), 3.45 (m, 8H, $CONCH_2$). MS (*m/z*, FD): 661 (M^+).

Bis(7-aza-1,4,10,13-tetrathiacyclohexadecane)-dipicolinic amide (5). The residue was purified by recrystallization from acetone–light petroleum to give a white solid (0.465 g, 64.0%), m.p. 118–119°C. Elemental analysis: found, C 47.59, H 6.52, N 5.45, S 34.94; $C_{29}H_{47}N_2O_2S_8$ requires C 47.96, H 6.52, N 5.79, S 35.32%. IR (KBr, cm^{-1}): 3060(w), 2920(m), 2840(w), 1640(w), 1580(w), 1565(w), 1470(m), 1430(m), 1140(m), 840(w), 750(w). ^1H NMR ($CDCl_3$, TMS): 1.85 (m, 4H, $SCH_2CH_2CH_2S$), 2.50–3.00 (m, 32H, CH_2S), 3.10 (m, 8H, $CONCH_2$), 7.50–7.90 (m, 3H, Ar-H). MS (*m/z*, FD): 726 (M^+).

Bis(7-aza-1,4,10,13-tetrathiacyclohexadecane)-1,3-xylene (6). The residue was purified by chromatography on silica gel with ethyl acetate–light petroleum (3 + 1) to give a light orange oil (2.315 g, 55.4%). Elemental analysis: found, C 51.75, H 7.48, N 3.82; $C_{30}H_{52}N_2S_8$ requires C 51.68, H 7.51, N 4.02. IR (film, cm^{-1}): 3020(w), 2940(s), 2910(s), 2805(s), 1600(w), 1580(w), 1430(s), 1200(s), 1120(s). ^1H NMR ($CDCl_3$, TMS): 1.85 (m, 4H, $SCH_2CH_2CH_2S$), 2.50–2.85 (m, 40H, SCH_2, NCH_2), 3.65 (s, 4H, $ArCH_2N$), 7.30 (m, 4H, Ar-H). MS (*m/z*, FD): 697 (M^+).

Liquid–liquid extraction of copper(I)

An aliquot (4 ml) of aqueous solution containing copper(II) ion (5×10^{-5} M), picrate ion, acetate buffer solution and sufficient hydroxylammonium sulphate (1×10^{-3} M) as reducing agent was placed in a 10-ml cylindrical glass tube fitted with a glass stopper. The ionic strength was adjusted as 0.1 with sodium sulphate. In studying the effect of pH on the extraction behaviour, the buffer solution was prepared with nitric acid (pH 3) or acetic acid and sodium acetate (pH 3–7) or lithium hydroxide (pH 7). After the addition of 4 ml of bisthiacrown ether solution in chloroform, the mixture was shaken for 30 min at 25°C and then centrifuged. The pH of the aqueous phase was measured and the concentration of copper in

aqueous phase was determined by atomic absorption spectrometry.

RESULTS AND DISCUSSION

Synthesis of ligands

The reaction time and yield of **1** are affected by the content of sodium amalgam. For example, when 3% sodium amalgam was used, the reaction time and yield were 39 h and 80.7% respectively, but when 10% sodium amalgam was used, the reaction time was shortened to 24 h and the yield was enhanced to 84.8%. It is very difficult to purify **2** and **4** without chromatography followed by recrystallization. In particular, the process of recrystallization from Et_2O is time consuming; the reddish crude product was sopped in Et_2O and white crystals formed on the flask wall after several weeks. However the recrystallization of **2** and **4** with other solvents was unsuccessful.

Effect of pH on extraction behaviour

The extraction of copper(I) with **1–6** from aqueous solution containing 5×10^{-4} M picrate ion into chloroform was examined in the pH range 2–8. A plot of the logarithmic distribution ratio of copper(I) against the pH of the aqueous phase is shown in Fig. 1. Different features appear between the bisthiacrown ethers **2–5** with an amide group in the bridge chain and the bisthiacrown ether **6** with an alkyl group in the bridge chain. The extractability of copper(I) is constant at 98% (log $D = 1.79$) with ligand **1** above pH 4.8, at 99% (log $D = 2$) with ligand **6** above pH 5.2 and decreases rapidly below pH 5 until becoming constant below about pH 3.6 (Fig. 1A). This pH dependence is similar to that for the extraction of copper(I) with other monothiacrown ethers [2,11]. However, when bisthiacrown ethers **2–5** are used, the extractabilty of copper(I) is constant at 15% (log $D = -0.78$) below pH 3.5 and increases slowly above pH 3.5 (Fig. 1B). Perhaps there are two main reasons for this pH dependence. First, the decrease in the extractabilty may be attributed to the decrease in the reducing power of hydroxylammonium sulphate in a highly acidic medium. Second, the difference between ligands

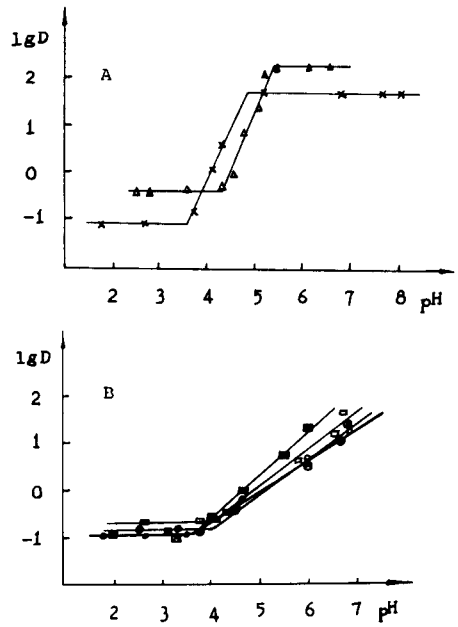

Fig. 1. Plots of log D vs. pH. Initial concentrations: 5×10^{-5} M copper(I), 5×10^{-4} M picrate, 2×10^{-3} M ligand **1** and 1×10^{-3} M ligands **2–6**. × = **1**; ○ = **2**, ⊗ = **3**; □ = **4**; ⊠ = **5**; △ = **6**.

1, **6** and **2–5** with regard to the pH dependence may be due to the protonation of ligands **1** and **6** (amines) in a highly acidic medium, whereas, the ligands **2–5** are amides and no protonation occurs in aqueous solution. The differences in the thiacrown ether structure between ligands **1**, **6** and **2–5** result in a large difference in the pH dependence.

Dependence on concentrations of the ligand and picrate

The extraction equilibria are shown in Fig. 2. The extraction constant K_{ex} is defined by the following equations:

$$Cu^+ + mL(o) + n pic^-_w \overset{K_{ex}}{\rightleftharpoons} CuL_m(pic)_n(o) \quad (1)$$

$$K_{ex} = [CuL_m(pic)_n]_o / [Cu^+][L]^m_o [pic^-]^n_w \quad (2)$$

$$\log D = \log K_{ex} + m \log[L]_o + n \log[pic^-]_w \quad (3)$$

The dependence on the concentrations of the ligand and picrate at pH 5.7 was examined. The relationship between the logarithmic ditribution

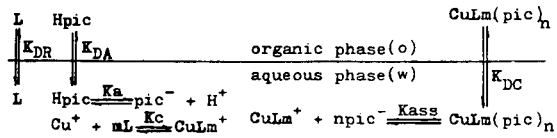

Fig. 2. Equilibria of liquid–liquid distribution.

ratio (log D) and the logarithm of the picrate concentration in the aqueous phase is shown in Fig. 3A and the plots of log D vs. the logarithm of the ligand concentration in organic phase are shown in Fig. 3B. All the plots are straight lines with slopes close to unity in Fig. 3A. The straight lines for **3–6** in Fig. 3B also have slopes close to unity, which means that $m = 1$ and $n = 1$ in the extraction of copper(I) with ligands **3–6**. Copper(I) ion forms a $[CuL]^+$ complex with ligands and then the ion pair is in the $[CuL]^+pic^-$ form, in other words, ligands **3–6** form 1:1 [ligand:copper(I)] sandwich-type complexes with copper(I). In Fig. 3B, the slopes for ligands **1** and **2** are greater than unity, which means that ligands **1** and **2** form both 1:1 and 2:1 [ligand:copper(I)] complexes with copper(I) and the plots represent a transition phase from 1:1 to 2:1 complex formation. Although ligand **2** consists of two crown ether moieties in same molecule, it can complex copper(I) either by means of the two moieties in same molecule or by means of the two moieties in different molecules. For bisthiacrown ethers **2–6**, the values of log K_{ex} were calculated from Eqn. 3 and the results are shown in Fig. 3A and B for each ligand. The log K_{ex} values given for **2–5** in Table 1 are only suitable for the extraction constant at pH 5.7. The order of log K_{ex} values is **6** > **5** > **4** > **3** > **2**.

Liquid–liquid extraction of various metals with ligands 1–6

The following metals were examined: class a metal, Cs^+; class b metals, Cu^+, Ag^+, Pd^{2+}, Cd^{2+} and Au^{3+}; and class ab metals, Co^{2+}, Ni^{2+}, Zn^{2+} and Cu^{2+}. The results for the extraction with ligands **1–6** into chloroform in the presence of picrate are given in Table 2. All experiments were carried out under the same conditions so that the results obtained can be mutually compared. As shown in Table 2, the extractions of class b metals such as Cu^+ and Ag^+ with these mono- and bisthiacrown ethers are excellent, but those of class a and ab metals are very poor. This is in accordance with HSAB theory. The more the aliphatic chain lengths of ligands **2–4** increase, the more their extractabilities with respect to various metals are enhanced. For class b metals (except Au^{3+}), bisthiacrown ethers except **2** are better than the corresponding mono-

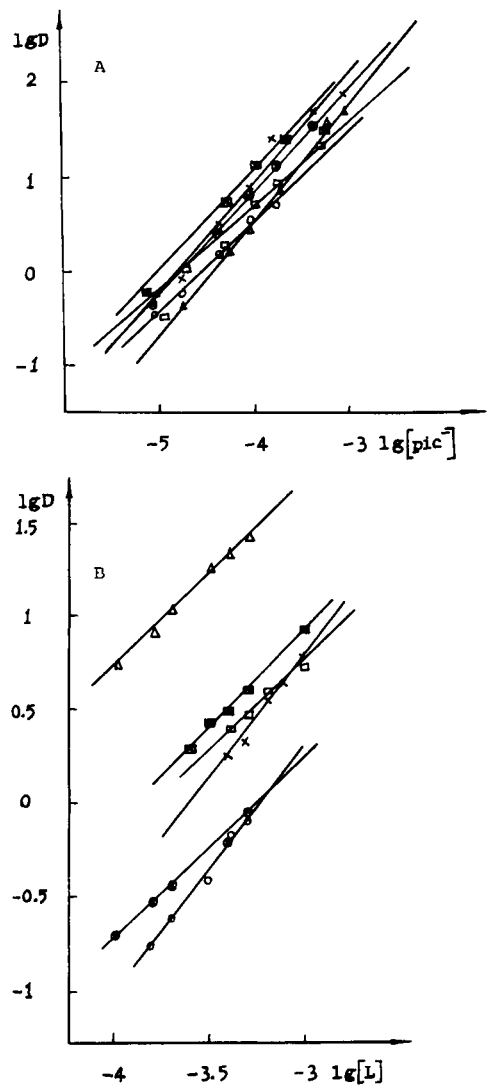

Fig. 3. Plots of log D vs. log[ligand] and log D vs. [picrate] at pH 5.7. Initial concentrations: (A) 5×10^{-5} M copper, 2×10^{-3} M ligand **1** and 1×10^{-3} M ligands **2–6** and (B) 5×10^{-4} M picrate. × = **1**; ○ = **2**; ⊗ = **3**; □ = **4**; ⊠ = **5**; △ = **6**.

TABLE 1

Extraction constants for copper(I) with ligands **1–6**

Ligand	**1**	**2**	**3**	**4**	**5**	**6**
Log K_{ex}	7.06	6.46	6.58	7.08	7.24	8.25

thiacrown ether **1** with respect to extractability. In contrast, for class ab metals, monothiacrown ether **1** is better than the bisthiacrown ether **2–6**. In comparison with the other bisthiacrown ethers, the chain length of bisthiacrown ether **2** is too short to complex metals well as it has two thiacrown ether moieties and each moiety sterically hinders the other moiety in the same molecule. This indicates that an adquate chain length is required. Comparing the results of the extractability among these bisthiacrown ethers **2–6**, **6** with an alkyl chain is the best.

Conclusion

This study of extraction equilibria with ligands **1–6** for copper(I) in the presence of picrate has shown that bisthiacrown ethers **3–6** extract copper(I) in the form of a 1 : 1 [ligand : copper(I)] ion pair $[ML]^+pic^-$ complex whereas monothiacrown ether **1** and bisthiacrown ether **2** extract copper(I) in a transition phase from 1 : 1 to 2 : 1 complex formation. Class b metals except for Cd(II) can be more efficiently extracted with **1–6**, with bisthiacrown ethers than with monothiacrown ethers and the efficiency increases with increasing chain length. It is better to bridge the two thiacrown ether moieties via an alkyl chain than via an amide group.

TABLE 2

Extraction of various metals in the presence of picrate with ligands **1–6** [a]

M	Class [17]	R (Å) [b]	pH	1	2	3	4	5	6
Cu^+	b	0.96	5.7	95.4	89.9	91.4	94.5	95.9	98.6
			4.2	20.5	7.3	8.3	12.9	14.8	38.1
Ag^+	b	1.13	5.7	97.4	97.0	99.2	99.5	99.0	99.7
Pd^{2+}	b	0.80	5.7	1.5	15.8	23.6	33.4	3.64	74.2
Cd^{2+}	b	0.99	5.7	1.7	1.7	2.6	2.6	2.6	2.6
Au^{3+}	b	0.85	5.7	74.7	40.8	43.7	36.7	40.8	66.5
Co^{2+}	ab	0.82	5.7	13.0	2.3	5.3	7.6	9.1	9.1
Ni^{2+}	ab	0.78	5.7	3.9	1.1	1.1	2.8	0	0
Zn^{2+}	ab	0.83	5.7	5.7	0	0	0	0	0
Cu^{2+}	ab	0.72	5.7	35.9	9.2	10.2	14.2	9.2	47.7
Cs^+	a	1.70	5.7	0	0	0	0	0	0

[a] Initial concentrations: 5×10^{-5} M M^{n+}, 5×10^{-4} M picrate, 2×10^{-3} M ligand **1**, 1×10^{-3} M ligands **2–6**. $I = 0.1$, pH = 5.7.
[b] The value for Cu^+ is the Pauling radius; other values are the Goldschmidt radius.

REFERENCES

1 W. Rosen and D.H. Bush, J. Am. Chem. Soc., 91 (1969) 4694.
2 K. Saito, Y. Masuda and E. Sekido, Anal. Chim. Acta, 151 (1983) 447.
3 S.G. Murray and F.G. Hartley, Chem. Rev., 81 (1981) 365.
4 V.B. Pett, L.L. Diaddario, Jr., E.R. Dokal, P.W.R. Corfield, C. Ceccarelli, M.D. Glick, L.A. Ochrymowycz and D.B. Rorabacher, Inorg. Chem., 22 (1983) 3661.
5 L.L. Diaddario, Jr., E.R. Dockal, M.D. Glick, L.A. Ochrymowycz and D.B. Rorabacher, Inorg. Chem., 24 (1985) 356.
6 B. De Groot, G.S. Hanan and S.J. Loeb, Inorg. Chem. 30 (1991) 2644.
7 H.J. Kim, J.H. Jeong and Y. Do, Bull. Korean Chem. Soc, 13 (1992) 463.
8 S.R. Cooper, S.L. Rawle, R. Yagbasan and D.J. Watkin, J. Am. Chem. Soc., 113 (1991) 1600.
9 E. Sekido, K. Chayama and M. Murio, Talanta, 32 (1985) 797.
10 T. Kumagai and S. Akabori, Chem. Lett., (1985) 1667.
11 K. Saio, S. Murakami and A. Muromatsu, Anal. Chim. Acta, 237 (1990) 245.
12 A.Yu. Nazarenko, V.V. Sukhan, V.M. Timoshenko and V.N. Kalinin, Zh. Neorg. Khim., 35 (1990) 2971.
13 N.A. Pasekova, I.V. Pletnev and E.V. Malkhasyan, Zh. Neorg. Khim., 36 (1991) 2971.
14 M. Oue, A. Ishigaki, Y. Matsui, T. Maeda, K. Kimura and T. Shono, Chem. Lett., (1982) 275.
15 M. Oue, A. Ishigaki, K. Kimura, Y. Matsui and T. Shono, J. Polym. Sci., 23 (1985) 2033.
16 M. Oue, K. Kimura and T. Shono, Anal. Chim. Acta, 194 (1987) 293.
17 S. Ahrland, J. Chatt and N.R. Davies, Q. Rev. Chem. Soc., 12 (1958) 265.

Capillary Electrophoresis

Principles, Practice and Applications

by **S.F.Y. Li**, *National University of Singapore, Singapore*

Journal of Chromatography Library Volume 52

Capillary Electrophoresis (CE) has had a very significant impact on the field of analytical chemistry in recent years as the technique is capable of very high resolution separations, requiring only small amounts of samples and reagents. Furthermore, it can be readily adapted to automatic sample handling and real time data processing. Many new methodologies based on CE have been reported. Rapid, reproducible separations of extremely small amounts of chemicals and biochemicals, including peptides, proteins, nucleotides, DNA, enantiomers, carbohydrates, vitamins, inorganic ions, pharmaceuticals and environmental pollutants have been demonstrated. A wide range of applications have been developed in greatly diverse fields, such as chemical, biotechnological, environmental and pharmaceutical analysis.

This book covers all aspects of CE, from the principles and technical aspects to the most important applications. It is intended to meet the growing need for a thorough and balanced treatment of CE. The book will serve as a comprehensive reference work and can also be used as a textbook for advanced undergraduate and graduate courses. Both the experienced analyst and the newcomer will find the text useful.

Contents:

1. Introduction. Historical Background. Overview of High Performance CE. Principles of Separations. Comparison with Other Separation Techniques. **2. Sample Injection Methods.** Introduction. Electrokinetic Injection. Hydrodynamic Injection. Electric Sample Splitter. Split Flow Syringe Injection System. Rotary Type Injector. Freeze Plug Injection. Sampling Device with Feeder. Microinjectors. Optical Gating. **3. Detection Techniques.** Introduction. UV-Visible Absorbance Detectors. Photodiode Array Detectors. Fluorescence Detectors. Laser-based Thermooptical and Refractive Index Detectors. Indirect Detection. Conductivity Detection. Electrochemical Detection. Mass Spectrometric Detection. **4. Column Technology.** Uncoated Capillary Columns. Coated Columns. Gel-filled Columns. Packed Columns. Combining Packed and Open-Tubular Column. **5. Electrophoretic Media.** Electrophoretic Buffer Systems. Micellar Electrokinetic Capillary Chromatography. Inclusion Pseudophases. Metal-complexing Pseudophases. Other Types of Electrophoretic Media. **6. Special Systems and Methods.** Buffer Programming. Fraction Collection. Hyphenated Techniques. Field Effect Electroosmosis. Systematic Optimization of Separation. **7. Applications of CE.** Biomolecules. Pharmaceutical and Clinical Analysis. Inorganic Ions. Hydrocarbons. Foods and Drinks. Environmental Pollutants. Carbohydrates. Toxins. Polymers and Particles. Natural Products. Fuel. Metal Chelates. Industrial Waste Water. Explosives. Miscellaneous Applications. **8. Recent Advances and Prospect for Growth.** Recent Reviews in CE. Advances in Injection Techniques. Novel Detection Techniques. Advances in Column Technology. Progress on Electrolyte Systems. New Systems and Methods. Additional Applications Based on CE. Future Trends.

References. Index.

1992 608 pages Hardbound
US$ 225.75 / Dfl. 395.00
ISBN 0-444-89433-0
1993 608 pages Paperback
Price: US$ 114.25 / Dfl. 200.00
ISBN 0-444-81590-2

"Everything seems to be there, any detection system you have ever dreamed of, any capillary coating, enough electrolyte systems to saturate your wits, and more..."

"...by far the most thorough and comprehensive book in the field yet to appear."

P.G. Righetti, Milan

ELSEVIER SCIENCE B.V.

ORDER INFORMATION

For USA and Canada
ELSEVIER SCIENCE INC.
P.O. Box 945
Madison Square Station
New York, NY 10160-0757
Fax: (212) 633 3880

In all other countries
ELSEVIER SCIENCE B.V.
P.O. Box 330
1000 AH Amsterdam
The Netherlands
Fax: (+31-20) 5862 845

US$ prices are valid only for the USA & Canada and are subject to exchange rate fluctuations; in all other countries the Dutch guilder price (Dfl.) is definitive. Customers in the European Community should add the appropriate VAT rate applicable in their country to the price(s). Books are sent postfree if prepaid.

ANABIOTEC 94

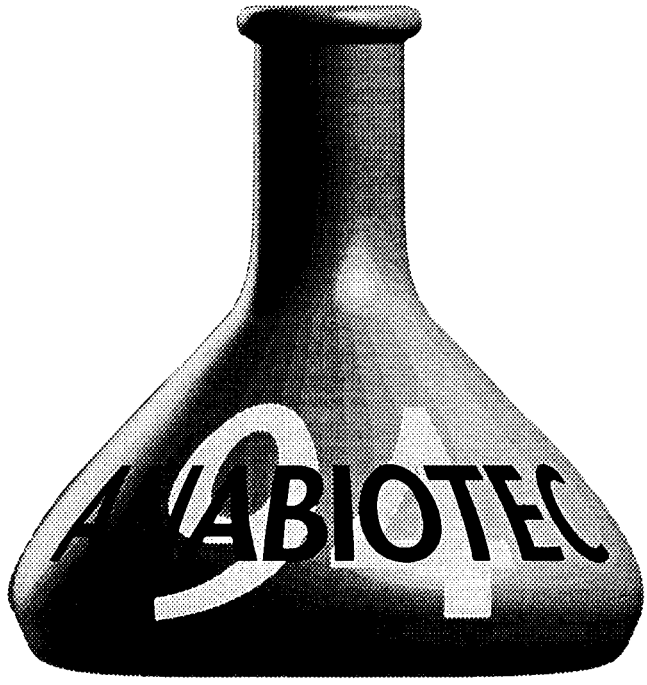

5th International Symposium on Analytical Techniques, Systems & Strategies in Biotechnology

---

31 October – 2 November 1994

Minneapolis Hilton & Towers, US

Learn of the new instruments and techniques for analytical chemistry
Improve monitoring of industrial scale processes
Update your strategies for clinical diagnosis
Meet international colleagues and contacts

The analytical chemistry of complex matrices involving species of a biological origin is a rapidly developing research frontier.

ANABIOTEC 94 – consisting of plenary sessions, selected original papers, posters and an exhibition – will address the wide array of research issues involved in this field. This symposium is the ideal forum for information exchange between the fields of analytical chemistry, biochemistry, clinical chemistry and biotechnology: you need to be there!

For further information send a copy of this advert, complete with your address details to:

Anabiotec 94 Conference Secretariat, Elsevier Science Ltd,
PO Box 150, Kidlington, Oxford OX5 1AS, UK.
Tel: +44 (0) 865 512242
Fax: +44 (0) 865 310981

PUBLICATION SCHEDULE FOR 1994

	S'93	O'93	N'93	D'93	J	F	M	A	M			
Analytica Chimica Acta	281/1 281/2 281/3	282/1 282/2 282/3	283/1 283/2	283/3 284/1 284/2	284/3 285/1–2 285/3	286/1 286/2 286/3	287/1–2 287/3 288/1	288/2 288/3 289/1	289/2–3 290/1 290/2			
Vibrational Spectroscopy		6/1			6/2		6/3		7/1			

INFORMATION FOR AUTHORS

Detailed "Instructions to Authors" for *Analytica Chimica Acta* was published in Volume 256, No. 2, pp. 373–376. Free reprints of the "Instructions to Authors" of *Analytica Chimica Acta* and *Vibrational Spectroscopy* are available from the Editors or from: Elsevier Science B.V., P.O. Box 330, 1000 AH Amsterdam, The Netherlands. Telefax: (+31-20) 5862459.

Manuscripts. The language of the journal is English. English linguistic improvement is provided as part of the normal editorial processing. Authors should submit three copies of the manuscript in clear double-spaced typing on one side of the paper only. *Vibrational Spectroscopy* also accepts papers in English only.

Rapid publication letters. *Letters* are short papers that describe innovative research. Criteria for letters are novelty, quality, significance, urgency and brevity. Submission data: max. of 2 printed pages (incl. Figs., Tables, Abstr., Refs.); short abstract (e.g., 3 lines); *no* proofs will be sent to the authors; submission on floppy disc; *no* revision will be possible.

Abstract. All papers and reviews begin with an Abstract (50–250 words) which should comprise a factual account of the contents of the paper, with emphasis on new information.

Figures. Figures should be prepared in black waterproof drawing ink on drawing or tracing paper of the same size as that on which the manuscript is typed. One original (or sharp glossy print) and two photostat (or other) copies are required. Attention should be given to line thickness, lettering (which should be kept to a minimum) and spacing on axes of graphs, to ensure suitability for reduction in size on printing. Axes of a graph should be clearly labelled, along the axes, outside the graph itself. All figures should be numbered with Arabic numerals, and require descriptive legends which should be typed on a separate sheet of paper. Simple straight-line graphs are not acceptable, because they can readily be described in the text by means of an equation or a sentence. Claims of linearity should be supported by regression data that include slope, intercept, standard deviations of the slope and intercept, standard error and the number of data points; correlation coefficients are optional.

Photographs should be glossy prints and be as rich in contrast as possible; colour photographs cannot be accepted. Line diagrams are generally preferred to photographs of equipment. Computer outputs for reproduction as figures must be good quality on blank paper, and should preferably be submitted as glossy prints.

Nomenclature, abbreviations and symbols. In general, the recommendations of IUPAC should be followed, and attention should be given to the recommendations of the Analytical Chemistry Division in the journal *Pure and Applied Chemistry* (see also *IUPAC Compendium of Analytical Nomenclature, Definitive Rules*, 1987).

References. The references should be collected at the end of the paper, numbered in the order of their appearance in the text (*not* alphabetically) and typed on a separate sheet.

Reprints. Fifty reprints will be supplied free of charge. Additional reprints (minimum 100) can be ordered. An order form containing price quotations will be sent to the authors together with the proofs of their article.

Papers dealing with vibrational spectroscopy should be sent to: Dr J.G. Grasselli, 150 Greentree Road, Chagrin Falls, OH 44022, U.S.A. Telefax: (+1-216) 2473360 (Americas, Canada, Australia and New Zealand) or Dr J.H. van der Maas, Department of Analytical Molecular Spectrometry, Faculty of Chemistry, University of Utrecht, P.O. Box 80083, 3508 TB Utrecht, The Netherlands. Telefax: (+31-30) 518219 (all other countries).

0003-2670/94/$07.00

This issue is printed on acid-free paper.

PRINTED IN THE NETHERLANDS

COAL

Typology - Physics - Chemistry - Constitution

Third, Completely Revised Edition

By **D.W. van Krevelen**

The first edition of the book *"Coal: Typology - Chemistry - Physics - Constitution"* appeared in 1961. In 1981 a new edition was published in which the text was unaltered proving that after 20 years the book was still considered a standard work in its field. The enormous activities in the 80's in the field of coal conversion processes (especially gasification and liquefaction) and the equally amazing development of instrumental techniques of observation and analysis prompted a complete revision and update of the book. The present edition contains almost 1000 pages compared to the 514 pages of its predecessors of 1961 and 1981. The number of illustrations has greatly increased from 253 to 574 and that of the tables from 76 to 208. These figures amply testify to the increase in coal research.

Compared with its former editions, the present book treats a considerable number of new subjects: modern concepts of geotectonics and of organic geochemistry; the problem of pseudohomogeneity of vitrinite; developments of the classification and systematics of coals and coal components (macerals); an exposé on electron microscopy and the most important instrumental physical methods of analysis (FTIR, NMR, ESCA and analytical pyrolysis combined with gas chromatography and mass spectroscopy); the principles of physical-statistical structure analysis based on the concept of additivity of a large number of molar functions; a revision of Seyler's ideas of discrete steps in coalification; an essay on coal fluorescence; and the survey on magnetic properties - magnetic susceptibility and magnetic resonance - is considerably enlarged. completely new chapter is added on cohesion and adhesion phenomena as found in coals. The chapter on solvent extraction and solubilisation is significantly enlarged and new concepts are discussed. The actions of hydrogen, molecular oxygen and oxidising agents on coal are updated and a newly written chapter treats the *"grand processes"* of coal conversion (combustion, gasification, carbonisation and liquefaction). Coal constitution in its diverse aspects is revised with a practically complete survey of many proposed coal models. Essays on synthetic coal analogues and on the simulation of natural coalification are added. Also new is the compendium, a set of comprehensive tables, containing the most important numerical data of this book in a fully comparative form.

Every chapter has its own bibliography, divided into general references (leading books on the treated subject) and special references, which are quotations of scientific papers discussed in the text. The extensive subject index, complete index of names and the compendium are provided in order to facilitate usage as an encyclopedic work.

Contents:

© 1993 Hardbound
Price: Dfl. 695.00 (US $ 397.00)
ISBN 0-444-89586-8

ORDER INFORMATION

For USA and Canada
ELSEVIER SCIENCE INC
P.O. Box 945
Madison Square Station
New York, NY 10160-0757
Fax: (212) 633 3880

In all other countries
ELSEVIER SCIENCE B.V.
P.O. Box 330
1000 AH Amsterdam
The Netherlands
Fax: (+31-20) 5862 845

US$ prices are valid only for the USA & Canada and are subject to exchange rate fluctuations; in all other countries the Dutch guilder price (Dfl.) is definitive. Customers in the European Community should add the appropriate VAT rate applicable in their country to the price(s). Books are sent postfree if prepaid.

ELSEVIER SCIENCE B.V.